Experimental study of fluid setting in natural porous media : application to reservoir rocks

Victor de Oliveira Fernandes

université de BORDEAUX

THESIS PRESENTED

TO OBTAIN THE QUALIFICATION OF

DOCTOR OF
THE UNIVERSITY OF BORDEAUX

DOCTORAL SCHOOL OF PHYSICAL SCIENCES AND

ENGINEERING

By Victor DE OLIVEIRA FERNANDES

Experimental study of fluid setting in natural porous media: Application to reservoir rocks

Under the supervision of Henri BERTIN

co-supervisors: Cyril CAUBIT and Jean LACHAUD

Presented on April 28th, 2023, before the jury composed of:

Mrs. AHMADI-SENICHAULT, Azita	Professor	ENSAM	President
Mr. FLEURY, Marc	Research Engineer	IFP Energies Nouvelles	Reviewer
Mr. ROSSEN, William	Emeritus Professor	TU Delft	Reviewer
Mr. BROSETA, Daniel	Professor	UPPA	Examiner
Mr. CAUBIT, Cyril	Research Engineer	TotalEnergies	Examiner
Mr. NICOT, Benjamin	Research Engineer	TotalEnergies	Examiner
Mr. BERTIN, Henri	Emeritus Research Director	University of Bordeaux	Supervisor
Mr. LACHAUD, Jean	Associate Professor	University of Bordeaux	Co-supervisor
Mr. NONO, Franck	Research Engineer	MODIS	Invited
Mr. PAIROYS, Fabrice	Research Engineer	TotalEnergies	Invited

Titre : Etude expérimentale de la mise en place de fluides dans des milieux poreux naturels : Application à des roches réservoir

Résumé : Dans le cadre de l'estimation et prévision de la productivité d'un réservoir d'hydrocarbures, la Perméabilité Relative (K_r) et la Pression Capillaire (P_c) lors des écoulements diphasiques sont des paramètres indispensables aux simulations numériques. Ces deux facteurs ne peuvent être obtenus qu'expérimentalement dans des laboratoires pétrophysiques, qui réalisent des expériences d'écoulement sur des échantillons de roche prélevés dans le réservoir à analyser. Dans le parcours de l'échantillon du réservoir au laboratoire, des modifications en termes de pression et température peuvent engendrer des changements du niveau de saturation et de la mouillabilité, qui ne seront plus représentatifs des conditions du réservoir.

Pour ré-établir ces conditions, une restauration d'états est réalisée. Cela consiste à laver l'échantillon pour éliminer l'huile native, les filtrats de boue de forage, des potentiels sels précipités et l'eau connée. Dans ce processus, de l'eau, du CO_2 et une variété de solvants organiques peuvent être utilisés pour assurer un lavage approprié, destiné à produire un échantillon mouillable à l'eau. Le lavage est suivi d'un séchage à l'étuve, ainsi qu'à un balayage de diazote (N_2). Ensuite, l'établissement de la saturation initiale en eau (S_{wi}) est réalisé, dans un processus appelé premier drainage, qui reproduit la phase de migration des hydrocarbures de la roche mère vers le réservoir. L'obtention d'une valeur de S_{wi} représentative de l'état initial du réservoir après le premier drainage est d'une grande importance, dès lors qu'elle impacte différents paramètres, tels que la saturation résiduelle, la perméabilité relative, la mouillabilité et la continuité des phases. La restauration d'états est finalisée avec une phase de restauration de la mouillabilité, aussi appelée macération, durant laquelle un vieillissement de l'échantillon dans l'huile brute en température est réalisé. Idéalement, l'injection de l'huile brute se fait en alternant les faces d'injection pendant la phase de macération. Cela permet la génération d'un profil de mouillabilité homogène.

Le travail de recherche présenté dans cette thèse vise à établir une comparaison claire entre les différentes techniques connues de mise en place du S_{wi} dans un système eau/huile sur des échantillons de roche de différentes dimensions, lithologies, perméabilités et porosités. On réalise une étude des impacts du choix d'une technique par rapport à une autre sur les principaux paramètres pétrophysiques (profils de saturation, K_r, P_c et mouillabilité) lors des phases de drainage et d'imbibition. En outre, pour concevoir un cycle expérimental optimal au vu des contraintes des techniques existantes, une nouvelle méthode de premier drainage a été conçue (Technique de Drainage Hybride - HDT), combinant les avantages de deux techniques classiques – le Déplacement Visqueux (VOF) et la Plaque Poreuse semi perméable (PP). L'utilisation d'outils d'imagerie à différentes échelles d'observation telles que la Résonance Magnétique Nucléaire (RMN - échelle du plug) et la Micro-Tomographie (µ-CT - échelle du pore), permettent une compréhension claire du comportement de l'échantillon soumis à des cycles expérimentaux de mesure de la K_r eau/huile et des tests de mouillabilité de type Amott-Harvey, supportant les hypothèses formulées lors de l'interprétation des résultats.

Les expériences imagées par RMN et µ-CT montrent que la méthode HDT est capable d'atteindre la valeur correcte de S_{wi} avec un profil de saturation homogène pour tous les cas étudiés. De plus, l'imagerie par RMN montre que l'injection par les deux faces pendant la macération est efficace pour générer un profil de mouillabilité homogène. Pour finir, une étude comparative du calage historique de l'imbibition de deux échantillons bimodaux initiés par VOF et HDT montrent que, parmi les deux, seul la méthode HDT nous permet d'accéder à la totalité du réseau poreux, ce qui est représentatif du comportement du réservoir.

Mots clés : Premier drainage, états initiaux, SCAL, mouillabilité, milieux poreux

---

Title: Experimental study of fluid setting in natural porous media: Application to reservoir rocks

Abstract: In the context of estimating and predicting the productivity of a hydrocarbon reservoir, the Relative Permeability (K_r) and the Capillary Pressure (P_c) in two-phase flow are essential parameters for numerical simulations. These two factors are exclusively obtained experimentally in petrophysical laboratories, which perform flow experiments on rock samples taken from the reservoir. As soon as the sample is drilled in the reservoir until its arrival in the laboratory, changes in pressure and temperature may modify fluid saturation and wettability, which will no longer be representative of the reservoir conditions.

To re-establish these conditions, a state restoration is performed. This consists of cleaning the sample to remove native oil, mud filtrates, potential precipitated salts, and connate water. In this process, water, CO_2, and a variety of organic solvents can be used to ensure proper cleaning to produce a water-wet sample. Cleaning is followed by conventional or vacuum-drying as well as flow through drying by nitrogen (N_2). The next step consists in setting initial water saturation (S_{wi}), in a process called primary drainage, which mimics the migration phase of hydrocarbons from the source rock to the reservoir. Obtaining a value of S_{wi} representative of the initial state of the reservoir after the primary drainage step is of great importance, since it impacts different parameters, such as residual saturation, relative permeability, wettability, and phase continuity. State restoration is finalized by a wettability restoration phase, also called ageing, while the sample is aged in crude oil at high temperature (typically 80 °C). Ideally, the injection of the crude oil is performed by alternating the injection faces during the ageing phase. This produces a homogeneous wettability profile.

This research study aims to establish a clear comparison between the different known techniques of primary drainage in a water/oil system on rock samples of different dimensions, lithologies, permeabilities and porosities. A study of the impacts of the choice of one technique over another on the main petrophysical parameters (saturation profiles, K_r, P_c and wettability) during the drainage and imbibition phases is performed. In addition, in order to design an optimal experimental cycle within the constraints of the existing techniques, a new method of primary drainage was designed (Hybrid Drainage Technique - HDT), combining the advantages of two classical techniques - Viscous Oil Flood (VOF) and Porous Plate (PP). The use of imaging techniques at different scales of observation with Nuclear Magnetic

Resonance (NMR - plug scale) and Micro-Tomography (µ-CT - pore scale), allow a clear understanding of the behavior of the sample submitted to experimental cycles of water/oil K_r definition and Amott-Harvey wettability tests, supporting the hypotheses assumed during the results interpretation.

The experiments imaged by NMR and µ-CT show that the HDT method is able to reach the correct S_{wi} target value with a homogeneous saturation profile for all the cases studied. Furthermore, NMR imaging shows that injection from both sides during ageing is efficient in generating a homogeneous wettability profile. Finally, a comparative study of the imbibition history-match of two bimodal samples initiated by VOF and HDT show that only the HDT method is able to access the entire pore network, which is representative of the reservoir behavior.

Keywords: Primary drainage, restored state, SCAL, wettability, porous media

---

Ecole Doctorale des Sciences Physiques et de l'Ingénieur

Acknowledgements

This thesis was carried out in collaboration between the Université de Bordeaux I and the I2M Laboratory and was financed by TotalEnergies by means of a CIFRE agreement. Therefore, I would like to thank the ANRT for having offered me the opportunity to carry out my thesis, and Mr. Laurent MAHO for the reception in the Petrophysics Laboratory of the CSTJF in Pau.

I would also like to thank Mr. Marc FLEURY and Mr. William ROSSEN for accepting the role of reviewers of this work, and Mr. Daniel BROSETA for the role of examiner. Moreover, I would like to thank Mrs. Azita AHMADI-SENICHAULT not only for presiding the jury, but also for being the lecturer of my first multiphase flow in porous media class back in 2016.

I thank Mr. Henri BERTIN not only for being my thesis director, but especially for showing me the beauty of scientific research and the different applications of flow in porous media. I thank him for his precise, subtle advice, always accompanied by good humor and affection. Thank you for giving me the opportunity to come back to France.

To Mr. Jean LACHAUD, thank you for your work of co-direction, your advice, and proposals. Thank you for always pushing me to integrate the TREFLE laboratory team, despite the distance and limitations imposed by the pandemic.

To Mr. Cyril CAUBIT, thank you for guiding me during these three years and showing me the complexity of the applied petrophysics. Thanks for the support, for giving me the freedom to interpret the subject in a way I did not think possible, and for always believing in me.

To Mr. Benjamin NICOT, Mr. Franck NONO and Mr. Fabrice PAIROYS, I thank you not only for accepting to participate in this jury, but for always, always receiving me with a smile when I landed in your offices with doubts, ideas, or uncertainties. Thank you for introducing me to the NMR, X-ray tomography and numerical simulation domains. I am deeply sincere when I say that it is an honor to be able to share the laboratory with professionals like you.

To Mr. Gerald HAMON, thank you for all the developed and well-shared knowledge about the Petrophysics domain, most precisely the states and wettability restoration.

I would like to thank all of those who have dedicated themselves to make the laboratory a pleasant place to be. In the Petrophysics lab of the CSTJF, I met amazing people that I hope to take with me for the rest of my life. I am afraid I will not mention them all, but I keep a special thought for Quentin, Laurent, Sandrine, Ata, Sophie, Nathalie, Regis, Pierre-Edouard, Manon... There are so many of them!

A really special thanks is addressed to Ana Luiza, my wife. She is the greatest partner I could have asked for. Thanks for dreaming my dream with me and help making it real. Nobody said it was easy, but with your love and support, I was able to make it through. You were the light to guide and ignite me every day. I love you.

I would like to thank my family, especially my parents, Magdo and Wanderleia, for the support, love, care and encouragement. I hope the path I follow makes you proud of your son. I love you.

I also think of everyone who, even on the other side of the ocean, gave me support along this journey. I think with affection to my *belle famille*, Mario, Graziela and Savio, my aunts, uncles, cousins, and friends, without whom life would be much less fun. Among these, I think fondly of Árthur and Kauê.

SUMMARY

Nomenclature 21
INTRODUCTION 25
1. Multiphase Flow in Porous Media 28
1.1. Petroleum Formation and Migration 28
1.2. Definition of porous media 30
1.2.1. Rock surfaces 30
1.2.2. Porosity 30
1.2.3. Fluid saturation 31
1.2.4. Permeability 31
1.2.5. Representative Elementary Volume (REV) 32
1.3. Interfacial curvature and Contact angle 33
1.3.1. Interfacial tension 33
1.4. Capillary pressure 34
1.4.1. Definition 34
1.4.2. Young-Laplace equation 34
1.4.3. Leverett-J function 36
1.4.4. Mercury Injection Capillary Pressure (MICP) 37
1.5. Wettability 38
1.5.1. Definition 38
1.5.2. Wettability alteration 39
1.5.3. Wettability tests 42
1.6. General characteristics of flow in porous media 45
1.6.1. Navier-Stokes Equations 45
1.6.2. Reynolds Number 46
1.6.3. Darcy's Law 46
1.7. Relative Permeability 48
1.7.1. Definition 48
1.7.2. Kr determination 50
1.7.3. Kr models 50
1.7.4. Effects of wettability on relative permeability and capillary pressure curves 52
1.7.5. Capillary number 56
1.7.6. Bond number 57
1.8. Conventional and Special Core Analysis 58

1.8.1. Initial States approaches 58
1.8.2. Typical experimental workflow – restored-state method 59
1.8.3. Primary drainage techniques 63
1.8.4. Impacts of wettability heterogeneities on flow in core samples 68
1.8.5. Waterflooding techniques 70
2. Imaging Techniques 73
2.1. Nuclear Magnetic Resonance 73
2.1.1. The nuclear spin 73
2.1.2. The vector model 75
2.1.3. The rotating frame 76
2.1.4. Signal detection 76
2.1.5. NMR relaxation measurements 78
2.1.6. Basic principles of MRI 84
2.1.7. NMR application to Petrophysics 85
2.2. Computed X-ray micro-tomography 90
2.2.1. Image segmentation 91
2.2.2. Differential imaging 93
3. Materials & Methods 95
3.1. Solid and fluid properties 95
3.1.1. Solids 95
3.1.2. Fluids 102
3.2. Methodology 104
3.2.1. Core cleaning and drying 105
3.2.2. Pore volume (Vp) determination 106
3.2.3. Steady-state gas permeability (Kg) 108
3.2.4. Brine saturation and steady-state (Kw) 109
3.2.5. Primary Drainage techniques 110
3.2.6. Ageing 115
3.2.7. Waterflooding 116
4. Results 117
4.1. Primary drainage challenges 117
4.1.1. Reaching the target Swi 117
4.1.2. Obtaining a homogeneous Swi profile 129
4.2. Wettability challenges 166
4.2.1. Wettability alteration 167

4.3. Waterflooding results (Viscous Oil Flood *versus* Hybrid Drainage Technique) 189
5. Conclusions and future work 199
5.1. Primary drainage 199
5.1.1. Viscous Oil Flood 199
5.1.2. Centrifugation 199
5.1.3. Porous Plate 200
5.1.4. Hybrid Drainage Technique 200
5.2. Ageing 200
5.3. Waterflooding comparison 201
5.4. Future work 201
6. References 203

LIST OF FIGURES

Figure 1 - Schematic representation of a petroleum reservoir (Tiab & Donaldson, 2015) 28

Figure 2 - Different scales of observation of porous media (Yra, 2006). 29

Figure 3 - Representation of a rock matrix with three sizes of grains: bigger in clear gray, medium in medium gray, smaller in darker gray and pores in white. 31

Figure 4 - Evaluation of porosity through a Representative Elementary Volume (modified from Helmig, 1997). 32

Figure 5 - Representation of the interface with two different curvatures between two fluids (Blunt, 2017) 35

Figure 6 - Expansion of the interface following both curvatures between two liquids (Blunt, 2017)..... 35

Figure 7 - Representation of the capillary rise experiment. 36

Figure 8 - Drainage and imbibition tests performed to the validation of the Leverett-J Function (Leverett, 1941). 37

Figure 9 - Representation of different wettabilities to the rock surface (Blunt, 2017). 38

Figure 10 - Effective contact angle and equivalent smooth surface in the Wenzel regime (Blunt, 2017). 39

Figure 11 - Schematic relation of disjoining pressure to wetting film thickness (Kovscek, Wong, & Radke, 1993) 40

Figure 12 - Representation of an asphaltene invasion on a water film. 40

Figure 13 - Representation of a pore previously fully water-saturated invaded by oil that changed the wettability where the green lines are thicker. 41

Figure 14 - Schematic representation of the cells used for spontaneous displacements. In the right, the spontaneous imbibition and in the left the spontaneous drainage (Oil in green and Water in blue) 43

Figure 15 - Typical curves for Spontaneous Imbibition (dashed) and Forced Imbibition (solid) 44

Figure 16 - Typical curves for Spontaneous Drainage (dashed) and Forced Drainage (solid) 44

Figure 17 - USBM method for wettability determination (Zinszner & Pellerin, 2007) 45

Figure 18 - Classic Darcy's experiment of injection of water in a sand pack column (Darcy, 1856). 48

Figure 19 - Schematic example of water-wet imbibition relative permeability and capillary pressure curves. 53

Figure 20 - Schematic representation of oil-wet imbibition relative permeability and capillary pressure curves. 54

Figure 21 - Representation of the mixed-wet case according to the description given by Blunt (2017) - relative permeability and capillary pressure imbibition curves. 56

Figure 22 - Capillary number correlation to additional oil recovery (Morrow et al., 1988). 57

Figure 23 - Example of a Klinkenberg gas permeability plot. 61

Figure 24 - Representation of experimental data obtained in USS Viscous Oil Flood. 64

Figure 25 - NMR imaging of the water saturation profile of a Bentheimer sandstone at the end of a Viscous Oil Flood (VOF) primary drainage. Capillary end effects are clearly visible close to the sample outlet. 65

Figure 26 - Bentheimer sandstone submitted to VOF followed by flow direction reversal – NMR profiles imaging. It is possible to observe a general imbibition of the brine present in the last cm after the last step of VOF (green line) on the final profile (orange-dashed line). 66

Figure 27 - Water saturation profile acquired by NMR after a Centrifuge primary drainage of a Bentheimer sandstone. Once again, the presence of CEE is clearly noticed close to the outlet. This experiment will be treated in more detail in the results section. 67

Figure 28 - Centrifugation primary drainage of a Bentheimer sandstone, imaged by NMR. The black solid line represents the water saturation profile following the first injection direction. The greend solid line represents the saturation profile after injection direction reversal. 67

Figure 29 - Water saturation profile of a Bentheimer sandstone after Porous Plate primary drainage, imaged by NMR. 68

Figure 30 - Schematic example of experimental data obtained during an unsteady-state waterflooding. 71

Figure 31 - Schematic example of mislead in the direct measurement of $Keff$ during USS waterflooding 72

Figure 32 - Representation of the Zeeman diagram for the ^{1}H nucleus in the presence of a magnetic field $\boldsymbol{B}0$, ... 74

Figure 33 - Schematic representation to the magnetic moments when there is no external applied magnetic field (a) and when there is an external applied magnetic field (b) (Ward-Williams, 2020). 75

Figure 34 - Schematic illustration of the Bloch vector model and the rotating frame of reference: (a) shows $\mathbf{M}_0$ precessing about $\mathbf{B}_0$ at $\boldsymbol{\omega}_0$ and (b) and (c) **M** precessing about B0 and B1 due to additional RF field $\mathbf{B}_1$ in the laboratory and in the rorating frame of reference (Bush, 2019). 76

Figure 35 – Schematic example of a time domain signal (a), and resultant NMR spectrum on the frequency domain (b), after Fourier transformation. Both real and imaginary parts are represented in the figures (Ward-Williams, 2020). 77

Figure 36 - Spin-lattice relaxation recovery pulse sequence. 78

Figure 37 - CPMG pulse sequence. 79

Figure 38 - Inversion recovery and CPMG pulse sequence for T1-T2 correlation experiments. 80

Figure 39 - Spatial T_1 pulse sequence. 82

Figure 40 - Spatial T_2 pulse sequence. 83

Figure 41 - Stimulated echo CPMG pulse sequence for the acquisition of D-T_2 response. 83

Figure 42 - SE-SPI NMR pulse sequence for measuring volume profiles in core samples. 85

Figure 43 - Example of (a) T_2 pulse relaxation sequence and (b) MICP on an Estaillades limestone (Tanino & Blunt, 2012). The dual-porosity characteristics of the sample are clear on both graphics. 86

Figure 44 - Schematic example of a T_2 relaxation measurement where oil and brine are separated by different relaxation mechanisms. Oil experiments a bulk fluid relaxation mechanism, related to its viscosity, and brine, experiments a surface relaxation mechanism, which is related to its surface to volume ratio (Fleury, 1998). 87

Figure 45 - Schematic representation of a T_1 - T_2 experiment, showing the effect of oil-wetness increase. 88

Figure 46 - Schematic representation of a T2,Diff chart, showing the oil and water signals and the trends for water and oil-wetness, pore size distribution and fluid viscosity. 89

Figure 47 – Schematic representation of a spatially-resolved T_2 relaxation time distribution a water-wet sample partially saturated in water and low-viscosity oil. 90

Figure 48 - Zeiss Xradia Versa 520 X-ray micro-CT and the Multi-Imagery cell. 91

Figure 49 - In the left we are able to observe dry raw image. In the right is shown the same image after a non-local means denoising. 92

Figure 50 - Grayscale histogram of an Estaillades at residual oil saturation. The first peak on the left represents the oil phase, the intermediate peak, the brine, and the biggest representation is the rock matrix. 92

Figure 51 - Segmented image of a dry Bentheimer sample. 93

Figure 52 - T_2 relaxation time distribution test on a brine saturated Bentheimer sandstone. 96

Figure 53 - Bentheimer sandstone primary drainage capillary Pc versus Sw curve (Porous Plate technique). 96

Figure 54 - T_2 relaxation time distribution test on a brine saturated Richemont limestone. 98

Figure 55 - Richemont limestone primary drainage capillary Pc versus Sw curve (Porous Plate technique). 98

Figure 56 - T_2 relaxation time distribution test on a brine saturated Estaillades limestone. 100

Figure 57 - T_2 relaxation time distribution for an oil-saturated Estaillades sample. 100

Figure 58 - Estaillades limestone primary drainage capillary Pc versus Sw curve (Porous Plate technique). 101

Figure 59 - T_2 Relaxation Time Distribution for R1 saturated in brine. 102

Figure 60 - Typical experimental workflow for a W/O waterflooding. 105
Figure 61 - Schematic representation of a Soxhlet extractor. 105
Figure 62 - Schematic representation of a pycnometer. 106
Figure 63 - Steady-state Kg measurement apparatus. 108
Figure 64 - Schematic representation of a Kw measurement setup. 109
Figure 65 - Example of a Kw set of datapoints for a Bentheimer sandstone sample. 110
Figure 66 - Classic Viscous Oil Flood setup. 111
Figure 67 - Porous Plate experimental setup. 112
Figure 68 - Schematic representation of the overburden cell. 114
Figure 69 - Schematic representation of the method, showing both fluid outlets. .. 115
Figure 70 - Schematic illustration of the experimental setup used for USS waterflooding. 116
Figure 71 - T_2 Relaxation Times distribution at the end of each step (BEN-VOF-01) – Isopar-L™ bulk relaxation time is represented by the green vertical line and the brine used (B1) is invisible in the T_2 spectrum. 118
Figure 72 - Water saturation profiles at the end of each flowrate step (BEN-VOF-01). 119
Figure 73 – History match of dP for the primary drainage of BEN-VOF-01. 119
Figure 74 – History match of water production (Vw) during BEN-VOF-01 primary drainage. 120
Figure 75 – History match of the Sw profiles obtained during BEN-VOF-01 primary drainage. 120
Figure 76 – Primary drainage Kr and Pc curves obtained from numerical simulation of BEN-VOF-01. 121
Figure 77 - T2 relaxation time distribution for the Estaillades sample using B3. 122
Figure 78 - Comparison of T_2 relaxation time distribution between EST-VOF-01 and the Estaillades limestones sample used in the study of Tanino & Blunt (2012). 123
Figure 79 - Comparison of the PTR distribution (MICP) between a twin sample of EST-VOF-01 and the sample used in the study of Tanino & Blunt (2012). 123
Figure 80 - Water saturation profiles at the end of each flowrate step using Marcol™-52 (EST-VOF-01). 124
Figure 81 - dP monitoring during EST-VOF-01 primary drainage. It is possible to notice that Q7 was prematurely stopped. The reason is the observation of a coloration in the outlet tubing that could mean fines migration. 125
Figure 82 - Final profile performed with Marcol™-52 and two following flowrate steps using FINAVESTAN-A-180B. 125
Figure 83 - Pore-entry capillary pressure versus Frequency for the Estaillades limestone samples. 126

Figure 84 - Capillary pressure field along the sample longitudinal axis during Q7 injection (EST-VOF-01). 126

Figure 85 - History-match of the experimental dP points during EST-VOF-01 primary drianage. 127

Figure 86 - History-match of the experimental water recovery (Vw) points during EST-VOF-01 primary drainage. 127

Figure 87 - History-match of the experimental Sw profiles at the end of each flowrate step during EST-VOF-01 primary drainage. 127

Figure 88 - Primary drainage Kr and Pc curves after history match of dP, Vw and Sw profiles. Marks in the $\boldsymbol{Kr}$ curves figure are originally from the work of (Ott et al., 2015). Dark marks in the Pc curve figure are originated from EST-PP-01. 128

Figure 89 - Brine production during BEN-CEN-01 centrifugation. 129

Figure 90 - Water saturation profile at the end of centrifugation (BEN-CEN-01). ... 130

Figure 91 - Brine production during initial centrifugation (blue line) and after swapping the orientation of the sample inside the centrifugation bucket (orange line). 130

Figure 92 - Water saturation profiles before and after swapping sample orientation inside the centrifuge bucket. 131

Figure 93 - Sw profiles advancing during EST-CEN-01 primary drainage by centrifugation. 132

Figure 94 - Sw profiles before and after swapping the plug orientation inside the centrifuge bucket. 132

Figure 95 - T_2 Relaxation Time distribution for BEN-VOF-01 at 4th Step of VOF and after reverse flow. Fluids saturating the sample are Isopar-L™ and B1. 133

Figure 96 - Water saturation profiles after flow reversal at the end of VOF (BEN-VOF-01). 133

Figure 97 - Comparison between the Viscous Oil Flood (OF in the figure) and the Porous Plate (PP) methods during primary drainage. There are two representations for each technique: the one in the left-hand side includes the main percolating cluster (in magenta for OF and in blue for the PP) and the images on the right-hand side had the main percolation cluster removed. 134

Figure 98 - Comparison between last step of viscous flooding and after injection sense reversal (in green). 134

Figure 99 - Brine production versus time for BEN-PP-01 and BEN-PP-02 primary drainage by Porous Plate. 136

Figure 100 - Saturation profiles advancing during Step 1 of BEN-HDT-01 ($Pc = 80\ mbar$). 137

Figure 101 - Elimination of capillary end-effects during Step 2 of BEN-HDT-01 ($Pc = 80\ mbar$). 137

Figure 102 – Saturation profiles advancing during Step 1 of BEN-HDT-02 ($Pc = 110\ mbar$). 138

Figure 103 – Elimination of CEE during Step 2 of BEN-HDT-02 ($Pc = 110\ mbar$). 138

Figure 104 - Brine production versus experimental time for samples RCH-PP-01 and RCH-PP-02. 139

Figure 105 - Water saturation profiles advancing during Step 1 of HDT (RCH-HDT-01 at Q = 3 cc/h)..... 140

Figure 106 - Elimination of capillary foot during Step 2 of RCH-HDT-01 at $Pc = 3.875\ bar$. 140

Figure 107 - Water saturation profiles advancing during Step 1 of HDT for RCH-HDT-02 ($Pc = 5\ bar$)..... 141

Figure 108 - Profiles homogenization during Step 2 of HDT for RCH-HDT-02 ($Pc = 5\ bar$). 141

Figure 109 - Experimental duration comparison for Bentheimer samples. 142

Figure 110 - Experimental duration comparison for Richemont samples. 142

Figure 111 - Pc versus Sw curve of EST-PP-01. 144

Figure 112 - RI versus Sw for EST-PP-01. 144

Figure 113 - T_2 Relaxation Time distribution of EST-HDT-01 @ $Sw = 100\%$ using B3. 145

Figure 114 - T_2 Relaxation Time distribution of EST-HDT-01 at the end of Step 1. In this case, we have Marcol^{TM}-52 and B3 as the saturating fluids. 145

Figure 115 - T_2 Relaxation Time distribution at the end of Step 1 of HDT (toluene/B3 system)..... 146

Figure 116 - Spatially-resolved T_2 of EST-HDT-01 after Step 1 of HDT. We have toluene as the oil phase and B3. The green circle highlights the porous plate $T2$ relaxation time response. 146

Figure 117 - Stack plot of T_2 relaxation time distributions curves of EST-HDT-01 after Step 1 of HDT. 147

Figure 118 - Evolution of the T_2 signal between the end of Step 1 and Step 2 of HDT (EST-HDT-01) using toluene and B3..... 148

Figure 119 - Spatial T_2 measurement of EST-HDT-01 at the end of Step 2 of HDT. Saturating fluids are still B3 and toluene. 148

Figure 120 - Stack plot of T_2 relaxation time distribution curves of EST-HDT-01 at the end of Step 2 of HDT..... 149

Figure 121 - Water saturation evolution after transition from Step 1 to Step 2 of HDT (EST-HDT-01). 149

Figure 122 - Sw profile of EST-HDT-02 at the end of primary drainage ($Pc = 1\ bar$). 150

Figure 123 - Double-spiral diffuser used for HDT experiments of Estaillades limestone samples. 151

Figure 124 - T_2 Relaxation Time distribution for EST-HDT-03-MP at So =100% using Marcol^{TM}-52. 151

Figure 125 - SE-SPI profile for EST-HDT-03-MP at So = 100%..... 152

Figure 126 - Spatially-resolved T_2 EST-HDT-03-MP at $Sw = 100\%$..... 152

Figure 127 - Stack plot of EST-HDT-03-MP saturated with B3. 153

Figure 128 – Porosity profiles of EST-HDT-03-MP obtained by NMR. 154

Figure 129 - Scans of the same slice with different saturating fluids: B2, High-Doped brine and Marcol™-52. 155

Figure 130 - Macro, unresolved and total porosity profile of sample EST-HDT-03-MP obtained by µ-CT differential imaging. 155

Figure 131 - Macro-pores longitudinal distribution obtained by NMR and µ-CT imaging (EST-HDT-03-MP). 156

Figure 132 - Total porosity profile obtained by NMR and µ-CT imaging (EST-HDT-03-MP). 156

Figure 133 – Brine-saturated EST-HDT-03-MP. We present four slices at different positions in the sample: (a) at 2 mm from the top, (b) 10 mm, (c) 10 mm from the bottom and (d) 2 mm from the bottom. 157

Figure 134 - EST-HDT-03-MP after Step 1 of HDT. 158

Figure 135 - Zoom in on images after Step 1 of HDT. 158

Figure 136 - Sw profiles at the end of Step 1 of HDT by NMR and µ-CT (EST-HDT-03-MP). 159

Figure 137 - Share of total Sw between micro and macro porosities after Step 1 of HDT (EST-HDT-03-MP). 159

Figure 138 - Comparison between (a) and (c) slices at the end of Step 1 (subscript .1) and at the end of Step 2 (subscript .2). 160

Figure 139 - Comparison between (b) and (d) slices at the end of Step 1 (subscript .1) and at the end of Step 2 (subscript .2). 160

Figure 140 - NMR and µ-CT profiles at the end of Step 2 of HDT (EST-HDT-03-MP). 161

Figure 141 - Share of total Sw between micro and macro porosities after Step 2 of HDT (EST-HDT-03-MP). 161

Figure 142 - Water saturation variation in the micro-porosity between Steps 1 and 2 of HDT (EST-HDT-03-MP). By normalizing the water saturation to the micro-porosity itself, we eliminate effects of porosity heterogeneity. 162

Figure 143 - R1 dP and Sw response to Step 1 of HDT with R1. 163

Figure 144 - T_2 Relaxation Distribution time tests during Step 1 of HDT primary drainage with R1 in Isopar-L™ and B5. 164

Figure 145 – T_2 Relaxation Time distribution during Step 2 of HDT with R1 in Isopar-L™ and B5. 165

Figure 146 - Saturation profiles evolution during Step 2 of HDT (R1). We present the profile at the end of Steps 1 and 2 in different colors in order to highlight them from the intermediate profiles obtained during Step 2 of HDT. 165

Figure 147 - Sw profiles during R2 primary drainage by HDT. 166

Figure 148 - Swi profiles of BEN-VOF-AM-02 and BEN-VOF-AM-03. 167

Figure 149 - T2 relaxation times distribution for BEN-VOF-AM-02 and BEN-VOF-AM-03 at Swi, before ageing with crude oil. 168

Figure 150 – T_2 relaxation time distribution test of samples BEN-VOF-02 and BEN-VOF-AM-03 after ageing. 169

Figure 151 - Brine production during spontaneous imbibition (BEN-VOF-AM-02 and BEN-VOF-AM-03). 169

Figure 152 - Sw profiles after spontaneous imbibition (BEN-VOF-AM-02 and BEN-VOF-AM-03). 170

Figure 153 - Sw profiles after forced imbibition (BEN-VOF-AM-02 and BEN-VOF-AM-03). 170

Figure 154 - Sw profiles after spontaneous drainage with Marcol™-52 (BEN-VOF-AM-02 and BEN-VOF-AM-03). 171

Figure 155 – Sw profile after primary drainage by Porous Plate (EST-PP-AM-01). 172

Figure 156 - Spatially-resolved T_2 measurement before ageing with EST-PP-AM-01 in Marcol™-52 and B4. 172

Figure 157 – Sw volume profiles before and after ageing (EST-PP-AM-01). 173

Figure 158 – Superimposition of T2 relaxation time distribution tests performed prior and after ageing with EST-PP-AM-01 in Marcol™-52 and B4. 173

Figure 159 - Spatially-resolved T_2 measurement after ageing with EST-PP-AM-01 in Marcol™-52 and B4. 173

Figure 160 – Sw profile after ageing and spontaneous imbibition, and the direction of crude oil injection during ageing (EST-PP-AM-01). 174

Figure 161 - Sw profile after forced imbibition (EST-PP-AM-01). 175

Figure 162 - Forced imbibition Pc versus Sw curve for EST-PP-AM-01. 175

Figure 163 - Sw profiles after forced imbibition and spontaneous drainage (EST-PP-AM-01). 176

Figure 164 - Pc versus Sw curve for EST-PP-AM-01 secondary drainage. We present the experimental points and the analytical Forbes correction. 177

Figure 165 - Sw profile after forced drainage (EST-PP-AM-01)..... 177

Figure 166 - dP monitoring during crude oil injection with flow reversal (EST-HDT-01). Color darkening represent time evolution, and negative values of dP represent inlet swapping as we reversed flow direction during ageing. 178

Figure 167 - T_2 curves before and after ageing (H_2O-based brine – B3 and toluene) - EST-HDT-01. 179

Figure 168 - Spatially-resolved T_2 test with EST-HDT-01 performed after ageing (Toluene as the oil phase and B4)..... 179

Figure 169 - Stack plot of the T_2 relaxation time distribution curves of EST-HDT-01 performed after ageing. 180

Figure 170 - T_2,Diff experiment for EST-HDT-01 after ageing (Marcol™-52 and B3). 180

Figure 171 - dP monitoring during crude oil injection with flow reversal (EST-VOF-01). 181

Figure 172 - Comparison of the T_2 response before and after ageing for sample EST-VOF-01 at Swi with Marcol™-52 and B4. 182

Figure 173 - T_2 Relaxation time distribution for EST-HDT-02 at Swi in crude oil (O1), after ageing (B4 as the brine phase). 183

Figure 174 - Spatially-resolved T_2 of EST-HDT-02 at Swi in crude oil (O1) after ageing (B4 as the brine phase). 183

Figure 175 - T_1/T_2 chart for EST-HDT-02 at Swi in crude oil (O1) after ageing and B4 as the invisible brine phase. 184

Figure 176 – Superimposition of T_2 results before and after ageing for EST-HDT-02 at Swi with Marcol™-52 and B4 as oil and brine phases, respectively. 184

Figure 177 - Spatially-resolved T_2 test of EST-HDT-02 at Swi with Marcol™-52 after ageing (B4 as the invisible brine phase) 185

Figure 178 - 4 sections of EST-HDT-03-MP after ageing. 185

Figure 179 – Two couples of slices in different positions in the sample where it is possible to observe brine emergence after the ageing step. 187

Figure 180 - Water saturation profiles of the macro porosity before and after ageing, and the macro porosity profile (EST-HDT-03-MP) 187

Figure 181 - Normalized macro pores Sw profiles before and after ageing (EST-HDT-03-MP). 188

Figure 182 - Sw profile of the unresolved porosity before and after ageing (EST-HDT-03-MP). 188

Figure 183 - Sw profiles after ageing obtained by NMR and µ-CT imaging (EST-HDT-03-MP). 189

Figure 184 - Comparison between T_2 Relaxation Times for EST-HDT-03-MP at Swi before and after ageing (Marcol™-52 and B4 as oil and brine phases, respectively). 189

Figure 185 - History-match of the dP experimental data of EST-VOF-01 waterflooding. 190

Figure 186 - History-match of the produced oil (VO) during EST-VOF-01 waterflooding. 191

Figure 187 - History-match of the Sw profiles during EST-VOF-01 waterflooding. . 191

Figure 188 - Kr and Pc imbibition curves for EST-VOF-01. 192

Figure 189 - History-match of the experimental dP values for EST-HDT-02 waterflooding. 193

Figure 190 - History-match of the oil production (VO) during EST-HDT-02 waterflooding. 193

Figure 191 - History-match of the water saturation profiles during EST-HDT-02 waterflooding. 194

Figure 192 - Kr and Pc imbibition curves for EST-HDT-02. 194

Figure 193 - Kr curves in linear and semi-log scale for EST-VOF-01 (lighter colors) and EST-HDT-02 (darker colors). 195

Figure 194 - Imbibition Kr and Pc curves for EST-HDT-01. 196

Figure 195 - EST-HDT-03-MP after waterflooding. The red circles highlight the smaller pores where it is possible to notice oil presence. 197

Figure 196 - Krw/Kro ratio for the waterflooding of EST-VOF-01 and EST-HDT-02. 197

Figure 197 - Average Sw profile and the normalized profiles for micro and macro porosities at Swi after ageing and at ROS (EST-HDT-03-MP). 198

Nomenclature

Abbreviations

A	Cross-section of the core plug
BT	Injected fluid breakthrough at the sample outlet
CEE	Capillary-End Effects
CEN	Centrifugation
HDT	Hybrid Drainage Technique
$ISSM$	In-Situ Saturation Monitoring
LOI	Loss on Ignition
$MICP$	Mercury Injection Capillary Pressure
NCS	Net Confining Stress
NMR	Nuclear Magnetic Resonance
PP	Porous Plate
PTR	Pore Throat Radius distribution
PV	Pore Volume
REV	Representative Elementary Volume
ROS	Experimentally-obtained Residual Oil saturation after waterflooding
$SCAL$	Special Core Analysis
SS	Steady-state technique for waterflooding
USS	Unsteady-state technique for waterflooding
VOF	Viscous Oil Flood
XRF	X-Ray Fluorescence test

Chemical formulations

Al_2O_3	Aluminum Oxide
BaO	Barium Oxide
$CaCl_2$	Calcium Chloride
CaO	Calcium Oxide
D_2O	Deuterium Oxide

Fe_2O_3	Ferric Oxide
KCl	Calcium Chloride
KI	Potassium Iodide
K_2O	Potassium Oxide
$MgCl_2$	Magnesium Chloride
MgO	Magnesium Oxide
MnO_2	Manganese Dioxide
$NaCl$	Sodium Chloride
$Na2O$	Sodium Oxide
Na_2SO_4	Sodium Sulfate
$P2O5$	Phosphorus Pentoxide
SiO_2	Silicon Dioxide
$SO3$	Sulfur Trioxide
SrO	Strontium Oxide
TiO_2	Titanium Dioxide
ZnO	Zinc Oxide
ZrO_2	Zirconium Dioxide

Dimensionless Groups

B_o	Bond Number
C_a	Capillary Number
Re	Reynolds Number

Nuclear Magnetic Resonance terms

$\boldsymbol{B_0}$	Magnetic field
D	Self-diffusion constant
G	Strength of the applied magnetic field
h	Planck's constant
HI	Hydrogen Index
$\boldsymbol{M_{x,y}}$	Transverse plane magnetization

$\boldsymbol{M_z}$	Longitudinal magnetization
$\boldsymbol{P}$	Spin angular momentum
SNR	Signal to noise ratio
T_1	Spin-lattice relaxation time constant
T_2	Spin-spin relaxation time constant
TI	Inversion Time
$\boldsymbol{\gamma}$	Gyromagnetic ration
$\boldsymbol{\mu}$	Magnetic momentum
$\boldsymbol{\rho_2}$	Transverse surface relaxivity
$\boldsymbol{\tau}$	CPMG pulse time spacing
$\boldsymbol{\omega_0}$	Larmor Precession frequency

Symbols

I_{AH}	Amott-Harvey wettability index
I_o	Amott-Harvey Index to oil
I_{USBM}	United States Bureau of Mines wettability index
I_w	Amott-Harvey Index to water
$J(S_w)$	Leverett-J function
K	Boltzmann constant
K_r	Relative Permeability
$K_{o,eff}$	Oil effective permeability
$K_{row}(Swi)$	Oil relative permeability to water at Initial Water Saturation
M	Molecular mass
N_a	Avogadro's Number
N_i	Phase "i" Corey exponent
P_c	Capillary Pressure
S_i	Phase "i" saturation
S_{in}	Phase "i" normalized saturation

S_{or}	Numerically-obtained Residual Oil saturation after history-matching of exp. data
S_{wi}	Initial Water Saturation
$S_{w,irr}$	Irreducible Water Saturation
U	Intermolecular cohesion energy
V_b	Bulk volume
V_g	Grain volume
V_i	Phase "i" volume
V_p	Pore volume

Greek letters

μ	Fluid viscosity
$\Pi(h)$	Disjoining Pressure
ρ	Fluid density
σ	Interfacial Tension
Φ	Porosity
ω	Centrifuge rotational speed

INTRODUCTION

In order to study and evaluate the potential production of a petroleum reservoir, numerical simulations are performed. The inputs for the numerical simulations are mainly the relative permeability and the capillary pressure curves during water injection. These data are exclusively obtained from laboratory experiments, which reproduce several stages that the reservoir undergoes during its exploitation.

The petrophysics experiments are conducted on rock samples extracted directly from the wells of the reservoir. The scientific field encompassing the investigation and realization of the experiments and simulations is called Core Analysis. In the experimental area of core analysis, three approaches are possible in order to conduct an experimental protocol that will provide relative permeability and capillary pressure data corresponding to the production of a reservoir:

- Fresh state: samples extracted from the wells are taken to an on-site laboratory where they undergo experiments without prior conditioning.

- Native (or preserved) state: well coring is performed by using specific coring tools, that aim to prevent fluid losses and pressure shifts, which could change fluid saturation and pore occupancy. In this case, the core samples may be transported to a specialized laboratory, located far from the extraction zone. The samples are submitted to laboratory measurements without prior conditioning, as the reservoir condition is presumed to be preserved.

- Restored state: Cored samples are taken to a specialized laboratory where they will undergo state restoration prior to experimental characterization. In this case, the sample is cleaned with the objective of removing native oil, mud filtrates, precipitated salts and connate water. This step is typically followed by N_2 flush and vacuum-oven drying. Then, the sample is saturated with the formation brine and the initial water saturation (S_{wi}) is settled by injecting oil (in the case of an oil/water experiment). After reaching the target value of S_{wi}, a wettability restoration is performed by ageing the core in its own crude oil at high temperature and pore pressure. After these steps, the sample is considered to be restored to its initial state of wettability and fluid settings.

When we take a closer look into what happens inside the porous medium during petroleum formation, we understand the complexity of recreating this system and all its particularities in the laboratory.

Regarding the pore scale before petroleum formation and oil migration, we would observe a fully water-saturated system, where only water would be in place. However, throughout the ages, the decomposition of organic matter present in the system has been generating a new phase – oil – and releasing gases issued from the process. Then the fluids have been distributed inside the porous medium following the density difference. Therefore, at the top of the reservoir we mainly find the gas phase, in the intermediate layer oil, and water is present at the bottom. Nonetheless, even in the upper and intermediate layers we find water, that is called connate water.

A very important step of these experiments is recreating the system described above with the correct quantities and conditions regarding petrophysical properties. This way, scientists can mimic in the laboratory the strategy for exploring the given field, handling to engineers in simulation analysis reliable data for their prediction programs.

As the time needed to restore initial conditions of core samples in the laboratory is scarce, various techniques have been developed in order to accelerate this process, especially regarding the step of recreating petroleum migration. However, as one may expect, each technique has its advantages and drawbacks, that must be evaluated to better suit each project considering its particularities.

This research project proposes a thorough analysis and comparison between three of the most common drainage techniques and a newly developed method by testing them on outcrop and reservoir rock samples from different lithologies, porosities and permeabilities. The analyzed parameters are homogeneity of the saturation profile, target S_{wi} and wettability alteration, which are visualized by Nuclear Magnetic Resonance (NMR) imaging. Complete drainage-imbibition cycles with an intermediate change in wettability by ageing are performed for comparing Viscous Oil Flood (most common primary drainage method) and Hybrid Drainage Technique (newly developed) on Estaillades samples. These experiments were imaged by both NMR and µ-CT, for providing core and pore-scale visualization of the different steps of the experimental cycle. The history-match of the experiments was done with CYDAR® numerical simulator for obtaining drainage and imbibition Relative Permeability (K_r) and Capillary Pressure (P_c) curves.

In the first chapter, we present the state-of-the-art of multiphase flow in porous media, with emphasis in the core analysis field, as an attempt of providing an exhaustive description of the underlying physical phenomena. We detail the background and historical prelude of the main experimental methods currently used in oil/water systems in core analysis regarding relative permeability and wettability experiments.

In the second chapter, we approach the background and basic physics of the imaging tools used in this study for core imaging. We detail µ-CT image treatment and the main tests we may perform by NMR for obtaining petrophysical parameters such as fluid saturations, wettability notions and fluids placement in the porous medium.

Then we move to the methodology chapter, where we present the rocks and fluids, the experimental methods and laboratory equipment necessary for performing oil/water drainage and imbibition cycles, with further detail to the primary drainage and ageing techniques to be tested.

The results section is divided into three challenges in core samples state restoration, which are specific to three different stages in the drainage/imbibition cycle of oil/water systems:

- Primary drainage challenges:

Primary drainage challenges are essentially reaching the target S_{wi} value represented by a homogeneous saturation profile. Moreover, we show that for the same mean S_{wi} value, pore occupancy may be different depending on the primary drainage technique used. This will impact wettability restoration, thus imbibition K_r and P_c.

- Wettability restoration:

The main challenge during the ageing step is obtaining a homogeneous wettability profile. We tested the three most current approaches for showing that only crude oil injection with flow reversal is able to generate an altered, homogeneous wettability profile.

- Waterflooding:

The waterflooding part of the experimental cycle represents the step where we will obtain the data input for the history-match that will provide imbibition K_r and P_c curves, which are the parameters we seek for reservoir simulation. We compared the imbibition behavior of two Estaillades samples that were initialized by two different primary drainage techniques at the same S_{wi} (Viscous Oil Flood and Hybrid Drainage Technique). The main objective is to confirm that, even though at the same initial water saturation and having followed the same ageing protocol, samples may behave differently depending on the primary drainage technique used.

We finish this study by the conclusions and future work section, where we make a small summary of the findings, interpretations and possible future studies that could complement the findings of this research.

1. Multiphase Flow in Porous Media

1.1. Petroleum Formation and Migration

The most common rocks that can accumulate petroleum are sedimentary rocks that account for about 66% of all rocks existing on Earth (Tiab & Donaldson, 2015).

The origin of these rocks is from physical, chemical, and biological degradation of large preexisting rocks – such as igneous and metamorphic rocks – into small fragments.

The formation of sandstones, for example, is a result of the transport and deposition of quartz grains and mixed rocks fragments from degradation of igneous, metamorphic and/or other sedimentary rocks on a basin area that will be later buried by sediments that will form the top of the reservoir.

The formation of petroleum occurs in specific areas where material deposition may happen. It may be the bottom of a lake, a bay or whatever geological formation that is able to receive and store soil material. This material deposition may occur by different ways. For example, if we take the case of a subsea petroleum formation, it is the deposit of soil material and organic matter that will generate petroleum further. At a given time, this system will be covered by an impermeable cap rock that will confine this system. As the decomposition of the fossils takes place, the pressure and temperature inside the system rise, increasing the genesis of petroleum and natural gases issued from the decomposition of the organic matter. Figure 1 shows a scheme of an idealized cross-section of an anticlinal trap that shelters oil and gas.

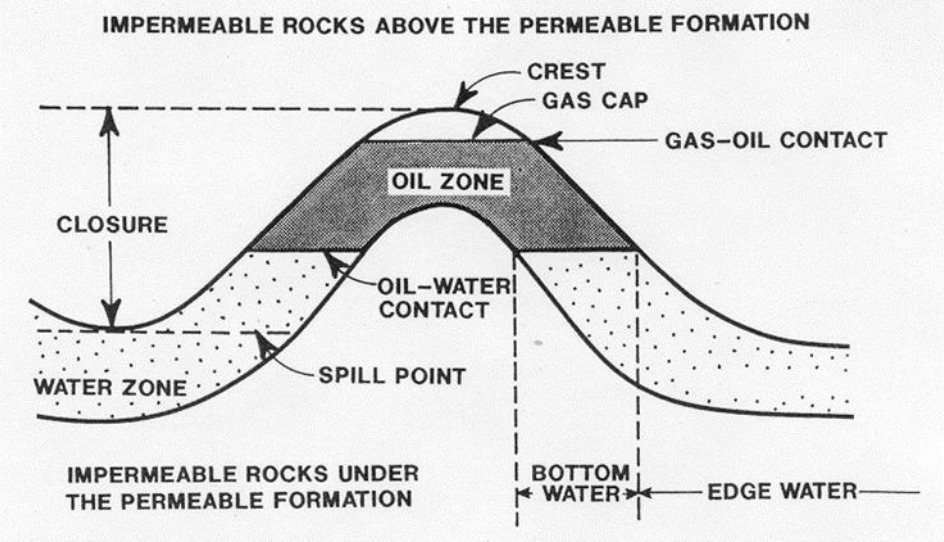

Figure 1 - Schematic representation of a petroleum reservoir (Tiab & Donaldson, 2015)

The petroleum genesis occurs in fine-grained sedimentary porous media, usually deposited in shallow marine environments during the geologic formation of a sedimentary basin. The particulate organic matter in this case is not much heavier than water, so its deposition happens together with the layers formation. At this low-energy environment, oxygen depletion leads to an anaerobic condition, where bacteria will tend to reduce organic compounds by the removal of oxygen from molecules, without attacking the carbon-carbon bonds of hydrocarbons. By further material deposition, the pressure and temperature of this environment experience a huge increase on the first formed kerogen mixed with fine-grained sediments. This process

places the materials even further out of thermodynamic equilibrium, which induces further reactions and transformations. During this stage, sediments are being compacted, reducing porosity and permeability and expelling water, while organic matter are undergoing major transformations. These conditions make kerogen evolves through liquid bitumen and liquid petroleum (Tiab & Donaldson, 2015).

After its formation, petroleum will undergo a first migration from the source rock, which is now a low porosity and extremely low permeability shale (or clays, in some cases), to the reservoir right above, where an accumulation will occur. This first expulsion happens from the application of physical stress on the source rock, where oil flows through a network of fine, thread like channels (Dickey, 1981).

The secondary migration is known as the flow from the accumulation region to the rest of the reservoir that is initially fully water-saturated. This is a slow migration process in which petroleum and gases flow upwards as a continuous phase in long filaments within the pores. Under these circumstances oil migration is driven by buoyant and hydrodynamic forces. Secondary migration ends as an accumulation in a structural stratigraphic trap, in a minimum time of one million years (Levorsen & Berry, 1967). The final configuration of a reservoir presents quite a homogeneous separation of fluids by density, which shows that individual hydrocarbon molecules are free to move within the reservoir.

One important petrophysics parameter when we analyze the pore scale is the preference of the pore surface to one fluid or another, this preference is called wettability. At first, as the pore surface had never been in contact with oil, it is essentially hydrophilic, a characteristic known in petrophysics as water wet.

The change in wettability of porous media is driven by the diffusion of some components present in the crude oil, such as phenols and pyridines, which are partially soluble in water (Cuiec, 1975). Once they manage to diffuse through the water films that covers the rock surface, they attach to the surface leaving a non-polar tail that will make a connection between the rock and the oil phase.

When dealing with multiphase flow in porous media it is important to state the different scales of observation of the porous medium itself, from the smaller (pore scale) to the bigger (reservoir scale). This can be illustrated by Figure 2 where we clearly see the different scales of interest.

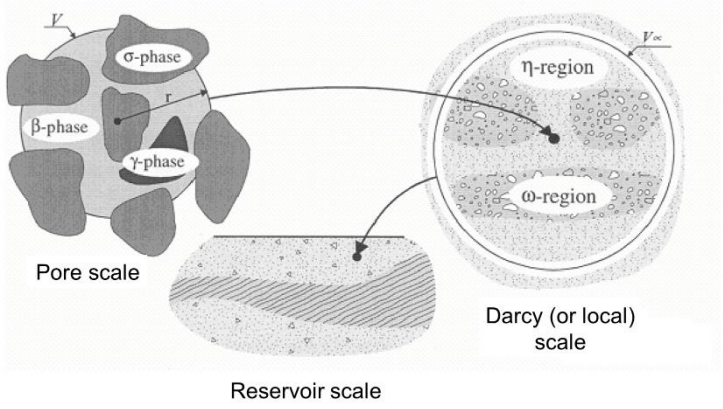

Figure 2 - Different scales of observation of porous media (Yra, 2006).

In this study, we will follow the hierarchy presented above, considering the physics at the pore scale filled by one or more fluids and move up to bigger scales. Then we will consider, in the same spirit, the movement of the fluids inside the porous media.

1.2. Definition of porous media

A porous medium may be simply defined by a matrix of solid matter that contains pores. The volume fraction of pores is called porosity. When the pores, or at least a fraction of them, are interconnected the medium is permeable and is characterized by its permeability.

In this work we focus on rock samples, so the solid matrix of porous media is composed of natural minerals that are connected by some sort of material that links the grains together. Further on we will describe the minerals that compose the rock samples.

1.2.1. Rock surfaces

The surface of the rock grains is primarily defined by the composition of the rock that prevails in the reservoir.

A sandstone reservoir is mainly composed of silica along with some other minerals. On the other hand, a carbonate reservoir is typically composed of calcium carbonate. The mineralogy of the rock has a big impact on the interactions between the rock surface and the fluids saturating the reservoir. For example, the interaction between the calcium carbonate of a limestone reservoir and brine may increase the pH of the latter, which would lead to asphaltene precipitation that would change the rock wettability.

1.2.2. Porosity

The solid components of rock samples, basically sand grains for the sandstones and particle of carbonate materials for limestones, do not combine to fit perfectly together due to their high degree of irregularity in shape. The void spaces found between them contain the fluids (liquids or gases) that form the reserve of a petroleum field. So, we define the rock porosity as the fraction of those void spaces over the total volume considered, as presented in equation (1) (Tiab & Donaldson, 2015):

$$\Phi = \frac{V_b - V_g}{V_b} = \frac{V_p}{V_b} \tag{1}$$

where Φ is the porosity, V_b is the bulk volume of the rock, V_g is the grain volume or the solid matrix volume and V_p is the pore volume of the rock.

An important aspect in the concept of porosity is that, for two packs of grains of the same dimension, the volume of pores, and thus the porosity, is not dependent on the size of the grains. This may be easily demonstrated by drawing a cube pack containing spheres representing the grains. Figure 3 shows a representation of a rock matrix with three sizes of grains. The blank spaces between the grains represent the pores.

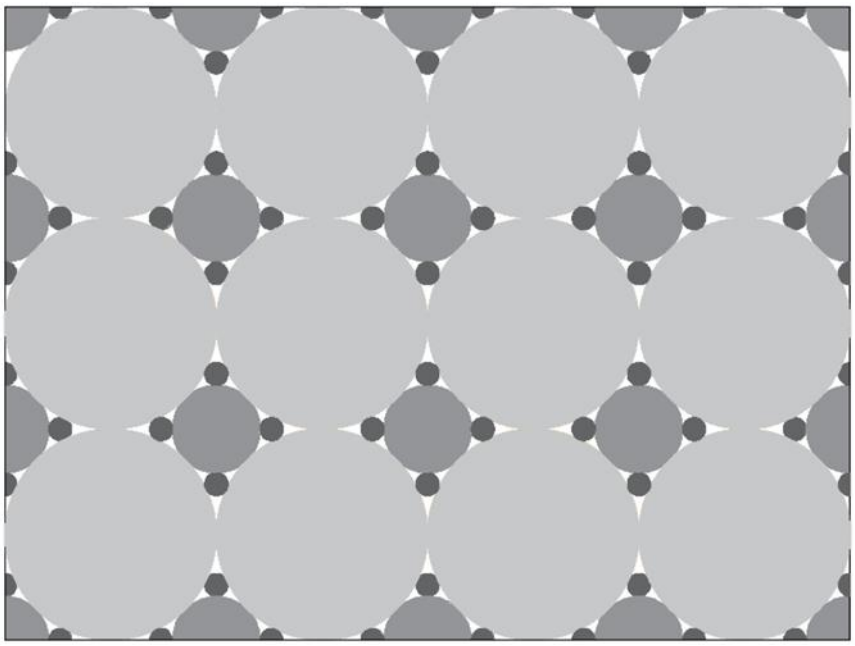

Figure 3 - Representation of a rock matrix with three sizes of grains: bigger in clear gray, medium in medium gray, smaller in darker gray and pores in white.

On the other hand, the sorting of grains sizes has a big impact on porosity, defining its quality as well as the degree of cementation, the amount of compaction during and after deposition and the method of packing (Tiab & Donaldson, 2015).

1.2.3. Fluid saturation

The voids that describe the porosity contain the fluids, representing the available volume for fluids accumulation in the porous medium. Therefore, an important parameter in order to know the reserve of hydrocarbons is the fluid saturation. It is defined as the fraction of the pore volume occupied by the phase "i", as referred in equations (2) and (3):

$$S_i = \frac{V_i}{V_p} \tag{2}$$

$$\sum_{i=1}^{n} S_i = 1 \tag{3}$$

1.2.4. Permeability

The second important physical property of a porous medium is the permeability. It is defined as the ability of the rock to let fluids flow through its pores and, differently from the porosity, the permeability is highly dependent on the grain sizes.

Grain size defines the number of restrictions found in a representative volume. Therefore, as there are more restrictions, also called pore throats, the more difficult it will be for the fluids to flow in the porous medium, thus the less permeable it will be.

The definition of the permeability is obtained from Darcy's Law (Darcy, 1856) and it will be presented in detail in the Darcy's Law section (Section 1.6.3).

1.2.5. Representative Elementary Volume (REV)

The observation of different phenomena in a porous medium is dependent upon the scale of observation, above all when we are dealing with petroleum studies. This is quite clear when we compare the scale of the reservoir (meters to kilometers), the scale of a core plug in a laboratory or the local scale (from some mm to cm), the pore scale (some microns) and the surface scale (where chemical interactions between fluid and the surface are observed).

When analyzing fluid-fluid and solid-fluids interactions, as well as grain size and distribution, pore size and homogeneity by classical fluid mechanics equations, we usually consider the pore scale. However, macroscale parameters are essential for the comprehension of the flow behavior, therefore a validation of the change of scale is necessary. For that matter, we consider a Representative Elementary Volume (REV) that must be big enough to comprehend a trustworthy observation of the parameters.

Taking the porosity as an example for the definition of REV, we can define it as in equation (4) presented below:

$$\Phi =< \gamma(\boldsymbol{x}) \geq \frac{1}{V}\int_{V} \gamma(\boldsymbol{x})\, dV \tag{4}$$

where V is the spherical domain of radius r occupied by the porous medium considered for the illustration of Figure 4 and where γ is a phase indicator defined as:

$$\gamma(x) = \begin{cases} 1, if\ \boldsymbol{x}\ \epsilon\ to\ a\ void \\ 0, if\ \boldsymbol{x}\ \epsilon\ to\ the\ solid\ matrix \end{cases}, \forall\ \boldsymbol{x}\ \epsilon\ V \tag{5}$$

The evolution of the porosity as a function of the volume of observation shown in Figure 4 helps to put in evidence the importance of the REV:

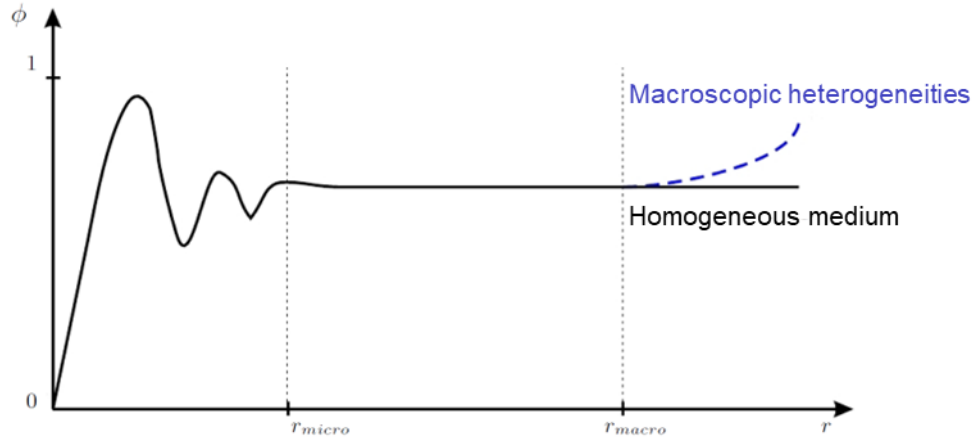

Figure 4 - Evaluation of porosity through a Representative Elementary Volume (modified from Helmig, 1997).

Between r_{micro} and r_{macro} we observe a constant value for porosity that represents a good volume of observation where the effect of scale is not sensitive. Therefore, we can say that REV must be sufficiently big to estimate the parameters relative to the pore scale and sufficiently small to be neglected when a bigger macroscopic volume of observation is considered (di Chiara Roupert, 2009).

When obeying these boundary conditions, the change from the pore scale to the local scale can be performed through the method of means, that will be used further on to describe some essential equations, like Darcy's Law.

1.3. Interfacial curvature and Contact angle

1.3.1. Interfacial tension

Before applying the general concept of interfacial tension in a porous media, let's first imagine a simpler system.

Taking two fluids in a general system, they will arrange in a way to minimize the area between them. For example, a small bubble of water in air will shape to a spherical shape once this minimizes the area of contact with air.

We can define an interfacial tension between these two fluids that is the energy per unit of area shared by the phases, or the change in free energy for a change in area, defined by equation (8):

$$\sigma = \frac{dF}{dA} \tag{6}$$

The sharing of the area by the fluids "costs" some energy, thus σ is the penalty of breaking intermolecular interactions between the two phases. This penalty differs from couple to couple, being bigger for phases with stronger intermolecular bonding (such as crystalline solid or metal) and smaller between similar fluids (such as oil and its gas under high pressure).

In an exercise to quantify the tension of some typical fluids, we briefly introduce the concept of surface tension, which is the energy per unit area of a surface between a fluid or solid and its vapor in thermodynamic equilibrium and in an isolated system. Therefore, we may denote U the intermolecular cohesion energy for one molecule of size a inside its own phase. In the interface between this phase and another will be given by $U/2$. So, we can say that the surface tension is given, approximately, by equation (7) (de Gennes, 1985; Hazlett, 1993):

$$\sigma \cong \frac{U}{2 \cdot a^2} \tag{7}$$

Considering a non-polar fluid (octane, for this example) where intermolecular interactions are largely van der Waals forces, $U \approx k \cdot T$, where $k = 1.3806\ 10^{-23}\ \frac{J}{K}$ is the Boltzmann constant. In addition, we can derive its surface tension from density and molecular mass (respectively $\rho = 703\ \frac{kg}{m^3}$ and $M = 0{,}114\ \frac{kg}{mol}$). So, we can use equation (8) to find its effective molecular size:

$$a \cong \left(\frac{M}{\rho \cdot N_A}\right)^{\frac{1}{3}} = 6.5\ 10^{-10}\ m \tag{8}$$

where $N_A = 6.022\ 10^{23}$ is Avogadro's number.

In possession of the effective molecular size for the octane, we may calculate the interfacial tension at ambient temperature ($T = 293\ K\ \therefore U = k \cdot T = 1.3806\ 10^{-23} \cdot 293 = 4.04\ 10^{-21}\ J$):

$$\sigma \approx 5 \frac{mJ}{m^2}$$

This exercise is just to have an order of magnitude, once the actual value of the surface tension for the octane is $\sigma = 22 \frac{mJ}{m^2}$. The difference comes from the fact that the octane has a larger cohesion energy than the one estimated in the exercise (Blunt, 2017).

If we look at water ($\sigma \approx 73 \frac{mJ}{m^2}$) and mercury ($\sigma \approx 425 - 485 \frac{mJ}{m^2}$) surface tensions, we notice the impact of the hydrogen and metallic bonds in the magnitude of σ.

1.4. Capillary pressure

1.4.1. Definition

The capillary pressure is a physical property defined by the difference in pressure between two immiscible fluids across the curvature of the interface between them at equilibrium (Tiab & Donaldson, 2015). It can be simply defined as the difference between the pressure on the non-wetting fluid (nw) and the pressure on the wetting fluid (w), as in equation (9):

$$P_c = P_{nw} - P_w \tag{9}$$

1.4.2. Young-Laplace equation

Defining a system with two fluids and a solid surface, we can identify as the wetting phase the fluid that has an affinity to the solid surface and the non-wetting phase the fluid having less affinity to coat or reside next to the surface. The interface defined between the two fluids follows a curvature that leads to a pressure difference between both phases. Inside a porous medium, the non-wetting phase has a higher pressure as it does not reside close to the surface. This configuration means that it needs higher pressure than the wetting phase to be forced into the porous medium (Blunt, 2017).

We can derive the Young-Laplace equation from this system, relating the pressure difference between the phases to the curvature of the interface described by them. When writing an energy balance, considering a change in volume of one of the phases, the work against the pressure difference is equal to the change in interfacial energy and is expressed by (10):

$$(P_{nw} - P_w)\, dV = \sigma\, dA \tag{10}$$

where dV is the infinitesimal change in volume of the non-wetting phase over the wetting phase, and dA the corresponding change in surface area.

Combining (9) and (10), we obtain:

$$P_c = \sigma \frac{dA}{dV} \tag{11}$$

If we consider a sphere of radius r, then the change in volume represents a change in radius by dr, then $A = 4 \cdot \pi \cdot r^2$, $V = \frac{4}{3} \cdot \pi \cdot r^3$ and so $\frac{dA}{dr} = 8 \cdot \pi \cdot r$ and $\frac{dV}{dr} = A = 4 \cdot \pi \cdot r^2$, we can define the capillary pressure on a spherical interface as expressed by equation (12):

$$P_c^{Sphere} = \frac{2 \cdot \sigma}{r} \tag{12}$$

Considering now an interface between two fluids that has two different curvatures. The first curvature is defined as having an angle α and a radius of curvature r_1 and the second curvature has an angle of β and a radius of curvature r_2. As it can be easily seen in Figure 5, the area of the interface is defined by $(\alpha \cdot r_1) \cdot (\beta \cdot r_2)$.

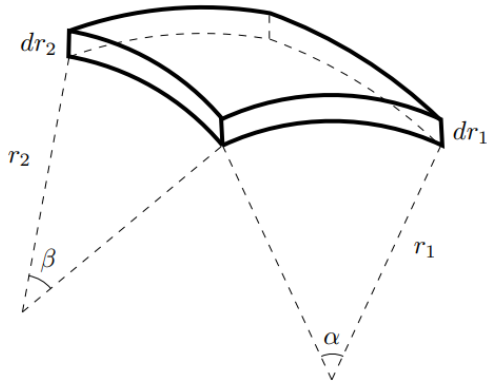

Figure 5 - Representation of the interface with two different curvatures between two fluids (Blunt, 2017)

If an infinitesimal (and equal) change in both radii, dr, takes place keeping the angles constant, the change in area of the interface may be described as $dA = (\alpha \cdot [r_1 + dr]) \cdot (\beta \cdot [r_2 + dr]) - \alpha \cdot \beta \cdot (r_1 \cdot r_2) \approx \alpha \cdot \beta \cdot (r_1 + r_2)dr$ .The change in volume in the new system is described by $dV = \alpha \cdot r_1 \cdot \beta \cdot r_2 \cdot dr$. Applying these results to (11), we may derive the Young-Laplace equation:

$$P_c = \sigma \left(\frac{1}{r_1} + \frac{1}{r_2}\right) = k.\sigma \tag{13}$$

where k is the curvature of the interface.

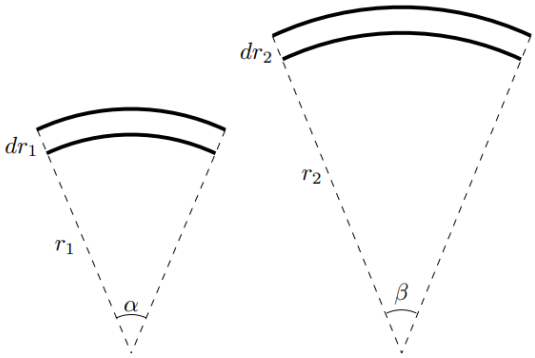

Figure 6 - Expansion of the interface following both curvatures between two liquids (Blunt, 2017)

We can notice that the radius of curvature may be either positive – in the case of looking at a fluid bulging out, in a convex configuration – or negative – in the case of a fluid bulging in, in a concave configuration.

Let's consider an oil/water system. As we classically consider $P_c = P_o - P_w$, if k is positive, oil is at a higher pressure than water; if k is negative, then water has a higher pressure.

When the fluids are at rest, the pressure in each phase is constant, which means that the capillary pressure and also the interface curvature are constant. So, in any system in a stationary regime, fluids radius may vary in space, but only if they keep the same value of k (Blunt, 2017).

We are now able to apply all these concepts to a widely known experiment, that is the capillary rise, or Jurin's Law (Jurin, 1718; Young, 1805; Leverett, 1941). When one face of the capillary tube of radius r is put inside the tub full of wetting fluid, for example, it will rise to a given height h defining a contact angle θ to the inner surface tube at the interface against the non-wetting fluid, as represented in Figure 7:

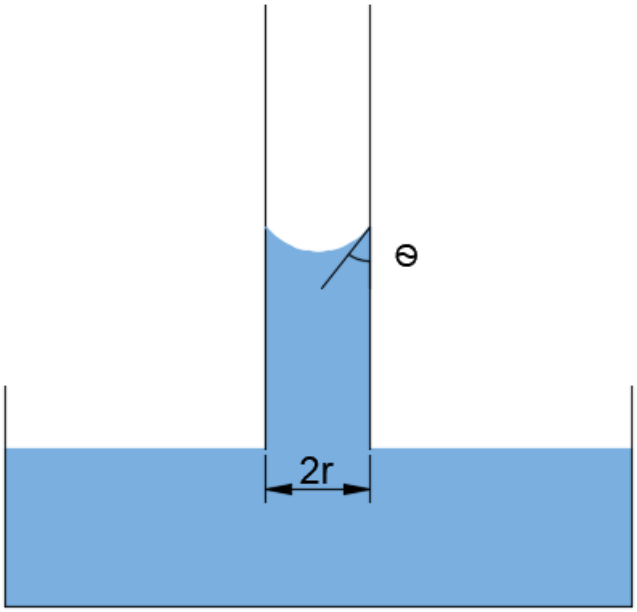

Figure 7 - Representation of the capillary rise experiment.

If r is small enough, we have the same curvature in the two directions (spherical), the radius of curvature may be described as $r_1 = r_2 = \frac{r}{\cos\theta}$. So, the capillary pressure may be adapted from (13) to be written as:

$$P_c = \frac{2 \cdot \sigma \cdot \cos\theta}{r} \tag{14}$$

This equation represents a good approximation when relating the capillary pressure to the pore throats. In a more complex system, this equation is still valid with r as the radius of the inscribed cross-section to the pore.

1.4.3. Leverett-J function

The Leverett-J function was determined in order to relate the pore throat radius with a typical capillary pressure to permeability. This approach is originated from the general idea that the capillary pressure curves of most natural porous materials have many features in common (Leverett, 1941). However, as some parameters are intrinsic to each rock type (*e.g.*, lithology, mineralogy), Leverett defined a

dimensionless function of saturation, the so-called Leverett-J function, that is written as:

$$J(S_w) = \frac{1}{\sigma * \cos\theta} * \sqrt{\frac{K}{\phi}} * P_c(S_w) \qquad (15)$$

where $J(S_w)$ is a dimensionless function depending only on water saturation.

One of the applications of Leverett-J function is deriving a reservoir representative capillary pressure from a mercury injection test, for example. This is done by extracting the J values from a mercury-injection capillary pressure experiment $P_C(Hg)$ and then P_C in primary drainage can be extracted from equation (15) by using the appropriate values of σ, $\cos\theta$ (usually 1 for Hg primary drainage), K (permeability) and ϕ (porosity). An example of the application of this relationship is shown in Figure 8:

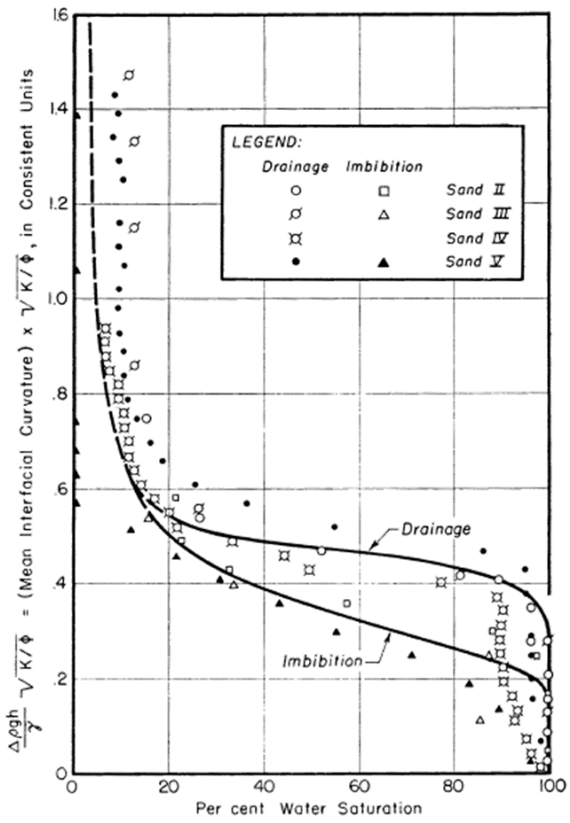

FIG. 4.—CORRELATION OF DATA FROM HEIGHT-SATURATION EXPERIMENTS ON CLEAN UNCONSOLIDATED SANDS.

Figure 8 - Drainage and imbibition tests performed to the validation of the Leverett-J Function (Leverett, 1941).

1.4.4. Mercury Injection Capillary Pressure (MICP)

The MICP test involves injecting mercury (Hg) into an evacuated and dry rock sample under controlled pressure – capillary pressure. Mercury (non-wetting phase) is injected into the rock at several capillary pressure steps, expelling mercury vapor (wetting phase) previously in place. Monitoring the mercury volume injected in the sample at different capillary pressure steps provide the P_c *versus* S_w (wetting-phase

saturation) curve, analog to the primary drainage capillary pressure curve. This curve may be converted for gas/water or oil/water system by normalization of the interfacial tension and contact angle using and adaptation of equation (14).

Moreover, pore throat size can be calculated from the capillary pressure curves. We employ equation (14) solved for "r" once again, but now to derive the pore throat radius. The equivalent pore throat radius penetrated by mercury at given capillary pressure is plotted against fractional pore volume injected "v". This relation is used to calculate a pore throat radius (PTR) distribution through the following derivative:

$$PTR = \frac{dv}{d[\log r]} \tag{16}$$

1.5. Wettability

1.5.1. Definition

The discussion about wettability will begin at the pore scale, as we will define primarily the concept of surface wetting by a fluid. The more general concept of wettability, which is defined at a larger scale (*e.g.*, the core scale), will be discussed further in this document.

Taking into consideration a system containing two fluids and a solid surface, we can define wetting as the ability of one fluid over the other to coat the solid surface, defined in the microscopic scale of the rock surface. The fluid having more preference to coat the surface is called the wetting fluid and, in opposition, the fluid that has less preference to coat the surface is called non-wetting (Blunt, 2017).

This definition, however, is a simplification of the reality, where the preference of coating the surface by one phase over another is variable within a range of wettability states. To create boundaries for the definition of the wetting and non-wetting phases, we use typically the contact angle of water to the solid surface. Figure 9 helps to illustrate this definition:

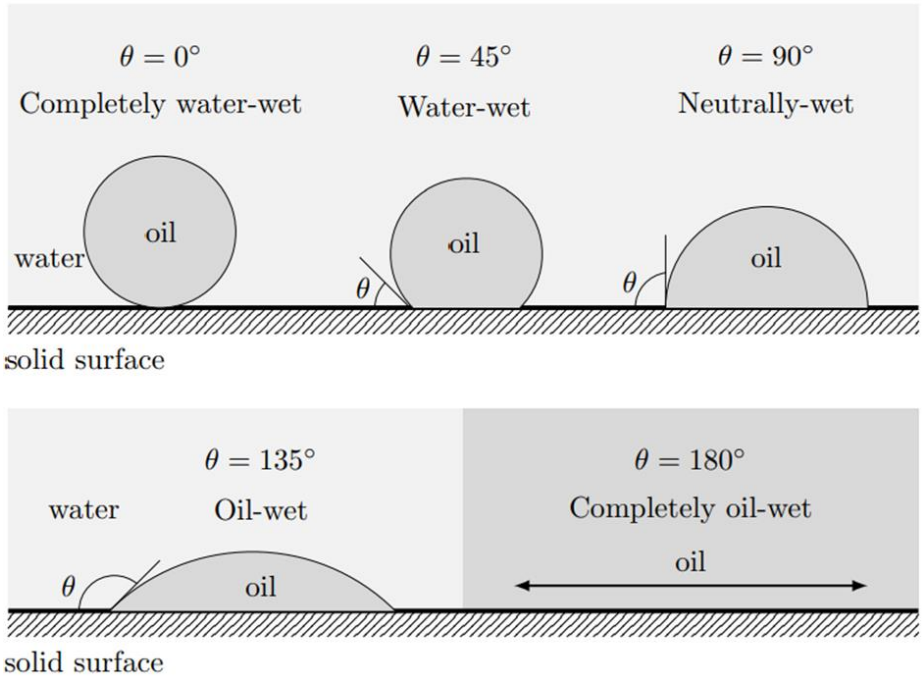

Figure 9 - Representation of different wettabilities to the rock surface (Blunt, 2017).

As we can see, there is a whole range of possible wettabilities to a homogeneous and flat solid surface, from completely water-wet to completely oil-wet. This is not the case in natural porous media (from core plug to whole reservoir) where we can have various local wettability conditions leading to a macroscopic heterogeneous wettability.

Moreover, the quantification of wettability from the contact angle does not consider the concept of rugosity, once a simplification to consider a flat surface is done. The Wenzel regime is defined when we consider that the wetting phase resides on a surface that is not smooth (de Gennes, 1985; Hazlett, 1993; de Gennes *et al.*, 2004). The usual approach is considering an effective contact angle defined for a smooth surface, considering that the wetting phase fills the grooves, crevices and corners of the rough surface, as presented in Figure 10:

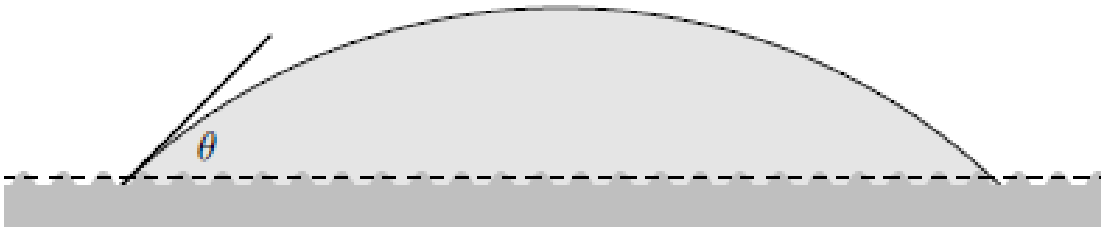

Figure 10 - Effective contact angle and equivalent smooth surface in the Wenzel regime (Blunt, 2017).

1.5.2. Wettability alteration

As seen before, it is considered that, initially, the natural wettability of a petroleum reservoir is water-wet as it contains only water. After oil formation in the mother rock and migration to the reservoir, an increase in pressure and temperature is observed. This generates physical conditions for wettability alteration, especially in locations in the reservoir where oil saturation is high.

As the pressure of the non-wetting phase rises compared to the pressure of the wetting phase, the wetting film thins and recedes into the corners of the pore (considering, in this case, a semi-star pore geometry). At this configuration, the film wetting the surface is flat, yet the capillary pressure is non-zero, as there is the application of capillary pressure from the non-wetting phase. Consequently, the standard Young-Laplace equation (13) does not describe properly the thin-film portion behavior. Therefore, for describing thin-film capillary pressure, a new term must be added to the Young-Laplace equation referred as the disjoining pressure $\Pi(h)$, which is a function of film thickness h (Derjaguin & Kussakov, 1939):

$$P_c = \sigma\left(\frac{1}{r_1} + \frac{1}{r_2}\right) + \Pi(h) \qquad (17)$$

The thin film thickness relation to the disjoining pressure is presented schematically in Figure 11:

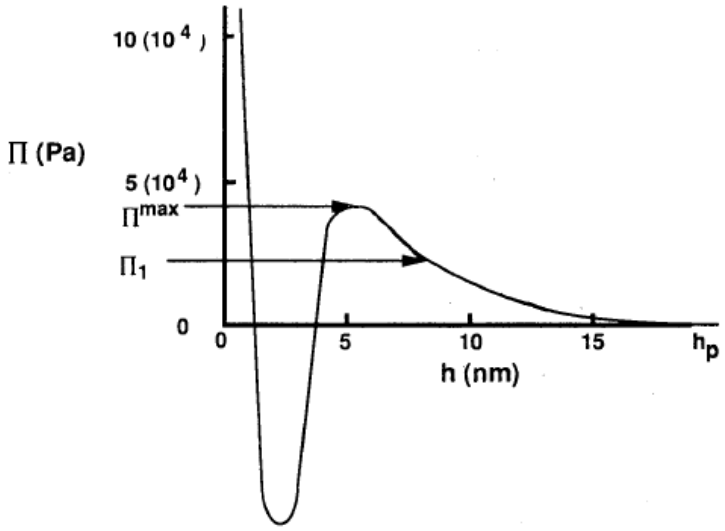

Figure 11 - Schematic relation of disjoining pressure to wetting film thickness (Kovscek, Wong, & Radke, 1993)

As we may observe, film thickness decreases monotonically with capillary pressure increase, until reaching a local maximum Π^{max}. This situation corresponds to a critical capillary pressure where the system will be unstable. When this capillary pressure is exceeded, the thicker outer film sheets away and only a molecularly adsorbed film resides close to the surface of the pore (Kovscek *et al.*, 1993).

When a thick water film collapses into a molecularly thin one, surface active components present in crude oil (*e.g.,* asphaltenes) may adsorb irreversibly to the pore surface. This mechanism of wettability alteration is based on polar interactions between oil, brine, and the rock surface. Asphaltenes are a heavy, polar fraction of crude oil, insoluble in low molecular weight paraffins (Buckley, 1995). These surfactants present in crude oil present a polar tail (that is attracted to water) and a non-polar tail (that is attracted to oil). If the crude oil is a poor solvent for its asphaltenes, they will be destabilized, which will enhance their interaction with the water films covering the rock surface, as presented in Figure 12.

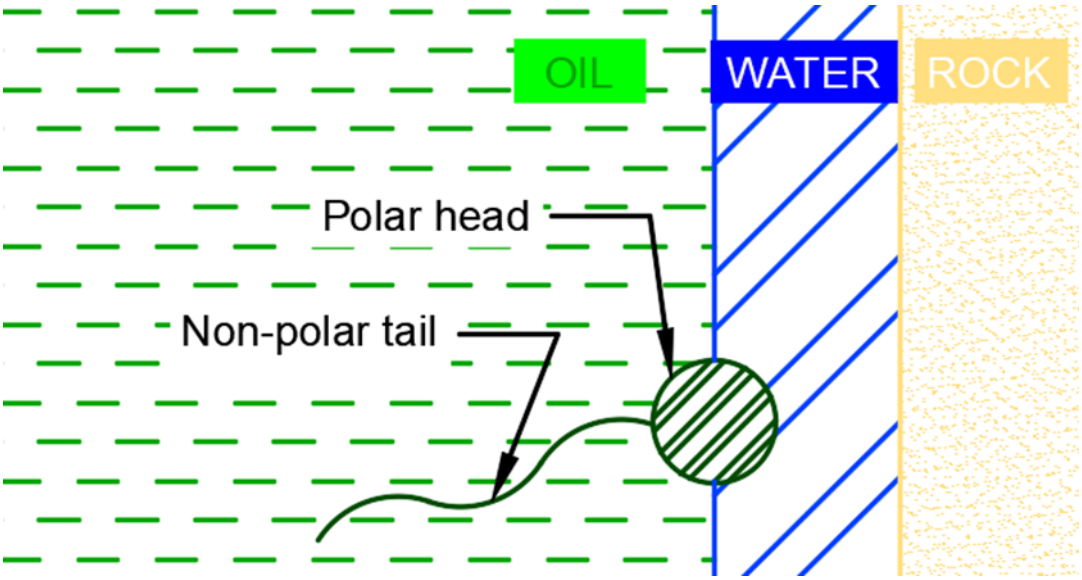

Figure 12 - Representation of an asphaltene invasion on a water film.

As the disjoining pressure is dependent on the layers thickness, wettability alteration will occur in intermediate parts of a pore, whereas in the corners, where the water layers are much thicker, the rock will remain water wet (Kovscek, 1993). Figure 13 schematically presents this situation:

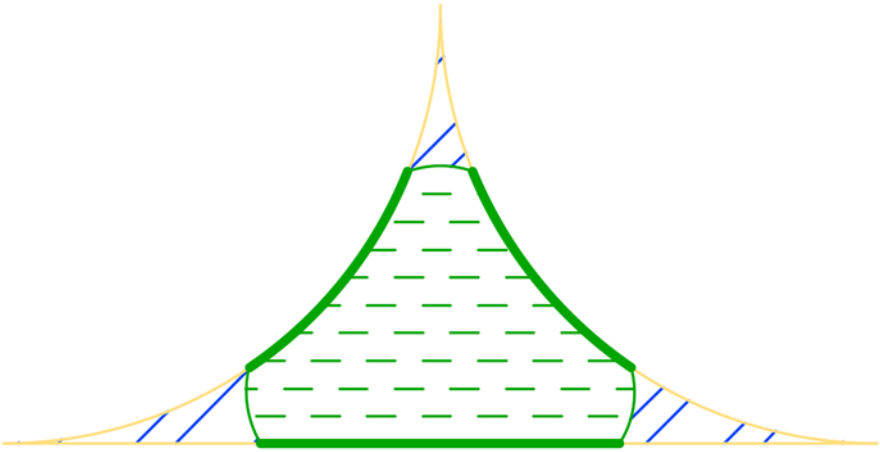

Figure 13 - Representation of a pore previously fully water-saturated invaded by oil that changed the wettability where the green lines are thicker.

The main crude oil/brine/solid interactions may be classified as it follows:

a. *Polar interaction between the oil phase and the rock surface in the absence of brine*

As described above, the interaction between the polar fraction of the crude oil represented by the head of the asphaltenes with polar surface sites in the rock.

b. *Surface precipitation of some components present in crude oil, notably surfactants as asphaltenes*

This point is a leading factor for wettability alteration in some specific conditions. In fact, the surface precipitation will be enhanced if the oil is a poor solvent for the asphaltenes (Buckley & Liu, 1998).

c. *Acid/base interactions that control surface charge at oil/water and solid/water interfaces*

The ionic composition of the brine plays an important role in oil/solid interaction. As polar functional groups in crude oil and in the mineral surface, in the presence of water, can behave as acids (giving up a proton and becoming negatively charged) or bases (gaining a proton and becoming positively charged) (Cuiec, 1975), it is clear that the acid/base interactions are important in the control of the wettability.

d. *Ion-binding or specific interactions between charged sites and higher valency ions.*

There are some ions present in the brine that may damper acid/base interactions, such as Ca^{+2}, and create interactions even stronger than those from acid/base (Buckley & Liu, 1998). This result has been verified by numerous authors that succeeded in changing the wettability of strongly water-wet sandstones by using connate brine containing significant amounts of divalent cations (Morrow *et al.*, 1986; Buckley & Morrow, 1990; Villard *et al.,* 1993; Jia *et al.*, 1994; Zhou *et al.*, 1995; Jadhunandan & Morrow, 1995; Morrow & Xie, 2001; Tong *et al.*, 2003; Tie *et al.*, 2003).

1.5.3. Wettability tests

After understanding the microscopic concept of wetting, that is defined at the surface scale, we will now move to the core scale, where the macroscopic concept of wettability will be extended through the analysis of the behavior of fluids during experiments in porous media.

a. Amott-Harvey and Amott-IFP methods

The Amott-Harvey wettability test (Amott, 1959) consists of performing a series of multiphase flows to determine the preference of the rock for one fluid over another by relating the volume of oil recovery during imbibition (spontaneous and forced) and the volume of water recovery during drainage (spontaneous and forced). The index is a composition of two intermediate indices – the Amott index to water, I_W, and the Amott index to oil, I_O. The only difference between the Amott-Harvey and Amott-IFP methods resides in the forced steps. While in Amott-Harvey tests the forced displacements are performed in the centrifuge, in Amott-IFP tests, the forced displacements are performed by fluid injection.

The test contains four main steps that are:

- Spontaneous imbibition

  After establishing initial water saturation (S_{wi}), the sample is immersed in brine contained in a cell equipped with a graduated burette at its top, where displaced oil from spontaneous imbibition will be trapped. The volume of brine imbibed by the sample in this phase is called $V_w(2)$.

- Forced imbibition

  The forced injection of brine in the sample is typically performed by centrifugation at multiple rotation speeds in incremental steps. The imbibed volume of brine during this phase is called $V_w(3)$.

- Spontaneous drainage

  Spontaneous drainage is the inverse of spontaneous imbibition. The sample is immerged in oil and the amount of oil spontaneously retained by the sample $V_o(2)$ is quantified by the volume of brine recovered in the graduated burette positioned in the bottom of the cell.

- Forced drainage

  The last step of the Amott cycle is the forced drainage. This process corresponds to the inverse process of the forced imbibition. The volume of oil retained by the sample during this step is called $V_o(3)$.

The main interest of the spontaneous displacements is to verify the ability of the rock to spontaneously imbibe one fluid over the other one that was previously inside the rock, which also indicates the continuity of the phase being imbibed. The forced displacements are done in order to know the saturation limits (Residual Oil Saturation – S_{or} - after forced imbibition and Irreducible Water Saturation – S_{wirr} - after forced drainage).

After establishing initial water saturation (S_{wi}) usually by centrifuge during first drainage (McPhee *et al.*, 2015), the core is put on spontaneous imbibition in brine. The spontaneous steps are typically done inside specific cells where the plug is completely

immerged and have all its faces in contact with the brine (for imbibition) and oil (for drainage). Figure 14 presents a scheme of these cells:

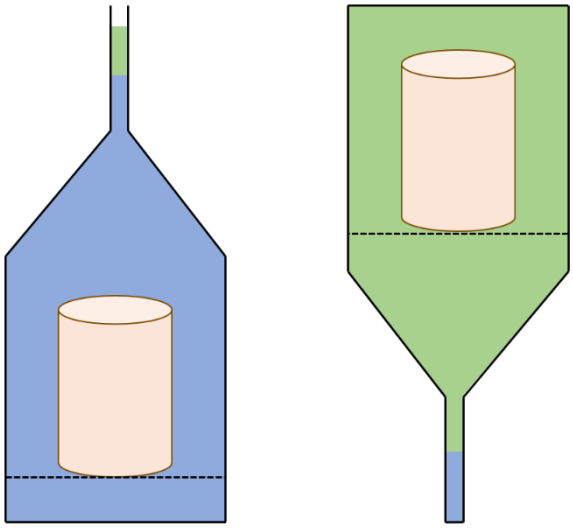

Figure 14 - Schematic representation of the cells used for spontaneous displacements. In the right, the spontaneous imbibition and in the left the spontaneous drainage (Oil in green and Water in blue)

The next step is the forced imbibition and takes the sample to a residual oil saturation. After this step, the Amott wettability index to water is obtained from equation (18):

$$I_W = \frac{V_w(2)}{V_w(2) + V_w(3)} \tag{18}$$

Then, we move to the last two steps, that are the spontaneous drainage and the forced drainage. Io is obtained from equation (19):

$$I_O = \frac{V_o(4)}{V_o(4) + V_o(5)} \tag{19}$$

After obtaining the wettability indices to both water and oil, we may proceed to the determination of the Amott Wettability Index, expressed by (20):

$$I_{AH} = I_W - I_O \tag{20}$$

The wettability of the rock sample may be classified according to the values reported in Table *1*:

I_{AH}	-1	-0.3	-0.1	0.1	0.3	1
Wettability	Oil-wet	Intermediate range				Water-wet
		Slightly oil-wet	Neutral		Slightly water-wet	

Table 1–Amott-Harvey wettability index rule

It is possible to notice an intermediate range of wettability from 0.3 to -0.3, where the rock will present no complete preference for one phase or the other. This wettability state is usually defined as mixed-wet, and the behavior of the rock to the tests may be considered as an intermediate between the extreme wettability states. The typical drainage and imbibition curves to each state of wettability are represented in Figure 15 and Figure 16:

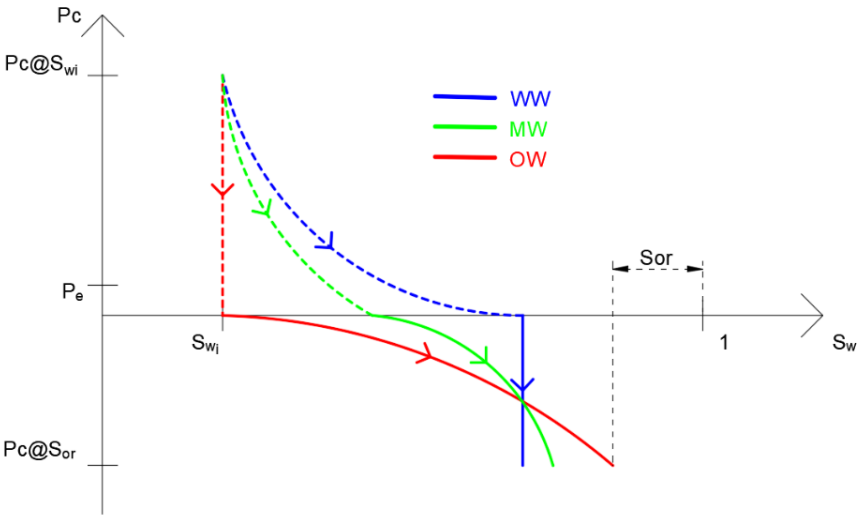

Figure 15 - Typical curves for Spontaneous Imbibition (dashed) and Forced Imbibition (solid)

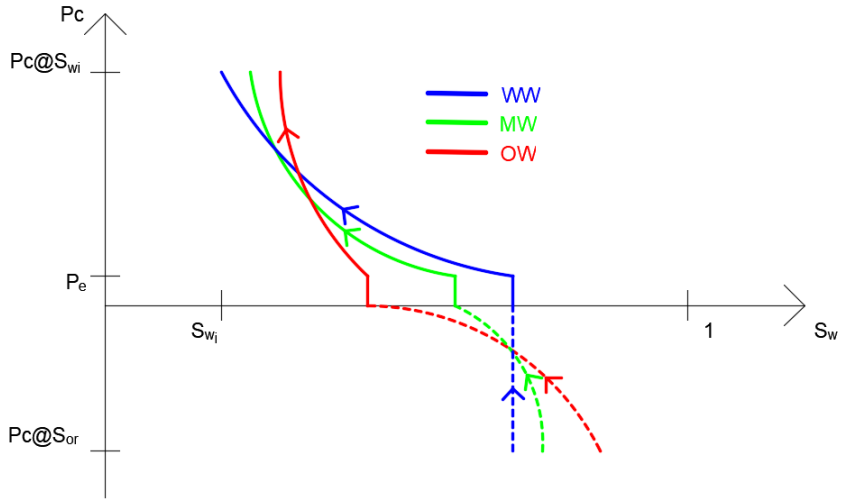

Figure 16 - Typical curves for Spontaneous Drainage (dashed) and Forced Drainage (solid)

b. USBM (United States Bureau of Mines) method

Starting from the same point as the Amott-Harvey tests (after establishing initial water saturation by primary drainage and altering sample wettability by ageing in crude oil), the USBM (Donaldson *et al.*, 1969), also called the centrifuge method, only considers forced displacements of oil and brine in the porous media.

It is essentially based on the principle that in strong wetting systems, the increase in saturation of a non-wetting fluid demands a high amount of work. In that case, the calculation is based on the ratio of the log of the areas below the $P_c(S_w)$ curves in drainage and in imbibition.

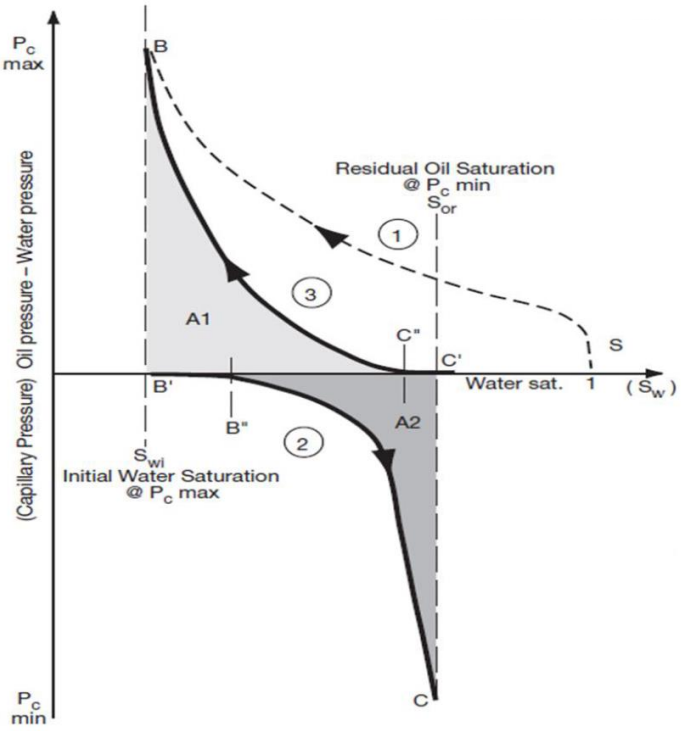

Figure 17 - USBM method for wettability determination (Zinszner & Pellerin, 2007)

The wettability index is calculated from equation (21):

$$I_{USBM} = log\left(\frac{A_1}{A_2}\right) \tag{21}$$

1.6. General characteristics of flow in porous media

Until this section, we have discussed the stationary states of fluids inside porous media. In the following sections, we will introduce notions of fluid motion in porous media.

1.6.1. Navier-Stokes Equations

The Navier-Stokes equations are used to describe mass and momentum conservation of continuous fluid flows. Mass conservation, established from mass balance considerations, writes:

$$\frac{\partial \rho}{\partial t} + \boldsymbol{\nabla} \cdot (\rho \boldsymbol{v}) = 0 \tag{22}$$

Momentum conservation was obtained from the expression of Newton's second Law of motion applied to a continuous fluid. The driving forces for flow are the pressure gradient and gravity, and the total acceleration for a moving fluid is given by $\frac{\partial \boldsymbol{v}}{\partial t} + \boldsymbol{v} \cdot \boldsymbol{\nabla v}$. The term that involves viscosity represents the resistance to the flow, which in the Navier-Stokes equation is the divergence of the stress tensor. In addition, as an analogy of the relationship between stress and strain in the Hooke's Law in solid mechanics, for fluid flow, it is assumed that stress is proportional to rate of change of the displacement (Blunt, 2017).

In equation (23) we have the representation of the Navier-Stokes equation for an incompressible Newtonian fluid of fixed viscosity μ (Navier, 1823; Stokes, 1845; Batchelor & Green, 1972):

$$\mu \cdot \nabla^2 \boldsymbol{v} = \rho \cdot \left(\frac{\partial \boldsymbol{v}}{\partial t} + \boldsymbol{v} \cdot \boldsymbol{\nabla v} \right) + \nabla P - \rho \cdot g \tag{23}$$

1.6.2. Reynolds Number

The Reynolds Number is a dimensionless number, defined as a ratio of inertial to viscous forces in the flow. According to the magnitude of the Reynolds Number, we are able to make simplifications to the momentum conservation appropriate for slow steady-state flows in porous media in order to represent the ratio of the non-linear term $\rho \cdot \boldsymbol{v} \cdot \boldsymbol{\nabla v}$ to the viscous dissipation $\mu \cdot \nabla^2 \boldsymbol{v}$. By considering a steady-state flow, we can neglect the time dependent term, $\frac{\partial \boldsymbol{v}}{\partial t}$, so that $\boldsymbol{v}$ will be only space dependent.

Estimate a derivative of the term $\boldsymbol{\nabla v}$ as $\frac{v}{l}$ where l is a representative length in the pore scale where we are supposed to observe a significant change in flow speed – notion of zero-velocity in the pore walls and maximum velocity at the center of the pore space. Therefore, we have $\rho \cdot \boldsymbol{v} \cdot \boldsymbol{\nabla v} = \rho \cdot \frac{v^2}{l}$ and $\mu \cdot \nabla^2 \boldsymbol{v} = \mu \cdot \frac{v}{l^2}$. By extracting the ratio of these terms, we obtain the Reynolds Number, presented in equation (24) (Reynolds, 1883):

$$Re = \frac{\rho \cdot v \cdot l}{\mu} \tag{24}$$

1.6.3. Darcy's Law

To explain Darcy's Law, let's consider a monophasic creeping flow in a porous medium. In the case of a creeping flow ($Re \ll 1$), inertial effects can be ignored; thus only viscous resistance is considered. From the steady-state Stokes flow that is governed by (23) and still neglecting the time dependent term and considering mass conservation as in equation (22), we have:

$$\mu \cdot \nabla^2 \boldsymbol{v} = \nabla P - \rho \cdot g \tag{25}$$

Let's consider a steady-state Stokes flow. Equation (25) leads to a linear relationship between the pressure gradient ∇P and flow speed $\boldsymbol{v}$. This condition may be verified by taking a solution $\boldsymbol{v} = \boldsymbol{v_0}$, and considering that velocity is zero close to the pore wall and a pressure gradient is applied across the system. Considering an arbitrary increase by a factor a in the term $\nabla P - \rho \cdot g$, the imposed pressure gradient in the system will experience the same increase by the factor a. Therefore, we may verify that a solution to (25) is $\boldsymbol{v} = a \cdot \boldsymbol{v_0}$. Alternatively, we may apply the same approach to show that the velocity term $\boldsymbol{v}$ is inversely proportional to the viscosity term μ (Blunt, 2017).

Hence, we have:

$$\boldsymbol{v} = -\frac{f(x)}{\mu} (\nabla P - \rho \cdot g) \tag{26}$$

The $f(x)$ is a positive function of position x that is only dependent on the geometry of the porous medium. We will see further that this function is, in fact, the permeability.

In order to find a solution to (26), we will come back to the averaging of its parameters relative to a Representative Elementary Volume (REV), where we will find the macroscopic flow integrated over some representative volume of the porous medium space, containing many pores through fluids flow. So, for an established REV, we can define an average flux $\boldsymbol{q}$ that is defined as a volume of fluid flowing perpendicular (by a normal vector $\boldsymbol{n}$) to an area of flow denoted by $\boldsymbol{A} = \int d\boldsymbol{A}$ per unit time:

$$\boldsymbol{q} \cdot \boldsymbol{n} = \frac{1}{A} \int \boldsymbol{v} \cdot d\boldsymbol{A} \tag{27}$$

In this integral, we include both void space where velocity assumes a finite value, and the solid, where velocity is zero.

Continuing in the averaging of parameters in (26), as in laboratory work the pressure gradient over the core sample is measured in specific points in a small region by means of pressure taps, the pressure gradient is calculated from the difference over a macroscopic distance. Therefore, we can define a pressure gradient as the difference in two points values over a macroscopic length (Whitaker, 1986).

Lastly, the averaging of the $f(x)$ function leads to a parameter that is dependent on the pore space structure and that relates both $\boldsymbol{q}$ and $(\nabla P - \rho \cdot \boldsymbol{g})$. So, we define the permeability K as a tensor.

After the averaging work on the parameters of (26), we are finally able to obtain Darcy's Law, that was introduced by Darcy after founding an empirical relationship to describe a flow in a pack of sand filters for fountains (Darcy, 1856):

$$\boldsymbol{q_i} = -\frac{K_{i,j}}{\mu} \left(\frac{\partial P}{\partial x_j} - \rho \cdot \boldsymbol{g_j} \right) \tag{28}$$

The experiment done by Henry Darcy in order to derive this relation is the basis for generally all the core analysis done in the laboratories. His experiment consisted in injecting one fluid in a pack of well-sorted sand and measuring the pressure at the inlet and at the outlet of this pack, as presented in Figure 18.

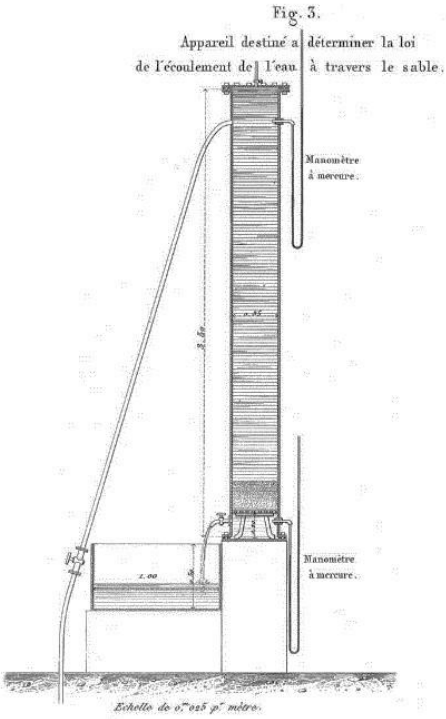

Figure 18 - Classic Darcy's experiment of injection of water in a sand pack column (Darcy, 1856).

It is interesting to notice that during its experiments, Darcy measured not the permeability of the sand pack, but the water conductivity. Given that he worked with a one-fluid system, he measured the hydraulic conductivity of the sand pack, given in m/s, which is a property homogeneous to fluid velocity and is dependent of the fluid. In order to deal with a property that is intrinsic to the porous media, we will prefer to use the concept of permeability, given in m^2 in the SI, which clearly indicates its dependence of the porous medium.

As in laboratory experiments we face situations where the imposed pressure gradient ∇P is much stronger than the gravitational term $\rho \cdot \boldsymbol{g}$, and as we define the characteristic length and area of flow respectively as L and A, we can simplify the notation of (28) by writing:

$$Q = \frac{k \cdot A \cdot (P_1 - P_2)}{\mu \cdot L} \tag{29}$$

where Q is the fluid flow rate through the section A, L is the length of the core plug and k is the averaged permeability of the sample.

1.7. Relative Permeability

1.7.1. Definition

Darcy's Law may also be extended to multiphase flows (Muskat & Meres, 1936; Wyckoff & Botset, 1936; Leverett, 1939). Let's consider the momentum and the continuity equations for a phase "i" in a porous medium:

$$-\nabla P_i + \rho_i \cdot g + \mu_i \cdot \nabla^2 \boldsymbol{v_i} = 0 \tag{30}$$

$$\nabla \cdot \boldsymbol{v_i} = 0 \tag{31}$$

As we are considering a multiphase flow (in this case, a system containing two fluids), in addition to the non-sliding condition between the fluid and the solid surface, we consider also this same non-sliding condition between the two fluid phases "i" and "j", which results in the same velocity for both phases at the interface.

$$\boldsymbol{v_i} = \boldsymbol{v_j} \tag{32}$$

The averaging of Stokes equations results in a generalized Darcy model where effective permeability tensors and crossed terms, accounting for the viscous interaction between phases, outcome (Whitaker, 1986; Lasseux *et al.*, 1996). In the work of (Zarcone & Lenormand, 1994), the authors showed that the coupling terms are negligible, so the generalized Darcy model empirically defined by Muskat (1937) may be used:

$$< \boldsymbol{v_i} >= -\frac{\boldsymbol{K_{i,j}}}{\mu_i}\left(\nabla < P_i >^i - \rho_i \cdot \boldsymbol{g}\right) \tag{33}$$

where $< \boldsymbol{v_i} >= \frac{1}{V}\int_V \boldsymbol{v_i}\, dV$ is the superficial average of the velocity of phase i, also called filtration velocity of phase i, and $< P_i >^i$ is the intrinsic average pressure of phase i.

As seen in (28), we have defined the permeability tensor $K_{i,j}$ that was dependent on the pore space geometry, once we faced a situation in which there is only one phase present in the system. However, as we are considering a two non-compressible phases system, the restrictions in the pore space are no longer simply defined by the pore geometry, but also by both phases present inside the porous structure. This increase of the restrictions is considered by the permeability tensor, which introduces the relative permeability term that is defined by the ratio of the effective permeability of one of the phases to the absolute permeability of the porous media:

$$K_{ri} = \frac{K_i}{K} \tag{34}$$

The relative permeability of phase "i", K_{ri}, represents the restriction imposed to the displacement of this phase by the other phase and the pore geometry. It is basically dependent on phases saturation, continuity, and rock wettability.

Therefore, for a simple horizontal unidimensional multiphase flow, we can write the adapted Darcy's model as:

$$Q_i = \frac{K_{r,i} \cdot K \cdot A \cdot \left(P_{i,1} - P_{i,2}\right)}{\mu_i \cdot L} \tag{35}$$

where Q_i is the volumetric flowrate of the phase i, $K_{r,i}$ is the relative permeability of the phase i, K is the absolute permeability of the porous medium, A is the cross-section of the core plug, $\left(P_{i,1} - P_{i,2}\right)$ is the pressure loss of the phase i across the length L and μ_i is the viscosity of phase i.

1.7.2. Kr determination

Although $K_{r,i}(S_w)$ may ideally be measured experimentally, it is impossible to define the totality of the curve by experimental means. In fact, it is possible to measure phases effective permeability at different points of water saturation to construct he curve. However, the determination of $K_{r,i}(S_w)$ is only possible by performing a transient inverse analysis of the experimental results, called history match.

The history match is performed with a numerical simulation that uses experimental data, usually pressure drop along the sample, phases production and saturation profiles *versus* time, to match the double $K_{r,i}(S_w)$ and $P_c(S_w)$. The approach when performing coreflood simulation is similar to reservoir simulation models but designed to operate at the core plug scale. Essentially, the simulator starts with estimate relative permeability values and adjusts the curves to history match production and pressure data and In-Situ Saturation Monitoring (ISSM) profiles (McPhee *et al.*, 2015).

In this work, we used the CYDAR® numerical simulator for performing the history-match of the multiphase flow experiments. CYDAR® is a numerical simulator for design and interpretation of petrophysical laboratory experiments. It is a product from the French Institute of Petroleum and New Energies (IFPEN) and is commercialized by Cydarex.

The boundary conditions for the numerical simulations of unsteady-state experiments are fully-described in Lenormand *et al.* (2017).

There are numerous (and non-unique) solutions for the equations in coreflooding simulation. Therefore, it is essential to define as many of the input parameters as possible.

Four conventional experimental options for relative permeability experiments exist: Unsteady-state, Steady-state, Centrifuge, and the Semi-Dynamic method. The Unsteady-state method will be further discussed in the corresponding section (Waterflooding techniques), as it was the used approach during this study.

1.7.3. Kr models

There are several models for defining $K_{r,i}(S_w)$ through numerical coreflood simulations. These models are mainly based on three different approaches:

- Capillary model

  These models are based on the capillary tubes hypothesis, which considers that the porous media is formed by a bundle of capillary tubes of different diameters. The characteristic length for the fluid to flow through the sample is given by the tortuosity of these tubes.

- Empirical model

  These models are based on laboratory experiments results, obtained mainly in the oil industry. These models are usually based on two fluid flow systems.

- Network model

  These models are based on Pore Network Modeling, where the flow equations (*e.g.*, Navier-Stokes) are solved for a geometry representing a porous medium.

In this work, we will discuss two empirical models: Corey and LET.

a. *Corey (Corey et al., 1956)*

Most common model for relative permeability definition, the Corey model considers that the relative permeability curves between each end-point saturation may be defined by a simple power function, based on a normalized saturation.

This model may be used for both drainage and imbibition relative permeability interpretation. In the case of an imbibition experiment, the normalized oil relative permeability, over the moveable oil saturation range (from $S_w = S_{wi}$ to $S_w = 1 - S_{or}$) is defined by (36):

$$k_{ron} = S_{on}^{N_o} \tag{36}$$

where S_{on} is a normalized oil saturation, given by:

$$S_{on} = \frac{1 - S_w - S_{or}}{1 - S_{wi} - S_{or}} = 1 - S_{wn} \tag{37}$$

By analogy, the normalized water relative permeability is given by:

$$k_{rwn} = S_{wn}^{N_w} \tag{38}$$

where S_{wn} is a normalized water saturation:

$$S_{wn} = \frac{S_w - S_{wi}}{1 - S_{wi} - S_{or}} = 1 - S_{on} \tag{39}$$

When experimental artifacts are prevented, N_o and N_w , which are called Corey exponents for the oil and water phase, carry important information regarding the rock wettability, as they define the dynamic behavior of fluids flow.

A useful rule of thumb for correlating wettability from Corey's exponents is presented in Table 2:

Wettability	N_o	N_w
Water-wet	2-4	5-8
Mixed-wet	4-6	3-5
Oil-wet	6-8	2-3

Table 2–Relation between wettability and Corey exponents for an oil-water system *(McPhee, Reed, & Zubizarreta, 2015)*.

b. *LET (Lomeland et al., 2005)*

Relative permeability results may present, in some cases, a sigmoidal behavior that may not be described by the Corey model. This is the case, for example, for dual-porosity samples.

To better represent this behavior and consider inflexion points and different curvatures, the authors have modified the Corey equations to integrate three empirical

power parameters, L, E and T, that allow to better represent the behavior at extreme points of water saturation.

For an oil-water system, the model is given by equations (40) and (41):

$$k_{row} = k_{row} \frac{(1 - S_w^*)^L}{(1 - S_w^*)^L + E \cdot (S_w^*)^T} \tag{40}$$

$$k_{rw} = k_{rw} \frac{(S_w^*)^L}{(S_w^*)^L + E \cdot (1 - S_w^*)^T} \tag{41}$$

where:

$$S_w^* = S_{wn} = \frac{S_w - S_{wi}}{1 - S_{wi} - S_{or}} \tag{42}$$

1.7.4. Effects of wettability on relative permeability and capillary pressure curves

Wettability is a factor which has a huge impact on relative permeability, as it controls fluid distribution in porous media. Therefore, it will modify the fluids flow paths, thus impacting each phase relative permeability and capillary pressure. An important note: as capillary pressure is defined as $P_c = P_{non-wetting} - P_{wetting}$, when dealing with modified wettability cases, a mislead in comprehension may arise. Therefore, for facilitating comprehension in the following analysis, we will always consider water as the wetting phase and oil as the non-wetting phase.

During waterflooding experiments, we may describe the behavior of each fluid according to the rocks wettability:

a. Water-wet

In a water-wet system, as we have seen, water coats the pore walls and oil is located in the center of the pores. Considering a triangular-shaped pore as in Figure 13, when the sample is at S_{wi}, state prior to waterflooding, water is in the form of films for intermediate parts of the pore and concentrated in the corners.

Therefore, when performing imbibition, capillary pressure gradient generated by the geometry variation between pore throats and bodies will increase the wetting phase velocity, feeding the wetting water film, thus increasing water saturation and reducing the non-wetting phase (oil) saturation. At some point during water saturation increase, a rupture of the non-wetting phase continuity will happen. This phenomenon is called snap-off trapping (Oh & Slattery, 1979). As the flow path for the oil phase during production is less tortuous than the porous media tortuosity, once this phase flows through the center of the pores, k_{row} is expected to decrease slowly until breakthrough, where it will drop sharply.

Considering that only one phase is moving in the porous medium, a relation to define the disjoining pressure where the oil phase, trapped in the form of droplets, could be remobilized was conceived (Lake, 1989).

$$\Delta\varphi_w + \Delta\rho \cdot g \cdot \Delta L \cdot \sin\alpha \geq \Delta P_c \tag{43}$$

where $\Delta\varphi_w$ is the potential of the wetting phase, $\Delta\rho$ is the density difference between fluids, ΔL is the droplet size and α is the angle between the main axis of the droplet and the horizontal.

As the remobilization of the trapped phase in a water-wet porous medium is difficult, after water breakthrough, no more oil production is noticed. Taking the example of homogeneous sandstone samples, the residual oil saturation for a water-wet rock is higher than in modified-wettability cases, typically $S_{or} \cong 25\%$. This value may vary in the case of heterogeneous limestones. Moreover, the presence of the trapped phase in the center of the pores limits water conductivity, as water flow path is more tortuous than the porous media itself. Therefore, for water-wet porous media, K_{rw} is expected to be low for the entire range of water saturation, reaching typical values of $0.05 \leq K_{rw,max} \leq 0.25$. Accordingly, capillary pressure will decrease slowly during oil production and water films thickening until production ceases after BT, close to S_{or}. At this point, no more oil production is expected, even though an increase in the water phase pressure, thus in the absolute capillary pressure, is performed.

Even though a $Pc = 0$ condition at the sample outlet ($z = L$) is applied for waterflooding experiments on rock samples, the water saturation profile of homogeneous water-wet plugs is expected to be uniform at the end of imbibition. This fluids configuration is valid, because additional imposed capillary pressure does not result in further oil production. Therefore, the capillary pressure gradient generated along the sample length during imbibition leads to a unique saturation value, equal to $S_w@S_{or}$. This effect may be visualized by the negative portion of the $\boldsymbol{P_c}$ *versus* S_w curve for water-wet samples.

A schematic example of water-wet imbibition relative permeability and capillary pressure curves are presented in Figure 19.

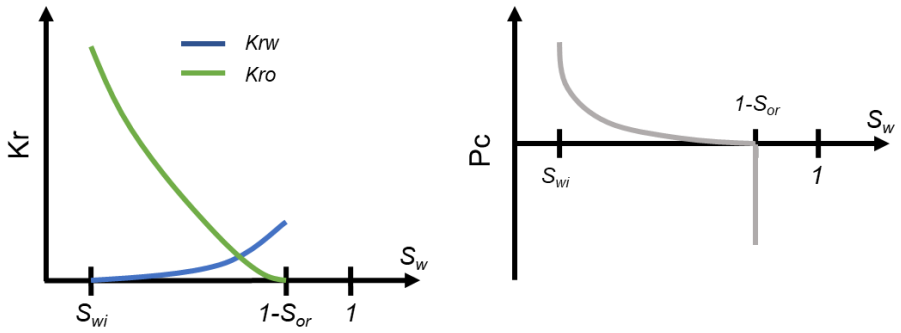

Figure 19 - Schematic example of water-wet imbibition relative permeability and capillary pressure curves.

b. Oil-wet

In the oil-wet case, the situation is inversed, as oil coats the pore walls and occupies the smaller pore spaces, whereas water is located in the center of the larger pores.

Assuming that the entire rock is oil-wet, the main displacement path will no longer be a percolation, as in the water-wet case, but an invasion percolation process. Water flows from the inlet, filling the larger throats and pores, until finding a connected path of wide throats and pores through the porous media. As water is expected to travel rapidly through the porous medium, an early breakthrough is expected (Blunt, 2017).

Regarding relative permeability curves, water relative permeability K_{rw} will increase rapidly, as it connects larger pores and throats, therefore having bigger conductance. Typical values of water relative permeability in the oil-wet case are $K_{rw,max} \geq 0.5$. As oil production will no longer follow a piston-like displacement, such as in the water-wet case, but a layer drainage, much less trapping will be observed. As oil wets the surface in a connected path, injecting water for a long time in increased water pressure will be effective on reducing oil saturation. For an oil-wet case, a residual oil saturation value is expected to be $S_{or} \leq 10\%$.

This situation has an implication in the capillary pressure curve for an oil-wet imbibition experiment. Once water saturation evolves even after BT, a saturation gradient will be observed in the negative part of the P_c curve. As the same $Pc = 0$ condition mentioned in the water-wet case section applies to oil-wet waterfloods, a capillary pressure gradient will result on a water saturation gradient along the sample longitudinal axis. This behavior explains the more significant presence of Capillary-End Effects (CEE) on oil-wet samples in comparison to the water-wet case. CEE is defined as a gradient of the wetting phase along the sample longitudinal axis, that is generated from a capillary pressure drop between inlet and outlet faces of the sample.

Although a small residual oil saturation value may be obtained in the laboratory by the Centrifugation method, most of the times it cannot be reached in the reservoir scale, as it demands numerous pore volumes of water to be injected, which is not economical in a bigger scale. In a very specific case combining gravitational drainage behind the water-front and high vertical permeability, it may be economical injecting more than one pore volume during reservoir production.

On the other hand, oil relative permeability drops sharply, as water occupies larger throats and pores. Nonetheless, oil is still connected throughout the core in the form of films. Therefore, k_{row} is small, but different from zero, as oil lay still flow.

A scheme for oil-wet relative permeability and capillary pressure curves is shown in Figure 20.

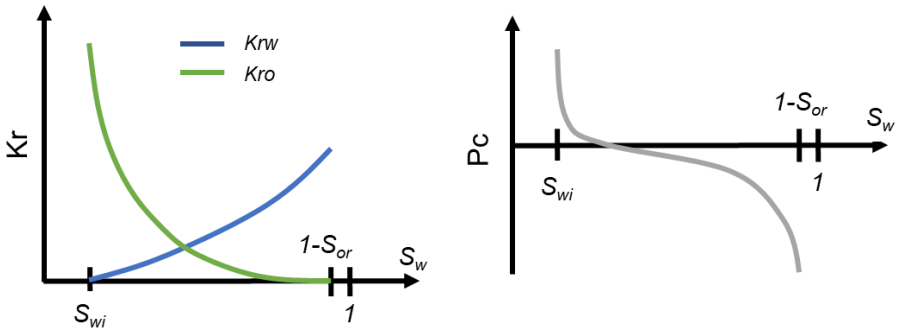

Figure 20 - Schematic representation of oil-wet imbibition relative permeability and capillary pressure curves.

c. *Mixed-wet*

The mixed-wet case is the most complex case, as there are several different definitions to describe a rock that has no strict affinity to one fluid or the other.

McPhee *et al.* (2015) define two different classifications of mixed wettability on core samples:

- Neutrally-wet: the system has a uniform non-preference for oil or water, i.e., spontaneous imbibition of either fluid.

- Fractionally-wet: the system have some areas that are attracted to oil and some areas that are attracted to water.

An interesting behavior is found on intermediate, uniformly distributed wettability (neutrally-wet systems), as oil recovery steadily decreases for a cumulative water injection as wettability becomes more oil-wet (Donaldson & Thomas, 1971). This result represents an inversed behavior than that observed for pure water-wet (lower oil recovery) and pure oil-wet rocks (higher oil recovery).

In fractionally-wet rocks, a different behavior is observed. Several studies were dedicated to proving that oil recovery in core samples vary not monotonically as a function of wettability index, and maximum oil recovery in the laboratory was found on mixed-wet systems (Amott, 1959; Owens & Archer, 1970; Morrow *et al.*, 1973; Jadhunandan & Morrow, 1991; Jerauld, 1997; Hamon & Roy, 2000).

Regarding the relative permeabilities curves shapes, a wide variation may be found depending on the type of mixed wettability: mixed-wet large, mixed-wet small, fractional-wet (Skauge & Ottesen, 2002; Skauge *et al.*, 2003). Nonetheless, Masalmeh presents an intermediate behavior for mixed-wet carbonates from Middle East, compared to the water-wet and oil-wet cases.

Recent works using Digital Rock Physics aiming to investigate fluid flow in the pore scale show a different result than the ones presented previously. The description provided by Blunt (2017) is presented in the following paragraphs.

In a fractionally-wet rock, where there is a mix of oil-wet and water-wet pores, initially, water will flow through small water-wet pores, behaving close to the water-wet case. As displacement proceeds, water starts to fill the oil-wet regions, thus describing a shape close to the oil-wet case from this point. We may expect than, that the k_{row} curve behaves, initially, between the water-wet and oil-wet cases and, close to S_{or}, as the oil-wet case. Typical values of residual oil saturation for the mixed-wet case are in the range of $0.1 \leq S_{or} \leq 0.2$.

For the water relative permeability, on the other hand, the behavior is quite different from the previous cases. As this is a percolation process, initially water fills the water-wet pores, trapping oil by snap-off, thus not increasing k_{rw}. Nonetheless, differently from the purely water-wet case, water is not connected throughout the sample in the form of films. Therefore, the oil-wet regions will be filled by a piston-like advance of water, although, not entirely connected to the wider regions of the pore space. During this process, an important change in saturation is observed, however water relative permeability is not increased, as there is poor connection of this phase. This process explains the low values of k_{rw} for the initial range of water saturation. After breakthrough of water, however, a better connectivity of the water phase will be reached. Therefore, a sharp increase in k_{rw} is expected, up to values around $0.2 \leq k_{rw} \leq 0.5$.

Regarding the capillary pressure curve, this behavior will also be observed, as presented in Figure 21.

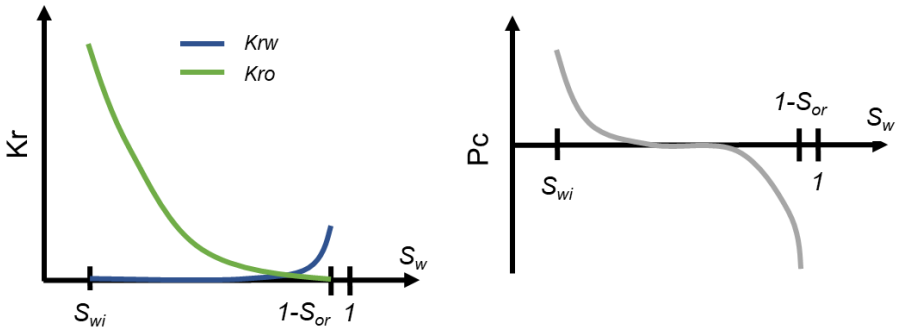

Figure 21 - Representation of the mixed-wet case according to the description given by Blunt (2017) - relative permeability and capillary pressure imbibition curves.

1.7.5. Capillary number

The concept of capillary number is originated from the notion of ratio between capillary and viscous forces. It is important to notice that the capillary number is not the dimensionless ratio of viscous to capillary effects at the pore scale. For that, it must be multiplied by porous medium and saturation-dependent quantities (Hilfer *et al.*, 2015). However, it is the most used relation to describe the forces acting in a porous medium flow. Typical values for capillary number considering a reservoir typical flow condition are $10^{-7} \leq C_a \leq 10^{-9}$ (Blunt, 2017).

Numerous expressions have been used in the literature to express the capillary number, many of which are equivalent (Taber, 1980; Larson, 1981; Chatzis & Morrow, 1984). They include the following one, that is used in this research:

$$C_a = \frac{\mu \cdot v}{\sigma} \tag{44}$$

where v is Darcy's velocity of the injected phase, μ is the viscosity, and σ is the interfacial tension between the fluids and the rock surface.

The importance of this dimensionless number relies on respecting reservoir flow conditions when performing laboratory experiments. This condition must be respected so that laboratory results may be extended to the reservoir scale, especially the possible artificial desaturation with high velocity (reduced $Sorw$ at high C_a application).

However, studies were conducted in the domain of Enhanced Oil Recovery for application of high capillary numbers in the reservoir for increasing oil recovery. This approach consists of increasing the capillary number for reaching an onset of mobilization of residual oil blobs from water-wet reservoirs and complete recovery of residual oil, usually reducing interfacial tension to extremely low values. The relationship between capillary number increase and additional oil recovery was largely tested on unconsolidated bead packs and consolidated sandstones of various wettabilities, and no universal relationship between $Sorw$ and C_a was found.

An example relating C_a increase to additional production ($Sorw$ decrease) on a sandstone, a sintered bead pack and an unconsolidated bead pack (all water-wet systems) is presented in Figure 22:

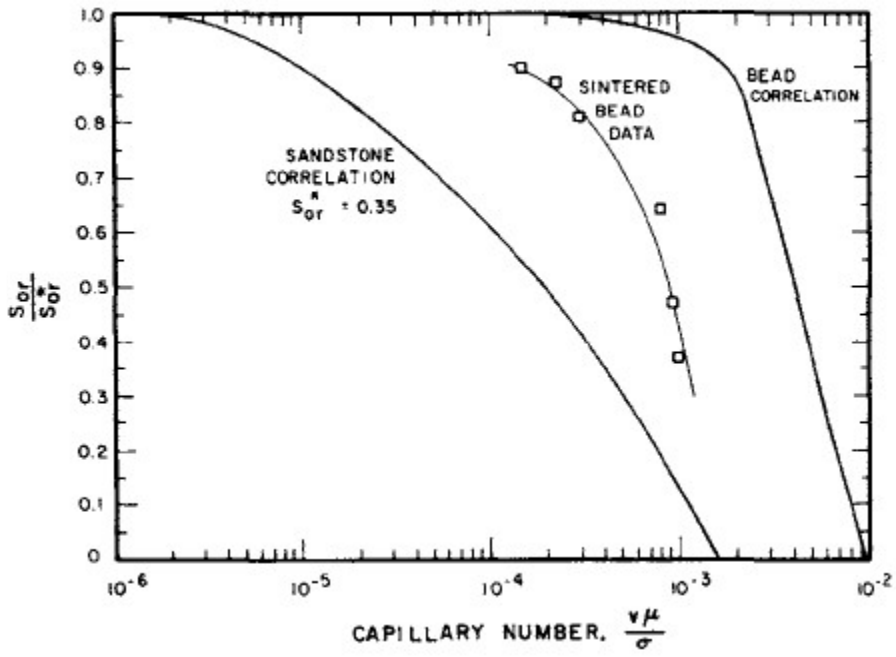

Figure 22 - Capillary number correlation to additional oil recovery (Morrow et al., 1988).

Notwithstanding, there are some cases where the classic definition of the capillary number may not be extended (*e.g.*, flow in natural fractures). In these cases, some authors worked in the definition of capillary numbers that incorporate the geometrical characterization of the fracture (AlQuaimi & Rossen, 2018).

1.7.6. Bond number

The Bond number (B_o) is a dimensionless number that relates gravitational forces to surface tension in the flow front of a fluid displacement (Bond & Newton, 1928).

The expression defining the Bond number is given by:

$$B_o = \frac{\Delta\rho \cdot g \cdot L^2}{\sigma} \tag{45}$$

where $\Delta\rho$ is the difference in density between the two phases of the system, g is gravity, L is a characteristic length (*e.g.*, a droplet size), and σ is the interfacial tension.

In the case of centrifuge experiments in the laboratory, the gravity term of equation (45) is replaced by the centrifugal acceleration ($\omega^2 \cdot r$), leading to the following relation (O'Meara Jr *et al.* 1992):

$$B_o = \frac{\Delta\rho \cdot \omega^2 \cdot r \cdot L^2}{\sigma} \tag{46}$$

A high Bond number ($B_o \gg 1$) indicates that the system is mostly affected by gravity forces. Inversely, a low Bond number ($B_o \ll 1$) indicates that capillary forces are dominant in fluid displacement. A simple example for illustrating this effect is placing a droplet on a completely non-wetting substrate: the droplet will be completely spherical, however if we increase its size, gravity forces will become larger, flattening the shape of the droplet.

For evaluating the dominance of one force over another inside a porous media, we may use inverse Bond number (Schechter *et al.*, 1994):

$$B_o^{-1} = C \cdot \frac{\sigma \cdot \sqrt{\frac{\Phi}{k}}}{\Delta\rho \cdot g \cdot H} \tag{47}$$

where $C = 0.4$ for the capillary tube model (Zhou & Stenby, 1990), and H is the characteristic length of the porous medium.

1.8. Conventional and Special Core Analysis

1.8.1. Initial States approaches

The Initial States approaches are based on the concept of keeping or recreating in the laboratory the same conditions found in the reservoir regarding petrophysical properties, such as fluid saturation, rock wettability, capillary and confining pressure, and temperature.

Once the measurement of certain properties of porous media directly from the well is impossible, laboratory analyses are needed for a good understanding of the reservoir. Additionally, coring a rock sample from the reservoir preventing the impact of all sources of contamination, and pressure and temperature drop is extremely difficult. If this operation fails, it may impact the distribution of fluids and enhance the deposit of asphaltenes or other heavy fractions of crude oil (Cuiec, 1975).

There are basically three possible Initial States approaches:

a. Fresh State

It consists of doing experimental study on the cores immediately after drilling without cleaning the sample. This method considers that, as experimental analysis are held in a short period of time after plug extraction, no substantial change in its saturation and wettability has occurred.

This technique is very rarely used in the industry for multiphase flow experiments, as these experiments demand an on-site specific laboratory with complex structure, a long core selection process.

b. Preserved State

This technique aims at avoiding exposing the core sample to situations that may disturb the natural conditions as in the reservoir, such as mechanical disturbance, exposure to air and water evaporation. This minimizes slow, long term wettability modification, considering it has remained preserved as the in-situ state (Anderson W. , 1986), besides shortening duration of lab work. However, it requires dedicated procedures, staff organization not only for coring, but also for shipping and preservation. Moreover, by using this technique, it is not possible to work on cores that have been stored for a long period of time once it may have lost its preserved characteristics.

c. Restored State

It is a technique that consists of rebooting the petrophysical conditions of the core plug to recreate all the steps that the sample has undergone prior coring. The same precautions taken to obtain preserved-state cores are valid for restored state cores.

Nonetheless, if one of these precautions is not satisfied, cores may be retreated to the correction of any mislead.

The main advantages of this technique are that it may help reverse the damage if wettability was altered during coring, tripping out or shipping and it enables the use of old cores. On the other hand, the issues are uncertainties related to the appropriate techniques for restoration, and the duration for core preparation.

The choice between the Fresh State or the Restored State approach was largely discussed by (Reed *et al.*, 2022). In this paper, the authors have developed a protocol to evaluate the possibility of performing a preserved state analysis rather than the restored state according to several conditions, such as the type of mud used, if a mud-tracer was used, if oil asphaltenes are stable, *etc*.

As we aimed at studying the methods for setting initial water saturation, we will focus on the restored state approach.

1.8.2. Typical experimental workflow – restored-state method

A typical workflow for the restored state method is described in detail here below:

a. Cleaning with solvents

As cores are usually drilled with wettability-altering, oil-based, surfactant containing muds, a special procedure in order to obtain proper analyses is needed (Wendel *et al.*, 1987).

The most used cleaning methods in petroleum laboratories are:

- Standard hot distillation/extraction (Soxhlet method (Soxhlet, 1879))

  Solvent, usually toluene, is continuously distilled at 110°C, condensed, and then distributed over the top of the sample in the Dean-Stark apparatus (Bynum & Koepf, 1957).

  An important question arises from the Soxhlet method using toluene for reservoir core plugs. As toluene boiling point is around 110 °C, water present in the sample will boil before the complete extraction of the crude oil. Moreover, water solubility in toluene increases considerably, which enhances this effect. This situation may enable a direct contact between crude oil and the mineral surface that is no longer protected by adsorbed water. This way, crude oil adsorption, thus wettability alteration may occur (Hirasaki *et al.*, 1990).

  The possible solutions would be to use solvents with lower boiling points, such as the Methylene Chloride, which has a boiling point of 40 °C (McCaffery *et al.*, 2002).

- Miscible flow through of solvents:

  Solvents are injected under pressure into the core placed in a coreholder. The main control for cleaning efficiency is the color of the solvent in the outlet tubing after the system was shut-in for several hours.

Both methods may be performed whether at room or elevated temperature. High temperature cleaning is recommended when the crude oil present in the sample contains paraffins. On the other hand, hot cleaning is not recommended when the

cores contain gypsum, as it may be converted to anhydrite (Bynum & Koepf, 1957; Hurd & Fitch, 1959).

The cleaning step is followed by drying the core samples. This action is usually performed by nitrogen (N_2) injection, followed by humidity-controlled oven drying at 80°C. Oven-drying should not exceed 100°C for samples containing clays as it would dry the water from the clays, causing destabilization, in some cases.

b. Petrophysical characterization

Before saturating the core sample with formation brine, porosity and absolute permeability are measured. There are different techniques for performing these measurements. In this work, we used the Helium Grain Volume technique for measuring solid volume, thus, pore volume. For the measurement of the gas permeability, we used a steady-state equipment.

The Helium Grain Volume measurement is performed in a pycnometer, that is composed of twin-cell helium porosimeter, that operates on the principal of Boyle's law, that states that, for an ideal gas and constant temperature, the product of pressure and volume in a closed system remains constant. This experiment is performed using Helium because it is a noble gas at ambient conditions and it has a small molecular size, enabling it to penetrate easily in the whole porosity.

To perform this measurement, helium is injected into a line system of chambers. First, helium is allowed into a reference volume of volume V_{ref}, at pressure P_{ref}. This volume is isolated by two valves V_1 and V_2. The expansion chamber, of volume V_{exp}, is composed of a matrix cup and is isolated by valves V_2 and V_3. As valve V_2 is opened, helium will expand to occupy all the available volume at a new pressure P_{exp}. The expanded pressure depends on the ratio of V_{ref} to V_{exp}, and is expressed by:

$$P_{ref}V_{ref} = P_{exp}\left(V_{ref} + V_{exp}\right) \tag{48}$$

The following step consists of placing the dry rock sample inside the matrix cup. The volume of the matrix cup will be reduced by the volume of the solid matrix of the rock sample (V_s). Repeating the steps described above, when V_2 is opened to allow helium to expand and occupy the whole system, it will invade the sample pore network. Therefore, the application of Boyle's Law becomes:

$$P_{ref}V_{ref} = P_{exp}\left(V_{ref} + V_{exp} - V_s\right) \tag{49}$$

If we rearrange and solve the equation for V_s, we have:

$$V_s = \frac{P_{exp}\left(V_{ref} + V_{exp}\right) - P_{ref}V_{ref}}{P_{exp}} \tag{50}$$

In possession of the sample grain volume, we obtain the pore volume by performing the difference between the bulk volume (total volume) and the grain volume. Non-destructive bulk volume measurements are limited to the caliper system, given that we use cylindrical samples, or by means of more sophisticated machines, usually using lasers. In this study, bulk volume was measured by a laser machine, that scans and generates a 3D model of the sample. This approach takes into consideration any kind of imperfection that are not captured by the caliper system.

Usually performed using nitrogen as the injected gas, steady-state permeability measurement follows (51) equation, at atmospheric conditions:

$$k_g = \frac{2 \cdot Q_0 \cdot P_0 \cdot \mu_g \cdot L}{A \cdot (P_1^2 - P_2^2)} \quad (51)$$

where, Q_0 is gas flow rate at atmospheric pressure, P_0 is measured atmospheric pressure, μ_g is the gas viscosity, L is the sample length, A is the cross-section of the sample, and P_1 and P_2 are inlet and outlet pressures, respectively.

As motion of gases in capillaries do not follow the same regime as liquids, a non-linearity condition appears when performing steady-state gas permeability. The degree of interaction between gas molecules and pore walls is described by:

$$\frac{4 \cdot c \cdot \lambda}{r} = \frac{b}{P_m} \quad (52)$$

where c is a constant, λ is the mean free path of a gas which is related to the inverse of the molecular weight of the gas, r is the mean pore (capillary) radius, P_m is the mean pressure and b is a measure of slippage between the gas molecules and the pore walls.

At lower densities, the molecules will collide less frequently with the pore wall, which means more slippage, thus b is enhanced and gas permeability is increased. At higher pressures, the gas molecules are closer to each other, behaving more like a liquid, experiencing a friction drag against at the side of the pore walls, thus decreasing gas permeability. This concept was interpreted by Klinkenberg (1941) to conceive an extrapolation of the measured gas permeability, where this effect would be negligible if an infinite gas pressure would be considered ($\frac{1}{P_m} \approx 0$). Therefore, to perform a Klinkenberg gas permeability, usually four mean pressures are measured, adjusting the system backpressure to obtain different points. Gas permeability data is plotted against the inverse of the mean pressure data. These should fall on a straight line as in Figure 23:

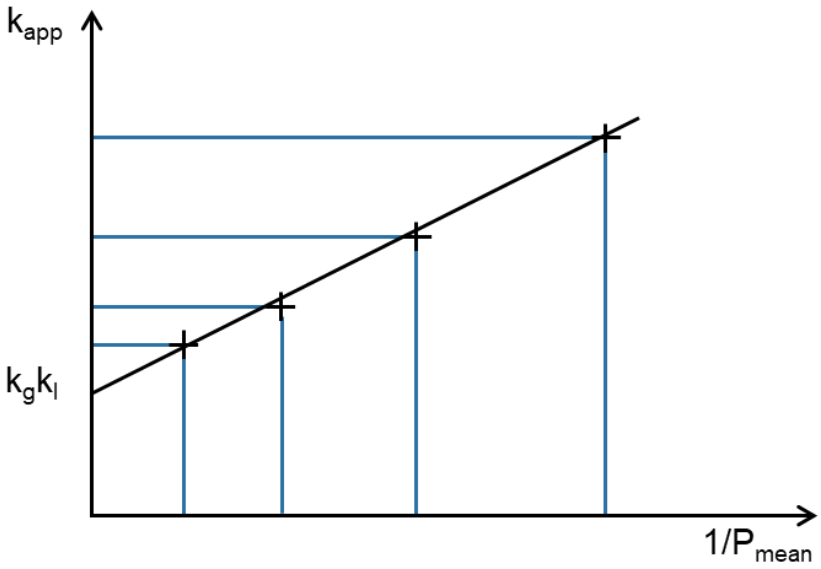

Figure 23 - Example of a Klinkenberg gas permeability plot.

The Klinkenberg permeability is calculated from the multi-pressure gas permeability data using equation (53):

$$k_g = k_l \cdot \left(1 + \frac{b}{P_m}\right) \quad (53)$$

We will discuss the pycnometer and the steady-state gas permeability equipment in the corresponding sub-sections in the Methodology chapter.

c. *Saturation with formation brine*

The influence of brine salinity and ionic composition has been underestimated for years. An illustration of this situation are Cuiec's deep wettability studies over the 70's and 80's, where 100 g/l NaCl brines were typically used for the experiments on reservoir cores (Cuiec, 1975; Cuiec, 1977; Cuiec, 1984).

During the 90's; some studies analyzed the influence of brine composition on wettability change for different lithologies. The main parameters taken into consideration were brine salinity, brine composition and cation valency, and pH (Brown & Neustadter, 1980; Jadhunandan & Morrow, 1995; Bousseau *et al.*, 1995; Tang & Morrow, 1997; Tang & Morrow, 1999; Sharma & Filoco, 2000; Zhang & Austad, 2006). All these studies show the importance of reproducing as closely as possible the characteristics of in situ brine on laboratory experiments.

After brine saturation, the liquid base permeability may be obtained from the direct application of Darcy's Law, as presented in equation (29).

d. *Primary drainage*

The drainage step drives the core to the desired initial water saturation, that is targeted following the S_{wi} *versus* height plot and the depth where the samples was cored. This is a key parameter for setting initial water saturation, as wettability is highly dependent on oil saturation.

When performing primary drainage, there are three main parameters that control which technique will be selected for setting S_{wi}. The parameters are reaching the target value of S_{wi}, experimental duration and rock consolidation. The different techniques for establishing initial water saturation on core sample will be thoroughly discussed in the corresponding section (Primary drainage techniques).

e. *Ageing in crude oil*

In a typical restored state workflow, the wettability restoration (alteration, in case of outcrop samples) is performed during the ageing step, and it represents the last step of the initialization of the core. The cores may be aged following different protocols that are deeply discussed in the corresponding section (Impacts of wettability heterogeneities on flow in core samples).

When altering the wettability by ageing in crude oil, a decrease in $k_{row}@Swi$ is expected between the previous value measured at the end of primary drainage and the new measurement performed after ageing in crude oil. This is explained by the bigger interaction between the oil and the rock surface after the rock has become oil-wet. Therefore, oil needs higher pressure to flow in the oil-wet case than in the water-wet case, because it flows at the rock surface and no longer at the center of the pores.

After the ageing step, the sample is considered to be at the restored state condition regarding fluids saturation and distribution and wettability, ready to undergo the following steps of the experimental cycle (*e.g.*, Amott-Harvey test, imbibition relative permeability, EOR studies).

1.8.3. Primary drainage techniques

There are three major primary drainage techniques in SCAL experiments, which main advantages and drawbacks are presented in Table 3:

Technique	Advantages	Drawbacks
Viscous Oil Flood	Fast method	Non-uniform saturation profile
	Standard injection rig and equipment	Difficult to reach low Swi values
	Possibility to obtain primary drainage Kr	Fines migration under high flowrate
Centrifugation	Faster than Porous Plate	Friable samples can be easily damaged
	Capillary pressure driven technique	Specific equipment needed
	More uniform saturation profiles than Viscous Oil Flood	Manipulation needed for further SCAL steps
Porous Plate	Homogeneous saturation profile	Time consuming
	Good method for friable samples	Capillary contact may be a problem
	Capillary pressure driven technique	Manipulation needed for further SCAL steps

Table 3–Advantages and Drawbacks of PD techniques *(McPhee, Reed, & Zubizarreta, 2015)*.

Different authors have worked to find a solution for a proper primary drainage technique that could reach a target S_{wi}, a homogeneous S_{wi} profile, with an acceptable experimental duration, preventing any additional handling between primary drainage and subsequent steps of the experimental workflow. Among them, we can highlight the Spinning Porous Plate (SPP) (Fleury, 2009) and the Toroidal Porous Plate (Pentland *et al.*, 2014).

The Spinning Porous Plate, which consists in placing a sample in contact with a multi-perforated porous plate and performing primary drainage by centrifuge, presents satisfactory results regarding the homogeneity of the saturation profile for 70mD sandstones at low S_{wi} targets. However, it fails in achieving the same homogeneity quality for tighter samples and at higher levels of S_{wi}. Furthermore, performing primary drainage in the centrifuge demands additional handling for following SCAL steps.

To overcome these combined issues, the Toroidal Porous Plate was proposed. However, the by-pass in this case only served for performing further flooding after setting S_{wi} by a classic Porous Plate primary drainage. Therefore, the main issue of the Porous Plate (long experimental duration) is not resolved.

a. Viscous Oil Flood

Most widely used technique for setting initial water saturation, the Viscous Oil Flood consists in injecting oil in an initially fully water-saturated sample at constant flowrate steps while measuring the pressure drop between inlet and outlet as well as

fluid production (Salathiel, 1973). This method may be performed whether by injection of both phases (steady-state) at different flowrate ratios or by injection of only one phase (unsteady-state). Until oil breakthrough, only water will be produced as oil percolates in the sample. After oil breakthrough, a production of both phases will be observed until brine production ceases, in the unsteady-state case. This is a fast technique that does not require a particular setup, being possible to be carried out in the same cell used for the following steps of SCAL (ageing and flooding) and by a simple injection rig.

Moreover, this is a technique that allows the direct measurement of end-point effective permeability from simple application of the multiphase Darcy's Law (McPhee *et al.*, 2015). For performing the measurement of $Keff\ (Sw)$, a steady flow of both the injected and produced phase, and a constant dP must be attained. For this reason, obtaining K_{eff} for both phases is only possible by the steady steady-state technique, once a steady flow of both phases for a given water saturation value is possible. In the case of unsteady-state experiments, the measurement of only the injected phase K_{eff} is possible, as only the injected phase may reach a steady flow.

In this work, we will focus on the unsteady-state technique, used on the experimental work.

During oil injection, there are three important data to record: pressure drop along the injection axis, water production at the outlet and the saturation profiles during flow (in the case of an experimental setup having an in-situ saturation monitoring system). According to McPhee *et al.* (2015), *in situ* saturation monitoring is recommended once it provides information about saturation profiles and the extent of Capillary-End Effects, which helps deconvolute the impact between capillary pressure and relative permeability to production history by numerical simulations

An illustration of these data is shown in Figure 24.

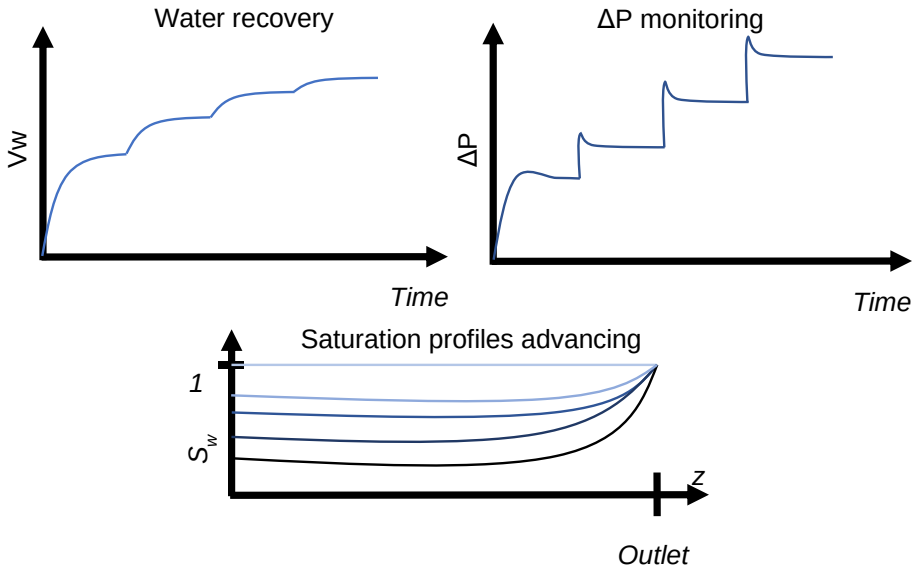

Figure 24 - Representation of experimental data obtained in USS Viscous Oil Flood.

Knowing ΔP, water production and flowrate *versus* time, a deconvolution can be done in order to determine primary drainage relative permeability and capillary pressure curves (Ramakrishnan & Cappiello, 1991; Fordham *et al.*, 1993; Lenormand

et al., 1993; Huang, 1998; Romanenko & Balcom, 2013). Capillary pressures obtained through deconvolution are usually described using analytical models, such as the LogBeta function (CYDAREX, 2021). The LogBeta function have three different definitions, usually used for primary drainage (threshold S_{max}), imbibition (threshold S_{min}) and secondary drainage (no threshold) deconvolutions.

The general P_c LogBeta function, with no threshold, is defined by:

$$P_c = -\frac{A}{\beta} P_0 \left(\ln \frac{S^{*\beta}}{1 - S^{*\beta}} - \ln \frac{(1 - S^*)^\beta}{1 - (1 - S^*)^\beta} \right) + b \tag{54}$$

The magnitude P_0 and the saturation S_0 are "physical parameters", and S_0 is the water saturation at $P_c = 0$. They are related to factor "b" by:

$$b = \frac{A}{\beta} P_0 \left(\ln \frac{S^{*\beta}_0}{1 - S^{*\beta}_0} - \ln \frac{(1 - S^*_0)^\beta}{1 - (1 - S^*_0)^\beta} \right) \tag{55}$$

The parameter "A" is calculated for the continuity of the curve.

In the case of primary drainage, the pressure threshold is usually applied at maximum normalized saturation value $S^* = 1$, and P_c for S^* lower than the threshold is defined as follows:

$$P_c > P_t \rightarrow P_c = P_0 \frac{1}{S^*} \tag{56}$$

On the other hand, for the imbibition case, the pressure threshold is typically applied at the minimum normalized saturation value $S^* = 0$, and P_c for S^* values greater than the threshold are defined according to the equation presented here below:

$$P_c < P_t \rightarrow P_c = -P_0 \frac{1}{(1 - S^*)} \tag{57}$$

The existence of Capillary End Effects (CEE) from capillary pressure drop along the sample is an important constraint (as seen in Figure 25 – experiment performed in this project, that will be discussed in more detail in the results section). Even though this problem is mitigated on steady-state experiments, it is still noticed on both approaches.

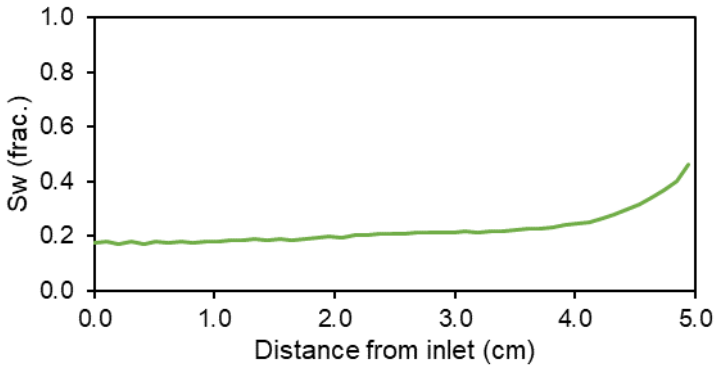

Figure 25 - NMR imaging of the water saturation profile of a Bentheimer sandstone at the end of a Viscous Oil Flood (VOF) primary drainage. Capillary end effects are clearly visible close to the sample outlet.

It was noticed by Leverett & Lewis (1941) that the wetting phase tends to get trapped due to a discontinuity in capillary forces. This generates a build-up in the wetting phase saturation close to the outlet thus reducing the non-wetting phase permeability. Moreover, a $P_c = 0$ condition applies to the sample outlet $z = L$. In the case of a primary drainage, where sample was initially brine-saturated, water saturation at null capillary pressure is zero ($Sw(Pc = 0) = 0$). This condition also contributes to CEE generation during VOF primary drainage.

As this phenomenon represents an experimental artifact, it must be corrected to represent the behavior of a real reservoir (where these effects will only be observed close to the production wells). For avoiding this situation, laboratories usually apply high flowrates to reduce Capillary-End Effects. Nonetheless, this does not represent actual flow in the reservoir. Besides, it may generate an instability of the flood front and lead to lower S_{wi} than the initial target. Moreover, this approach may cause irreversible damage in the core, such as fines migration and additional pore volume creation, impacting further measurements once the rock matrix has been modified.

A solution to eliminate capillary end effects is reversing the direction of oil injection. Although this method may produce a homogeneous saturation profile, two major issues may outcome:

- Unwanted imbibition from the mobilization of the brine concentrated at the sample outlet. This brine will be displaced towards the inlet, increasing water saturation at these points. This phenomenon can be seen in Figure 26.
- Formation of disconnected oil clusters that will adversely affect wettability restoration and impact effective permeability measurements, as showed by (Nono *et al.*, 2022).

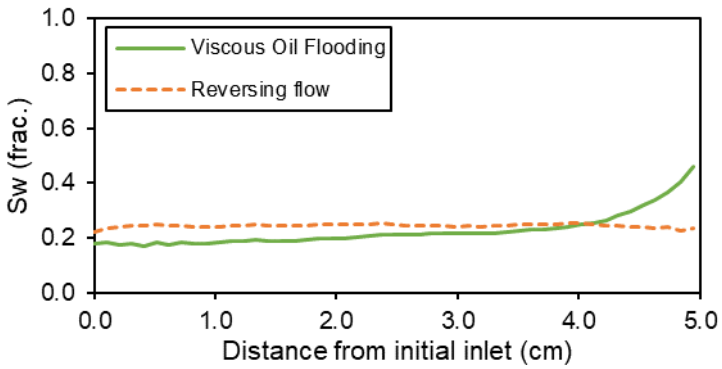

Figure 26 - Bentheimer sandstone submitted to VOF followed by flow direction reversal – NMR profiles imaging. It is possible to observe a general imbibition of the brine present in the last cm after the last step of VOF (green line) on the final profile (orange-dashed line).

b. Centrifuge

Centrifugation is another widely used technique for setting initial oil saturation. This technique was introduced by (Hassler & Brunner, 1945). It consists in placing a rock sample inside a centrifuge machine that will induce an injection pressure through centrifuge forces imposed by high-speed rotation. If we consider only a one-dimensional flow, the capillary pressure at a radius *r* is given by Eq. (58).

$$P_c(r) = \frac{1}{2} \cdot \Delta\rho \cdot \omega^2 \cdot (R^2 - r^2) \tag{58}$$

where P_c is capillary pressure, $\Delta\rho$ is the difference between the densities of fluid phases, ω is the rotational speed of the centrifuge, and R is the distance between the centrifuge central axis and the sample outlet.

The issues of this technique are not only the presence of capillary end effects (as seen in Figure 27), but also the possibility of not desaturating the outlet face of the sample. This effect comes from the boundary condition when r is equal to R in Eq. (58), which gives $P_c = 0$, then, $S_w = 1$.

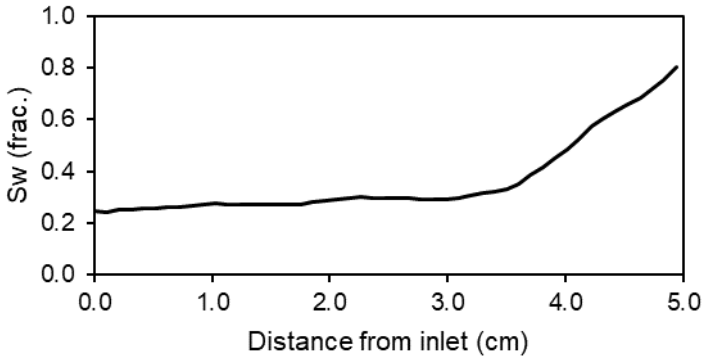

Figure 27 - Water saturation profile acquired by NMR after a Centrifuge primary drainage of a Bentheimer sandstone. Once again, the presence of CEE is clearly noticed close to the outlet. This experiment will be treated in more detail in the results section.

The solution for these problems is to reverse injection direction, such as in the Viscous Oil Flood case; however, this leads to the same issues, with an aggravating factor: by imposing a gradient in capillary pressure in the other direction, the control of the homogeneity of the saturation profile is extremely difficult. A mislead in the control of the homogenization of the saturation profile will generate a situation such as in Figure 28.

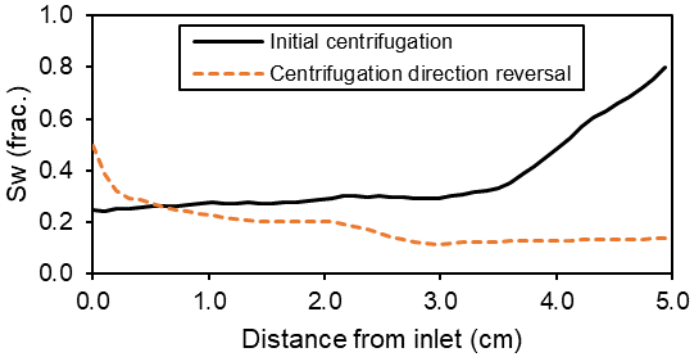

Figure 28 - Centrifugation primary drainage of a Bentheimer sandstone, imaged by NMR. The black solid line represents the water saturation profile following the first injection direction. The greend solid line represents the saturation profile after injection direction reversal.

In addition, the centrifuge method limits sample size, it may induce sample damaging from high-speed rotation and manipulation is generally needed to unload the sample from the centrifuge machine and load it into the coreflooding cell, where further displacements will be performed.

Nonetheless, capillary end effects are not always phenomena that need to be minimized. Some experiments have been designed to take advantage of this effect, for example, to speed up the measurement of the capillary pressure curve, as

presented by (Fleury, 1998; Green *et al.*, 2008; Faurissoux *et al.*, 2018; Danielczick *et al.*, 2021).

c. Porous Plate

The semi-permeable membrane method or the Porous Plate, as it is largely known, consists of placing a water-wet semi-permeable ceramic in the outlet face of the sample and injecting oil at constant pressure through several steps. The Porous Plate technique was first introduced to measure capillary pressure *versus* water saturation in a water/gas system (McCullough *et al.*, 1944), being further extended to water/oil systems. This process can be done individually by using special coreholders or on a batch basis, by using a specific apparatus. Nonetheless, the use of individual coreholders at reservoir confining stress is recommended (McPhee *et al.*, 2015). As the water production can be monitored, it is possible to draw the $Pc\ (Sw)$ curve at the end of the experiment.

For performing this technique, a water-saturated semi-permeable ceramic plate is placed in the outlet of the sample, in which oil will be injected at constant pressure steps (in the case of an oil/water experience). The ceramic has a high entry-pressure threshold due to its small pores and for being strongly water-wet. The oil phase is considered to be connected along the sample, which generates a homogeneous capillary pressure, thus a homogeneous saturation profile. Figure 29 presents the S_{wi} profile at the end of a Porous Plate experiment executed in this project, which will be presented in more detail in the results section.

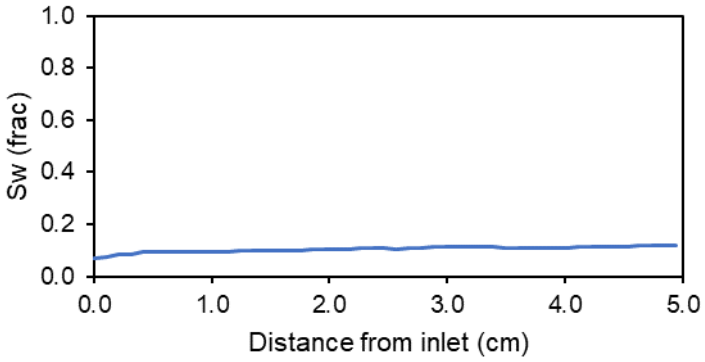

Figure 29 - Water saturation profile of a Bentheimer sandstone after Porous Plate primary drainage, imaged by NMR.

The Porous Plate technique is considered as the reference once it better reproduces what happens during petroleum migration in terms of fluids motion. The main issue of this technique is the experimental time needed to reach the target S_{wi}, due to the extremely-low permeability of the porous plate. Another drawback is the need of unloading the porous plate from the overburden cell to perform further SCAL steps.

1.8.4. Impacts of wettability heterogeneities on flow in core samples

For a proper initialization, there are some principles that must be followed during cleaning, primary drainage, and ageing steps.

Reaching a correct value of S_{wi} at the end of primary drainage is important because wettability alteration is dependent on the oil saturation in the sample. This evidence was analyzed by different authors on both sandstone and limestone outcrop samples (Jia *et al.*, 1991; Jadhunandan & Morrow, 1991; Zhang & Austad, 2005).

However, simply reaching a target value of S_{wi} may hide some traps, such as the presence of Capillary End-Effects (CEE). A good example was presented in Figure 26, where both saturation profiles are at the same mean S_{wi}; however they are notoriously different; CEE are clearly present in one of the curves.

As wettability change during ageing is dependent on fluid saturations, a non-uniform wettability profile will result from a sample which capillary end effects have not been removed. Therefore, this situation must be avoided in a typical restored state protocol.

Furthermore, maintaining a homogeneous saturation profile during ageing is a necessary but insufficient condition for obtaining a homogeneous wettability profile. This situation raises the question about the best ageing method.

a. Static ageing in sealed vessels at elevated temperature:

This technique was widely used for wettability alteration (Wendel *et al.*, 1987; Villard *et al.*, 1993; Zhou *et al.*, 1995; Jadhunandan & Morrow, 1995; Tang & Morrow, 1997; Morrow & Xie, 2001; Tie & Morrow, 2003; Esfahani *et al.*, 2003; Tong & Morrow, 2005; Al-Mahrooqi *et al.*, 2005; Tie & Morrow, 2005; Hognesen *et al.*, 2005; Austad *et al.*, 2008; Johannesen *et al.*, 2008). However, Spinler *et al.* (1999), Spinler *et al.* (2002), and Standnes & Austad (2000) showed that this could generate a radial heterogeneous wettability in the sample. The apparent wettability of the plug varied from strongly water-wet at the center to moderately water wet near the edges. It was speculated that this observation is the consequence of the diffusion of the surrounding crude oil into the plug during the aging period.

In the work from Mascle *et al.* (2019) this behavior was also verified from the observation of 2D saturation profiles during spontaneous water imbibition. Moreover, the authors cut the sample in half along the longitudinal axis, after the experiment. A concentration of asphaltene and resin deposits could be observed in the outer part of the core plug.

b. Core plugs flushed with crude oil during ageing, without flow reversal:

Another usual approach to age the sample consists of oil flushing in high temperature during the ageing step (Wolcott *et al.*, 1993). As the degree of wettability change depends on the amount of crude oil that flows through the sample (Jia *et al.*, 1991), this approach would be preferred over the static ageing.

In the work from (Graue *et al.*, 2002), despite a homogeneous saturation profile at the end of primary drainage, a heterogeneous wettability profile was produced by performing unidirectional crude oil flush. Johannesen *et al.* (2008) confirmed experimentally that this method generates the worst longitudinal heterogeneity of wettability.

c. Core plugs flushed with crude oil during ageing, performing flow reversal:

This approach consists of reversing the injection direction of crude oil during ageing. Graue *et al.* (2002) compared the different ageing methods and concluded that this is the most efficient technique for performing homogeneous wettability restoration.

Moreover, the works from Aspenes *et al.* (2003), Johannesen *et al.* (2006), and Johannesen *et al.* (2007) also presented solid results regarding wettability homogeneity by performing a multidirectional crude oil flooding during ageing.

1.8.5. Waterflooding techniques

This phase begins after the wettability restoration performed by ageing the core plug in crude oil. At this stage, the sample is at the same initial water saturation S_{wi} as at the end of primary drainage. During the waterflooding step, oil will be produced, taking the sample from S_{wi} to an experimental Remaining Oil Saturation, called ROS.

It is important to state that laboratory waterflood experiments provide true residual oil saturation to water (S_{orw}) exclusively in the case of homogeneous strong water-wet rocks, as most remaining oil is trapped as discontinuous droplets at the pore scale. At any other case than strongly water-wet, S_{orw} cannot be reached and is over estimated. This situation happens because oil is produced through films mechanisms.

The waterflooding techniques may be divided between displacing tests and permanent flow. Between the waterflooding techniques, we may highlight the Unsteady-state, Steady-state, Centrifugation, and the Semi-Dynamic Method.

In this work, we will concentrate on the Unsteady-State technique (USS) for performing waterflooding experiences.

The unsteady-state technique of waterflooding is a dynamic displacement test, where the main objective is to displace the oil phase by brine injection following a constant flowrate step. This method allows obtaining effective permeability values at end-point water saturation, which will be useful for defining a portion of the relative permeability curve.

Obtaining the relative permeability curve from this method is based on the works of Buckley & Leverett (1942) and Welge (1952), which allow the approximation of the saturation values in the displacement front and the mean saturation upstream the displacing front. The hypothesis for this experiment are the following:

- Homogeneous porous media
- Capillary pressure effects are negligible both in the extremities and in the saturation front zone
- The flow is linear (one-dimensional), unidirectional, and stable
- Fluids are non-miscible, Newtonian and incompressible, and their properties are constant during the test.

As the unsteady-state method allows only the measurement of the effective permeability of the displacing phase; a point of K_{eff} can only be acquired after the BT. Therefore, an USS waterflooding experiment will provide only a portion of the K_r curve (between BT and ROS).

During the initial phase of the experiment, assuming incompressible fluids, only oil is produced at the outlet face of the sample at the same rate of brine injection, therefore following linear production. After water breakthrough (BT) in the outlet face of the sample, both displacing and displaced phases will be produced; and the displaced phase production is no longer linear. The injection continues until no more oil is produced; thus, the sample is at constant saturation. Therefore, inlet and outlet flow are equivalent. At this moment, effective permeability may be measured simply using Darcy's law for multiphase flow, equation (35). The experiment continues by increasing flowrate to reach different values of water saturation.

The intermediate relative permeability data are determined either analytically (using Jones and Roszelle methods (Jones & Roszelle, 1978)) or numerically, via coreflood simulation. Nonetheless, the analytical approach proposed by the Jones and Roszelle method does not take into consideration the presence of CEE and provide K_r information exclusively after water BT.

For the interpretation of an unsteady-state waterflooding, monitoring of differential pressure between inlet and outlet, oil production and saturation profiles monitoring are necessary. A schematic example of a waterflooding experiment data is presented in Figure 30.

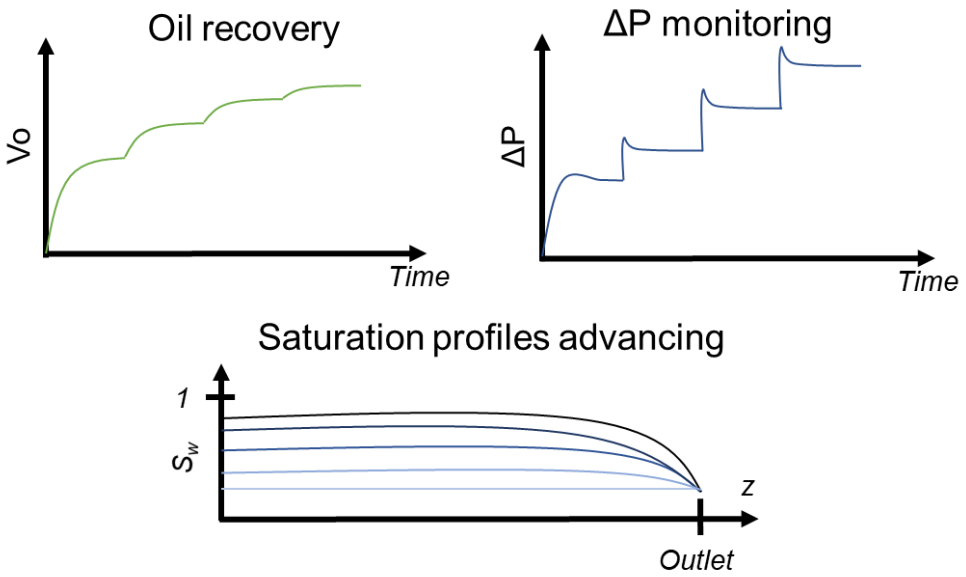

Figure 30 - Schematic example of experimental data obtained during an unsteady-state waterflooding.

As we may see in the saturation profiles presented in Figure 30, Capillary-End Effects are a usual artifact observed during fluids displacements. As Darcy's law for multiphase flow considers a homogeneous saturation along the sample, CEE mislead the direct measurement of effective permeability; dP measured will be higher than the correct value for the corresponding water saturation, thus decreasing the measured effective permeability.

After a coreflood simulation where these artefacts will be removed, the corrected curves of relative permeability will be defined. An example of the errors generated by the direct measurement of K_{eff} in the presence of CEE is represented by the crosses in Figure 31. It is possible to notice that the crosses do not follow the correct trend of the simulated K_r.

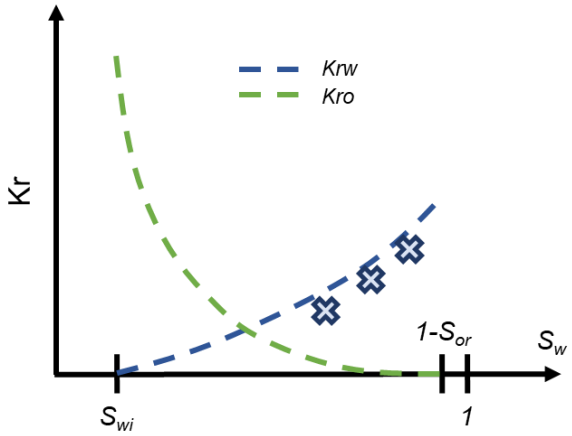

Figure 31 - Schematic example of mislead in the direct measurement of K_{eff} during USS waterflooding.

2. Imaging Techniques

Visualizing and understanding the behavior of fluids inside the pore space is essential in the Petrophysics domain. It allows not only the definition of important static parameters, such as porosity and fluid saturations, but also contributes to the comprehension of the dynamic behavior of porous media, through saturation profiles monitoring, wettability, and pore occupancy.

Two main techniques used in petrophysical laboratories, Magnetic Resonance Imaging (MRI) and X-ray Micro-Tomography (µ-CT), have both seen their first use in the medical domain for different purposes.

In the medical domain, MRI is a tool used to diagnose soft-tissue problems. This technique produces images by using a contrast agent that is affected by the way fluids present in the body relax. The properties of these fluids, particularly their viscosity, are what cause the contrast agent to work in MRI. On the other hand, µ-CT imaging bases the contrast of its images on the density difference between tissues. In the Petrophysical domain, we may define that by performing MRI we are interested in understanding the behavior of fluids in porous media (greater viscosity contrast), and by performing µ-CT, we are mostly attracted by the visualization of the solid matrix.

In this work, we used MRI and µ-CT to obtain important parameters for the understanding of the primary drainage process, such as saturation profiles, indications of wettability, fluids distribution in the porous media and pore occupancy.

2.1. Nuclear Magnetic Resonance

Nuclear Magnetic Resonance (NMR) measures the interaction between protons within the nucleus of a tuned element under an applied magnetic field. This allows the definition of the volume of this element present inside the sample and their placement in terms of contact with a solid surface.

The first NMR experiments were performed independently by Bloch (1946) and Purcell *et al.* (1946). Nonetheless, a further exploration of this technique was achieved after the discovery of the chemical shift effect (Arnold *et al.*, 1951) and the construction of permanent magnets capable of generating more homogeneous magnetic fields (Anderson W. A., 1956; Arnold J. , 1956).

In the Petrophysics domain, Nuclear Magnetic Resonance is used in downhole measurements, for fluid and reservoir characterization, and as desktop laboratory equipment, for porosity measurement and the identification of the placement of fluids inside porous media. These NMR tools are usually tuned to the resonant frequency of protons inside the Hydrogen nucleus, as this is the most present element in reservoir fluids. In this work, the NMR setup consists of a GeoSpec 12 MHz low-field spectrometer by Oxford Instruments, equipped with magnetic field gradients on the vertical axis.

In the following sub-sections, a brief description of the NMR theory is provided and its application to SCAL is presented. A more fundamental description may be found in the literature (Callaghan, 1991).

2.1.1. The nuclear spin

The spin is a fundamental property of any elemental particle. This property is quantified by the quantum number I that is the number of unpaired protons and neutrons, which takes quantized positive or null values in half integer steps. The net

spin of NMR-active nuclei generates a spin angular momentum $\boldsymbol{P}$, that, for an isolated nucleus, takes discrete values driven by the quantum number "I". The spin angular momentum $\boldsymbol{P}$ is defined by (59):

$$\boldsymbol{P} = \frac{h}{2 \cdot \pi}[I(I+1)]^2 \tag{59}$$

where h is Planck's constant. I can be integral or half integral, and for the most studied nuclei, ^{13}C and ^{1}H, $I = {}^{1}/_{2}$.

For a non-zero spin nuclei, $\boldsymbol{P}$ generates a magnetic field having an associated magnetic momentum $\boldsymbol{\mu}$, given by (60):

$$\boldsymbol{\mu} = \gamma \cdot \boldsymbol{P} \tag{60}$$

where γ is the gyromagnetic ratio of the nucleus.

In the absence of an external magnetic field, magnetic moments of induvial nuclei are randomly oriented, with a net moment, $\boldsymbol{M}_0$, equal to zero. By applying a static external magnetic field in the z direction, $\boldsymbol{B}_0$, for a nucleus with spin $I = {}^{1}/_{2}$, nuclear spins align according to this applied magnetic field, adopting one of the energy levels states (between $I = {}^{1}/_{2}$ and $I = -{}^{1}/_{2}$). This orientation phenomenon is called the Zeeman effect, and each level is given a magnetic quantum number, m. The energy associated to each state, result of the interaction between a nuclear dipole moment and the magnetic field, is described by (61):

$$E = -\boldsymbol{\mu} \cdot \boldsymbol{B}_0 \tag{61}$$

A transition between energy states may occur from photon absorption or emission, quantized by:

$$\Delta E = h \cdot v = \left|\gamma \cdot \frac{h}{2 \cdot h} \cdot \Delta I \cdot \boldsymbol{B}_0\right| = \gamma \cdot \frac{h}{2 \cdot h} \cdot \boldsymbol{B}_0 \tag{62}$$

where v is the nucleus resonance frequency.

A Zeeman diagram for the ^{1}H atom is presented in Figure 32, where two possible energy states occur – a lower energy α-state, with spins aligned with $\boldsymbol{B}_0$, and the higher energy β-state, with spins not aligned with $\boldsymbol{B}_0$.

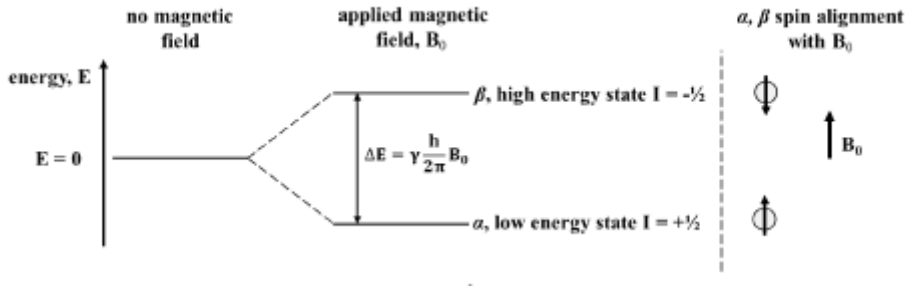

Figure 32 - Representation of the Zeeman diagram for the ^{1}H nucleus in the presence of a magnetic field $\boldsymbol{B}_0$,.

The population ratio of the two spin states at thermal equilibrium is given by the Boltzmann distribution, presented in (63):

$$\frac{N_\beta}{N_\alpha} = exp\left(-\frac{\Delta E}{k_B \cdot T}\right) \quad (63)$$

where, $N_{m,I}$ is the population of the m_I spin state, k is the Boltzmann's constant ($1.38 \cdot 10^{-23} JK^{-1}$) and T is the absolute temperature.

2.1.2. The vector model

The transition between these two states of energy are the source of NMR signal, and they are formally from a quantum mechanical nature. Nonetheless, these concepts may be translated into a more physical and conceptual approach, analogous to classical angular momentum, known as the vector model. We will apply this model to describe the behavior of a ^{1}H nucleus.

Applying a magnetic field causes a torque on the magnetic moment, $\boldsymbol{\mu}$, of each ^{1}H nucleus. The angular momentum generated is expressed by:

$$\frac{d\boldsymbol{P}}{dt} = \boldsymbol{\mu} \times \boldsymbol{B} \quad (64)$$

where $\boldsymbol{P}$ is the angular momentum and $\boldsymbol{B}$ is the applied field. For generality, magnetization and applied field are expressed in vector notation.

The ensemble average of the individual magnetic moments is defined as the magnetization vector, $\boldsymbol{M}$. When there is no application of an external magnetic field, the direction of individual magnetic moments is random due to thermal motion. However, when an external magnetic field $\boldsymbol{B_0}$ is applied, a slight energetic preference for the magnetic moments will be noticed, as they will align with the applied magnetic field. Even though individual magnetic moments seems to be random, the ensemble average has a net alignment in the direction of the field. The described phenomenon may be schematically observed in Figure 33:

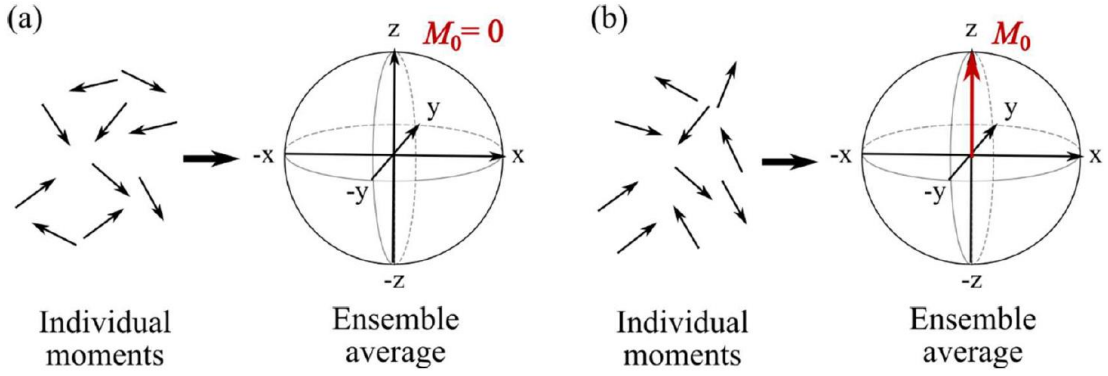

Figure 33 - Schematic representation to the magnetic moments when there is no external applied magnetic field (a) and when there is an external applied magnetic field (b) (Ward-Williams, 2020).

An additional oscillating radio-frequency magnetic field $\boldsymbol{B_1}$ may be applied to the background field $\boldsymbol{B_0}$. This field corresponds to the radiofrequency section of the electromagnetic spectrum, known as RF pulses. The pulses are applied for a short duration (<1 ms) and rotate the magnetization vector $\boldsymbol{M_0}$ with angular frequency, ω_0, disrupting from its original alignment with the field $\boldsymbol{B_0}$. When this occurs, the torque

causes a precession of the nuclear spins about the $\boldsymbol{B_0}$ field. This motion is known as the Larmor precession, $\boldsymbol{\omega_0}$, and for a static field aligned with the z-direction may be described mathematically as:

$$\boldsymbol{\omega}_0 = -\gamma \cdot \boldsymbol{B}_0 \tag{65}$$

NMR experiments measure the evolution of bulk magnetization $\boldsymbol{M}$ following the RF pulse in the transverse x-y plane. Therefore, $\boldsymbol{B}_1$ must oscillate in resonance with $\boldsymbol{B}_0$, so that $\boldsymbol{B}_1$ tips $\boldsymbol{M}$ into x-y, where $\boldsymbol{M}$ simultaneously precesses about both $\boldsymbol{B}_0$ at ω_0, and $\boldsymbol{B}_1$ at ω_1.

2.1.3. The rotating frame

The fact of applying different magnetic fields through various radio-frequencies may easily complexify the reference frames in the laboratory. A convention to simplify this situation consists of denoting a rotating reference frame, with axes, x', y' and z'. This reference frame rotates with the same angular frequency as the Larmor precession about z in the laboratory frame, such that, in the rotating frame, $\boldsymbol{B_1}$ appears to be static and $\boldsymbol{M}$ simply precesses about $\boldsymbol{B_1}$ in the rotating frame, as seen in Figure 34.

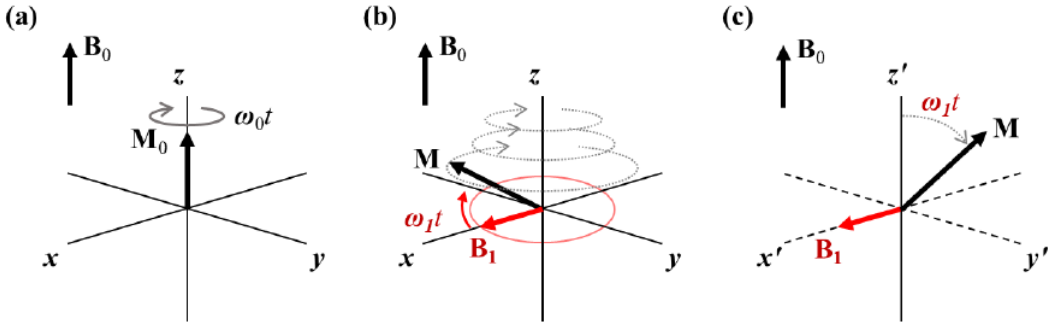

Figure 34 - Schematic illustration of the Bloch vector model and the rotating frame of reference: (a) shows $\boldsymbol{M_0}$ precessing about $\boldsymbol{B_0}$ at $\boldsymbol{\omega_0}$ and (b) and (c) $\boldsymbol{M}$ precessing about B0 and B1 due to additional RF field $\boldsymbol{B_1}$ in the laboratory and in the rorating frame of reference (Bush, 2019).

Controlling the magnitude and the duration, t_p, of the applied field $\boldsymbol{B}_1$, the degree of rotation may be chosen such that:

$$\theta = \omega_1 \cdot t_p = \gamma \cdot \boldsymbol{B}_1 \cdot t_p \tag{66}$$

Typically, $\boldsymbol{B}_1$ will be fixed and the different degrees of rotation will be selected by varying the duration of the pulse. For a 90° pulse-acquire experiment, transverse signal $\boldsymbol{M}_{x,y}$ following an exponential trend:

$$\boldsymbol{M}_{x,y} = \boldsymbol{M}_0 \cdot e^{i\omega_0 t} \tag{67}$$

2.1.4. Signal detection

A spin system precesses about a $\boldsymbol{B}_0$ field when perturbed. We may decompose this precession into two components: one in the z-direction and another transverse component in the x-y plane. The transverse magnetization precesses at the Larmor frequency, with a decreasing magnitude due to relaxation processes.

Usual laboratory spectrometers have detection coils in the x-y plane detecting $\boldsymbol{M}_{x,y}$ decay, which induces an oscillating current at ω_0, which are digitized and provide the NMR signal. This signal is known as Free Induction Decay (FID). For detecting both the direction and magnitude of the magnetization, both the x and y components of the magnetization are required. As it is rarely possible to position two isolated coils in the laboratory spectrometer, an alternative approach is performed, known as quadrature detection. The signal detected by the coils is split into two equivalent parts, which are 90° out of phase with each other. This allows two transverse signal components, which are proportional to the magnetization, to be separately sampled into real and imaginary parts:

$$S(t) = S_x(t) + iS_y(t) \tag{68}$$

A typical FID signal for a single-resonant chemical component follows an exponential decay, that occurs simultaneously with an oscillatory process, caused by the Larmor precession. Therefore, the Fourier transform of the time domain results in a Lorentzian line shape in the frequency domain. The frequency domain signal $S(\omega)$ is a complex number and is composed of the real part (absorption lineshape) and the imaginary part (dispersion lineshape), as seen in Figure 35.

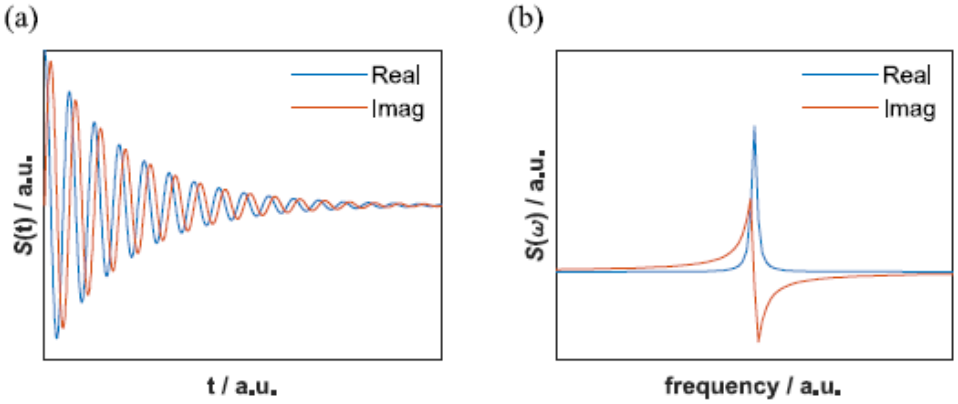

Figure 35 – Schematic example of a time domain signal (a), and resultant NMR spectrum on the frequency domain (b), after Fourier transformation. Both real and imaginary parts are represented in the figures (Ward-Williams, 2020).

As $S(t)$ is directly proportional to $M(t)$, which itself is proportional to the number of spins in a sample, NMR may be classified as volumetrically quantitative. Measurement sensitivity is improved by temperature decrease and the increase in sample volume, gyromagnetic ratio, and field strength.

The signal-to-noise ratio (SNR) of NMR measurements is represented by a Gaussian distribution about the true sample signal, and is expressed by:

$$SNR = \frac{\mu_{signal}}{\sigma_{noise}} \tag{69}$$

where μ_{signal} is true signal intensity and σ_{noise} is the standard deviation of noise.

SNR may be improved by repeating NMR scans multiple times, as true signal is proportional to the number of scan and noise scales with the square root of the number

of scans. Between successive scans, a recycle delay RD is used, allowing complete relaxation to $\boldsymbol{M}_0$.

2.1.5. NMR relaxation measurements

In the presence of a background magnetic field $\boldsymbol{B}_0$, a general alignment of the magnetization vector will be noticed. Nonetheless, when an external magnetic field $\boldsymbol{B}_1$ is applied, the nuclear spin system will have an energy excess represented by non-equilibrium spin distributions with transverse and longitudinal magnetization. This condition will be dissipated to the surrounding system in a process called relaxation.

This relaxation process may be monitored through the restoration of the magnetization in the z-direction or the loss of magnetization in the x-y plane. These two usual relaxation mechanisms are called spin-lattice relaxation and spin-spin relaxation, respectively, and may characterize a system, once they are influenced by sample composition, phase, motion, and microscopic structure.

a. Spin-lattice relaxation

The spin-lattice relaxation is represented by the energy transfer from the spins to its surroundings when returning to equilibrium after the application of an external magnetic field $\boldsymbol{B}_1$. For measuring the time needed for this process to be completed, an inversion recovery pulse sequence is performed. First, a 180° pulse is applied to invert the magnetization and a specific delay, called Inversion Time (TI), is respected for the spins to recover their initial magnetization aligned with the $\boldsymbol{B}_0$ field. After the delay, a 90° pulse is applied to tip the sample magnetization into the transverse plane for detection. The sequence is schematically presented in Figure 36.

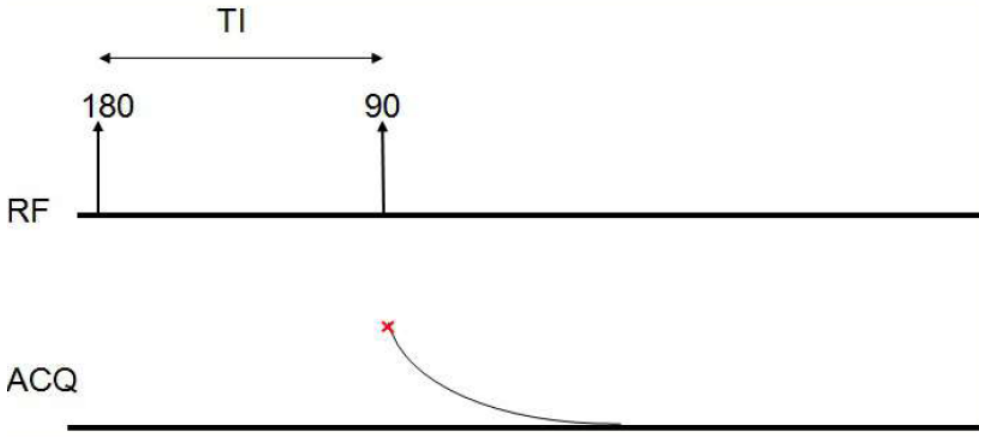

Figure 36 - Spin-lattice relaxation recovery pulse sequence.

A complete spin-lattice relaxation experiment consists of repeating this sequence at different TI's and measuring the spin-lattice relaxation time constant, T_1.

Assuming that the relaxation has an exponential behavior, the spin-lattice relaxation is described by:

$$\frac{d\boldsymbol{M}_z}{dt} = -\frac{(\boldsymbol{M}_z - \boldsymbol{M_0})}{T_1} \tag{70}$$

where, $\boldsymbol{M}_0$ is the equilibrium magnetization.

For an inversion recovery experiment, the 180° pulse generates an initial magnetization of $-\boldsymbol{M}_0$. Therefore, solving the differential equation assuming

$\boldsymbol{M}_z(t=0) = -1$, we may obtain the magnetization of the inversion recovery experiment defined by:

$$\boldsymbol{M}_z(t) = \boldsymbol{M}_0\left(1 - 2 \cdot e^{-\frac{t}{T_1}}\right) \tag{71}$$

T_1 may be affected by environmental effects, such as temperature. Therefore, a recycle delay of around $5 \times T_1$ is respected for the system to reestablish thermal equilibrium before performing the 90° tilt.

b. *Spin-spin relaxation*

The spin-spin relaxation time constant, T_2, is an irreversible process that occurs due to energy exchange between molecular spins, resulting in the loss of phase coherence of the spins and hence the decay of the transverse magnetization $\boldsymbol{M}_{xy}$.

Another cause of signal decay results from local inhomogeneities in the $\boldsymbol{B}_0$ magnetic field. This causes spins in different parts of the sample to precess at different Larmor frequencies, generating a dephasing process called T_2^*, which is reversible. The combined effects of spin-spin relaxation, T_2, and the reversible spin dephasing T_2^* can be expressed by:

$$\frac{1}{T_2^*} \approx \frac{1}{T_2} \cdot \gamma \cdot \Delta\boldsymbol{B}_0 \tag{72}$$

where $\Delta\boldsymbol{B}_0$ are the magnetic field variations.

T_2 is generally measured following a Carr-Purcell-Meiboom-Gill (CPMG) spin-echo sequence (Carr & Purcell, 1954; Meiboom & Gill, 1958), as presented in Figure 37:

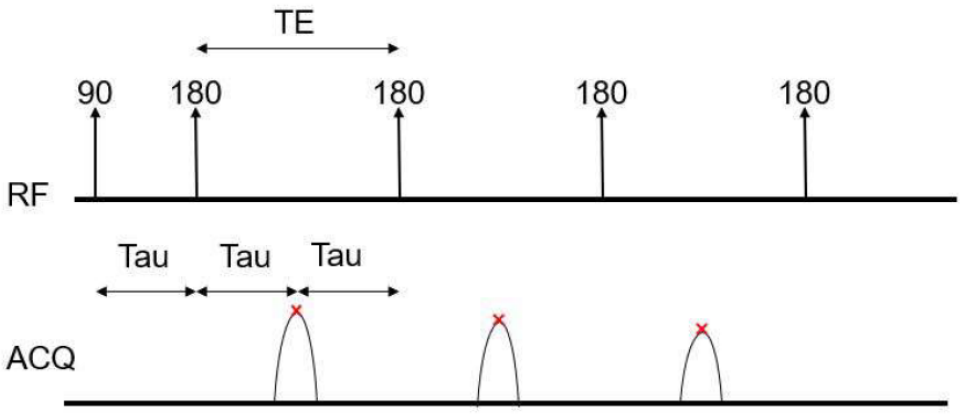

Figure 37 - CPMG pulse sequence.

The sequence consists of a 90° RF pulse that tilts the spins into the transverse plane. This is followed by a series of 180° RF pulses reversing the spin orientation. That is when the reversibility of dephasing from T_2^* is exploited, as it generates spin echoes, and $\boldsymbol{M}_{xy}$ is monitored with time.

The time between the first 90°-180° pulse must be equal to half the echo time (TE) between 180°-180° RF pulses. This is called the CPMG condition and, if not satisfied, will generate destructive echo interferences and a more rapid decay,

impacting the accuracy of T_2 values. By choosing short interecho times, we may reduce molecular diffusion effects, which reduces its contribution to signal loss.

Assuming an exponential behavior, T_2 recovery is described by:

$$\frac{d\boldsymbol{M_{xy}}}{dt} = -\frac{\boldsymbol{M_{xy}}}{T_2} \tag{73}$$

The solution for the differential equation gives:

$$\boldsymbol{M_{xy}}(t) = \boldsymbol{M_{xy}} \cdot e^{-\frac{t}{T_2}} \tag{74}$$

In the same way as for the T_1 experiment, the magnetization during spin-spin relaxation will be proportional to the signal. Therefore, equation (74) may be fitted to the data acquired from a CPMG experiment to derive the T_2 time constant. For all practical results, $T_2 \leq T_1$.

c. The T_1-T_2 correlation experiment

A combination of T_1 and T_2 experiments can be done to allow the acquisition of both parameters from a single 2D experiment. This experiment is performed by pre-conditioning spins with an inversion-recovery sequence, followed by a CPMG sequence for acquisition, as presented in.

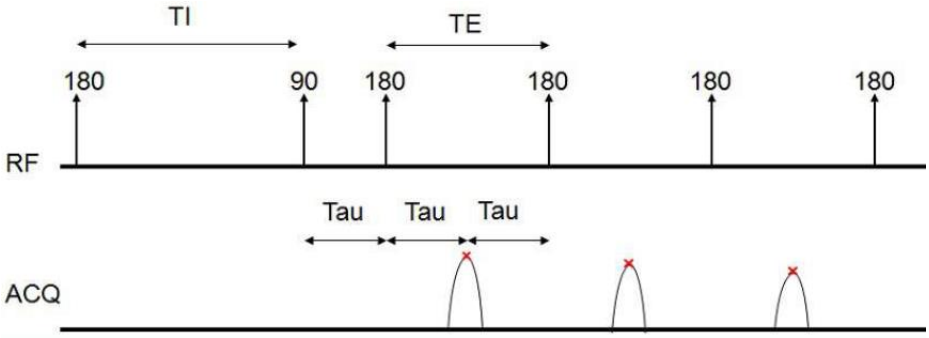

Figure 38 - Inversion recovery and CPMG pulse sequence for T1-T2 correlation experiments.

In bulk liquids, molecular tumbling are fast and isotropic; Thus, $T_1 \approx T_2 \rightarrow {}^{T_1}/_{T_2} \approx 1$. Inside a porous medium, if the hydrogen spins of the fluid experiment an additional influence by surface diffusion, the T_2 response will be faster, as molecular tumbling is slow and anisotropic. Therefore, $T_1 > T_2 \rightarrow {}^{T_1}/_{T_2} > 1$ (McDonald *et al.*, 2005).

The resultant T_1 and T_2 distributions may be described by the following fundamental relations (Gallegos *et al.*, 1987; Davies *et al.*, 1991):

$$\frac{1}{T_1} = \frac{1}{T_{1,B}} + \rho_1 \frac{S_p}{V_p} \tag{75}$$

$$\frac{1}{T_2} = \frac{1}{T_{2,B}} + \frac{1}{T_{2,S}} + \frac{1}{T_{2,D}} \tag{76}$$

where $T_{1,2}$ indicates measured T_1 or T_2.

Whereas T_1 is decomposed in two, T_2 relaxation experiments are decomposed in three mechanisms. They are due to the molecular motion in fluids, surface relaxivity at the pore wall and molecular diffusion in internal field gradients. Each of these mechanisms are dependent on physical properties of both the fluid and the solid matrix.

The bulk relaxation term is related to the measured fluid viscosity, following (77):

$$T_{2,B} = \frac{T}{\mu} \tag{77}$$

where T is absolute temperature and μ is fluid viscosity.

The second relaxation mechanism is called the surface relaxation. It is related to the hydrogen nuclei relaxation when it approaches paramagnetic ions, such as iron or manganese, usually present on the rock surface. In a porous medium where the measured fluid wets the surface, surface relaxation time is given by:

$$T_{2,S} = \frac{1}{\rho_2 \left(\frac{S}{V}\right)} \tag{78}$$

where ρ_2 is the transverse surface relaxivity and $\left(\frac{S}{V}\right)$ is the ratio between the surface wetted by the fluid and the occupied volume.

The third mechanism is given by the diffusion of molecules in magnetic field gradients, called diffusion relaxation. Due to its relatively small impact on NMR measurements, it is often considered as nuisance. In a classic Carr-Purcell-Meiboom-Gill (CPMG) pulse sequence, the diffusion relaxation time is given by:

$$T_{2,D} = \frac{3}{(\gamma G \tau)^2 D} \tag{79}$$

where γ is the hydrogen gyromagnetic ration, G is the strength of the field gradient, D is the self-diffusion constant of the relaxing fluid, and τ is the CPMG pulse time spacing.

Together, these three terms compose the NMR transverse (spin-spin) relaxation time distribution, that in the time domain are expressed as:

$$A(t) = A(0) e^{-\left(-t/T_{2,B}\right)} e^{-\left(-t/T_{2,S}\right)} e^{-\left(1/3\gamma^2 G^2 D \tau^2 t\right)} \tag{80}$$

The relation between each relaxation time component may be seen as a competition, in which one is likely to prevail. Indeed, when multiple fluids are present inside a porous medium, the fluid wetting the surface will undergo a surface relaxation while the fluids not wetting the surface, thus placed in the center of the pores, will undergo a bulk fluid relaxation. This is a way of estimating wettability from T_2 measurements.

As seen in equations (75) and (76), T_1 and T_2 are both affected by the term $\frac{S_p}{V_p}$. Neglecting the effect of the diffusive term on (76), assuming $T_{1,B} \approx T_{2,B}$, and taking the ratio between (75) and (76) and the definition given by (78),we have:

$$\frac{T_1}{T_2} = \frac{T_{1,S}\left(T_{2,S} + T_B\right)}{T_{2,S}\left(T_{1,S} + T_B\right)} \tag{81}$$

Considering that, for porous media, generally $T_{1,2,S} \ll T_B$, we have:

$$\frac{T_1}{T_2} \approx \frac{T_{1,S}}{T_{2,S}} = \frac{\rho_2}{\rho_1} \tag{82}$$

This condition is limited by bulk relaxation times and pore sizes, as signal proportion between nuclei in pore centers (bulk relaxation) and interacting with the solid surface (surface relaxation) may overlap (Mitchell & Fordham, 2014)

Therefore, one of the several applications of the relation between T_1 and T_2 in the petrophysics domain is studying the rock wettability, and this has been extended over the last decade (Katika *et al.*, 2016; Valori *et al.*, 2017; Korb *et al.*, 2018; Fleury & Deflandre, 2003; Godefroy *et al.*, 2001).

This application will be further discussed in sub-section Wettability estimation from T_1 and T_2 relaxation times.

d. Spatially-resolved relaxometry sequences

Up to now, we have seen techniques giving a mean response of the sample regarding fluids saturation and wettability, and a 1D quantification of the fluids presence in the sample. If we are interested in exploring not a mean response of the sample, but the relaxation at different slices, we may use spatially-resolved NMR relaxometry sequences. In a nutshell, these sequences represent performing either T_1 or T_2 relaxometry sequencies on multiple slices of the sample. This way, parameters such as pore size distribution, sample heterogeneity, fluids saturation and attraction to the solid surface may be resolved spatially.

We will call Spatial T_1 and Spatial T_2 the spatially-resolved sequences for T_1 and T_2, respectively. The timing diagrams for both these sequences are shown in Figure 39 and Figure 40:

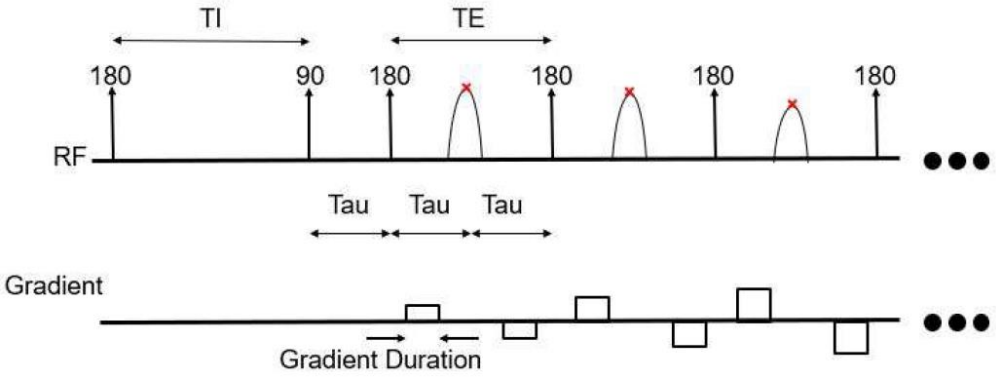

Figure 39 - Spatial T_1 pulse sequence.

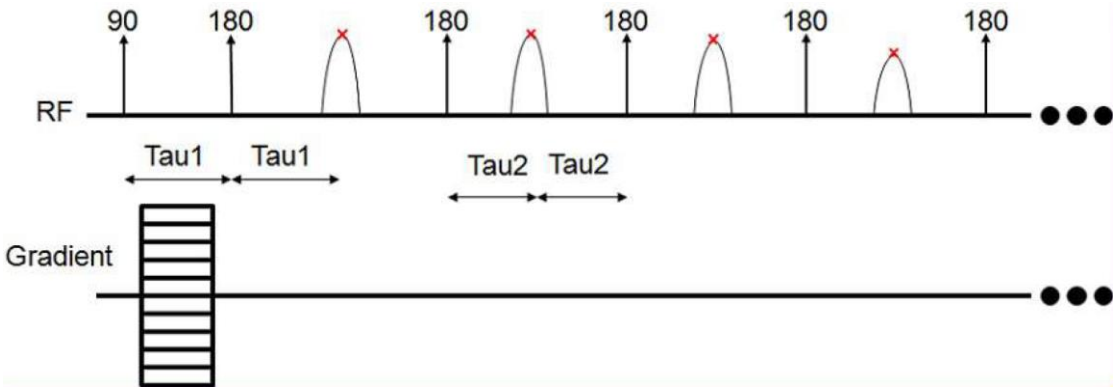

Figure 40 - Spatial T_2 pulse sequence.

e. The $Diff, T_2$ sequence

In order to explore a multi-dimensional measurement of fluids diffusion and T_2 relaxation times distribution, a diffusion editing sequence followed by a CPMG may be performed (Hürlimann & Venkataramanan, 2002). The sequence, shown in Figure 41, is composed of two distinct parts. The initial part is composed of a stimulated echo sequence, where the variation of the stimulated echo Tau, τ_{STE}, allows the sensitivity to diffusion to be varied systematically. For this reason, this is called an editing sequence. The second part of the sequence is composed of a long series of 180° pulses, for the determination of T_2 relaxation time.

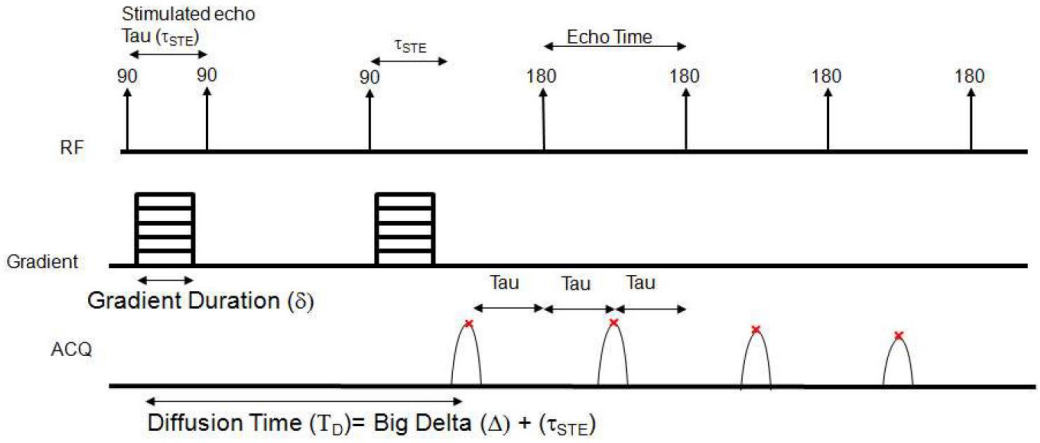

Figure 41 - Stimulated echo CPMG pulse sequence for the acquisition of D-T_2 response.

Echo times (TE) are usually chosen to be the lowest possible, in order to remove the dependency of decay times to diffusion.

The application of the maps produced by this sequence on fluids saturation definition and wettability evaluation will be thoroughly discussed in sub-sections Fluids saturation and Wettability estimation from T_1 and T_2 relaxation times.

$D - T_2$ maps may also be used for estimating tortuosity of porous materials. Nonetheless, this application requires long TE, thus having limited use. $D - T_2$ maps with low TE measure the restricted diffusion of hydrogen spins inside the pores. If we want to explore $D - T_2$ maps for estimating tortuosity, we need to let these hydrogen spins diffuse not only inside its own pore, but also through the pore throats. The main issue of doing this is that setting long TE will allow the detection of only long T_2 relaxation times.

2.1.6. Basic principles of MRI

Magnetic Resonance Imaging is capable of adding a spatial resolution to NMR measurements. This is obtained by spatially varying the applied magnetic field by applying an additional magnetic field gradient to $\boldsymbol{B}_0$, called $\boldsymbol{G}$. This way, the Larmor frequency of the sample response to the application of this gradient will vary spatially according to the spin position $\boldsymbol{r}$, following the equation:

$$\omega(\boldsymbol{r}) = \gamma(\boldsymbol{B_0} + \boldsymbol{G} \cdot \boldsymbol{r}) \tag{83}$$

An infinitesimal volume element dV at a given position $\boldsymbol{r}$ with spin density $\rho(\boldsymbol{r})$, contains $\rho(\boldsymbol{r})dV$ spins. Neglecting relaxation, the total signal, dS, within the volume element is given by:

$$dS(\boldsymbol{G}, t) = \rho(\boldsymbol{r})e^{[i\gamma(\boldsymbol{B}_0 + \boldsymbol{G}\cdot\boldsymbol{r})t]}dV \tag{84}$$

Combining equations (83) and (84), and assuming that the system is in resonance in the rotating frame, whereas $\boldsymbol{B_0} = 0$, we may write $S(t)$ as:

$$S(t) = \iiint \rho(\boldsymbol{r})e^{[i\gamma \boldsymbol{G}\cdot\boldsymbol{r}t]}d\boldsymbol{r} \tag{85}$$

We may simplify this relationship by assuming the **k**-space vector as it follows:

$$\boldsymbol{k} = \frac{\gamma \boldsymbol{G} t}{2\pi} \tag{86}$$

Therefore, substituting (86) on (85), highlights the Fourier relationship between time domain signal and spatial spin density, as seen in (87). Moreover, its inverse yields the Fourier conjugate, from which spin density in real space, $\rho(\boldsymbol{r})$, is obtained:

$$S(\boldsymbol{k}) = \iiint \rho(\boldsymbol{r})e^{[i2\pi \boldsymbol{k}\cdot\boldsymbol{r}]}d\boldsymbol{r} \tag{87}$$

$$\rho(\boldsymbol{r}) = \iiint \rho(\boldsymbol{r})e^{[-i2\pi \boldsymbol{k}\cdot\boldsymbol{r}]}d\boldsymbol{k} \tag{88}$$

The k-space may be traversed by either varying the $\boldsymbol{G}$ term (phase-encoding), or the gradient duration, t (frequency encoding). This formalism was first introduced by (Mansfield & Grannell, 1973) for helping simplify the description of MRI experiments.

In this work, we used a Spin-Echo Single-Point Imaging (SE-SPI) NMR pulse sequence to obtain a volume profile of our samples (Beyea, *et al*., 2000). This method phase encodes individually each echo in a CPMG train to get a profile. This sequence is useful for samples with longer T_2 relaxation times, once, for this sequence, $\tau \geq 524\ \mu s$. The used SE-SPI pulse sequence is schematically presented in Figure 42:

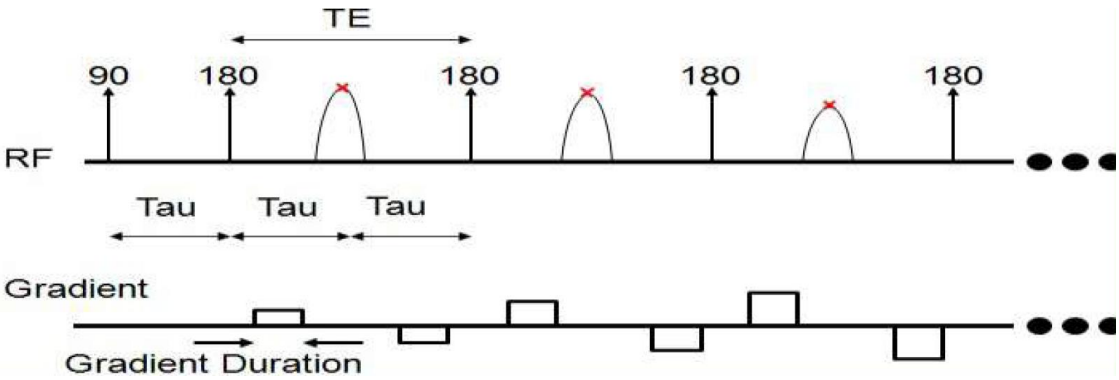

Figure 42 - SE-SPI NMR pulse sequence for measuring volume profiles in core samples.

2.1.7. NMR application to Petrophysics

NMR tools used in the oil and gas industry are usually tuned to measure the response of protons from hydrogen nucleus, as this is the dominant atom found in reservoir fluids. By means of the fluids response to the NMR measurements, we are able to estimate some parameters, such as porosity, clay-bound water, permeability and fluid saturations, and also the way fluids are set in the porous medium (if it is attracted and coats the rock surface or if it is repelled and is placed in the center of the pores).

a. Porosity estimation

As NMR signal is proportional to nuclear spin density, signal volumetric quantification is possible using the Hydrogen Index. This way, by applying the appropriate corrections and calibration for a fully-saturated porous medium, we may obtain, among other properties, the pore volume (Timur, 1969). HI is defined at standard temperature and pressure (STP) as:

$$HI = \frac{quantity\ of\ Hydrogen\ in\ the\ sample}{quantity\ of\ Hydrogen\ in\ pure\ water\ at\ STP} \tag{89}$$

This term is measured by calibrating the NMR signal intensity response for known sample volumes against that of water:

$$HI = \frac{\left(M_{0,fluid} / V_{fluid}\right)}{\left(M_{0,H_2O} / V_{H_2O}\right)} \tag{90}$$

where M_0 is the initial signal intensity and V is fluid volume. M_0 is determined by extrapolating FID or CPMG responses to zero time (Appel, 2004; Schön, 2011).

Performing a T_2 pulse relaxation sequence on a fully-water saturated sample. Applying the appropriate Hydrogen Index correction, the measured NMR volume will correspond to that of the pore volume. Therefore, we may define an NMR porosity measurement as:

$$\Phi_{NMR} = \frac{V_{T2,NMR}}{V_t} \tag{91}$$

b. Pore size estimation

The relation between T_2 relaxation and pore size in saturated porous media was first discussed by (Brownstein & Tarr, 1979). The subject inspired works from different authors that worked on establishing relationships between this parameter and reference methods for defining pore size distribution for reservoir rocks and shales (Davies & Packer, 1990; Davies *et al.*, 1991; Munn & Smith, 1987; Fleury & Romero-Sarmiento, 2016).

Take a porous medium fully-saturated with brine. When hydrogen atoms present in brine are excited during a relaxation experiment, they will be free to diffuse across an isolated pore. As they diffuse, they interact with other nuclei, which will liberate energy through relaxation mechanisms. As we know, NMR spin relaxation in porous media is enhanced by strong interactions at the pore-grain surface. When nuclei collide with the pore wall, a relaxation will occur, and it will be captured by $T_{1,2}$ experiments. In small pores, the probability of hydrogen nuclei to collide against the pore wall is bigger than for big pores. Therefore, NMR spin relaxation times are shorter for small pores, thus $T_{1,2}$ relaxation time distribution is proportional to pore size.

Take the example of a T_2 pulse relaxation sequence performed on a dual-porosity water-wet sample saturated with brine. In this case, hydrogen nuclei present in smaller pores will have more tendency to collide with the pore walls, which will enhance spin relaxation, thus resulting on a shorter T_2 relaxation time. For bigger pores, on the other hand, the fewer interaction between hydrogen nuclei with the pore wall will result on a longer T_2 relaxation time. An illustrative example of this analysis is presented in Figure 43 (experiment discussed in more details in the results section), together with an MICP experiment on a sample of the same rock.

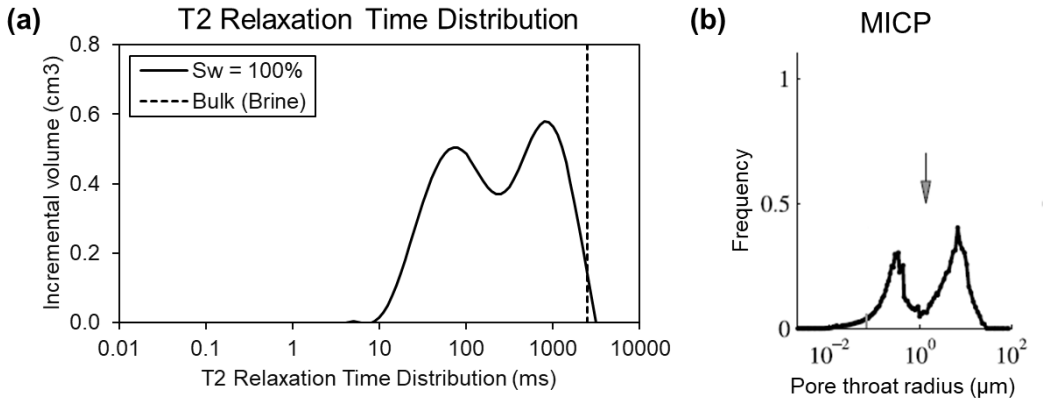

Figure 43 - Example of (a) T_2 pulse relaxation sequence and (b) MICP on an Estaillades limestone (Tanino & Blunt, 2012). The dual-porosity characteristics of the sample are clear on both graphics.

It is important to highlight the fact that T_2 pulse relaxation sequences gives a pore size estimation, whereas MICP gives the pore-throat size distribution. The above figure, therefore, does not represent a comparison between T_2 pulse relaxation sequence and MICP, as they are sensitive to different physical properties.

c. Fluids saturation

As seen, NMR measurements carry information about the volume of each phase saturating a porous medium. Though, it is logical to presume that in a multi-phase system it may be possible to extract information regarding fluids saturation.

Take a sample at initial water saturation in an oil-water system for a water-wet rock. As water coats the surface, hydrogen nuclei present in the oil phase will not interact with the pore wall, thus this phase will only experience a bulk fluid relaxation. On the other hand, as brine coats the pore wall, hydrogen nuclei present in the brine phase will experiment a surface relaxation. If the relaxation times associated to the two relaxation mechanisms on the two phases are different, it is possible to differentiate each phase on the relaxation time distribution spectrum.

An example of the described situation is schematically presented in Figure 44:

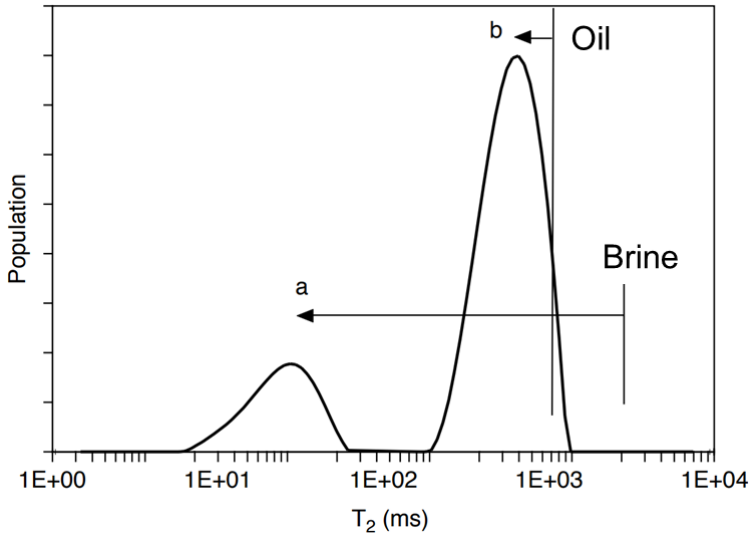

Figure 44 - Schematic example of a T_2 relaxation measurement where oil and brine are separated by different relaxation mechanisms. Oil experiments a bulk fluid relaxation mechanism, related to its viscosity, and brine, experiments a surface relaxation mechanism, which is related to its surface to volume ratio (Fleury, 1998).

Another possibility for defining fluids saturation is by using a $D - T_2$ sequence. This measurement is presented as a two-dimensional map of intrinsic diffusion coefficient D *versus* transverse relaxation time T_2. Therefore, as this measurement is based on both the fluids inner diffusive time constant and their response to a T_2 sequence, this is a powerful tool for separating fluids signals, thus their respective volume in the porous media (Hfirlimann *et al.*, 2002; Hürlimann *et al.*, 2003). This solution is well-fitted for cases where there is an overlapping on fluids response on T_2 relaxation time spectrum and enough contrast between their diffusion times.

Thus, for defining fluids saturation from T_2relaxation measurements, we take the ratio between the measured volume corrected with its Hydrogen Index and NMR pore volume. The standard approach is always considering the same fluid when performing these manipulations (*e.g.*, in the case of an experiment where D_2O-based brine will be used, as only the oil phase will produce NMR signal, pore volume characterization and profile at fully-saturated sample must be measured at $So = 100\%$).

d. Wettability estimation from T_1 and T_2 relaxation times

In the previous sections, we have discussed the impact that the affinity of the rock surface for one or the other fluid may impact T_1 and T_2 parameters. Therefore, one important application of NMR measurements on the Petrophysical domain is on wettability analysis. A complete review of classical NMR wettability evaluation methods may be seen in the work from (Valori & Nicot, 2019).

In this work, we will use T_2 pulse relaxation for an initial, shallow understanding of rock surface preference for brine or oil. Moreover, ratio between T_1 and T_2 will be used as a more consistent tool for understanding surface affinity strength and adsorption energy during the experimental cycle (McDonald *et al.*, 2005; Mitchell *et al.*, 2009; D'Agostino *et al.*, 2014).

The T_1-T_2 experiment result is a chart where it is possible to infer about the rock's wettability according to the magnitude of the T_1/T_2 ratio, which is represented by an up-left diagonal shift, as represented in the scheme of Figure 45:

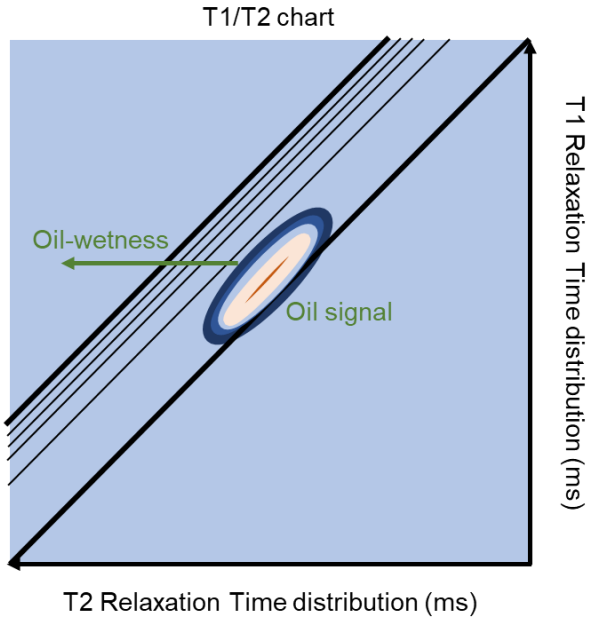

Figure 45 - Schematic representation of a T_1 - T_2 experiment, showing the effect of oil-wetness increase.

The combination of these concepts may be extended for a spatially-resolved analysis of wettability using Spatial T_1 and Spatial T_2 sequences. This application of spatially-resolved sequences among others will be more thoroughly discussed in the following sub-section.

Another possibility for evaluating wettability on rock samples is the $D - T_2$ sequence (Freedman & Heaton, 2004; Flaum *et al.*, 2005). By monitoring the divergence between measured and bulk self-diffusion times of the fluid, we may infer the affinity of the rock for this fluid. If diffusion times are above bulk fluid diffusivity, this might indicate the presence of internal gradient values (Sun & Dunn, 2002; Hürlimann, *et al.*, 2004), whereas lower values suggest the presence of restricted diffusion. As fluids diffusivity and relaxation times are related to each other through viscosity (Lo *et al.*, 2002), responses shorter than this relation is usually related to surface relaxation of the oil phase, thus indicating a change in wettability. These effects and a typical $D - T_2$ chart are presented in Figure 46:

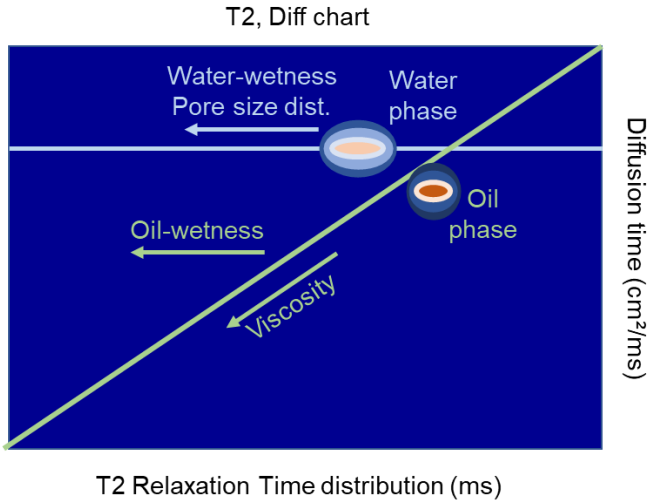

Figure 46 - Schematic representation of a T2,Diff chart, showing the oil and water signals and the trends for water and oil-wetness, pore size distribution and fluid viscosity.

e. *Along-axis heterogeneity*

The interests of performing a spatially-resolved measurement of T_1 and T_2 are numerous. If SE-SPI provides along-axis information of fluids volume but is not capable of separating the signal from two fluids, spatially-resolved sequences are capable to go even further. As these sequences are based on performing T_1 and T_2 measurements on slices along the core longitudinal axis, it will provide not only information about longitudinal fluids saturation, but also an indication of longitudinal wettability and possible heterogeneities.

Porosity heterogeneities may be identified by performing experiments on samples fully-saturated on their wetting fluid. Taking the example of a brine-saturated water-wet rock sample, its longitudinal response to the Spatial T_2 relaxation sequence will provide insights about pore size distribution along the sample axis, as this response is related to the surface to volume ratio term of equation (76).

As in T_2 pulse relaxation sequences, the identification of two fluids is based on having a sufficient contrast in relaxation times between them. This is dependent on pore sizes, which will impact the wetting fluid signal, and on the non-wetting fluid viscosity, that will define its bulk relaxation time. A schematic example of a spatially-resolved T_2 acquisition of a water-wet sample saturated with oil and brine is shown in Figure 47. In this case, we are representing a sample having a monotonic pore-size distribution that is small enough so that signal from the low-viscosity oil and from the water wetting the rock surface do not overlap.

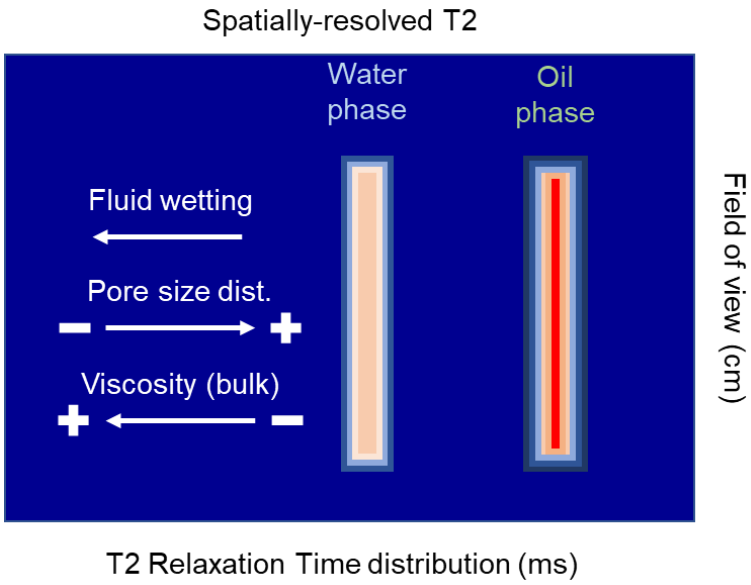

Figure 47 – Schematic representation of a spatially-resolved T_2 relaxation time distribution a water-wet sample partially saturated in water and low-viscosity oil.

Moreover, the concept of using T_1/T_2 for wettability indication may be extended to a longitudinal analysis. This way, the identification of potential wettability heterogeneities along the sample axis is possible.

This approach was tested in this work and will be presented in the appropriate results section.

2.2. Computed X-ray micro-tomography

X-ray microtomography is a non-destructive imaging method for accessing the materials inner structure. It was first developed for medical imaging of bones and tissues. Its use in oil and gas laboratories has increased in the last decades as it may provide vital information about the core samples. The possibility of imaging its inner structure for detecting local heterogeneities, and sample damage or fissure prior plugging is an important application of this tool.

Nonetheless, its application may be extended further, by performing whole-sample imaging at different steps during a SCAL workflow. The X-ray Micro CT equipment used in this work is a Zeiss Xradia Versa 520, that is presented in Figure 48:

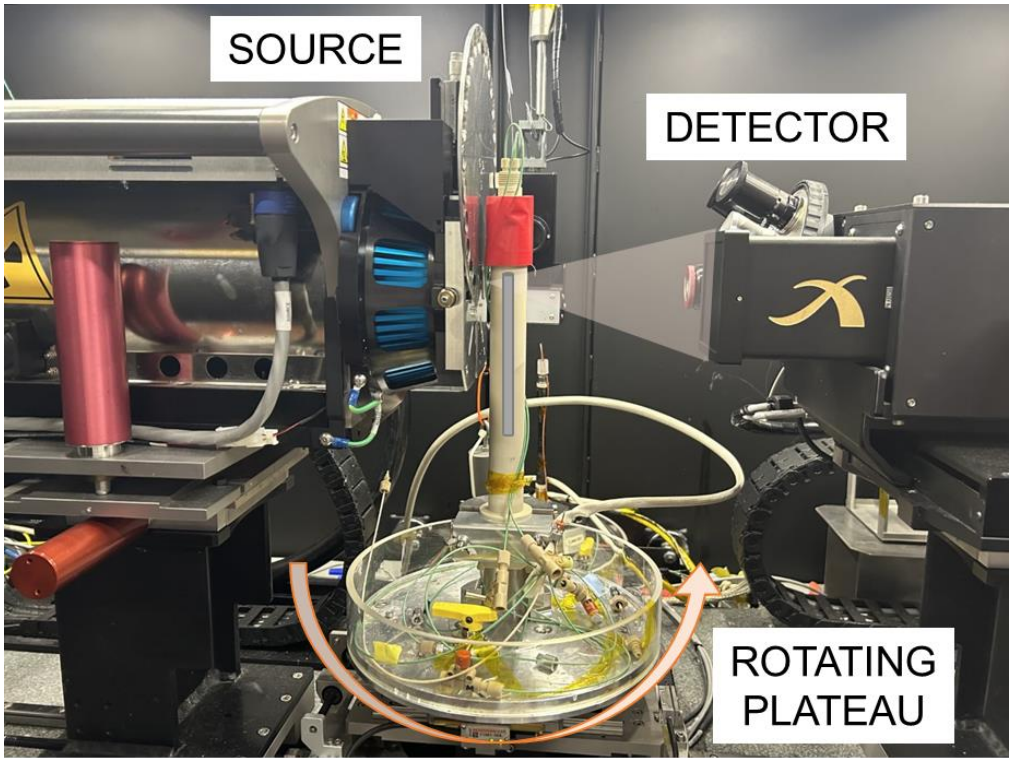

Figure 48 - Zeiss Xradia Versa 520 X-ray micro-CT and the Multi-Imagery cell.

In order to obtain a good resolution, allowing a proper visualization of the inner structure of the rock, samples with reduced dimensions must be used, usually called mini-plugs. The imaging process consists in placing the sample in a 360° rotating platform, positioned between the x-ray source and the detector. The conic X-ray beam emitted by the source will cross the sample, and the attenuation will be measured by the detector. The detector will process a two-dimensional grayscale image and the sample will be rotated over 360° to acquire the set of projections (radiographies).

Each gray level intensity in the image grayscale represents a phase present in the sample (solid grains, brine and oil). From these projections, a 3D reconstruction is performed, generating a numerical model of the sample, composed of thousands of slice images. The spacing between each image is that of a pixel size; thus, every pixel on the slice image is called a voxel as it carries a third dimensional information besides its position on the x-y plane.

2.2.1. Image segmentation

The information present on each voxel may be used in the image processing to obtain information at the pore-scale. In this work, image processing was done using Mango® software developed by the Australian National University (ANU) and the open-source software ImageJ. Three-dimensional rendering was performed using the open-source software Paraview. The processing steps are performed as described in the following paragraphs:

a. Dataset preparation

Prior processing, an image usually must be prepared by improving the signal to noise ratio. For that, several denoising filters may be used (Sheppard *et al.*, 2004). An example of filter used in pre-processing is the non-local means denoising filter (Buades *et al.*, 2011). It consists of taking a mean of the surrounding pixels in order to

smooth the area. The main disadvantage of this approach is the risk of losing contrast in the interface between fluids. An example of the application of this method is presented in Figure 49, where it is possible to see the difference between raw and filtered images.

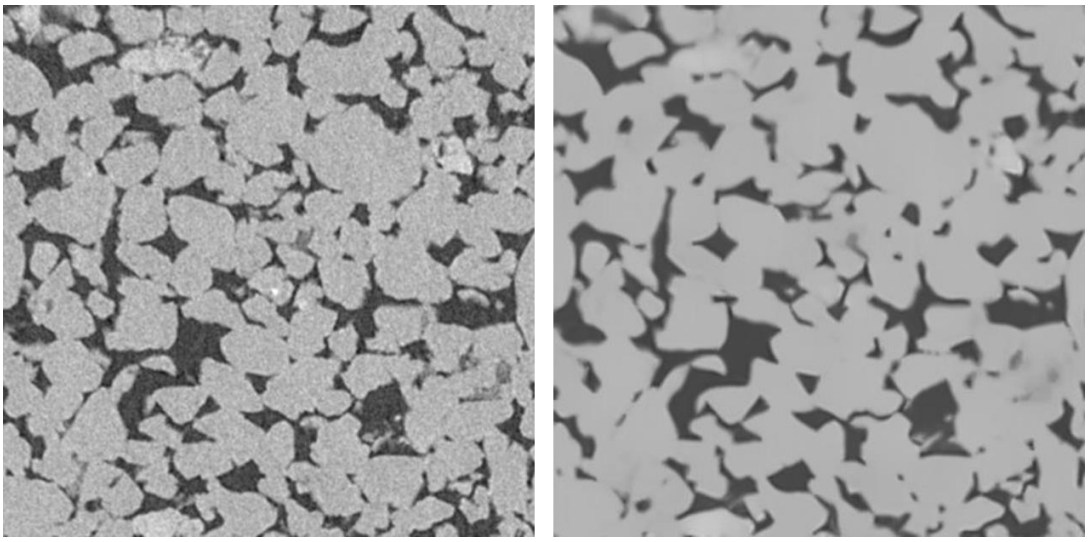

Figure 49 - In the left we are able to observe dry raw image. In the right is shown the same image after a non-local means denoising.

b. Segmentation

On a typical 16-bit image (grayscale ranging from 0 to 65535) of a porous rock, the difference in the grayscale will define the rock matrix and the voids (pores). This difference is based on how X-rays are attenuated by each of these elements. In a more complex system, with the presence of two fluids (*e.g.*, brine and oil), each phase of the system will attenuate differently, thus occupying different levels in the grayscale spectrum. A typical grayscale spectrum of a two-phase system is presented in Figure 50:

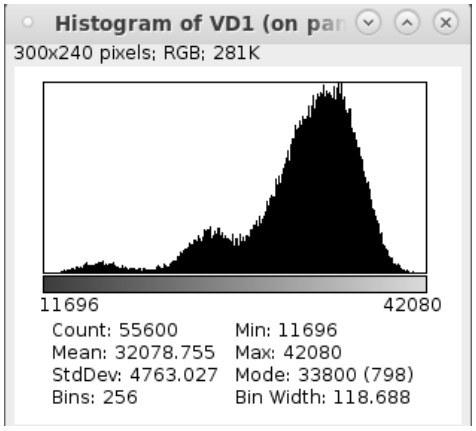

Figure 50 - Grayscale histogram of an Estaillades at residual oil saturation. The first peak on the left represents the oil phase, the intermediate peak, the brine, and the biggest representation is the rock matrix.

For facilitating the calculation of the contribution of each phase to the total volume, the image is first converted into an 8-bit image, which will reduce the grayscale to a range between 0-256. Then, image segmentation will be applied, assigning a single gray value for each phase. For that, a threshold in grayscale is defined for each phase determination, also considering the transition between the phases in the grayscale. There are some methods for segmentation that rely on machine learning

able to provide reliable results after training the algorithm. In this work, Trainable Weka Segmentation was used (Arganda-Carreras *et al.*, 2017).

In Figure 51 we may see the segmentation of Figure 49. We identify the pores (darker gray) and the grains (lighter gray). This routine is repeated for the entire set of slice images.

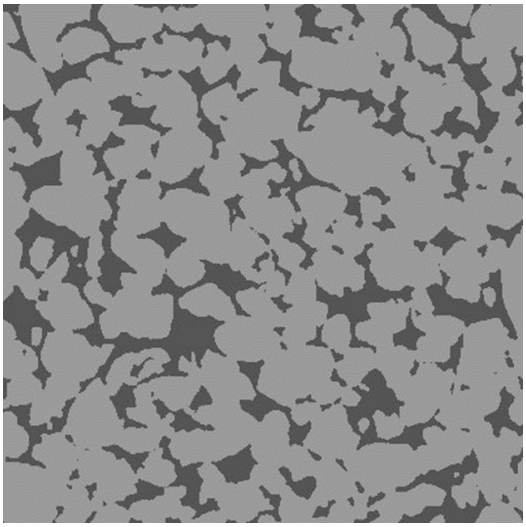

Figure 51 - Segmented image of a dry Bentheimer sample.

c. Quantification

After setting one value corresponding to each phase in the grayscale, a quantification of each phase along the whole stack of images may provide porosity (in the case of imaging a dry rock) and fluids saturation (when a system with multiple phases is imaged).

Moreover, by analyzing the group of voxels corresponding to one phase, we may infer if the phase is connected or disconnected along the pore space, in the form of ganglia or brine or oil. This quantification and position of disconnected elements will be useful for identifying different kinds of rock wettability.

2.2.2. Differential imaging

In the last section, we present the approach and protocol used to obtain information from images which resolution provide enough voxels to be segmented into different phases. After initial segmentation by the application of thresholds in the grayscale histograms, phases may be quantified by voxel counting.

Nonetheless, there are some cases where the resolution obtained in µ-CT imaging is not necessary to resolve the whole pore network of the rock samples. This is usually the case of limestones, that are known to have a very complex pore space whose structure and connectivity have a significant impact on single and multiphase flow (Cantrell & Hagerty, 1999, Bijeljic *et al.*, 2013; Apourvari & Arns, 2016;). For a complete description of flow and reactive transport processes in porous media, unresolved porosity needs to be quantified and its contribution to flow must be understood (Mangane *et al.*, 2013).

The solution for obtaining information on the unresolved fraction of the porosity is to perform differential imaging. In this study, we followed an experimental protocol to obtain information about the unresolved porosity of the Estaillades limestone

sample that is slightly different from the one presented by Lin *et al.* (2016). Based on three different scans of the sample saturated with different fluids, three phase segmentation is used to separate the rock matrix, macro pores and unresolved pores. The three different fluids used are: 100% saturated with high-doped brine (KI @ 300 g/l), 100% saturated with the brine used in the experiment, and 100% saturated in synthetic mineral oil (Marcol^{TM}-52). The differential image obtained between the high-doped brine state and the oil-saturated state can maximize the phase contrast between grain phase and pore phase. In addition, the oil-saturated state provides a good approximation of the grayscale values obtained during multiphase flow experiments. The differential image between these two states scan is obtained from:

$$CT_{differential} = CT_{high-doped} - CT_{oil} + CT_0 \quad (92)$$

where CT_x are the CT number of each voxel, and CT_0.is a large positive constant, typically 65.535, to avoid negative values.

From the differential image obtained, two grayscale thresholds are defined to separate the rock matrix (lower values in the grayscale), the unresolved pores (intermediate grayscale values) and the macro pores (higher grayscale values). These images are then segmented using a two-step watershed algorithm, as described by Lin *et al.* (2016).

After identifying the unresolved porosity range of values in the grayscale and performing the images segmentation, an average porosity value must be assigned to the unresolved pores. For this purpose, we assign an average porosity of 0 and 1 for the grayscale peaks corresponding to the rock matrix $\bar{\varphi}_{grain}$ and the macro pores $\bar{\varphi}_{macro}$, respectively. The average porosity values within the unresolved pores $\bar{\varphi}_{sub}$ is obtained by a linear interpolation between $\bar{\varphi}_{grain}$ and $\bar{\varphi}_{macro}$, as presented in equation (93):

$$\bar{\varphi}_{sub} = \left(\frac{\bar{\varphi}_{macro} - \bar{\varphi}_{grain}}{CT_{macro} - CT_{grain}}\right)\left(CT_{sub} - CT_{grain}\right) = \frac{CT_{sub} - CT_{grain}}{CT_{macro} - CT_{grain}} \quad (93)$$

3. Materials & Methods

In this section we will define the rocks and fluids used in this work, as well as defining the methodology and equipment necessary for conducting conventional and special core analysis experiments, with main attention on the primary drainage techniques tested.

3.1. Solid and fluid properties

3.1.1. Solids

Rocks are divided in two main groups regarding their sedimentology: sandstones and limestones. In the following sub-sections, the petrophysical characteristics of each rock, such as mineralogy, porosity, permeability, pore size distribution (from NMR T_2 relaxation time distribution) and primary drainage capillary pressure curves will be presented.

a. Bentheimer sandstone

The Bentheimer sandstone is an outcrop sample from the Valanginian age (Early Cretaceous), extracted in Germany. This rock is mainly composed of silica, as shown in Table *4*, where we are able to observe a complete description of the Bentheimer mineral composition after an X-ray Fluorescence (XRF) test.

Mineral	XRF (%)
SiO_2	92.25
TiO_2	0.36
Al_2O_3	2.96
Fe_2O_3	1.08
MnO	0.02
MgO	0.31
CaO	0.42
P_2O_5	0.02
BaO	0.01
SO_3	0.02
LOI	1.30
Na_2O	0.27
K_2O	0.89

Table 4-Mineralogy of the Bentheimer sandstone from XRF test (provided by TotalEnergies laboratory)

A T_2 relaxation time distribution for a Bentheimer sample fully saturated with brine, which provides a glimpse about its pore size distribution, is presented in Figure 52. It is important to notice that the rock T_2 relaxation time is smaller than the brine

bulk T_2 relaxation time (represented by the vertical line), which is an indication that the fluid wets the rock surface.

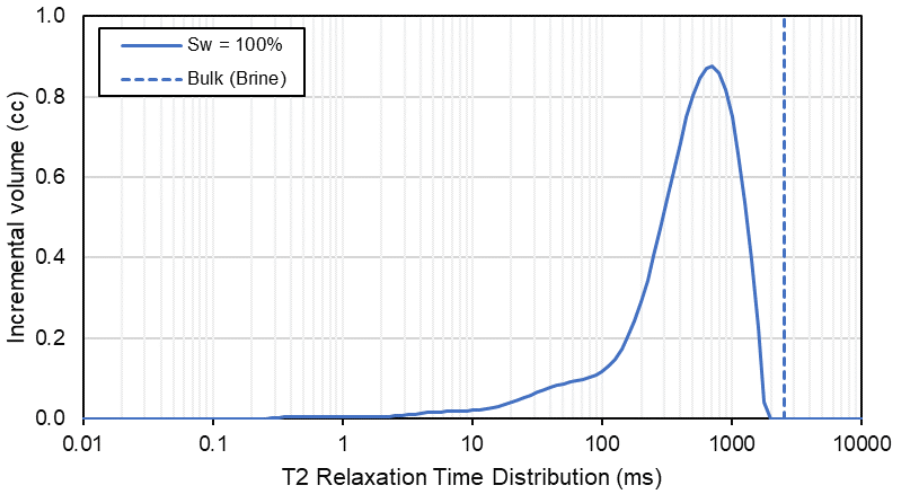

Figure 52 - T_2 relaxation time distribution test on a brine saturated Bentheimer sandstone.

We may observe the presence of a characteristic pore size, that represents around 90% of the total pore volume, and a distribution of smaller pores (signal under 100 ms). This is in agreement with the results presented by Andriamananjaona, who used the same rock in her work (Andriamananjaona, 2020).

A primary drainage capillary pressure *versus* water saturation curve obtained from a Porous Plate experiment is presented in Figure 53. It is possible to observe the effect of big pores and high permeability, with a primary drainage P_c *versus* S_w curve that has a low entry-pressure and a low-pressure transition range.

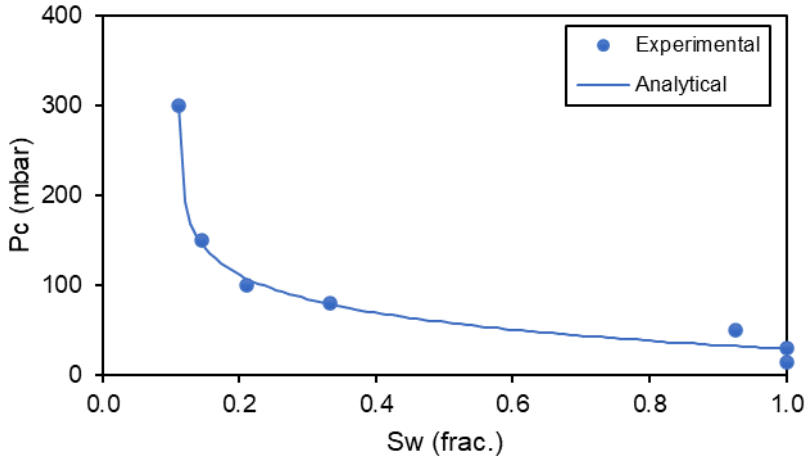

Figure 53 - Bentheimer sandstone primary drainage capillary P_c versus S_w curve (Porous Plate technique).

Multi-phase experiments for testing the different primary drainage techniques were conducted on Bentheimer samples. This rock was also used for the validation of the Hybrid Drainage Technique. Table *5* presents the petrophysical characteristics of these samples, following the nomenclature used in this work for their identification according to the method used for setting S_w. The first three letters represent the rock (*e.g.*, BEN for Bentheimer, EST for Estaillades, RCH for Richemont), and the following two or three letters represent the primary drainage technique used (*e.g.*, VOF for

Viscous Oil Flood, CEN for Centrifuge, PP for Porous Plate and HDT for Hybrid Drainage Technique).

Sample Name	Vp (Φ)	Kw
BEN-VOF-01	13.37 cc (23.3 %)	2005 mD
BEN-VOF-AM-02	14.57 cc (25.5 %)	2352 mD
BEN-VOF-AM-03	14.35 cc (25.2 %)	2110 mD
BEN-PP-01	15.35 cc (26.9 %)	1857 mD
BEN-PP-02	14.73 cc (25.4 %)	2034 mD
BEN-CEN-01	14.58 cc (25.5 %)	1793 mD
BEN-HDT-01	13.45 cc (23.7 %)	1832 mD
BEN-HDT-02	15.48 cc (27.2 %)	1996 mD

Table 5-CCA of the Bentheimer sandstone samples used in the tests

The AM inscription in samples BEN-VOF-AM-02 and BEN-VOF-AM-03 represent that these samples were not submitted to waterflooding after the ageing step, but they followed an Amott-IFP cycle after states initialization. These samples were used for testing the effect of performing static or dynamic ageing.

b. Richemont limestone

The Richemont limestone is an outcrop sample from the Turonian age (Superior Cretaceous), extracted from a stone-pit in France. This rock is mainly composed of calcite. X-ray Fluorescence (XRF) results of a Richemont sample are presented in Table *6*:

Mineral	XRF (%)
SiO_2	0.57
TiO_2	0.02
Al_2O_3	0.20
Fe_2O_3	0.19
MnO	0.01
MgO	0.51
CaO	55.14
P_2O_5	0.02
BaO	0.01
ZrO_2	0.01

ZnO	0.01
SrO	0.02
SO_3	0.27
LOI	43.21

Table 6-Mineralogy of the Richemont limestone from XRF test (provided by TotalEnergies laboratory)

A T_2 relaxation time distribution for a Richemont sample fully saturated in brine, that provides a glimpse about its pore size distribution, is presented in Figure 54:

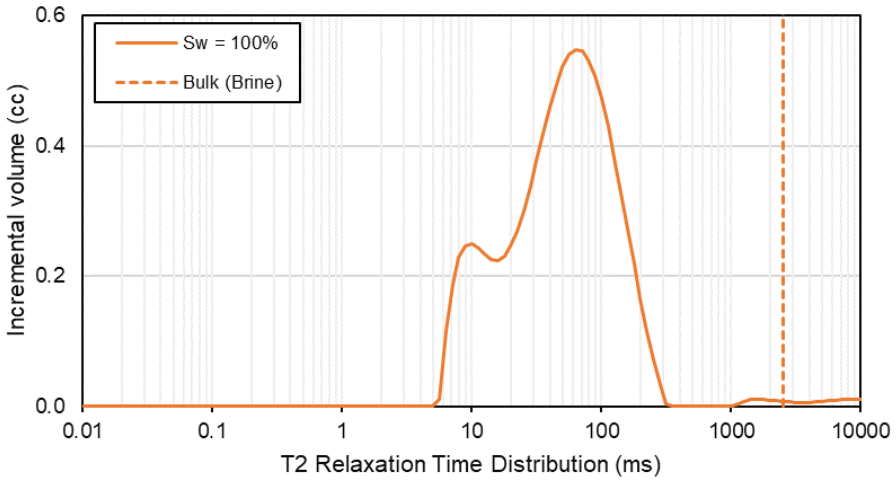

Figure 54 - T_2 relaxation time distribution test on a brine saturated Richemont limestone.

It is interesting to notice that the T_2 relaxation times for the Richemont sample has a strong shift to the left. This behavior is due to its reduced pore sizes, which is noticed in the porosity, brine permeability, significantly lower than the other rocks, and the P_c *versus* S_w curve (presented in Figure 55), which shows a high-pressure entry and a noticeable gradient in the transition range. Moreover, the bigger porosity of this sample represents around 82% of the total pore volume.

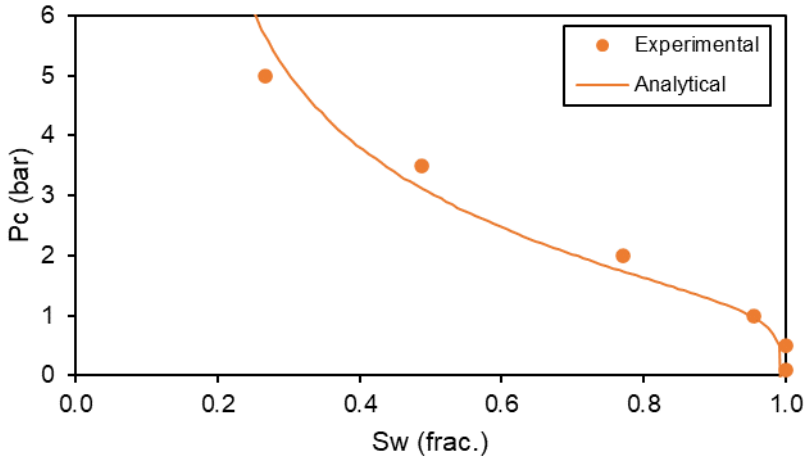

Figure 55 - Richemont limestone primary drainage capillary P_c versus S_w curve (Porous Plate technique).

CCA results for the Richemont samples used during the tests are presented in Table *7*. Due to its reduced permeability, this is a difficult rock for performing multiphase flow with the available material. For this reason, this rock was only used in the proof of concept of the Hybrid Drainage Technique that was validated for high and low permeability samples (Bentheimer sandstone and Richemont limestone, respectively).

Sample Name	Vp (Φ)	Kw
RCH-PP-01	8.94 cc (15.6 %)	0,78 mD
RCH-PP-02	9.95 cc (17.6 %)	0,80 mD
RCH-HDT-01	9.36 cc (16.4 %)	0,76 mD
RCH-HDT-02	9.36 cc (16.4 %)	0,76 mD

Table 7-CCA of the Richemont limestone samples used in the tests

c. Estaillades limestone

The Estaillades limestone is an outcrop sample from the Burdigalian age (Early Miocene), also extracted from a stone-pit in France. This rock is usually classified as a carbonate, which is mainly composed of calcite. Results from an X-ray Fluorescence (XRF) test on the Estaillades samples used in this work are presented in Table *8*:

Mineral	XRF (%)
SiO_2	0.09
TiO_2	0.01
Al_2O_3	0.12
Fe_2O_3	0.14
MnO	0.01
MgO	0.45
CaO	54.75
P_2O_5	0.07
BaO	0.01
ZrO_2	0.01
ZnO	0.01
SrO	0.04
SO_3	0.18
LOI	43.61

Table 8-Mineralogy of the Estaillades limestone from XRF test (provided by TotalEnergies laboratory).

A T_2 relaxation time distribution for an Estaillades sample fully saturated in brine that provides a glimpse about its pore size distribution is presented in Figure 56:

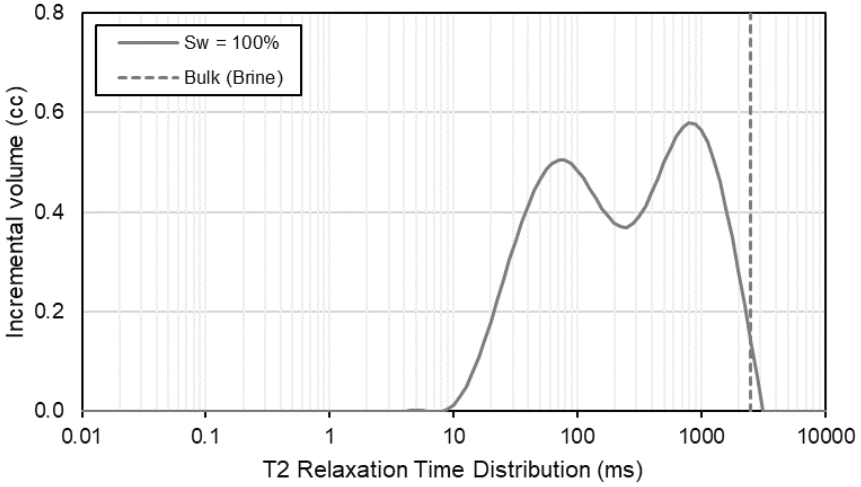

Figure 56 - T_2 relaxation time distribution test on a brine saturated Estaillades limestone.

The bimodal pore structure of the Estaillades sample is easily noticed in the T_2 relaxation time distribution, where two typical pore sizes are present. Once more, a left-shift from the bulk signal of the brine confirms that brine is wetting the pore walls.

It is interesting to notice that from T_2 tests done on Estaillades samples saturated in mineral oil (one important step of NMR characterization, which will be further discussed in sub-section 3.1.2), the dual-porosity characteristic of this sample is not observed. This is an indication that, even for a fully oil-saturated sample, oil does not interact with the pore surface, otherwise it would experiment a left-shift on its T_2 relaxation time compared with bulk fluid relaxation. The reason for this behavior is supposed to be the presence of a thin water film that coats pore walls regardless the drying and vacuum oil saturation steps. The T_2 relaxation result is presented in Figure 57:

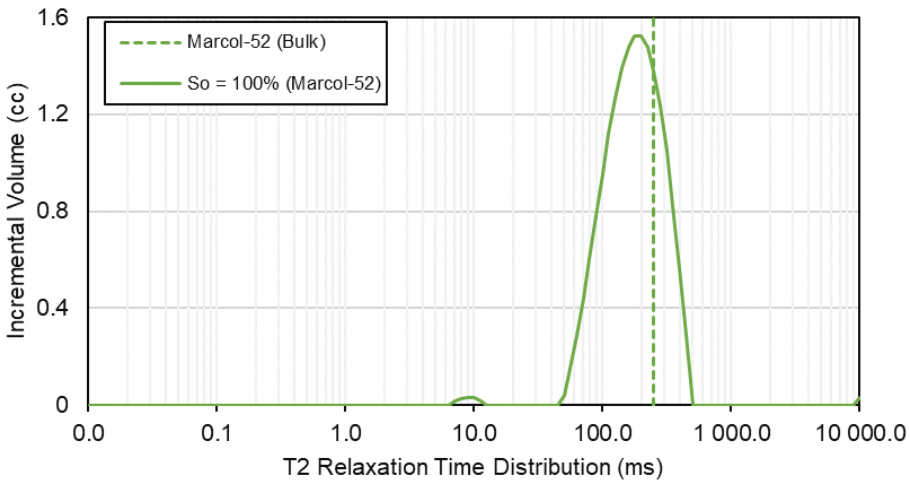

Figure 57 - T_2 relaxation time distribution for an oil-saturated Estaillades sample.

The P_c *versus* S_w curve, measured in this work, is presented in Figure 58. Further discussion regarding its representation of the dual-porosity characteristic of the Estaillades rock will be done in the results section dedicated to EST-PP-01.

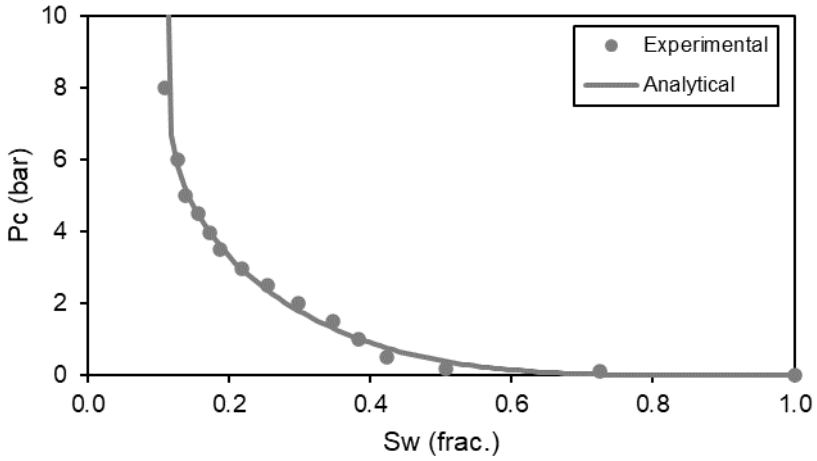

Figure 58 - Estaillades limestone primary drainage capillary P_c versus S_w curve (Porous Plate technique).

This sample was used for testing viscous oil flood, centrifuge, porous plate and the Hybrid Drainage Technique. Due to its characteristics, it represents an interesting case study for samples that are difficult in obtaining the target S_{wi}. The petrophysical characteristics (porosity and brine permeability) as well as the nomenclature of the Estaillades samples used in this work are presented in Table *9*.

Sample Name	Vp (Φ)	Kw
EST-VOF-01	17.06 cc (30.5 %)	196 mD
EST-PP-01	15.76 cc (27.5 %)	201 mD
EST-PP-AM-01	15.85 cc (27.6 %)	215 mD
EST-CEN-01*	17.02 cc (30.0 %)	71 mD
EST-HDT-01	16.49 cc (28.8 %)	131 mD
EST-HDT-02	18.08 cc (31.6 %)	260 mD
EST-HDT-03-MP	0.62 cc (28.1 %)	103 mD

Table 9-CCA of the Estaillades limestone samples used in the tests

EST-CEN-01 was submitted to a g/w centrifuge drainage

Sample EST-HDT-03-MP represents a mini-plug of 10 mm in diameter and 30 mm in length. This sample is better suited for µ-CT experiments, where we are to reach a voxel size of around 5,15 µm. Moreover, thanks to the new Muti-Imagery experimental cell, we were able to perform NMR imaging on this same sample, which gives us results from two different imaging methods.

d. *Reservoir sample*

Two limestone reservoir samples were used for expanding the tests of the Hybrid Drainage Technique. For confidentiality purposes involving the project from where these samples belong, the reservoir plugs will be named R1 and R2.

The primary drainage step on full-size cores of this reservoir was problematic, as the target S_{wi} was impossible to reach. For this reason, this plug represents an interesting test for HDT, as the new technique proposes a solution for these particular cases. The results of these tests will be presented in the appropriate section (Reservoir samples R1 and R2).

A T_2 relaxation time distribution test on a brine saturated sample is presented in Figure 59. From this result we may identify a well-defined dual-porosity, as in Estaillades limestone, which gives an indication of why it was a hard task to reach the target S_{wi} by Viscous Oil Flood. The influence of the bimodal pore structure on the primary drainage step will be thoroughly discussed in the Conclusions and future work.

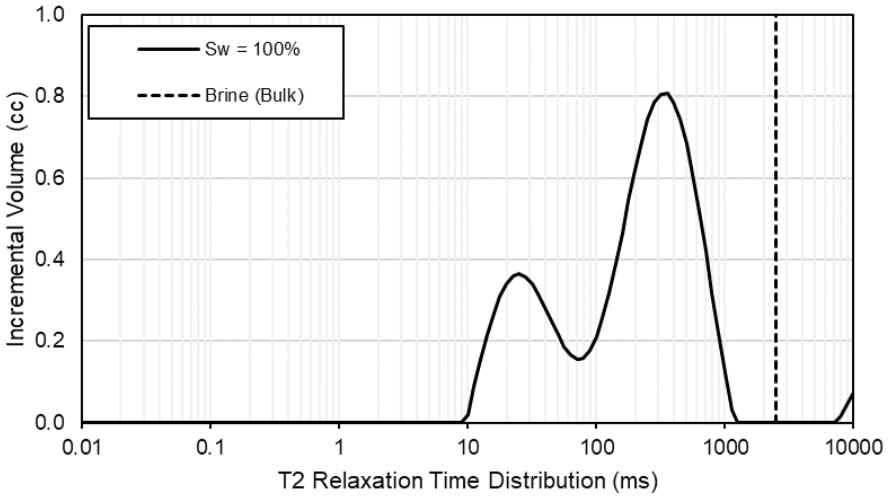

Figure 59 - T_2 Relaxation Time Distribution for R1 saturated in brine.

The CCA results for these samples is presented in Table *10*.

Sample Name	Vp (Φ)	Kw
R1	13.63 cc (24.0 %)	28 mD
R2	13.26 cc (23.3%)	16 mD

Table 10-CCA of the reservoir samples used in the tests

3.1.2. Fluids

a. *Brines*

During this study we have worked with different brine compositions. According to what we intended to observe in each experiment, we doped our brine with some elements.

For most of our NMR experiments we have used deuterium oxide (D_2O) for the aqueous phase. As this element is NMR-invisible, it allowed an unambiguous visualization of hydrocarbon during NMR sequences. Furthermore, as we have

double-imaged our samples on NMR and µ-CT, Potassium Iodide (KI) was added to the aqueous solution, which improves X-Ray attenuation.

Nonetheless, for some experiments, the detection of both brine and hydrocarbon NMR signals was required, notably during the validation of the Hybrid Drainage Technique on dual-porosity samples (EST-HDT-01 and R1 cases).

Moreover, we have also added salts containing divalent cations ($CaCl_2$) for enhancing wettability alteration during the ageing phase. According to several works, water-wetness of sandstones are supposed to decrease with increase in divalent cation concentration in resident brine (Morrow *et al.*, 1986; Buckley & Morrow, 1990; Villard *et al.*, 1993; Jadhunandan & Morrow, 1995; Tang & Morrow, 1999).

The nomenclature, composition, density, and dynamic viscosity (measured at room temperature of 20°C) of the different brines used in our experiments are presented in Table *11*.

Sample Name	Composition	Density	Viscosity
B1	D_2O + KI @ 70 g/l	1.16 g/cc	1.19 cP
B2	D_2O + KI @ 50 g/l + $CaCl_2$ @ 20 g/l	1.15 g/cc	1.26 cP
B3	H_2O + KI @ 50 g/l + $CaCl_2$ @ 20 g/l	1.05 g/cc	1.06 cP
B4	D_2O + $CaCl_2$ @ 24,1 g/l + $MgCl_2$ @ 8,2 g/l + Na_2SO_4 @ 0,75 g/l + KCl @ 0,52 g/l + NaCl @ 101 g/l	1.20 g/cc	1.61 cP
B5	H_2O + $CaCl_2$ @ 24,1 g/l + $MgCl_2$ @ 8,2 g/l + Na_2SO_4 @ 0,75 g/l + KCl @ 0,52 g/l + NaCl @ 101 g/l	1.05 g/cc	1.26 cP

Table 11-Brines nomenclature, composition, and basic characteristics

b. Oils

During every sequence of fluid displacement performed in this study we have used mineral synthetic oil. Overall, we have used three different mineral oils according to their viscosity and density. The choice between them was mainly concentrated on their T_2 bulk relaxation times. For instance, we sometimes observe signal overlapping when performing T_2 relaxation sequences in a sample containing H_2O brine and heavy oil. To deal with this situation, we miscibly replaced the heavy, viscous oil, by a lighter, less viscous oil. Usually, this is sufficient for a proper separation of the brine and oil phases signals. Table *12* presents the base characteristics (density and viscosity at 20°C) of the oils used in this work.

Oil Name	Density	Viscosity
Isopar-L™	0.76 g/cc	1.34 cP
Marcol™-52	0.83 g/cc	12 cP
FINAVESTAN A 180 B	0.86 g/cc	63.60 cP
Toluene	0.86 g/cc	0.56 cP

Table 12-Oil references and basic characteristics

Toluene is presented in this table because it was used once in this work as the oil phase during a sequence of T_2 measurements, due to its extremely low viscosity.

The use of crude oil (named O1) was exclusive for the ageing step and for measuring effective oil permeability to water at S_{wi}. The crude oil was chosen after its SARA (Saturates, Aromatics, Resins and Asphaltenes) characteristics, specifically its asphaltene content, its difference between TAN (Total Acid Number) and TBN (Total Base Number), and WAT (Wax Appearing Temperature). These results, measured at laboratory ambient temperature of 20°C, are presented in Table *13*.

Parameter	Value
Density	0.90 g/cc
Viscosity	42.44 cP
WAT	N/A
TAN	1.4 mg KOH/g
TBN	2.1 mg KOH/g
API	26°
Distilled	17.2 % wt.
Residue	82.2 % wt.
Asphaltenes	2.3 % wt.
Saturates	27.8 % wt.
Aromatics	59.2 % wt.
Resins	13.0 % wt.

Table 13-O1 crude oil characteristics (provided by TotalEnergies laboratory).

Furthermore, for experiments performed in the new Multi-Imagery Cell, Galden® HT270 fluorinated oil from Solvay was used as confinement fluid, as it produces no NMR signal.

3.2. Methodology

The experimental cycle adopted in this study begins with the core cleaning step to remove any possible trace of pollutant in the sample. For outcrop samples, a “soft” Soxhlet cleaning with a "toluene + 2-propanol" cycle is performed with a solvent color control at the end of the cycle. This step is followed by the conventional core analysis (CCA) experiments for the determination of the base petrophysical characteristics: plug geometry, total volume, pore volume, gas permeability and brine permeability. Then, the sample is saturated with formation brine, brine permeability is measured, and we perform the primary drainage step. During primary drainage, the objective is to reach the target value of S_{wi} and obtain a homogeneous saturation profile. This is important as the ageing step, which follows primary drainage, must homogeneously

alter the wettability of the sample. After wettability alteration, the sample states are considered to be restored. The following steps depend on which Special Core Analysis (SCAL) test will be performed.

A typical experimental workflow is presented in Figure 60.

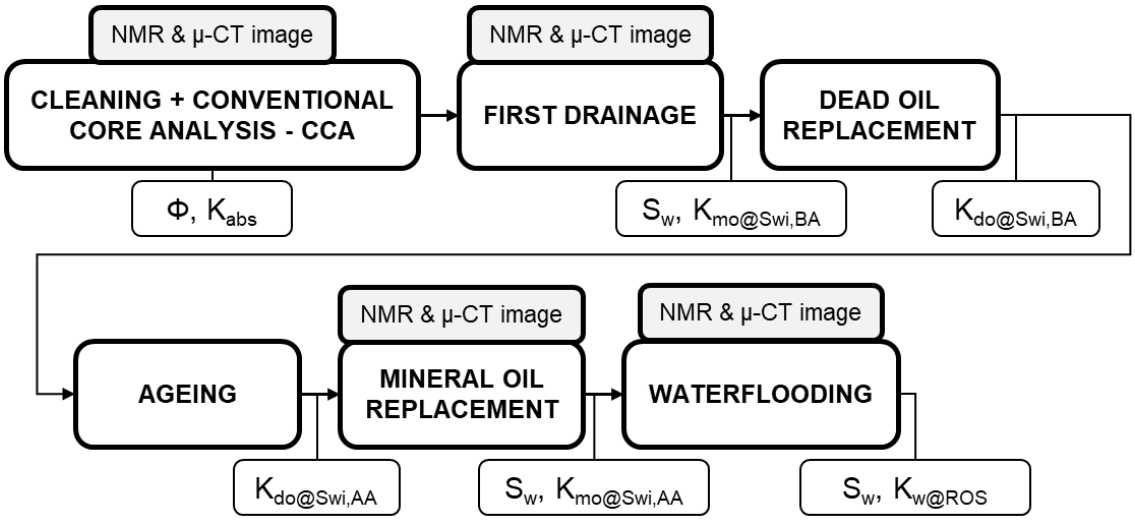

Figure 60 - Typical experimental workflow for a W/O waterflooding.

In the case of an Amott-Harvey cycle, the waterflooding would be substituted by the spontaneous and forced imbibitions, followed by the spontaneous and forced drainages, as described in the Amott-Harvey and Amott-IFP methods section.

3.2.1. Core cleaning and drying

a. Soxhlet extraction

For performing this technique, a Soxhlet apparatus similar to the one schematically presented in Figure 61, is used.

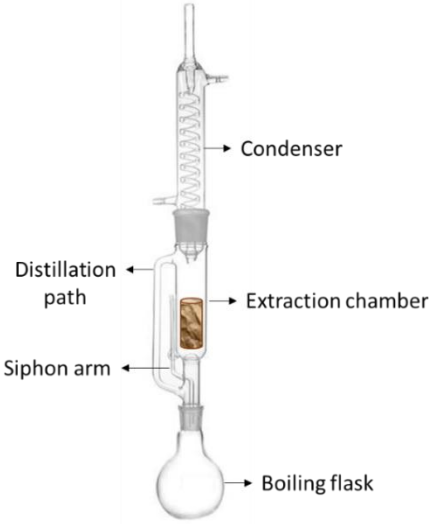

Figure 61 - Schematic representation of a Soxhlet extractor.

This equipment is composed of an extraction chamber where the sample is placed, beneath a boiling flask that will be heated for solvent evaporation. The solvent vapor travels through a distillation path until it reaches the condenser, where it will condense and drip into the extraction chamber. As the process continues, solvent will

fill the extraction chamber, submerging the sample and diffusing into the pore space, leaching out impurities. Once the solvent reaches the level detection (or the top of the siphon arm), it flows back to the solvent flask.

The operator controls the discoloration of the solvent, as it may dissolve organic components present in the rock sample. If this is the case, solvent must be changed. After no more discoloration is observed, the cycle is complete. This process is performed for at least 72 hours at the beginning of the experimental cycle of outcrop samples, in a typical toluene, toluene/2-propanol azeotropic (70/30) and 2-propanol sequence. For tighter and/or reservoir samples, it may take longer, maybe lasting some weeks in cycles with different solvents.

b. Miscible flow through of solvents

The same solvent sequence may be performed using the miscible flow method. For performing this cleaning technique, the sample is mounted in an overburden cell (Hassler-type cells are usually used) under confinement pressure and solvents are injected in the sample at constant flowrate steps by a pump. This process aims to solvate and displace resident hydrocarbons and aqueous fluids from the sample. During the different solvent injection cycles, soak or stasis periods are performed. It consists of stopping flow and letting the solvent diffuse and dissolve organic compounds potentially present in the sample.

In the same way as in the Soxhlet extraction method, solvent color is controlled in the outlet tubing, giving an indication of the best time to stop flowing solvents. A typical flush clean sequence includes toluene, toluene/2-propanol azeotropic (70/30) and 2-propanol cycles.

After following one of the cleaning protocols, the sample is mounted in a Hassler-type cell for N_2 flow through drying, followed by heat drying in a humidity-controlled oven. The sample mass is monitored until mass stabilization, represented by a variation lower than ± 0.01 g over three or four successive measurements over 2-3 days (McPhee *et al.*, 2015).

3.2.2. Pore volume (Vp) determination

a. Pycnometer volume determination

The pycnometer method is used to determine the solid volume of the rock sample. Knowing this parameter, we are able to estimate the effective pore volume by subtracting this value from the total volume of the sample. The apparatus is presented in Figure 62:

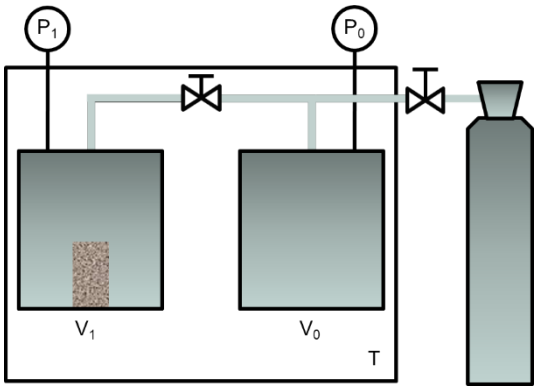

Figure 62 - Schematic representation of a pycnometer.

Volumes V_0 and V_1 are initially known. With the system at ambient pressure, we perform a first run with no sample. We close the connection between chambers and impose a given pressure P_0 on chamber V_0. The second step is to open the connection. Gas will expand to occupy both chambers at a new pressure P_{0x}.The final expanded pressure, P_{0x}, will depend on the ratio of V_0 to V_1:

$$P_0 \cdot V_0 = P_{0x} \cdot (V_1 + V_0) \tag{94}$$

A dry core sample is then placed in chamber V_1, which will reduce the volume of the chamber by the amount of the total solid volume of the sample, V_s. Repeating the expansion sequence, Boyle's law becomes:

$$P_0 \cdot V_0 = P_{0x} \cdot (V_1 + V_0 - V_s) \tag{95}$$

Solving for V_s, we have:

$$V_s = \frac{P_{0x} \cdot (V_1 + V_0) - P_0 \cdot V_0}{P_{0x}} \tag{96}$$

Knowing V_s, we can obtain the sample porosity by:

$$\Phi = \frac{V_t - V_s}{V_t} = \frac{V_p}{V_t} \tag{97}$$

b. μ-CT pore volume determination

As presented in the corresponding section (2.2.1), a pore volume determination from μ-CT imaging is possible. For that, we need to image the sample at a dry state and perform a sequence of image processing, consisting of segmentation and quantification.

During segmentation we separate the voids from the solid matrix by their different values in the grayscale and we assess the fraction of voxels representing the void space. Performing a sum over the entire length of the sample we are able to define a pore volume profile. A porosity profile may outcome if we take the pore volume profile and divide by the total volume of each slice.

c. NMR T_2 pore volume determination

As mentioned in sub-section b (Pore size estimation), we can estimate the pore volume from T_2 relaxation time sequence. In our case, we use this step for the NMR characterization of our samples on the mineral oil used during the flooding steps.

To perform this measurement, we saturate the sample in mineral synthetic oil (usually Marcol™-52) and perform both T_2 relaxation time sequence and SE-SPI. By performing the appropriate corrections with a controlled volume of reference, we obtain the pore volume of our sample and the 100% saturated longitudinal profile. It is important to relax the same fluid through the experimental cycle, keeping a coherence between measurements. This avoids problems regarding hydrogen index correction. In this way, we are able to use this information as the 100% state for defining the saturation at different steps of the experimental cycle.

3.2.3. Steady-state gas permeability (Kg)

After cleaning, drying and pore volume determination, the sample is prepared for the steady-state Kg measurement. The equipment used for the steady-state Kg is composed of:

- *Injection equipment and coreholder*

A system for controlling the gas inlet pressure that will be applied through several pressure steps of the experiment. The maximum injection pressure is usually limited to around 7 bars.

Hassler-type cell, which confines the sample by the application of an overburden pressure and has inlet and outlet platens in both sample ends.

- *Pressure and flowrate monitoring equipment*

Pressure gauges placed upstream of the inlet and downstream of the outlet of the Hassler cell. This equipment will measure the pressure drop along the sample, which will be applied to equation (51). Special attention must be given for high permeability sample, as increased flowrates are used for producing higher pressure values for reaching proper metrology conditions. Nonetheless, this approach may induce turbulence flow either in the sample and in the tubing, which will result in a significant underestimation of the permeability.

A method for controlling outlet pressure, such as a backpressure regulator, is needed for flow control in high permeability samples and in Klinkenberg measurements. In the same way, a flowrate measurement system downstream of the sample is necessary.

Moreover, if flowrate is measured at atmospheric condition, a barometer is needed to measure atmospheric pressure and allow the appropriate correction through the following equation:

$$Q_m = \frac{Q_0 P_0}{P_m} \tag{98}$$

where Q_m is the mean flowrate, Q_0 is flow rate at atmospheric pressure, P_0 is measured atmospheric pressure and P_m is the mean pressure.

A schematic illustration of the setup used during steady-state Kg measurement is shown in Figure 63.

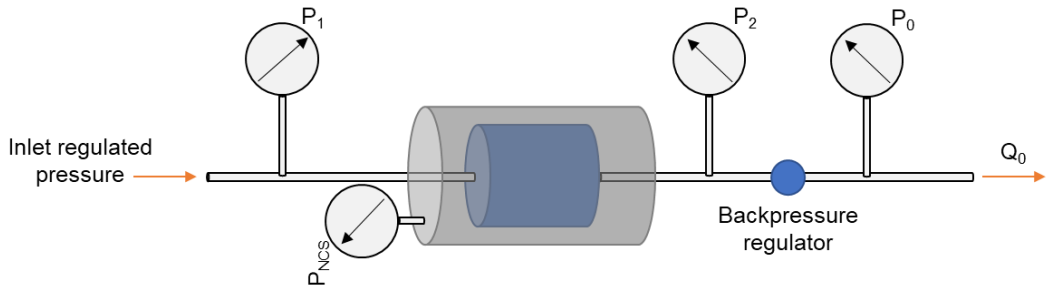

Figure 63 - Steady-state Kg measurement apparatus.

3.2.4. Brine saturation and steady-state (Kw)

Steady-state liquid absolute permeability measurements are quite simple; however, they are less usual in the industry as it is more complicated to handle a large number of plugs at once. This is the reason why this measurement is usually preconized in SCAL programs.

Plugs may be saturated inside a sealed vessel or directly inside the coreholder. In our case, as we developed a coreholder that needed no handling after mounting the dry sample, we saturated the plugs directly inside the overburden cell.

For this process, the plug is placed in a Viton® sleeve and loaded inside the cell, where Net Confining Stress (NCS) is applied. A vacuum pump is connected to the upper inlet tubing of the cell in order to generate a vacuum prior to fluid saturation. When the absolute pressure in the sample reaches values below 10^{-5} bar, the setup is considered ready for fluid saturation. A burette containing the formation brine is then connected to the bottom inlet tubing of the cell and the valve is opened. As brine flows into the cell, the graduated burette allows controlling the brine volume imbibed in the system. When an equilibrium is reached and no more brine flows into the cell, a brine-saturated pump is connected to the inlet tubing and keeps the system under a minimum pressure of 15 bars for at least 8 hours. Finished this step, the system is kept under a pore pressure of around 2 bars (in our experiments) for avoiding brine degassing, and it is ready to begin Kw tests.

The experimental apparatus for this experiment is similar than the one used for Kg tests. Basically, a volumetric pump is used to inject brine in the sample at different flowrate steps, and a differential pressure gauge monitors pressure drop during the experiment. A schematic example is presented in Figure 64:

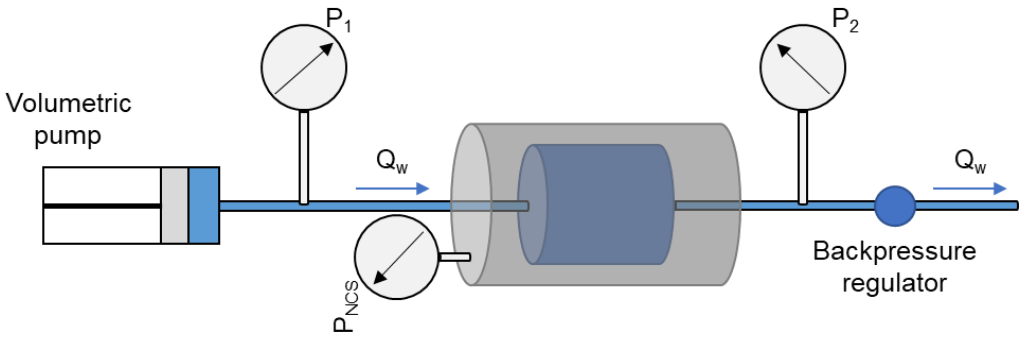

Figure 64 - Schematic representation of a Kw measurement setup.

As Darcy's Law for 1-fluid horizontal flow (equation (29) is a linear equation, we may plot $\frac{Q}{A}$ *versus* $\frac{\Delta P}{L}$, which should fall into a straight line, with slope equal to $\frac{k}{\mu}$. Therefore, we may determine brine permeability by a linear regression of $\frac{Q}{A}$ *versus* $\frac{\Delta P}{L}$ datapoints. We usually perform at least 4 increasing and 4 decreasing flowrate steps during the experiment. Pressure drop monitoring must show a repeatability when decreasing flowrate steps, otherwise it would indicate fines migration and/or a modification of the porous medium. An example of a brine permeability set of datapoints is presented in Figure 65:

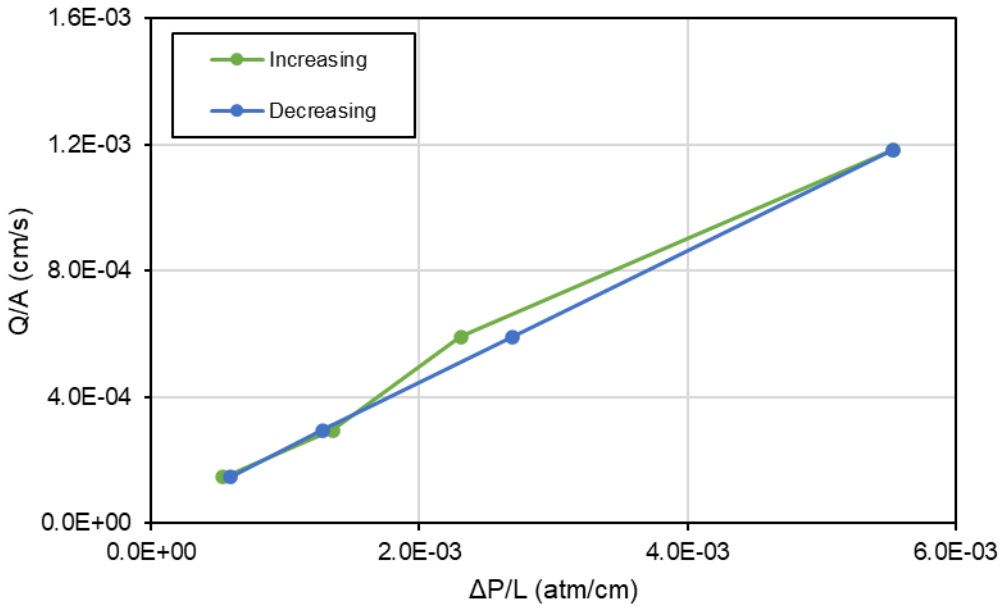

Figure 65 - Example of a Kw set of datapoints for a Bentheimer sandstone sample.

3.2.5. Primary Drainage techniques

a. Viscous Oil Flood

The setup necessary for this experiment can be divided in three sets of equipment:

- *Injection equipment and coreholder*

Classic Viscous Oil Flood setups use a Hassler Cell, usually made in stainless steel. As shown in the schematic here below, the Hassler Cell consists of an inlet piston with two inlet ports (one for fluid injection and one pressure port) and another piston containing two outlet ports (one fluid production port and one pressure port). A Viton® sleeve holds the plug sample, which undergoes a confining pressure ensured by a hydraulic pump.

The displacement equipment contains a pump capable of regulating the injection flowrate and a backpressure regulator located at the output of the system to maintain the fluid pressure above the bubble point of oil (or to minimize gas expansion from core inlet to outlet in gas/water experiences).

- *Pressure monitoring equipment*

The pressure ports present in the pistons allow the measurement of the pressure drop along the sample directly from the core by using a pressure transducer. This configuration reduces the impact of external sources of error in this measurement.

- *Collector equipment*

The collector equipment is used in order to measure production along the experiment. It consists of a fraction collector that is able to separate the produced fluid (water) and the injected fluid (oil/gas). The injected fluid may undergo a loop path to recycle fluids.

Moreover, as this method is subject to Capillary End-Effects because of the pressure drop along the sample, an injection direction reversal is usually performed.

An interesting way of easily swapping inlet and outlet tubing is by means of a 4-way valve. A typical setup is presented in Figure 66:

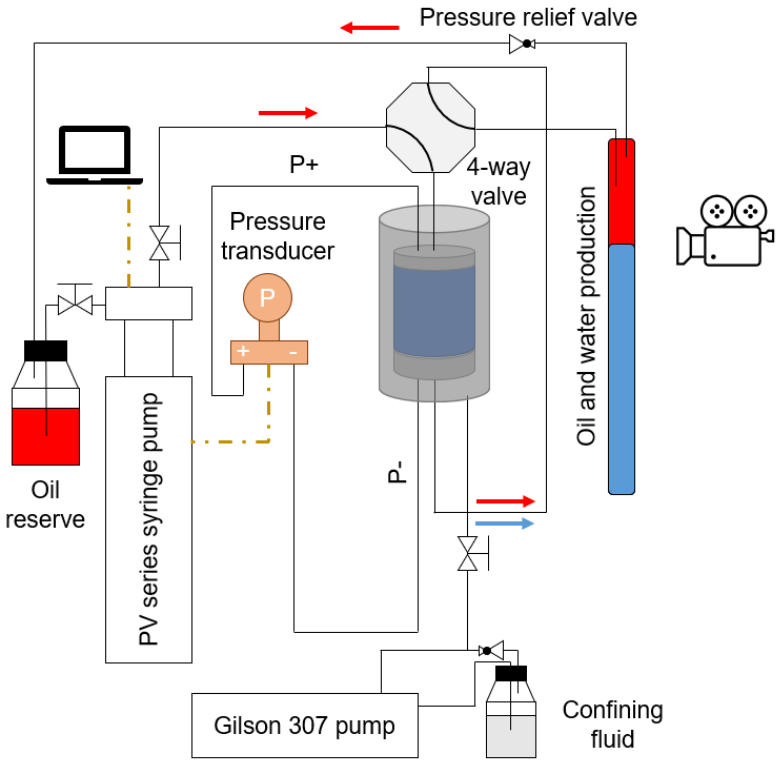

Figure 66 - Classic Viscous Oil Flood setup.

An experimental cell made of Polyether ether ketone (Peek) was developed during this project and may replace the classic Hassler Cell in order to allow the constant imaging of the sample during drainage. By using this equipment, monitoring of the saturation profiles advancing and the water production by NMR or by µ-CT is possible. This information is useful when deconvoluting the experimental artifacts by numerical simulations during the history match of the experiment.

The main changes between the experimental setup presented in Figure 66 and the one adapted to NMR and µ-CT imaging are the use of the Multi-Imagery overburden cell itself, the presence of the NMR spectrometer or the µ-CT, and the fluorinated oil as confining fluid.

At first, only the displaced phase (water) is produced in the outlet face of the system, thus observing a linear production stage, until the displacing phase reaches the outlet. This is called the breakthrough and, from this moment on, both fluids are produced simultaneously and the plot of the produced phase as a function of time are no longer linear.

The injection continues until no more production is observed. After this condition is reached, we may start the next injection flowrate. Once no more brine production is observed and oil is being recycled in the last flowrate step, the plug is considered to be at initial water saturation (S_{wi}). At this point, flow reversal is performed to homogenize the S_{wi} profile. The best way to control the profile homogenization from injection direction reversal is In-Situ Saturation Monitoring (ISSM).

After obtaining the homogeneous saturation profile, an end-point oil effective permeability measurement can be done. This measurement is similar to a K_w

measurement, but this time oil is injected instead of brine. Furthermore, flowrate steps during this measurement should never exceed the last flowrate step of Viscous Oil Flood, otherwise additional production, thus generation of a heterogeneous saturation profile would be noticed.

b. *Porous Plate*

As for the viscous displacement techniques, the apparatus for Porous Plate experiments, presented in Figure 67, can be divided in three sets of equipment:

- *Injection equipment and coreholder*

The same Hassler cell may be used for this experiment.

The displacement equipment, however, must contain a pump capable of regulating the injection pressure; That is why the pumps used in this experiment are classically mono-piston pumps: they can advance or regress to the target pressure step.

- *Pressure monitoring equipment*

As there is no pressure drop in this experiment, the invasion of oil in the sample may be considered as quasi-static. The pressure monitoring equipment is only composed of the pressure transducer that communicates with the injection pump.

- *Collector equipment*

The collector equipment for this experiment is slightly different from the viscous displacement technique. Once only water is produced during this experiment, the monitoring is done by burettes directly connected to pressure transducers that converts the height (thus mass) of the water column above it into produced volume. This technique allows an extremely precise measurement of the water production.

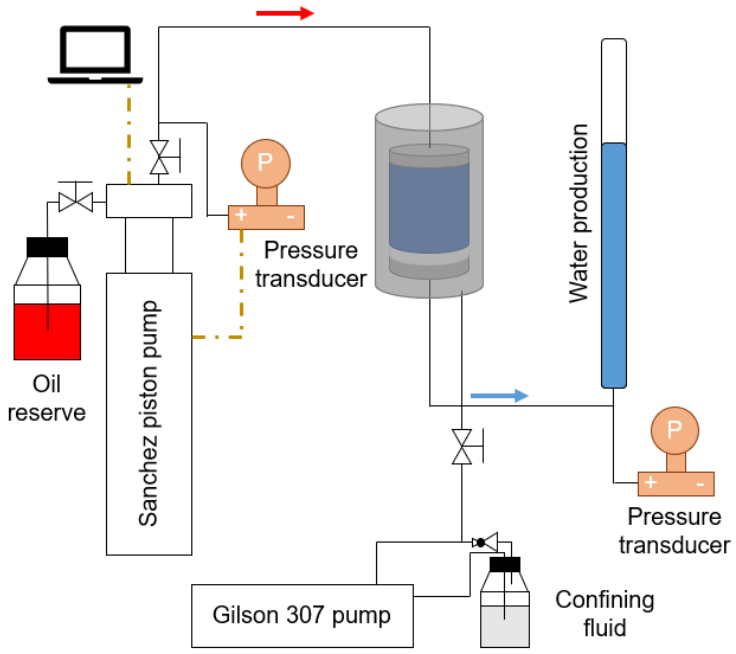

Figure 67 - Porous Plate experimental setup.

c. *Centrifuge*

To perform primary drainage by centrifugation, the brine-saturated sample is loaded inside a bucket that is filled with oil and fixed to the rotor of the centrifuge machine. These buckets have a transparent graduated tube connected to their bottom face, where produced brine is collected during centrifugation. A stroboscopic light placed inside the centrifuge machine flashes at the same frequency as the rotational velocity of the centrifuge. This produces the illusion of a static system and allows production monitoring by a high-resolution non-intrusive camera. This camera takes images of the burette during the experiment and an image treatment is performed for the quantification of the production.

Rotational speed steps are followed as brine is produced by the application of centrifugal forces. Brine production ceases when centrifugal and capillary forces achieve equilibrium. For precise definition of production equilibrium, produced brine must be plotted against time in the logarithmic scale.

After equilibrium is reached at the end of the last step of rotational speed, the sample is considered at initial water saturation. As in the Viscous Oil Flood method, a heterogeneous saturation profile will be present in the sample. For dealing with this situation, sample is once again loaded in the centrifuge, this time in an inverted position (upside down). The machine is set to turn for limited time to homogenize the saturation profile. The results presented in the appropriate section will show that the control of profile homogenization is quite poor.

d. *Hybrid Drainage Technique*

Inspired by the challenges and the propositions made by different authors, we proposed a new Hybrid Drainage Technique (HDT) capable of not only reducing experimental time in comparison to a classic Porous Plate primary drainage, but also generating a homogeneous saturation profile (Fernandes *et al.*, 2022).

The principle of the Hybrid Drainage Technique consists of coupling Viscous Oil Flood and Porous Plate for performing fast primary drainage, free from capillary end effects, as the final step of the method is capillary-driven and generates a homogeneous capillary pressure field in the sample.

To perform this technique, the rock sample is loaded in an overburden cell together with a mono-perforated porous plate placed downstream of the sample. This perforated porous plate is then mounted on a base-plate (called platen in what follows) constituted of two isolated outlets: one central outlet directly connected to the porous plate bypass (hereafter called Outlet 1), and one lateral outlet positioned immediately downstream the porous plate (called Outlet 2). The presence of an O-ring ensures the isolation between both outlets that are connected to valves out of the cell. Both outlets are connected to separate valves downstream of the lines. This way, if the valve connected to the central by-pass is closed, fluids must flow through the porous plate to access the lateral outlet in the platen, reproducing the same process as in a classic Porous Plate drainage.

The design of the overburden cell and the platen housing the porous plate, as well as the Hybrid Drainage Technique were filed for patent (France Brevet n PAT22-

056, 2022 and France Brevet n PAT22-055, 2022, respectively)[1]. A schematic drawing of the overburden cell is shown in Figure 68.

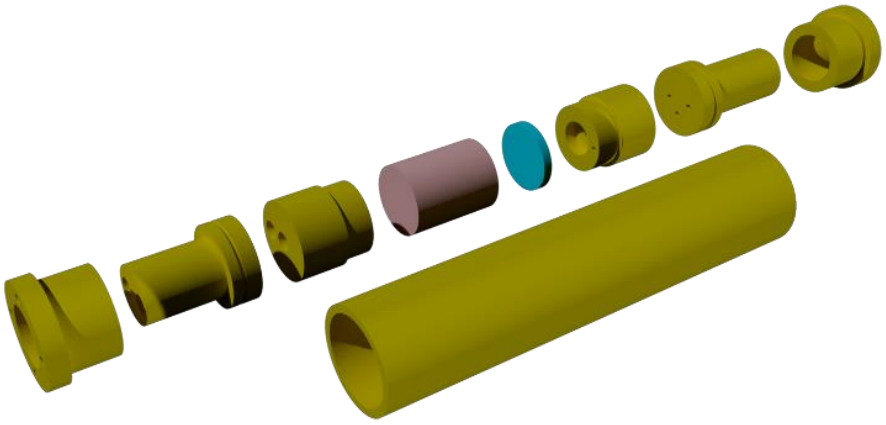

Figure 68 - Schematic representation of the overburden cell.

As well as in other capillary-driven techniques (*e.g.*, Porous Plate and Centrifuge) knowing the target P_c is mandatory for reaching a correct S_{wi} value in the Hybrid Drainage Technique.

The HDT is composed of two steps: an initial oil injection similar to the Viscous Oil Flood technique and a second part similar to the Porous Plate technique, where capillary foot produced during Step 1 will be eliminated.

- *Step 1:*

At first, oil is injected into the sample at constant pressure keeping Outlet 1 opened and Outlet 2 closed. Oil displaces water initially in place through the bypass of the porous plate (Outlet 1). This phase will generate a non-uniform saturation profile due to capillary end effects, such as in a classic Viscous Flooding. The end of Step 1 is achieved when no more water is produced after oil breakthrough. At this moment, the goal is to minimize capillary foot by imposing a constant pressure on the whole sample that will homogenize fluid saturations, which will be performed in Step 2.

- *Step 2:*

The transition to Step 2 consists in swapping the outlet valves: Outlet 1, previously opened, is closed, and Outlet 2, previously closed, is opened. Therefore, a transition to a capillary-driven injection is initiated, where capillary pressure will be controlled by the porous plate. No modification is made regarding the injection pump once it is set in pressure regulation mode at the target inlet pressure. A schematic illustration showing both outlets and the way they are distributed is shown in Figure 69.

[1] These are TotalEnergies internal references for both patents.

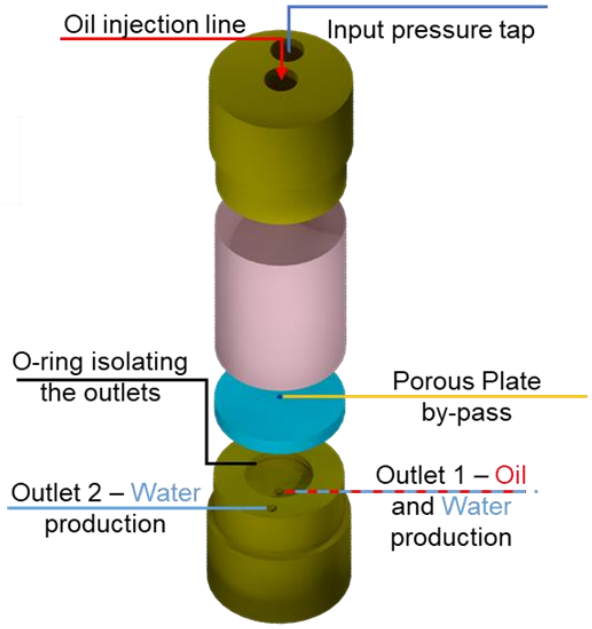

Figure 69 - Schematic representation of the method, showing both fluid outlets.

The main benefits of this technique are experimental time reduction and a homogenous saturation profile generation. The time reduction is due to fast water production from Viscous Oil Flood while the latter results from a very quick transition to Porous Plate drainage without removal from the cell. In addition, the sample is immediately ready for further testing as it always remains in the experimental cell with confining stress.

3.2.6. Ageing

After establishing initial water saturation, the sample is submitted to a wettability alteration through ageing in crude oil. As primary drainage was performed using mineral synthetic oil, a miscible change to crude oil must be done. However, synthetic and crude oil interaction must be avoided at all costs because mineral oil is considered to be a precipitant. Surface precipitation of asphaltenes present in crude oil when they interact with alkanes were observed in the literature (Buckley *et al.*, 1998; Buckley & Wang, 2002).

An alternative for replacing mineral oil by crude oil is passing by an intermediate step, called toluene flush. Dissolving crude oil with toluene stabilizes asphaltenes, which prevents their precipitation. Therefore, in a first step, mineral oil is replaced by toluene, then crude oil is injected into the sample. Typical protocols mention that flushing 3 Vp of toluene and 3 Vp of crude oil is sufficient for a complete miscible replacement. In this work, dP and the color in the outlet tubing were monitored to ensure a complete replacement.

Ageing temperature and duration was largely discussed in the literature (Cuiec, 1977; Anderson, 1986; Jadhunandan & Morrow, 1991; Villard *et al.*, 1993; Jadhunandan & Morrow, 1995). After an overall review, we considered that an ageing duration of two weeks at 80 °C would be sufficient for a complete wettability alteration.

Crude oil is flushed in both directions, in order to generate a homogeneous wettability profile (the 4-way valve enables this operation). The only cases for which this approach was not adopted were samples BEN-VOF-AM-03 and EST-PP-01. The

first case represents an Amott-IFP test on a sample submitted to static ageing. This result will be compared to BEN-VOF-AM-02, which followed the same protocol, except for the ageing technique, where a crude oil reversal flow was adopted. In the case of the Estaillades sample, we intended to show that, even for a sample initiated with a homogeneous saturation profile after primary drainage, a heterogeneous wettability profile may be generated if no crude oil flow reversal is performed during ageing. Therefore, in this case, we have performed mono-directional flush of crude oil during ageing.

3.2.7. Waterflooding

As discussed in sub-section 1.8.5, we adopted the unsteady-state technique in this work.

All USS waterflooding experiments were conducted inside the new Multi-Imagery overburden cell. This allowed the obtainment of saturation profiles during imbibition.

Experiments, as in USS primary drainage tests, were conducted in gravity stabilized condition (cell in the vertical position, with brine injection from the bottom). This prevents gravity override and situations where the ratio between gravity and viscous forces becomes significant (especially in cases using extremely low flowrates).

A constant flowrate of brine injection was adopted, which allows a precise control of relative permeability changes during the tests through pressure and fractional flow monitoring. As well as in USS primary drainage, pressure drop across the sample is measured by pressure gauges positioned upstream and downstream of the sample. Produced fluids are recovered in a graduated burette, and NMR monitoring provides additional information about real time in-situ saturation. A typical experimental setup is presented in Figure 70:

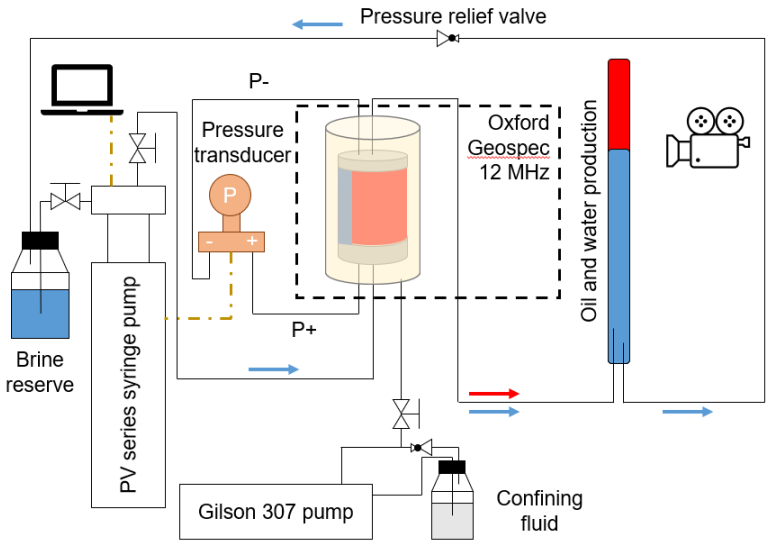

Figure 70 - Schematic illustration of the experimental setup used for USS waterflooding.

Waterflooding continues until pressure drop and oil production stabilize. The different flowrate steps are done until no more oil is produced at the end of the final flowrate step. At this point, a brine effective-permeability measurement is performed. It is important to notice that, as discussed in sub-section 1.8.5, the measured value of $k_{rw@ROS}$ may be affected by the presence of CEE.

4. Results

We have presented the challenges and methodology to perform proper states restoration in the previous sections. We will now detail the experimental results obtained during this work.

Among the several steps of the experimental protocol previously presented in Figure 60, we highlight primary drainage and ageing as the crucial processes for a reservoir-representative fluids setting in plug samples. Therefore, we divided the results section in order to list the challenges we have faced when performing the initialization of the samples and what are the impacts of adopting some of the "classical" approaches (*e.g.*, Viscous Oil Flood for primary drainage and static ageing).

All outcrop samples have undergone the same cleaning and drying protocol. We used the Soxhlet extractor method on a 3-cycle basis and monitoring solvent color:

- *First cycle: Toluene*
- *Second cycle: Toluene/2-propanol azeotropic*
- *Third cycle: 2-propanol*

Then, the core plugs were dried in the oven with mass stabilization control.

Reservoir samples, however, passed by flow-through solvent cleaning before the Soxhlet extraction. Samples were mounted in Hassler cells and followed the same injection cycles protocol; however longer soaking periods were respected. Solvent color monitoring indicated the end of each step:

- *First cycle: Toluene*
- *Second cycle: Toluene/2-propanol azeotropic*
- *Third cycle: 2-propanol*

This protocol was followed in order to remove remaining crude oil fractions by interaction with solvent at room temperature, which would not enhance water evaporation prior to complete oil removal. Even though we have obtained a proper solvent color control during flow-through of solvents cleaning, the Soxhlet method was used, because of the dual-porosity characteristics of these reservoir samples. In contrast to flow-through, this method promotes a better interaction of the solvent to the totality of the sample porosity, as solvent diffuses through the pore space more easily. Therefore, the same 3-cycle protocol was respected.

At the end of the 3 steps, the core was dried by N_2 injection followed by oven drying until mass stabilization.

All NMR and/or µ-CT monitored experiments were performed in the new Multi-Imagery cell, using Galden® HT270 fluorinated oil as confining fluid. Experiments that did not require constant imaging monitoring were performed on classic Hassler Cells, using distilled water as confining fluid. All experiments were performed at constant Net Confining Stress (NCS) of $P_{NCS} = 30\ bar$.

4.1. Primary drainage challenges

4.1.1. Reaching the target Swi

For a long time, establishing initial water saturation had a secondary role in a SCAL protocol, as results would be considered satisfactory by simply reaching the S_{wi}

target. However, this approach may hide some experimental artifacts (especially saturation profiles heterogeneity) depending on the adopted method. This is the case for experiments initialized by Viscous Oil Flood and Centrifugation, because they impose a capillary-pressure gradient in the sample.

Furthermore, S_{wi} target may be difficult to reach in some specific cases, specially where pore connectivity is poor. In these cases, techniques based purely on viscous displacement, such as VOF, are not effective, as oil preferentially flows through bigger porosity, leaving the smaller porosity unflushed.

BEN-VOF-01

We have defined an S_{wi} target of 20% for this Bentheimer sample submitted to primary drainage by Viscous Oil Flood.

We have used B1 and Isopar-L™ for performing an imaged VOF at 4 flowrate steps, which are presented together with the capillary numbers in Table *14*:

Flowrate Step	Flowrate	Capillary Number
Q1	6 cc/h	$5.3\ 10^{-8}$
Q2	100 cc/h c	$8.8\ 10^{-7}$
Q3	400 cc/h	$3.5\ 10^{-6}$
Q4	800 cc/h	$7.0\ 10^{-6}$

Table 14-Flowrate steps and capillary number for BEN-VOF-01 primary drainage

To obtain water saturation profiles, we first performed T_2 and SE-SPI profile sequences on the oil-saturated plug sample. This way, by taking the difference between T_2 and profiles measured during the experiment, we may extract saturation information, as well as the water saturation profiles. T_2 relaxation experiments and water saturation profiles advancing during the experiment are presented in Figure 71 and Figure 72:

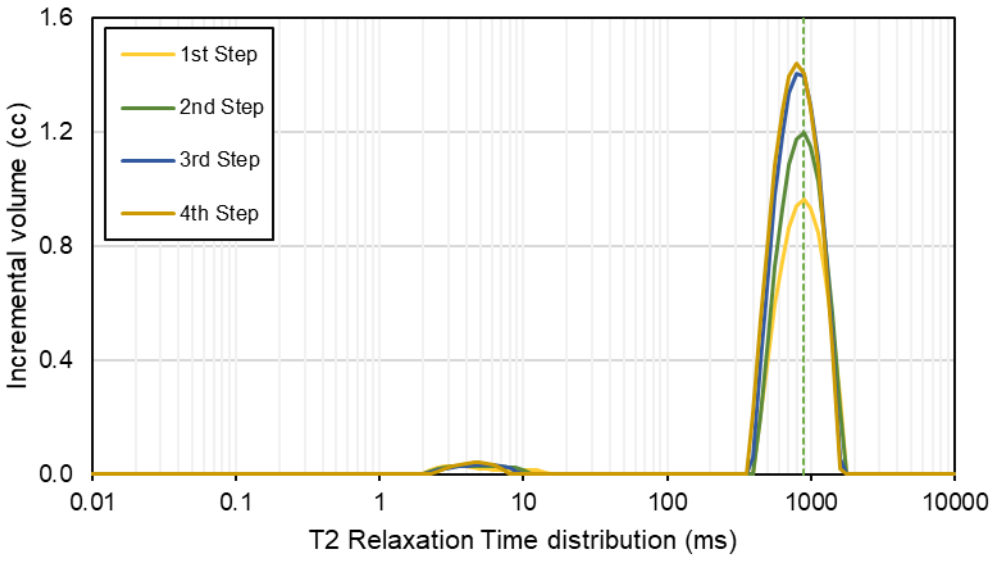

Figure 71 - T_2 Relaxation Times distribution at the end of each step (BEN-VOF-01) – Isopar-L™ bulk relaxation time is represented by the green vertical line and the brine used (B1) is invisible in the T_2 spectrum.

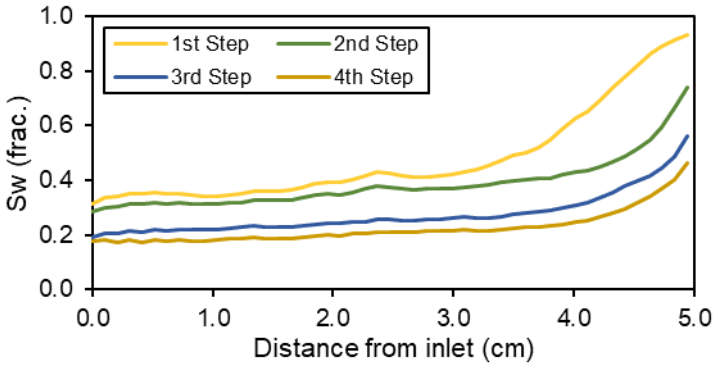

Figure 72 - Water saturation profiles at the end of each flowrate step (BEN-VOF-01).

If we consider only the T_2 relaxation response at the end of the 4th step, we confirm that the target value of S_{wi} was successfully reached ($S_{wi,4th\ step} = 22.5\ \%$). Nonetheless, a quick observation of the last water saturation profile is sufficient to notice the presence of Capillary-End Effects. This is a clear situation where, despite reaching the correct S_{wi} target, we still do not have the appropriate conditions for continuing the experimental cycle. The current technique to deal with CEE is reversing injection direction, which is able to homogenize the saturation profile. The results obtained by this approach will be further discussed in the next section.

Furthermore, we have performed the history match of BEN-VOF-01 primary drainage. Using dP, Vw data and S_w profiles, we made a numerical simulation to obtain drainage K_r and P_c curves. The matches between experimental and simulated data are presented in Figure 73, Figure 74, and Figure 75.

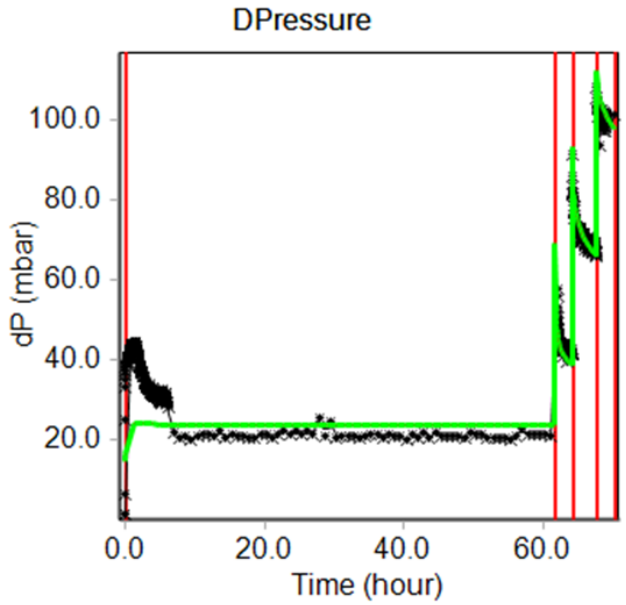

Figure 73 – History match of dP for the primary drainage of BEN-VOF-01.

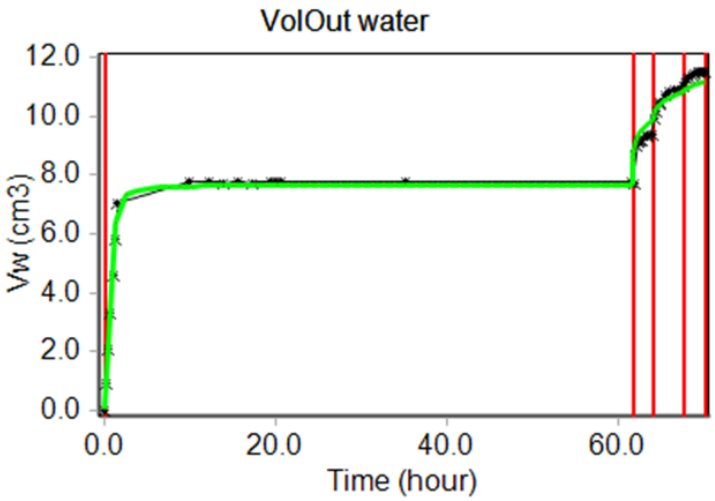

Figure 74 – History match of water production (V_w) during BEN-VOF-01 primary drainage.

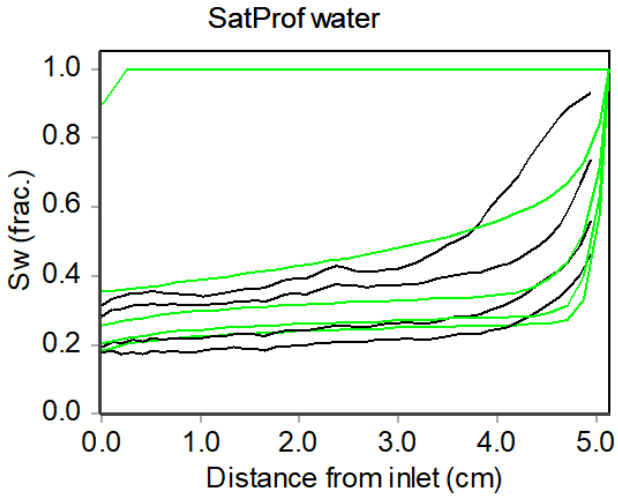

Figure 75 – History match of the S_w profiles obtained during BEN-VOF-01 primary drainage.

The resulting K_r and P_c curves obtained after the history match of dP, V_w and S_w profiles during primary drainage are presented in Figure 76:

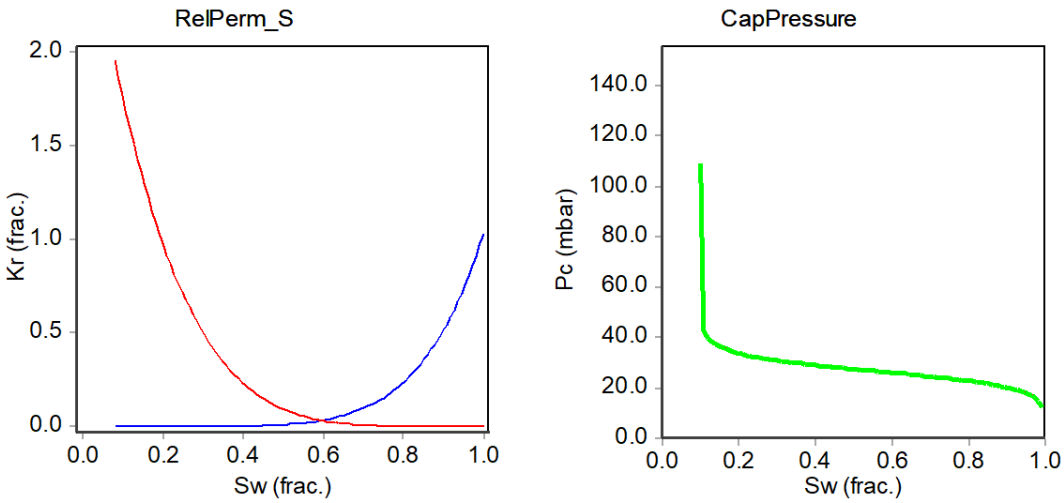

Figure 76 – Primary drainage K_r and P_c curves obtained from numerical simulation of BEN-VOF-01.

We used the Corey K_r model and LogBeta for relative permeability and capillary pressure deconvolution, respectively. Corey exponents and P_c parameters are presented in Table *15* ($S_{wi} = 0.1$):

Parameters	Corey Exponents
N_w	6.0
N_o	5.0
S_{wi}	0.08
$K_{rw,max}$	1.00
$K_{ro,max}$	1.97
P_o	14.80 mbar
β	0.86

Table 15-Set of parameters for BEN-VOF-01 primary drainage

It is important to state that the Bentheimer sandstone is a homogeneous, water-wet sample, with some clay content. In these cases we may face K_{ro} values greater than 1, which means that oil permeability at irreducible water saturation ($S_{w,irr}$) is greater than the absolute permeability (K_w). This is explained by a lubrication of the pore network by brine wetting the pore walls, which facilitates oil flow, thus increasing its relative permeability (McPhee *et al.*, 2015).

EST-VOF-01

Performing a primary drainage for a low target value of S_{wi} on an Estaillades sample using a viscous controlled technique seems to be a challenging task. Taking a closer look to the work published by different authors, it is easily noticed that dropping below 50% with a viscous-controlled method is a harsh task (Gao *et al.*, 2019; Lin *et al.*, 2021; Nono, 2014).

A S_{wi} value lower than 50% was only obtained by performing the Porous Plate Method. This behavior may be explained from the primary drainage water relative permeability curves shape presented in (Ott *et al.*, 2015) and the vacuolar structure of this rock (Nono, 2014). Even though primary drainage is performed in strongly water-wet rock conditions, K_{row} is controlled by the big pores, without contribution of the smaller porosity.

Moreover, in the work of (Blunt, 2017), the displacement path for a waterflooding on an Estaillades sample was discussed, and the conclusion was that the poor connectivity between large and small porosities generates a snap-off trapping phenomenon. This result may be extended to the primary drainage process. This behavior is inherent to the pore network composition of this rock.

These results were confirmed in this work, where a primary drainage by Viscous Oil Flood was performed on EST-VOF-01. The bimodal character of both the porosity and pore throat radius were verified during initial characterization.

NMR T_2 relaxation measurement using B3 (Figure 77) presents the pore size distribution As this is an outcrop sample, strongly water-wet, T_2 surface relaxation controls the signal. Therefore, the T_2 curve describes the pore size distribution.

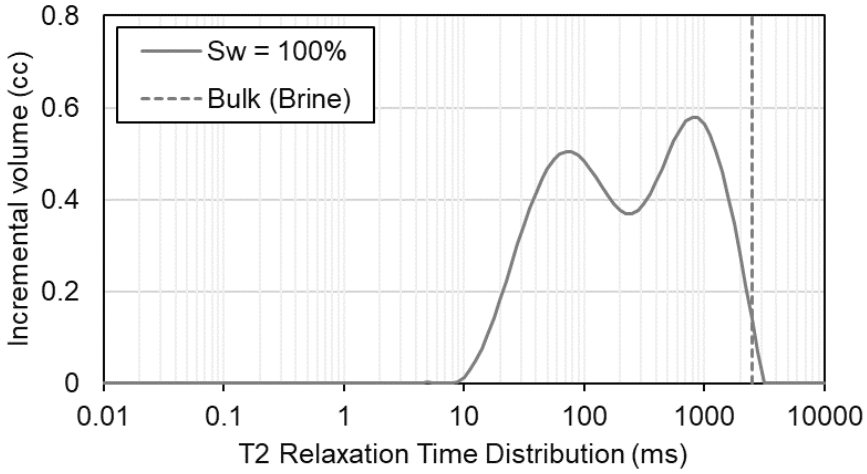

Figure 77 - T2 relaxation time distribution for the Estaillades sample using B3.

It is interesting to compare this result with the one obtained by Tanino & Blunt (2012). On their study, they also find a dual-porosity distribution from T_2 relaxation time distribution tests, although this effect is less pronounced. A comparison between both results is presented in Figure 78:

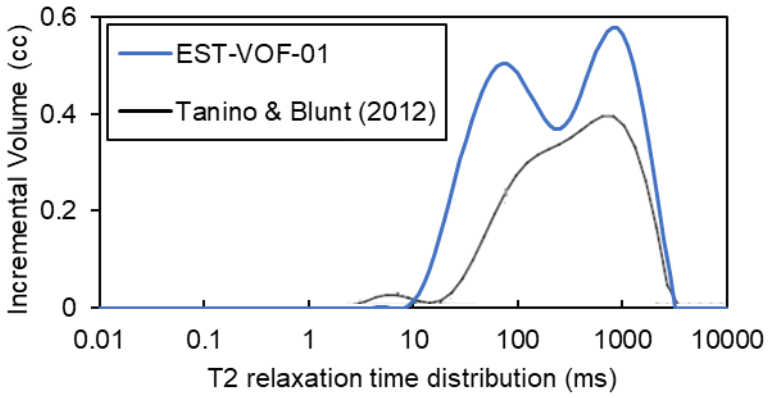

Figure 78 - Comparison of T_2 relaxation time distribution between EST-VOF-01 and the Estaillades limestones sample used in the study of Tanino & Blunt (2012).

The Pore Throat Radius (PTR) distribution of the Estaillades rock was obtained by an MICP test performed on a twin sample of EST-VOF-01. As we did for the pore size distribution, we are also able to compare the results obtained in this study with the ones presented by Tanino & Blunt (2012). The comparison between both studies is presented in Figure 79:

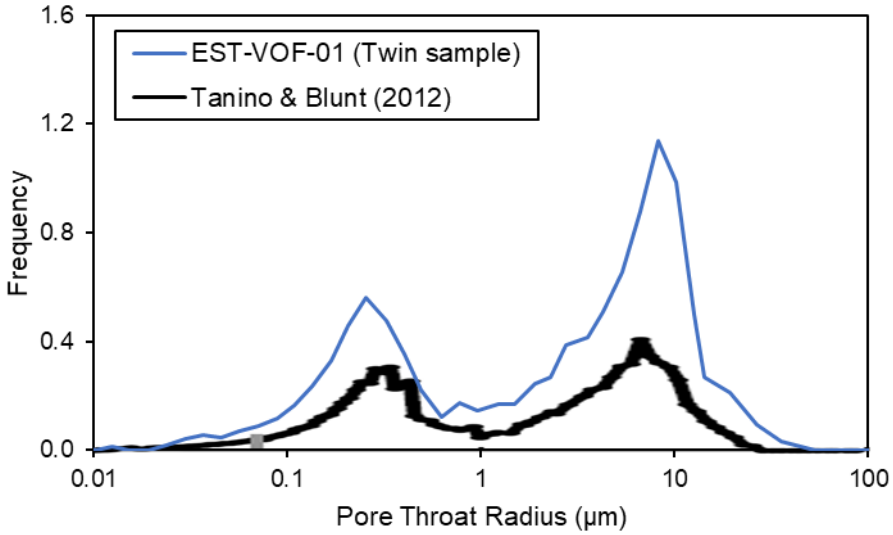

Figure 79 - Comparison of the PTR distribution (MICP) between a twin sample of EST-VOF-01 and the sample used in the study of Tanino & Blunt (2012).

It is important to state that NMR T_2 relaxation time distribution and MICP provide different results: NMR access the pore size distribution and MICP the pore throat radius distribution. Considering this point, it is interesting to observe that, even though the samples present different pore size distribution, their pore throat radius is similar (the difference in the signals amplitude is a result of the non-normalization of the tests).

In this study, we are mainly concentrated in comparing primary drainage techniques ability to reach the target S_{wi} value with a homogeneous saturation profile. As pore entry-capillary pressure is controlled by the pore throat radius, it is reassuring to observe the same behavior for tests performed by two completely independent laboratories.

The target value of S_{wi} for this sample was 20%. For that, we initially used B2 and Marcol^{TM}-52 and defined 5 flowrate steps for this experiment. The choice of a more viscous oil was imposed for increasing capillary number without increasing flowrate, which could damage the sample. Flowrate steps used in this experiment are presented in Table *16*:

Flowrate Step	Flowrate	Capillary Number
Q1	6 cc/h	4.8 10^{-7}
Q2	60 cc/h	4.8 10^{-6}
Q3	180 cc/h	1.4 10^{-5}
Q4	360 cc/h	2.9 10^{-5}
Q5	720 cc/h	5.7 10^{-5}

Table 16-Flowrate steps and capillary number for EST-VOF-01 primary drainage, using Marcol^{TM}-52

The same NMR imaging protocol used for BEN-VOF-01 was used in this case, with continuous T_2 and SE-SPI profile sequences for drainage monitoring. The saturation profiles are presented in Figure 80:

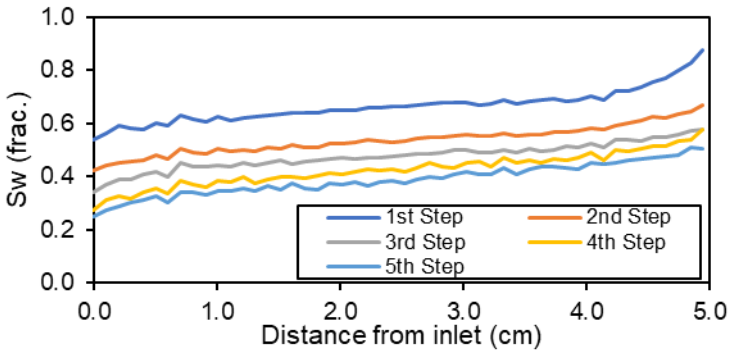

Figure 80 - Water saturation profiles at the end of each flowrate step using Marcol^{TM}-52 (EST-VOF-01).

As expected, regardless the use of high capillary number during flooding, the target was not reached. On an attempt to reach lower values of water saturation, we have miscibly replaced Marcol^{TM}-52 by FINAVESTAN-A-180B, which has a 5-times greater viscosity. We injected at two flowrates, as in Table *17*:

Flowrate Step	Flowrate	Capillary Number
Q6	120 cc/h	5.0 10^{-5}
Q7	180 cc/h	7.5 10^{-5}

Table 17-Flowrate steps and capillary number for EST-VOF-01 primary drainage (FINAVESTAN-A-180B)

During the first additional step (Q6) using a more viscous oil we observed a lower dP than that obtained during step Q5, which was expected as we reduced the capillary number. Nonetheless, when performing the transition to Q7 we reached a higher value of dP by increasing the capillary number to considerably elevated values for this kind

of experiment. The dP curve for the whole experiment is presented in Figure 81, where it is possible to observe the points evoked above.

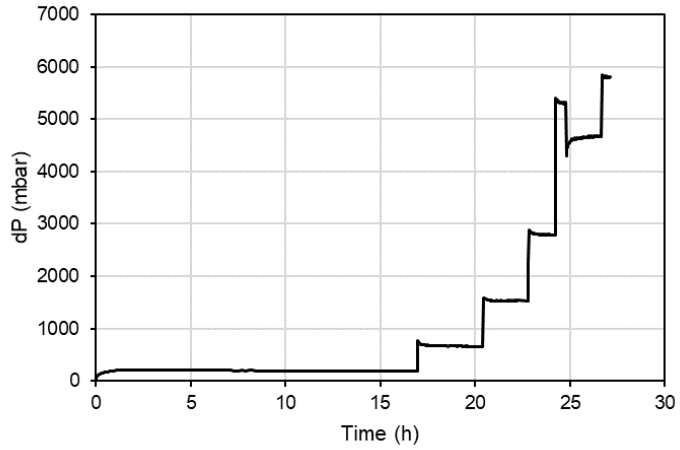

Figure 81 - dP monitoring during EST-VOF-01 primary drainage. It is possible to notice that Q7 was prematurely stopped. The reason is the observation of a coloration in the outlet tubing that could mean fines migration.

Nonetheless, the increase in dP did not result on additional brine production in the burette, even though NMR showed smooth changes in the profiles. The S_w profiles at the end of steps Q5 (last step performed using Marcol^{TM}-52), Q6 and Q7 are presented in Figure 82.

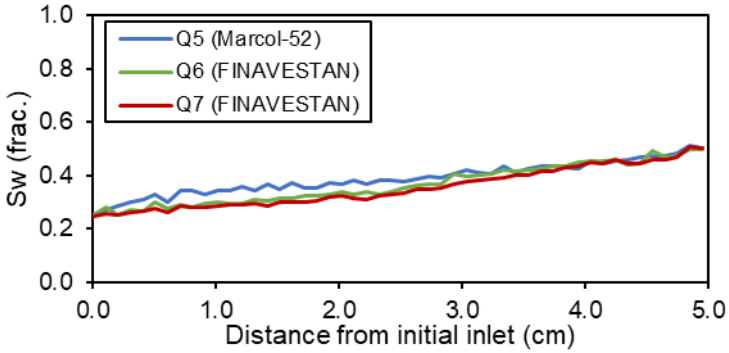

Figure 82 - Final profile performed with Marcol^{TM}-52 and two following flowrate steps using FINAVESTAN-A-180B.

Moreover, the main risk in attaining such high capillary number is fines migration, which may cause clogging and modification of the rock pore matrix. Therefore, as the approach has proven to be useless regarding additional brine production and noticing a different coloration in the outlet tubing, which could represent fines migration, we stopped Q7 sooner than intended.

This experiment represents an example where the target value of S_{wi} could not be reached by the VOF technique, regardless all the efforts of performing the bump rates and using a more viscous oil. Moreover, we face Capillary End-Effects presence at the end of drainage. The main reason for not reaching lower values of S_{wi} by VOF on a dual-porosity sample is that the applied capillary pressure is not homogeneous. Taking the PTR distribution presented in Figure 79 and converting the horizontal axis in pore-entry capillary pressure, we observe that the threshold to access the majority of the smaller porosity is at $P_c = 1bar$. This relation is presented in Figure 83.

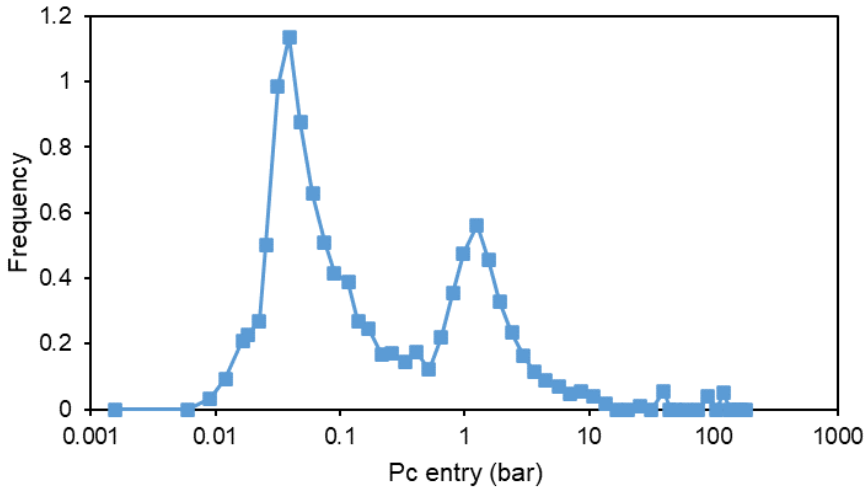

Figure 83 - Pore-entry capillary pressure versus Frequency for the Estaillades limestone samples.

Analyzing the capillary pressure field along EST-VOF-01 axis at the last flowrate step of VOF, we notice that the $P_c = 1\ bar$ threshold was not attained for the totality of the sample, but for only 60% of the length (3 cm from the inlet face). This P_c field is presented in Figure 84 .

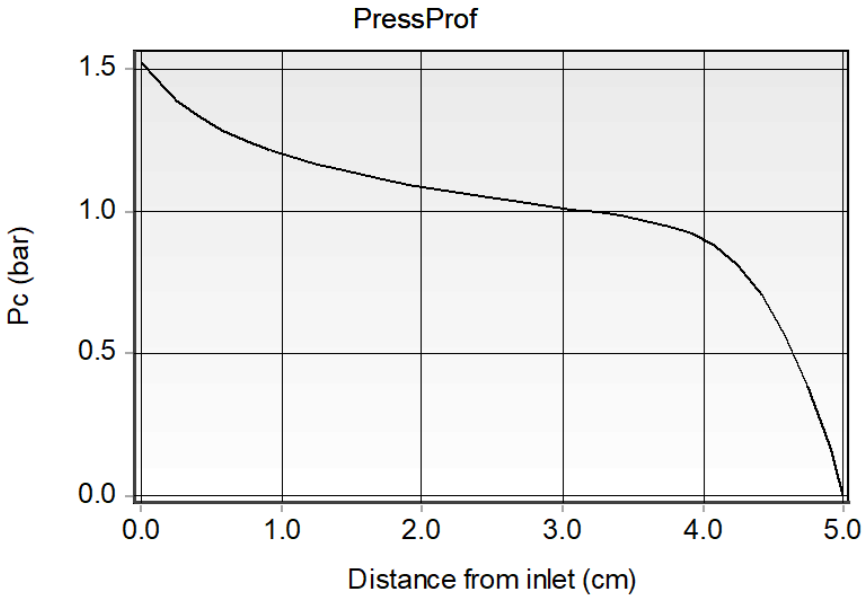

Figure 84 - Capillary pressure field along the sample longitudinal axis during Q7 injection (EST-VOF-01).

For a matter of deeper understanding of the mechanisms that controlled oil flow in this case, we have performed a history match of the pressure drop (dP), brine production (V_w) and S_w profiles for the initial 5 steps to define primary drainage K_r and P_c curves. Input data for K_r was extracted from the work of Ott *et al.* (2015) and the primary drainage P_c was obtained during the EST-PP-01 experiment. We did not allow the capillary pressure curve to be optimized during history-match, as we are sure about this parameter.

The match for dP, V_w and S_w profiles are presented in Figure 85, Figure 86, and Figure 87. The green lines represent the history match and black dots represent experimental data:

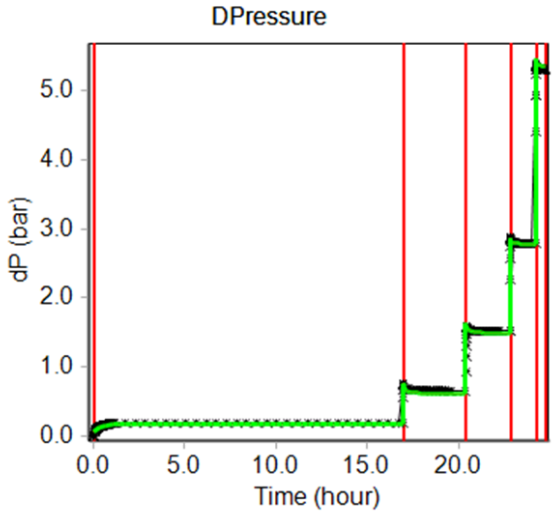

Figure 85 - History-match of the experimental dP points during EST-VOF-01 primary drianage.

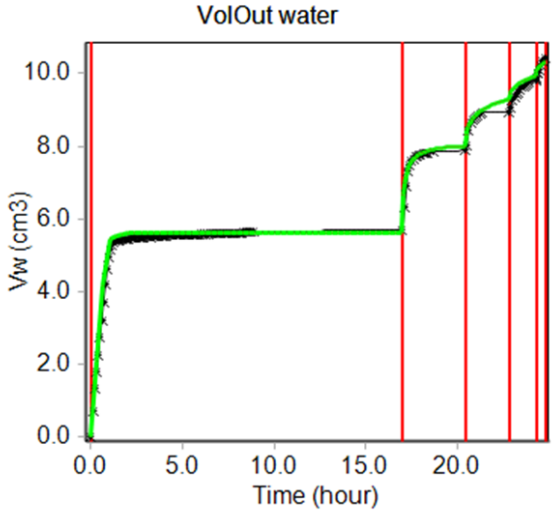

Figure 86 - History-match of the experimental water recovery (V_w) points during EST-VOF-01 primary drainage.

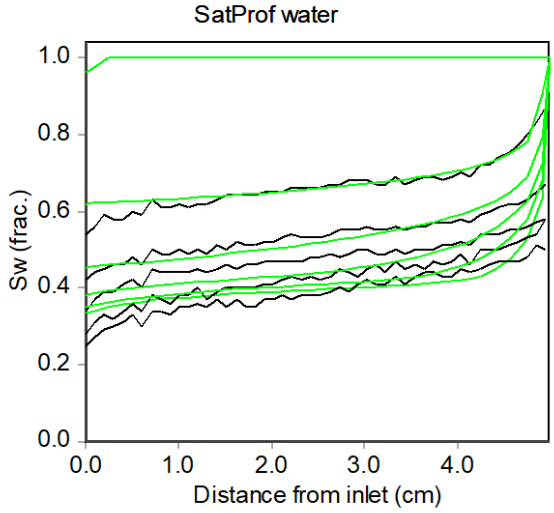

Figure 87 - History-match of the experimental S_w profiles at the end of each flowrate step during EST-VOF-01 primary drainage.

The resulting K_r and P_c curves are presented in Figure 88.

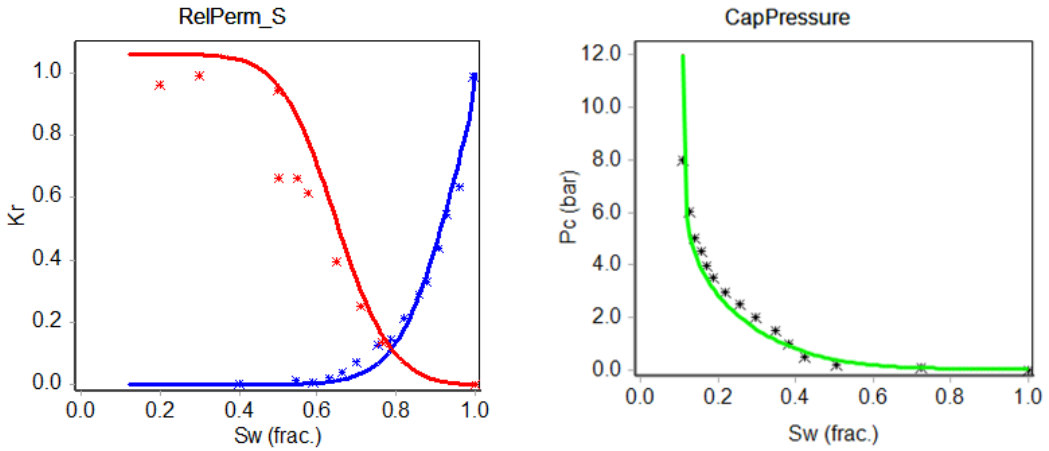

Figure 88 - Primary drainage K_r and P_c curves after history match of dP, V_w and S_w profiles. Marks in the $\boldsymbol{K_r}$ curves figure are originally from the work of (Ott et al.*, 2015). Dark marks in the P_c curve figure are originated from EST-PP-01.*

For the history match of both Estaillades primary drainage K_r and P_c curves, we used the LET model. These parameters are presented in Table *18* ($S_{wi} = 0.12$):

Water parameter	Value	Oil parameter	Value
L	8.8	L	1.8
E	1.5	E	2.5
T	0.6	T	5.0
Parameter	**Value**	**Parameter**	**Value**
$K_{rw,max}$	1.00	S_{wi}	0.12
$K_{ro,max}$	1.06		
L	4.01	P_o	14.754 bar
E	4.26		
T	0.28	P_t	0 bar

Table 18-Set of parameters used for EST-VOF-01 primary drainage K_r and P_c history match.

It is possible to observe the influence of the smaller porosity of the Estaillades sample from its history-matched primary drainage K_r curves. An important increase of K_{ro} at high water saturation values is noticed (values greater than 50 %), when oil invades big pores quickly desaturating this fraction of the porosity. Then, we notice that K_{ro} sharply stops its increase at S_w values around 40%. This indicates that the smaller porosity, which is still saturated with water, does not contribute to the oil flow. Moreover, due to the poor pore connectivity of this rock, brine placed in the smaller porosity is not flooded when a viscous-controlled method is used, which is the case of the Viscous Oil Flood. Further in this study, deeper attention will be dedicated to methods capable of removing water from these pores.

4.1.2. Obtaining a homogeneous Swi profile

In the last section we showed one case where the correct target value of S_{wi} was reached, nonetheless the presence of CEE would affect the following steps of the experimental workflow. Moreover, we presented a second case were S_{wi} targets were not attained due to a dual-porosity condition of the pore matrix. In this section we will address the challenge of setting a homogeneous S_{wi} profile during primary drainage and the potential impacts of choosing one approach over another.

BEN-CEN-01

This oil/water centrifuge test using a Bentheimer sandstone aimed to establish initial water saturation targeting a capillary pressure value from equation (58). Moreover, we tested the standard in the industry for eliminating CEE, that consists of swapping the sample orientation in the centrifuge bucket and spinning at the last rotational speed until production stabilization.

Target capillary pressure value is equal to $P_c = 200\,mbar$. We used B1 and Isopar-L™ as couple of fluids during this test. Three rotational speed steps were used during this test, and they are presented in Table *19*:

Rotational speed	Inlet P_c (o/w)	Bond Number
500 rpm	107 mbar	1.2 10^{-5}
600 rpm	154 mbar	1.7 10^{-5}
700 rpm	210 mbar	2.3 10^{-5}

Table 19-Rotational speed steps, inlet P_c and Bond Number for BEN-CEN-01 drainage by centrifugation.

We monitored brine production during centrifugation from pictures, taken by a high-resolution camera, of the burette connected to the centrifuge bucket. Brine production *versus* time is presented in Figure 89.

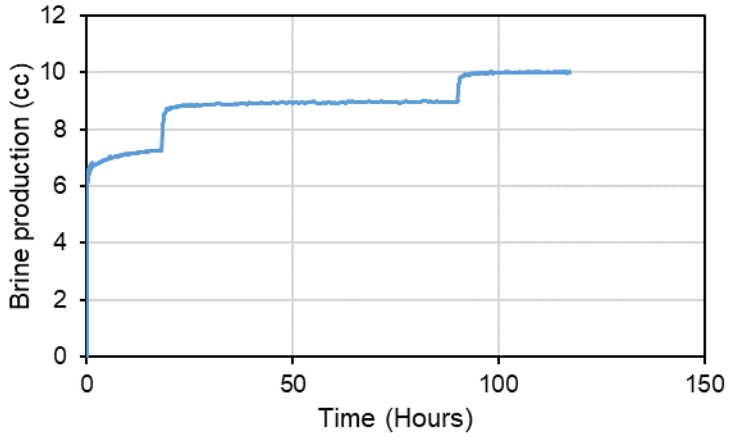

Figure 89 - Brine production during BEN-CEN-01 centrifugation.

One can notice the high permeability and low pore entry-pressure of the Bentheimer sandstone as it rapidly produces around 6 cc at extremely low speed.

At the end of the last step of centrifugation, we unloaded the sample from the centrifuge bucket to perform a T_2 and SE-SPI measurements in the NMR. T_2

Relaxation Time are useful for controlling the sample saturation and SE-SPI profile (Figure 90) presents the extent of CEE at this stage of the experiment.

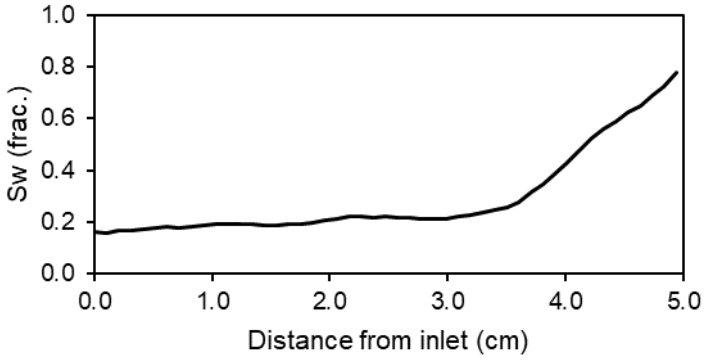

Figure 90 - Water saturation profile at the end of centrifugation (BEN-CEN-01).

The sample is loaded back again into the centrifuge bucket, but at an opposite orientation, in order to apply the capillary pressure in the other direction, homogenizing the profile. The current standard is to set the same rotational speed as the last step and wait for brine production equilibrium. We noticed brine production during this period, as it may be seen in Figure 91.

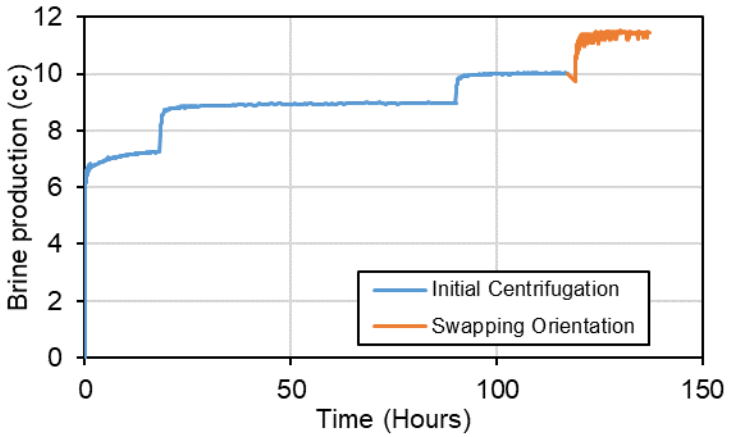

Figure 91 - Brine production during initial centrifugation (blue line) and after swapping the orientation of the sample inside the centrifugation bucket (orange line).

After performing another SE-SPI profile measurement by NMR, it is possible to notice that we did not homogenize the S_w profile but that we displaced CEE in the other direction of the sample (Figure 92). This experiment is a clear example that controlling CEE elimination in the centrifuge is difficult and methods are still uncertain. Moreover, T_2 test also showed brine production after swapping the plug orientation, as we decreased the average water saturation.

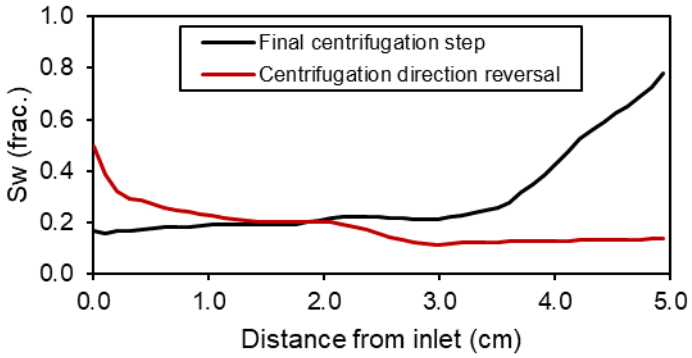

Figure 92 - Water saturation profiles before and after swapping sample orientation inside the centrifuge bucket.

- $\overline{S_{w_{700\ \mathrm{RPM}}}} = 29.4\%$
- $\overline{S_{w_{Swapped}}} = 18.4\%$

EST-CEN-01

In order to test an alternative method for homogenizing S_w profiles at the end of centrifugation, we performed a gas/water centrifugation with an Estaillades plug sample initially saturated with B3. Rotational speed steps for this experiment are presented in Table *20*, as well as the inlet gas P_c and the converted oil P_c (considering Marcol™-52 characteristics):

Rotational speed	Inlet P_c (g/w)	Inlet P_c (o/w)	Bond Number
500 rpm	0.22 bar	0.13 bar	$7.5\ 10^{-7}$
750 rpm	0.50 bar	0.29 bar	$1.7\ 10^{-6}$
1000 rpm	0.89 bar	0.52 bar	$3.0\ 10^{-6}$
1500 rpm	2.01 bar	1.17 bar	$6.7\ 10^{-6}$
2000 rpm	3.58 bar	2.09 bar	$1.2\ 10^{-5}$
3000 rpm	8.04 bar	4.69 bar	$2.7\ 10^{-5}$

Table 20-Rotational speed steps, inlet P_c for both g/w and o/w couples, and Bond Number for EST-CEN-01 drainage by centrifugation.

Between each step of centrifugation, we performed an SE-SPI profile imaging by NMR in order to observe the extent of CEE at each step. We derived the water saturation by performing the ratio of each profile and the initially brine-saturated profile (which represents $S_w = 100\%$). The S_w profiles during the experiments are presented in Figure 93:

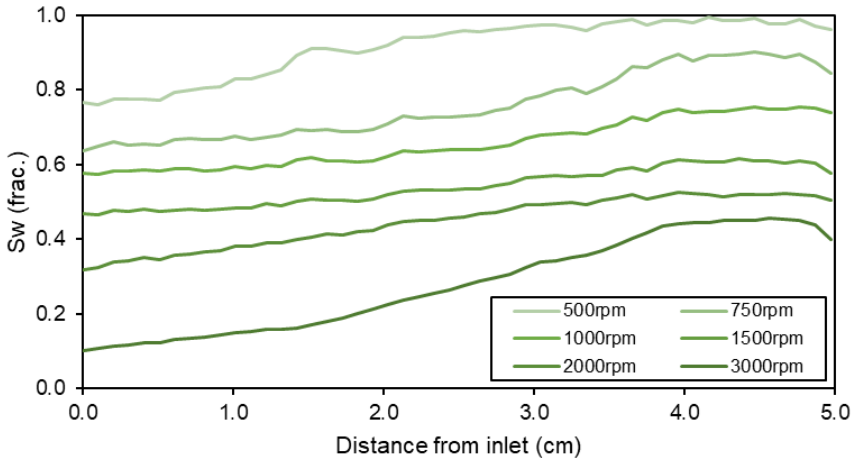

Figure 93 - S_w profiles advancing during EST-CEN-01 primary drainage by centrifugation.

In the same way as in the case of BEN-CEN-01, we swapped the orientation of the plug inside the centrifuge bucket for S_w profile homogenization; Nonetheless, in this case we used a different approach: we used a reduced rotational speed (1000 rpm) to impose reduced capillary pressure for better controlling the profiles, and reduced duration (1 hour) to prevent the re-generation of CEE. At the end of this orientation swap process, we have noticed no additional brine production neither in the burette nor by the T_2 test. The resulting profile is presented in Figure 94 together with the S_w profile after the last step of centrifugation.

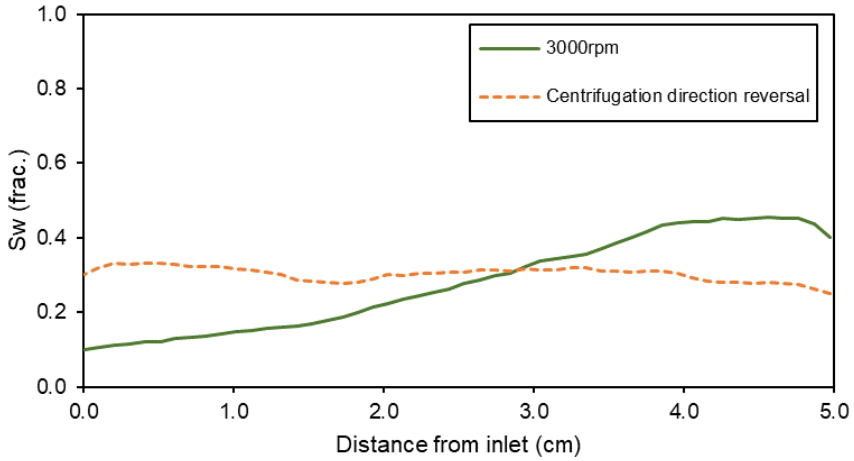

Figure 94 - S_w profiles before and after swapping the plug orientation inside the centrifuge bucket.

- $\overline{S_{w_{3000\ \mathrm{RPM}}}} = 27.9\%$
- $\overline{S_{w_{\mathrm{Swapped}}}} = 28.3\%$

We observe an improvement regarding the control of CEE in this case compared to BEN-CEN-01, which may be explained by the different protocol used in this case. However, we notice that the profile homogenization has the consequence of imposing an important imbibition in the sample, which is not representative of the first migration of hydrocarbons in the reservoir.

BEN-VOF-01 (Continuation)

At the end of the section where we presented the experimental results for BEN-VOF-01 we have indicated the solution for dealing with CEE during VOF. The most usual solution for this is reversing injection direction and keeping the same flowrate as in the last step prior to swapping.

We have performed the reversal flow for homogenizing BEN-VOF-01 saturation profile. T_2 relaxation experiment and water saturation profiles from SE-SPI sequence are presented in Figure 95 and Figure 96:

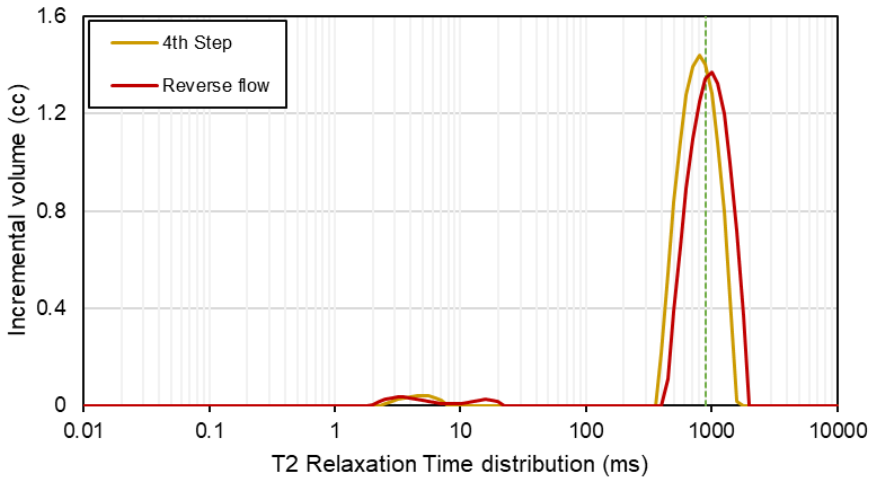

Figure 95 - T_2 Relaxation Time distribution for BEN-VOF-01 at 4th Step of VOF and after reverse flow. Fluids saturating the sample are Isopar-L™ and B1.

- $S_{w_{4^{th}\ step}} = 22.5\ \%$
- $\overline{S_{w_{Reverse\ flow}}} = 24.4\ \%$

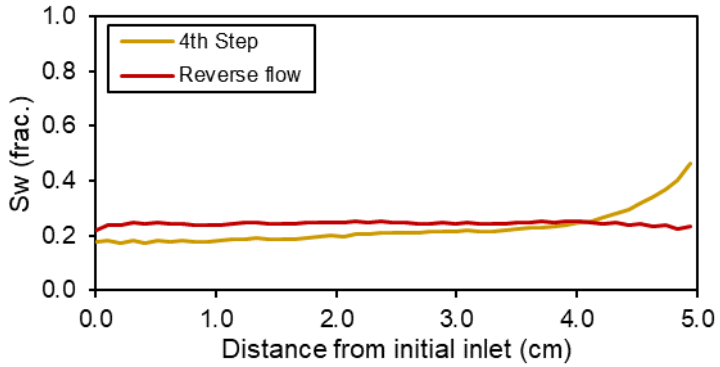

Figure 96 - Water saturation profiles after flow reversal at the end of VOF (BEN-VOF-01).

At a first look, this approach may seem to be a precise solution for dealing with CEE, as no additional brine production was observed when performing the swap, neither in the burette nor by NMR analysis, and SE-SPI profiles present a satisfactory profile homogeneity.

However, if we take a more careful look to both curves close to the first inlet face, we may observe a gap between them, the profile after reversal flow is beneath the mono-sense injection profile. This is coherent with the no additional production observed, nonetheless it indicates that brine initially concentrated close to the outlet

due to CEE was then imbibed during flow reversal, no longer in a drainage invading process, but as in a waterflooding.

Considering that this experiment was performed in a water-wet condition, as no wettability altering fluid is involved in the cycle until this point, the mobile brine will trap an important amount of oil during flow reversal. Moreover, as cluster sizes tend to be larger close to the outlet during initial flood due to lower capillary pressure in this region, when reversal flow is performed, oil will tend to be trapped in larger clusters, generating a heterogeneous cluster distribution in the sample which may lead to heterogeneous wettability. These results were presented by Nono *et al.* (2022), and the authors have compared the cluster formation and connectivity during primary drainage between the Viscous Oil Flood and the Porous Plate methods, as we may observe in Figure 97.

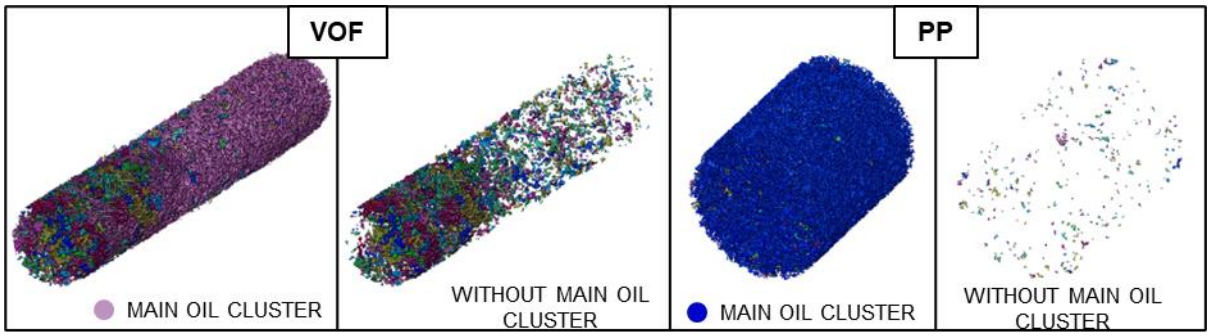

Figure 97 - Comparison between the Viscous Oil Flood (OF in the figure) and the Porous Plate (PP) methods during primary drainage. There are two representations for each technique: the one in the left-hand side includes the main percolating cluster (in magenta for OF and in blue for the PP) and the images on the right-hand side had the main percolation cluster removed.

EST-VOF-01 (Continuation)

The same protocol of saturation profiles homogenization used for BEN-VOF-01 was applied to EST-VOF-01. A reverse flow was performed following the same flowrate as in the last step (Q7). No further production was observed, and Figure 98 presents the saturation profiles before and after flow direction reversal.

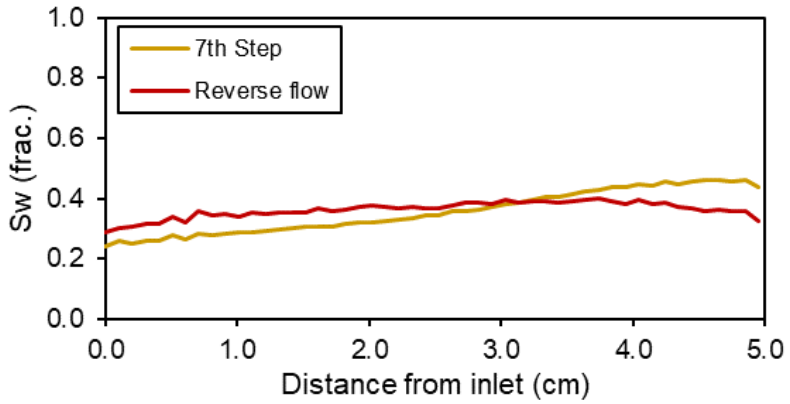

Figure 98 - Comparison between last step of viscous flooding and after injection sense reversal (in green).

- $\overline{S_{w_{7^{th}\ step}}} = 35.6\ \%$
- $\overline{S_{w_{Reverse\ flow}}} = 36.3\ \%$

The approach of reversing flow is indeed effective for eliminating Capillary End-Effects. However, we observe the same imbibition phenomenon as in the Bentheimer case. Considered as an experimental artifact, this effect is not representative of the reservoir migration phase. Therefore, its effects on the Restored State method must be studied deeper.

The proof of concept of the Hybrid Drainage Technique

The development of the Hybrid Drainage Technique answers to the following challenges:

- Produce homogeneous saturation profile
- Reach a target value of S_{wi}
- Reduce the experimental time compared to the Porous Plate Method.

The results comprehending its proof of concept and its different applications are presented in the following sections.

a. Bentheimer sandstone

Four Bentheimer sandstone samples were used for the proof of concept of the Hybrid Drainage Technique. For this purpose, we targeted two levels of capillary pressure by both Porous Plate and HDT, which represents four different experiments using the same fluids (B1 and Marcol^{TM}-52). These tests are compared two by two regarding the S_{wi} value reached at the end of drainage and the duration for each experiment. Moreover, we measure the S_{wi} profiles at the end of HDT for validating the technique regarding the achievement of a homogeneous profile. For quantification of the homogenization in the transition between Steps 1 and 2 during HDT, we have established two metrics, beyond the average water saturation ($\overline{S_w}$):

- *Standard-deviation of the water saturation profile points ($\sigma\ (S_w)$)*

  For this metric, we calculated the standard deviation of the multiple S_w points in the profiles from the average S_w. We used the classical definition of standard-deviation:

$$\sigma(S_w) = \sqrt{\frac{1}{N-1}\sum_{i=1}^{N}\left(S_{w\,i} - \overline{S_w}\right)^2} \tag{99}$$

where N is the amount of S_w points composing the S_w profile, S_{w_i} is the water saturation value at position "i", and $\overline{S_w}$ is the average water saturation.

- *Maximum – Minimum water saturation points in the S_w profile, called $Max - min(S_w)$*

  In this case, we performed the difference between the maximum and the minimum S_w values in the water saturation profile.

  The applied capillary pressure values are presented in Table *21*:

Sample name	Applied P_c
BEN-PP-01	80 mbar
BEN-PP-02	110 mbar
BEN-HDT-01	80 mbar
BEN-HDT-02	110 mbar

Table 21-Applied P_c for HDT and PP experiments on Bentheimer sandstone samples

BEN-PP-01 and BEN-PP-02

Both samples were saturated with B1, and primary drainage was performed by injecting Marcol™-52 at a single pressure step. Production monitoring was performed as described in the corresponding methodology sub-section (Porous Plate), with a graduated burette connected to a pressure transducer that converts the pressure applied by the increasing brine column into height, then into produced volume.

We present in Figure 99 the brine production *versus* experimental time for both samples:

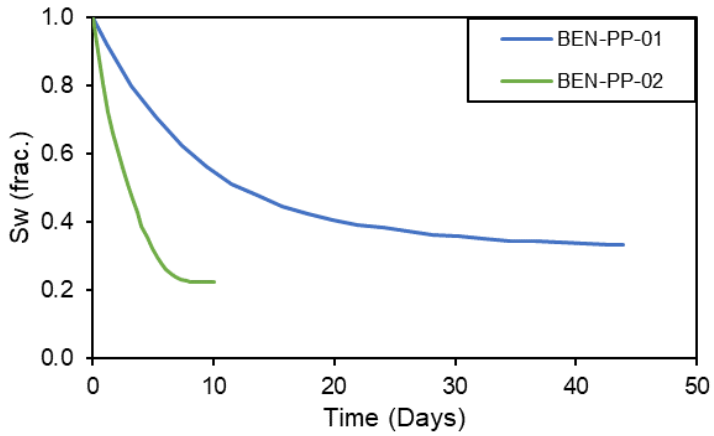

Figure 99 - Brine production versus time for BEN-PP-01 and BEN-PP-02 primary drainage by Porous Plate.

As we targeted two different S_{wi} values, experimental duration is different between BEN-PP-01 and BEN-PP-02. It is interesting to notice that equilibration delay is longer for the higher S_{wi} value than for the lower S_{wi} value. Even though less brine is drained in the case of BEN-PP-01, applying a lower capillary pressure makes the experiment longer than draining at higher capillary pressure, which is the case of BEN-PP-02.

BEN-HDT-01

This experiment represents the test of HDT for a high S_{wi} target, thus applying a lower capillary pressure. In the same way as for the two Porous Plate tests, this experiment was conducted using brine B1 and Marcol™-52.

During Step 1, we controlled inlet pressure at $Pc = 80\,mbar$ and we monitored saturation profiles advancing by performing sequential SE-SPI NMR imaging. This result is presented in Figure 100:

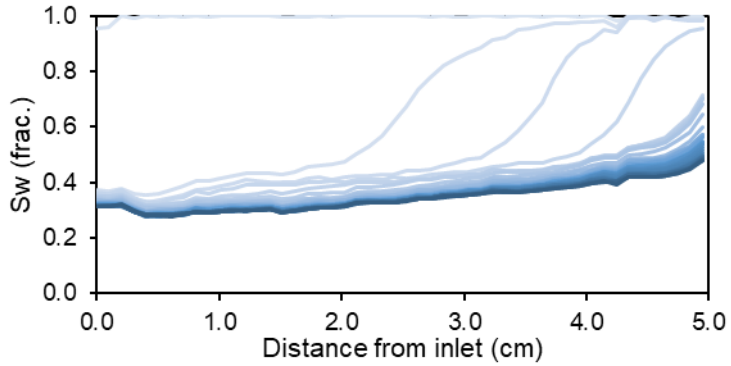

Figure 100 - Saturation profiles advancing during Step 1 of BEN-HDT-01 ($P_c = 80\ mbar$).

At the end of Step 1, it is possible to notice the presence of CEE. This result is expected because the regime is viscous, which leads to a pressure drop between the inlet and the outlet.

The metrics at Phase 1 for BEN-HDT-01 are:

- $\overline{S_w} = 34\ \%$
- $\sigma\ (S_w) = 4\ \%$
- $Max - min\ (S_w) = 20\ \%$

After no further production is observed, we performed the transition to Step 2, closing Outlet 1 and opening Outlet 2 of the Multi-Imagery Cell at constant inlet pressure. During this step, it is possible to notice a more important water production at the last fraction of the sample, as capillary pressure becomes homogeneous along the longitudinal axis and CEE are eliminated. This process is observed in Figure 101.

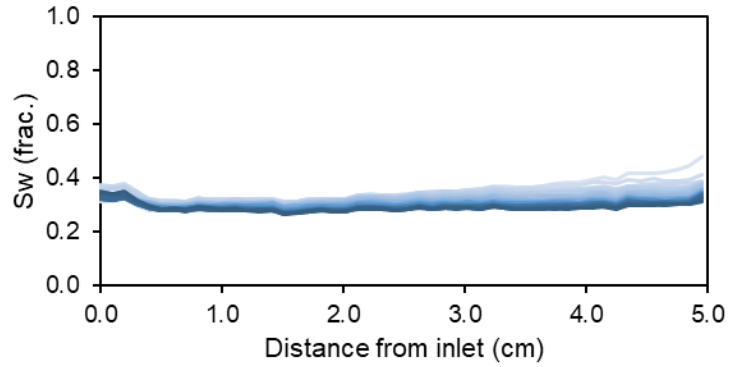

Figure 101 - Elimination of capillary end-effects during Step 2 of BEN-HDT-01 ($P_c = 80\ mbar$).

The metrics at the end of the Hybrid Drainage Technique for BEN-HDT-01 are representative of the Capillary End-Effects elimination:

- $\overline{S_w} = 29\ \%$
- $\sigma\ (S_w) = 1\ \%$
- $Max - min\ (S_w) = 8\%$

BEN-HDT-02

In this case, we have tested the low S_{wi} target case, applying an inlet pressure of $Pc = 110\ mbar$ during the experiment. We have performed the same SE-SPI

imaging protocol, and we are able to observe the saturation profiles advancing on Figure 102:

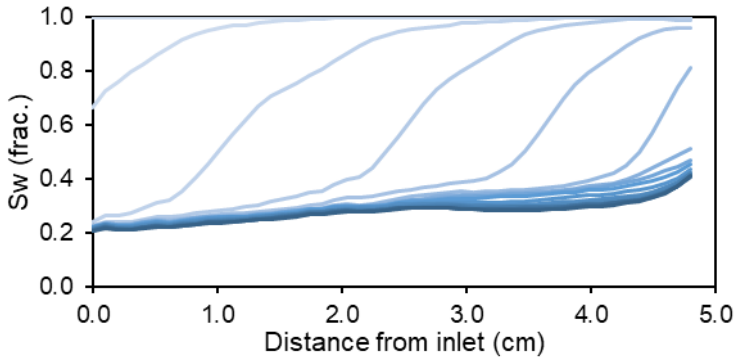

Figure 102 – Saturation profiles advancing during Step 1 of BEN-HDT-02 ($P_c = 110\ mbar$).

It is possible to notice an oil shock front invading the sample quickly desaturating it to a value close to S_{wi} for the inlet fraction of the sample. At this point, we have:

- $\overline{S_w} = 27\ \%$
- $\sigma\ (S_w) = 3\ \%$
- $Max - min\ \ (S_w) = 20\ \%$

After transition to Phase 2, it is possible to observe, in Figure 103, the successive elimination of the capillary foot close to the outlet face of the sample.

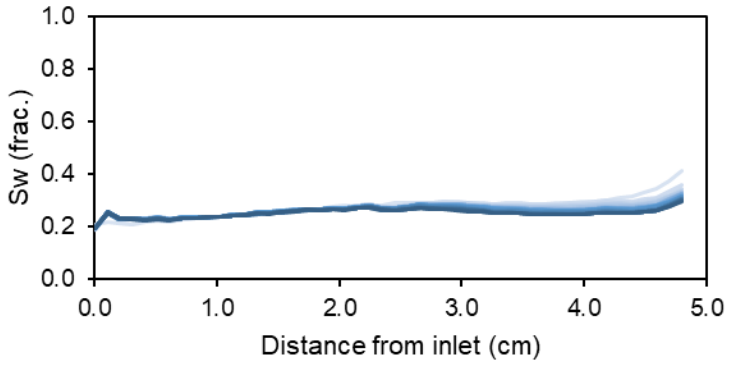

Figure 103 – Elimination of CEE during Step 2 of BEN-HDT-02 ($P_c = 110\ mbar$).

In Figure 103, it is still possible to observe a small CEE in the last half cm of the sample. As fully saturated NMR imaging (used for initial characterization of the samples) shows no abnormal saturation behavior in this zone we consider that this effect does not represent a heterogeneity issue. Even though this test has respected the production cessation criteria, a longer Step 2 would probably have homogenized the saturation profile, mitigating CEE.

Therefore, at the end of HDT for BEN-HD-LS, we have the following metrics:

- $\overline{S_w} = 25\ \%$
- $\sigma\ (S_w) = 2\ \%$
- $Max - min\ \ (S_w) = 13\ \%$

During Step 1 of both experiments, it is possible to notice the shock front on the saturation profile as oil enters the sample at high velocity, quickly decreasing water saturation to a value close to S_{wi}.

b. Richemont limestone

The four Richemont samples were also used for the proof of concept of the Hybrid Drainage Technique. We have chosen this specific rock as a test for its reduced permeability, as we wanted to show that the technique is suitable for a large range of values. We followed the same protocol and used the same couple of fluids (B1 and Marcol™-52) as in the proof of concept with the Bentheimer sandstone samples, performing both PP and HDT at the same levels of capillary pressure and observing the duration of each experiment until stabilization.

The experiments are divided as presented in Table *22*:

Sample name	Applied P_c
RCH-PP-01	3.875 bar
RCH-PP-02	5.0 bar
RCH-HDT-01	3.875 bar
RCH-HDT-02	5.0 bar

Table 22-Applied P_c for HDT and PP experiments on Richemont limestone samples

RCH-PP-01 and RCH-PP-02

These experiments were performed following the same protocol used for BEN-PP-01 and BEN-PP-02 and the same couple of fluids were used (B1 and Marcol™-52). Applied capillary pressures were adapted for the lower permeability of the Richemont limestone compared to the Bentheimer sandstone. Brine production *versus* experimental time for both experiments are presented in Figure 104:

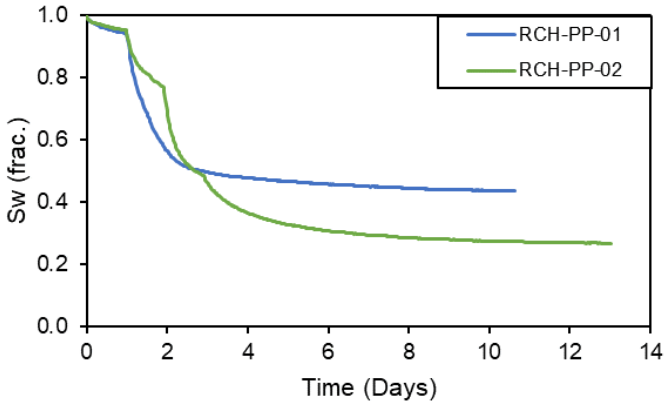

Figure 104 - Brine production versus experimental time for samples RCH-PP-01 and RCH-PP-02.

In contrast to what was observed for BEN-PP-01 and BEN-PP-02, the experimental duration, in this case, depends mostly on the amount of brine drained and less in the applied capillary pressure. This behavior may be explained by the higher capillary pressures applied in this case compared to the Bentheimer case.

RCH-HDT-01

This sample followed a particular approach compared to RCH-HDT-02, BEN-HDT-01 and BEN-HDT-02, as we have performed Step 1 of HDT at constant flowrate, not at constant inlet pressure. This option was adopted in this particular case because we wanted to perform a history match of the primary drainage in order to obtain $\boldsymbol{K_r}$ and $\boldsymbol{P_c}$ curves by inverse analysis of differential pressure drop and water production.

Applying a constant flowrate of $Q = 3\frac{cc}{h}$, we monitored the evolution of the saturation profile by NMR. These results are presented in Figure 105:

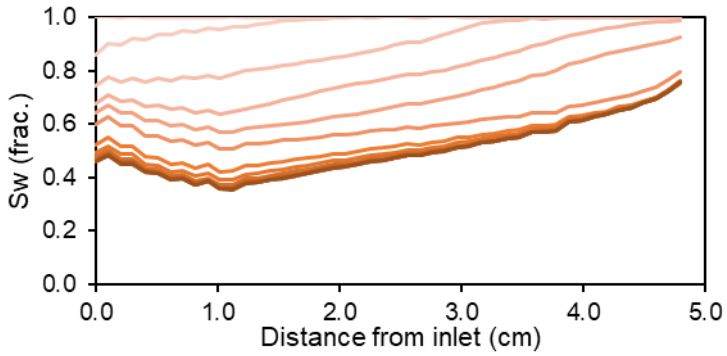

Figure 105 - Water saturation profiles advancing during Step 1 of HDT (RCH-HDT-01 at Q = 3 cc/h).

The metrics for the final saturation profile of RCH-HDT-01 are as follows:

- $S_w = 50\ \%$
- $\sigma\ (S_w) = 9\ \%$
- $Max - min\ \ (S_w) = 40\ \%$

When water production cease and we observed no further motion in the profiles, we moved on to the Step 2, applying a constant pressure of $Pc\ = \ 3.875\ bar$, which represented the equilibrium dP measured by the pressure gauges at the end of Step 1, closed Outlet 1 and opened Outlet 2.

After the transition to Phase 2, it was possible to observe a clear equilibration of the saturation profiles, with Capillary End-Effects elimination, as presented in Figure 106. However, an effect on the profile observed close to the inlet was not corrected after the transition.

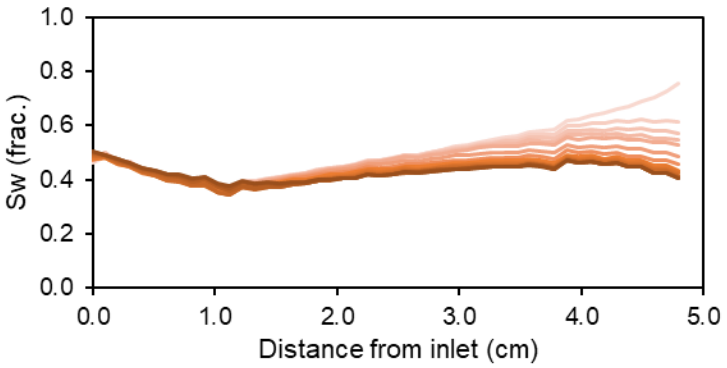

Figure 106 - Elimination of capillary foot during Step 2 of RCH-HDT-01 at $P_c = 3.875\ bar$.

The homogenization is also clearly described by the metrics used for measuring profile homogeneity:

- $\overline{S_w} = 43\ \%$
- $\sigma\ (S_w) = 2\ \%$
- $Max - min\ \ (S_w) = 13\ \%$

A better performance could be expected on the Max – Min and standard deviation parameters at the end of Phase 2 if the profile was not impacted by an effect in the S_w at the inlet of the sample.

RCH-HDT-02

The second Richemont sample submitted to the proof of concept of HDT had a lower S_{wi} target, therefore we used a constant inlet pressure of $Pc\ = 5\ bar$ for the whole primary drainage experiment. Saturation profiles advancing during Step 1(Outlet 1 opened and Outlet 2 closed) are presented in Figure 107.

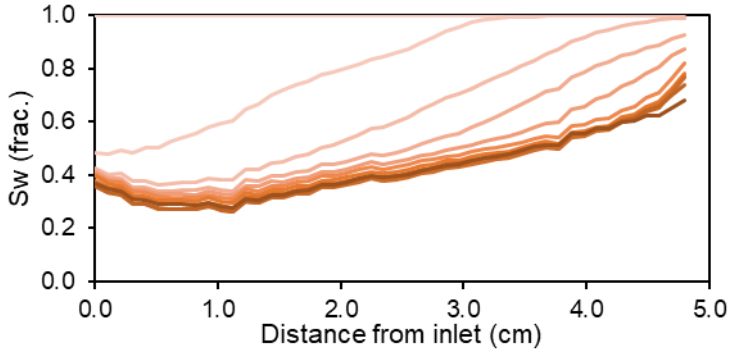

Figure 107 - Water saturation profiles advancing during Step 1 of HDT for RCH-HDT-02 ($P_c = 5\ bar$).

At the end of Step 1 for RCH-HDT-02, we obtained:

- $\overline{S_w} = 42\ \%$
- $\sigma\ (S_w) = 10\ \%$
- $Max - min\ \ (S_w) = 41\ \%$

After performing the transition to Step 2, the homogenization of the saturation profile can be observed in Figure 108.

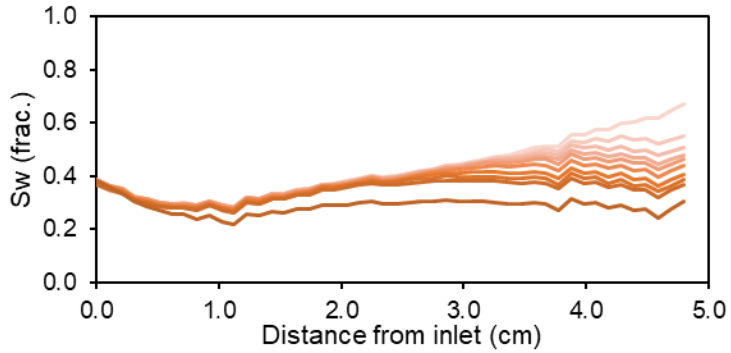

Figure 108 - Profiles homogenization during Step 2 of HDT for RCH-HDT-02 ($P_c = 5\ bar$).

At the end of primary drainage, we have observed the following metrics regarding profiles homogeneity:

- $\overline{S_w} = 29\ \%$
- $\sigma\ (S_w) = 2\ \%$
- $Max - min\ \ (S_w) = 16\ \%$

Nonetheless, the effect in the saturation profile close to the inlet, already observed for the RCH-HDT-01 sample, is also present in this case. This effect is possibly due to the inlet diffuser format. The diffuser used for these experiments was a classical “bull’s-eye”, which may concentrate flow streamlines, bypassing a portion of the inlet face of the sample, not properly desaturating it. The problem involving diffusers used on coreflooding experimental cells have already been discussed in some papers (Nono *et al.*, 2019). We used a new dual-spiral diffuser for EST-HDT-02 (presented further in the document), which was useful for the elimination of this effect.

Furthermore, we have measured the experimental duration for the 8 experiments (4 PP and 4 HDT) used in the proof of concept of HDT, and a comparison between them is presented in Figure 109 and Figure 110. In these figures, we show the experimental time needed for reaching the target S_{wi} using both techniques.

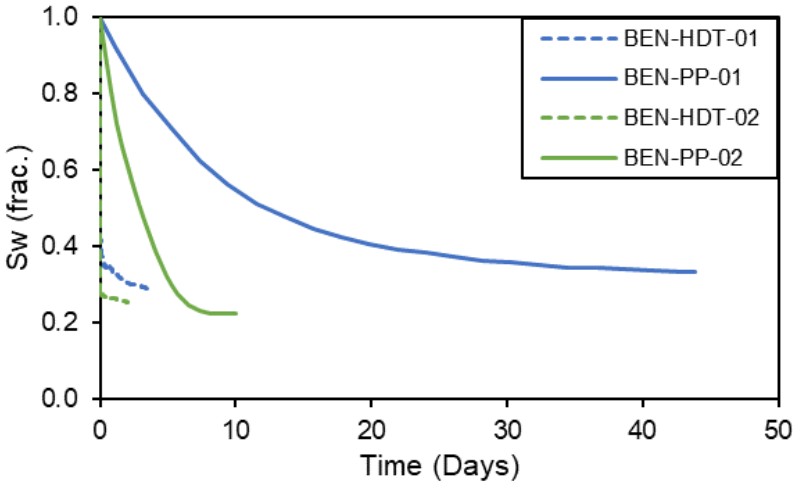

Figure 109 - Experimental duration comparison for Bentheimer samples.

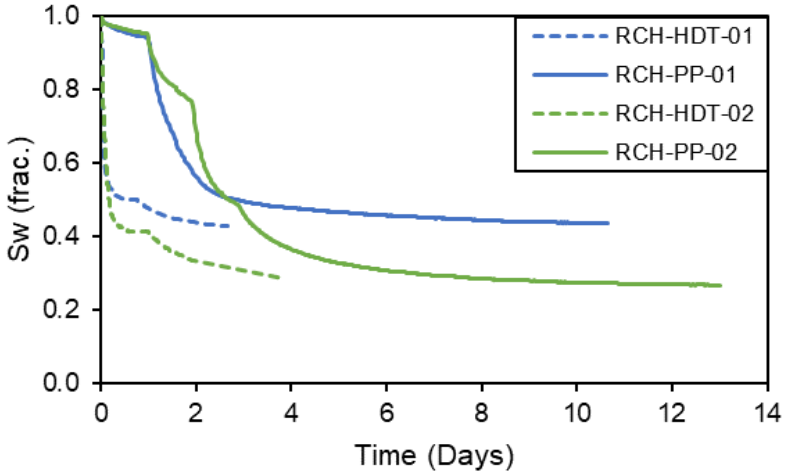

Figure 110 - Experimental duration comparison for Richemont samples.

c. The solution for bimodal cases

Authors that have previously worked with Estaillades limestone have reached an S_{wi} lower than we have obtained for EST-VOF-01. For that, they have used the Porous Plate, which is a capillary-controlled method that enables oil to invade smaller pores by the application of higher capillary pressure. We performed a Porous Plate primary drainage to confirm the possibility to reach our target S_{wi} of 20 % using this method.

Notwithstanding, as HDT is also a capillary-controlled method that allows targeting an S_{wi} value from the P_c *versus* S_w curve, it should be able to deal with the dual-porosity issue, attaining the correct initial water saturation value, providing a homogeneous saturation profile in reduced experimental time compared to the Porous Plate.

EST-PP-01

In order to define a P_c *versus* S_w relation useful for our numerical simulations and to confirm that we are able to reach low values of S_{wi} with a capillary-controlled technique, we performed a primary drainage with the Porous Plate method on an Estaillades sample, together with resistivity measurements (PCRI). We selected 14 pressure steps for a precise definition of the first drainage P_c *versus* S_w curve, that are presented in Table *23*:

# Pressure steps	Applied P_c
1	0.1 bar
2	0.2 bar
3	0.5 bar
4	1.0 bar
5	1.5 bar
6	2.0 bar
7	2.5 bar
8	3.0 bar
9	3.5 bar
10	4.0 bar
11	4.5 bar
12	5.0 bar
13	6.0 bar
14	8.0 bar

Table 23-Pressure steps for EST-PP-01 Porous Plate primary drainage

For this experiment we used B2 and Marcol™-52 as couple of fluids. The P_c *versus* S_w curve is presented in Figure 111:

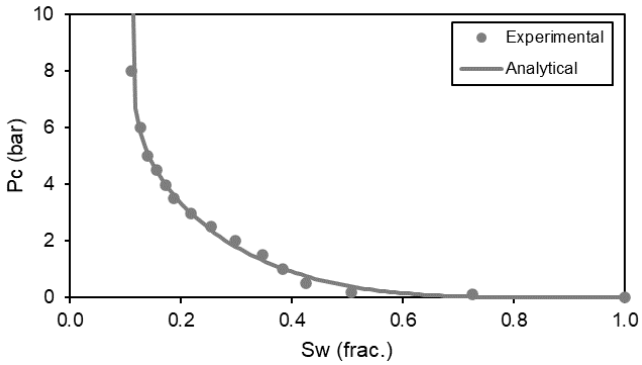

Figure 111 - P_c versus S_w curve of EST-PP-01.

The dual-porosity nature of this sample may be observed in the P_c *versus* S_w curve. We may notice that for water saturation values around 30%, the primary drainage P_c curve assumes a non-smooth behavior, representing the transition from bigger to smaller pores. This agrees with what was observed during the primary drainage step of EST-VOF-01.

Another interesting feature of this experiment is the electrical response of the sample to PP primary drainage. The plot of the resistivity index (RI) *versus* S_w in a log-log scale presents a non-linear shape, and trend shifts. In other conditions, this deviation may be associated to wettability, however as in this case we are dealing with an outcrop sample, this behavior may only be related to the dual-porosity characteristics of the sample. This result is presented in Figure 112:

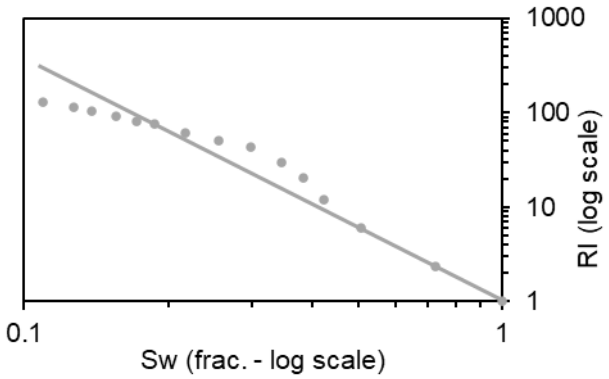

Figure 112 - RI versus S_w for EST-PP-01.

EST-HDT-01

This experiment was designed to deal with the difficulty in reaching a target S_{wi} below 35% in experiments performed on Estaillades samples (bi-modal porosity). Obtaining values lower than 35% did not represent a concern when performing primary drainage using the Porous Plate technique. Therefore, the Hybrid Drainage Technique arises as a solution for dealing with this problem on reduced experimental duration compared to PP.

This experiment was conducted in the same conditions as EST-VOF-01, however, as we wanted to prove that HDT would be effective in desaturating brine present in smaller pores during primary drainage, we have used a hydrogen-based brine (B3) instead of a deuterium-based brine. By adopting this approach, both the water and the oil phases generate NMR T_2 relaxation signals. This way, we are able to monitor the behavior of both fluids during the experimental cycle. Considering that

HDT is effective in desaturating brine present in the small pores during Step 2 (slow, capillary-controlled flow), we must be able to notice a modification in both NMR T_2 relaxation signals.

A T_2 relaxation time distribution measurement was performed on the brine-saturated sample. The result, presented in Figure 113, shows unambiguously the dual-porosity characteristic of this sample, with one T_2 peak at around 70 ms representing the smaller pores, and another T_2 peak at around 794 ms representing the bigger pores.

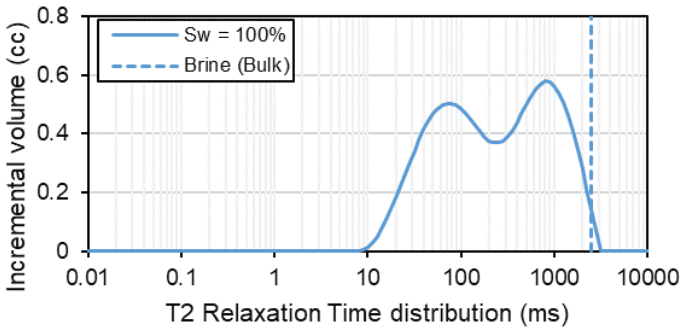

Figure 113 - T_2 Relaxation Time distribution of EST-HDT-01 @ $S_w = 100\%$ using B3.

We performed Step 1 of HDT following two injection flowrate steps using Marcol™-52. We monitored saturation change using a graduated burette connected to the outlet tubing of our sample. As both the oil and the brine phases produce NMR signal, it is not possible to perform a saturation profile monitoring during drainage by SE-SPI sequences. Moreover, a separation of the T_2 relaxation times from oil and brine is not possible, as they are superimposed in the T_2 spectrum. This situation, presented in Figure 114, occurs due to the viscosity of Marcol™-52 ($\mu_{M-52} = 12\ cP$), which results in a T_2 bulk relaxation time of approximately 200 ms.

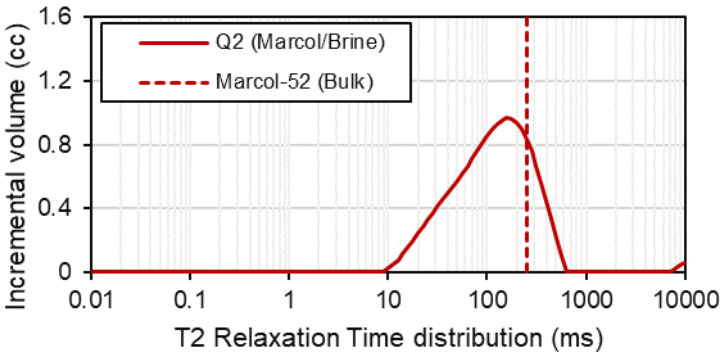

Figure 114 - T_2 Relaxation Time distribution of EST-HDT-01 at the end of Step 1. In this case, we have Marcol™-52 and B3 as the saturating fluids.

In order to distinguish the different fluids in the T_2 spectrum, we have miscibly replaced Marcol™-52 by toluene. As toluene has a much lower viscosity ($\mu_{Tol} = 0.56\ cP$), its T_2 bulk relaxation time is greater than that of Marcol™-52, following eq. (77). This way, we were able to indistinctly separate T_2 signals from the oil (toluene) and brine phases, allowing the calculation of fluids saturation. Furthermore, the analysis of the T_2 relaxation time test gave us an indication that brine was mainly located in the smaller pores. Consequently, bigger pores were occupied by the oil

phase (toluene), as we have estimated from the results obtained on VOF. This test is presented in Figure 115.

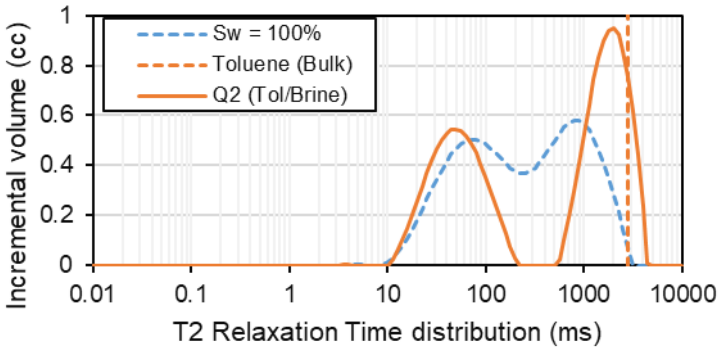

Figure 115 - T_2 Relaxation Time distribution at the end of Step 1 of HDT (toluene/B3 system).

We have superimposed the measurement at $S_w = 100\%$ with the one at the end of Step 1 on toluene, where we may observe a clear separation of signals from brine and oil (toluene). Therefore, it is possible to confirm that performing primary drainage on a dual-porosity sample by a viscous-controlled method is not effective in desaturating brine present in the smaller pores, as its signal is roughly the same as in the acquisition at full brine saturation. Bigger pores, on the other hand, seem to be properly desaturated during Step 1.

As in this HDT experiment we have used a H_2O-based brine; brine saturating the porous plate also contributes to overall T_2 signal and overlaps with signal from brine in the smaller porosity in the regular T_2 relaxation time distribution experiment. In order to properly separate the volume contribution of the brine in the porous plate and the brine present in the sample at S_{wi}, we use the spatially-resolved T_2 measurement. This experiment may be presented either in a T_2 *versus* field of view chart, with a color gradient representing volume in each pixel or as a profile stack plot, where T_2 measurements for each slice are presented in a curves stack. We may observe these two representations for the Spatially-resolved T_2 experiment of EST-HDT-01 at S_{wi} before ageing in Figure 116 and Figure 117.

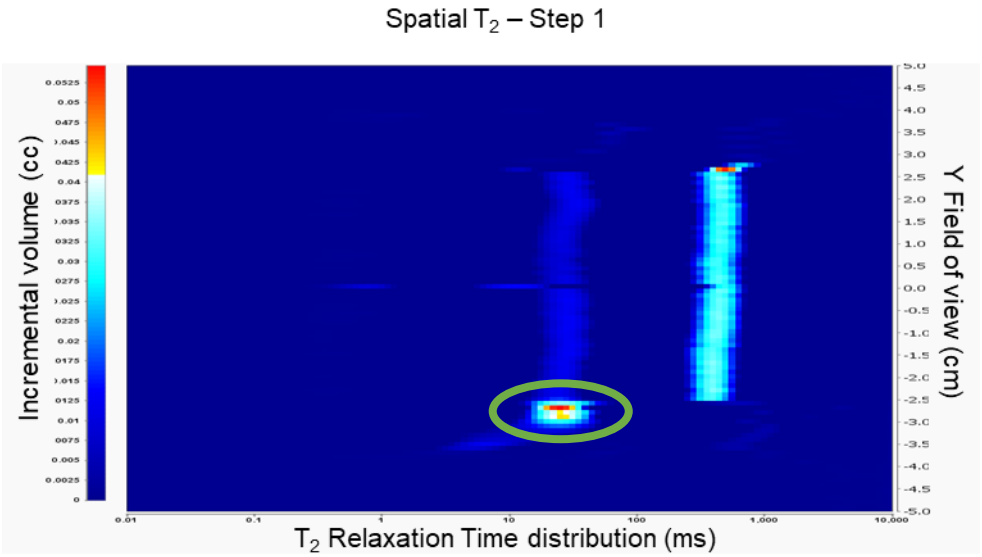

Figure 116 - Spatially-resolved T_2 of EST-HDT-01 after Step 1 of HDT. We have toluene as the oil phase and B3. The green circle highlights the porous plate T_2 relaxation time response.

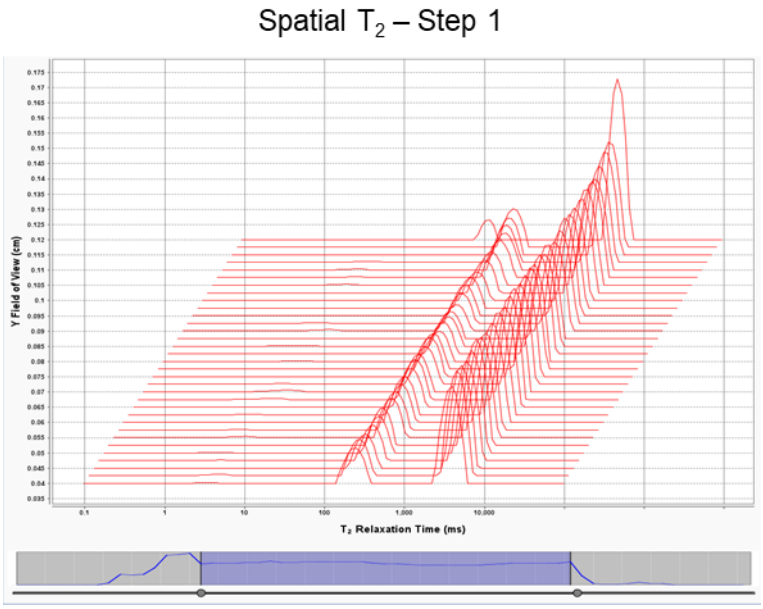

Figure 117 - Stack plot of T_2 relaxation time distributions curves of EST-HDT-01 after Step 1 of HDT.

Figure 116 shows unambiguously the T_2 relaxation time of the brine-saturated porous plate (highlighted by the green circle). It is clearly visible that its relaxes at the same T_2 as the small porosity, justifying the necessity of performing spatially-resolved measurements in the case of this sample.

In the case of the curves stack plot presented in Figure 117, we limited the field of view to present exclusively the T_2 relaxation time distribution curves corresponding to the sample.

We performed the transition to Step 2 (porous plate) with the same couple of fluids (toluene/brine) under NMR monitoring. The change to a capillary-controlled method allows oil to invade the smaller pores, such as observed in the pure Porous Plate experiment (EST-PP-01).

Keeping the same couple of fluids allows a clear visualization of what happens in both porosities simultaneously. As toluene (oil phase) is non-wetting, its signal will not horizontally shift from its bulk T_2 relaxation time even when it invades the smaller porosity. However, the T_2 signal amplitude will increase, meaning that the toluene volume in the sample has increased. The confirmation that toluene invades smaller pores is provided by the brine T_2 signal. We notice a progressive decrease in brine volume, represented by the decrease in its T_2 signal amplitude. As brine is the wetting phase, its T_2 relaxation time response is controlled by the $\frac{S}{V}$ factor. Hence, it is also possible to observe a light shift in brine T_2 relaxation time towards lower T_2 values. This behavior is explained by what is occurring at the pore scale. As toluene invades the smaller porosity as a non-wetting phase, it occupies progressively the center of the pores. Therefore, brine is concentrated close to the rock surface and corners, thus increasing the $\frac{S}{V}$ of the surface T_2 factor presented in equation (76), reducing brine T_2 relaxation time. The process described above can be observed in Figure 118.

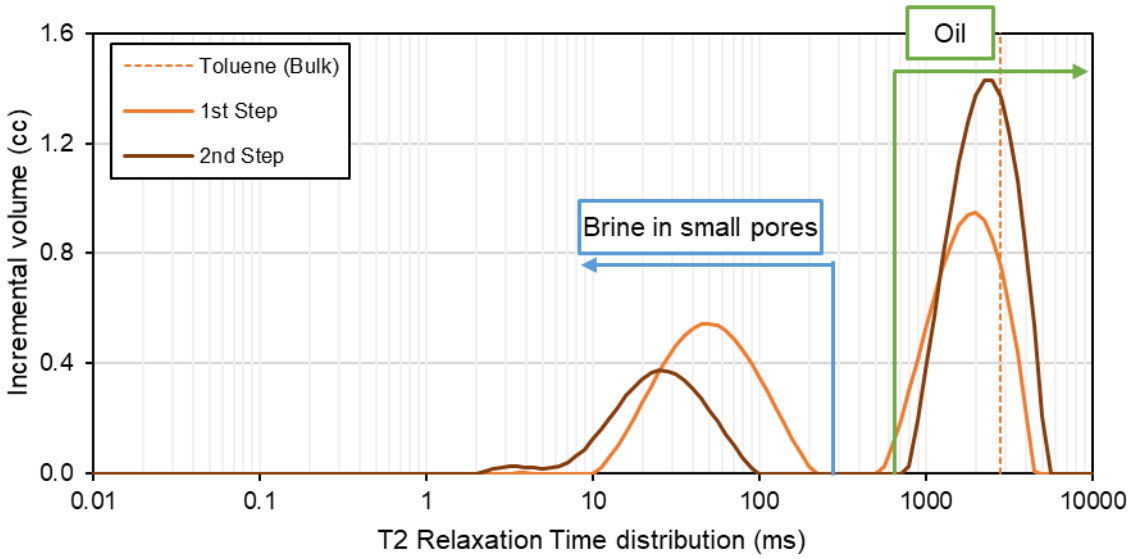

Figure 118 - Evolution of the T_2 signal between the end of Step 1 and Step 2 of HDT (EST-HDT-01) using toluene and B3.

As previously mentioned, spatially-resolved tests are necessary for an unambiguous understanding of these phenomena, because of T_2 signal produced by the brine-saturated porous plate.

We present in Figure 119 and Figure 120 the spatially-resolved tests performed at the end of Step 2. Comparing these results to the ones observed at the end of Step 1, it is possible to confirm the hypotheses announced above, with a left-shift combined with a decrease in the amplitude of the brine phase and an increase in toluene T_2 bulk relaxation time amplitude at the same position in the T_2 spectrum.

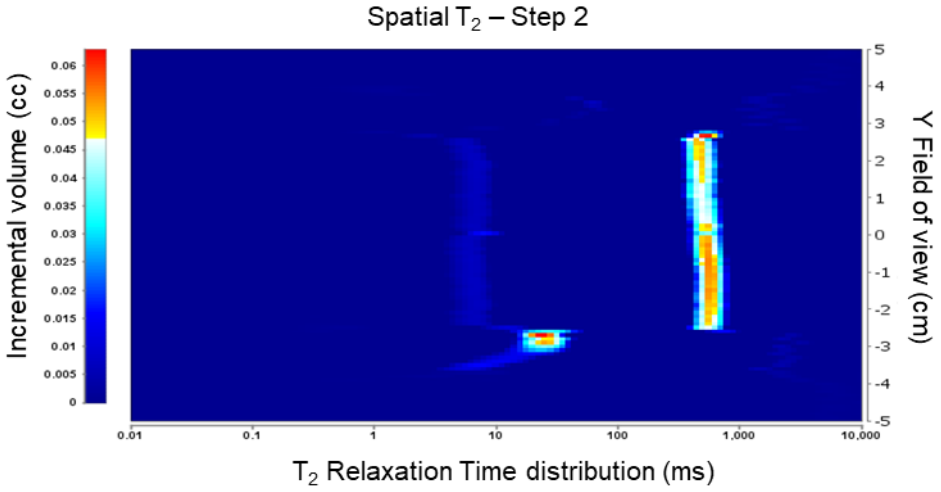

Figure 119 - Spatial T_2 measurement of EST-HDT-01 at the end of Step 2 of HDT. Saturating fluids are still B3 and toluene.

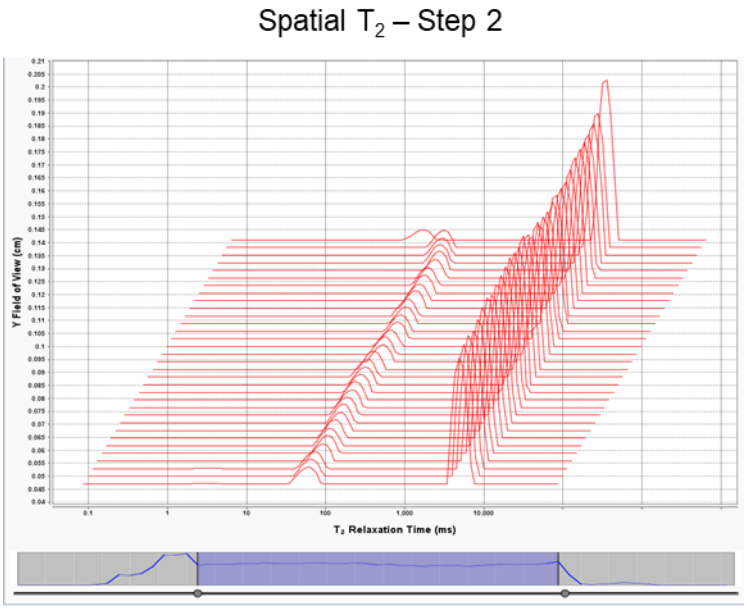

Figure 120 - Stack plot of T_2 relaxation time distribution curves of EST-HDT-01 at the end of Step 2 of HDT.

By treating the data acquired during spatially-resolved T_2 measurements at the end of Steps 1 and 2, we are able to estimate the S_w profiles. For that, we make an approximation and consider that brine signal in both Steps comes exclusively from the signal measured around 10 ms. This is an approximation, because we consider that even at the end of Step 2 brine is still present in the bigger porosity in the form of films and located in the corners. However, this signal could be hidden by the toluene T_2 bulk relaxation signal.

Thus, considering those assumptions we present in Figure 121 the S_w profiles at the end of Steps 1 and 2:

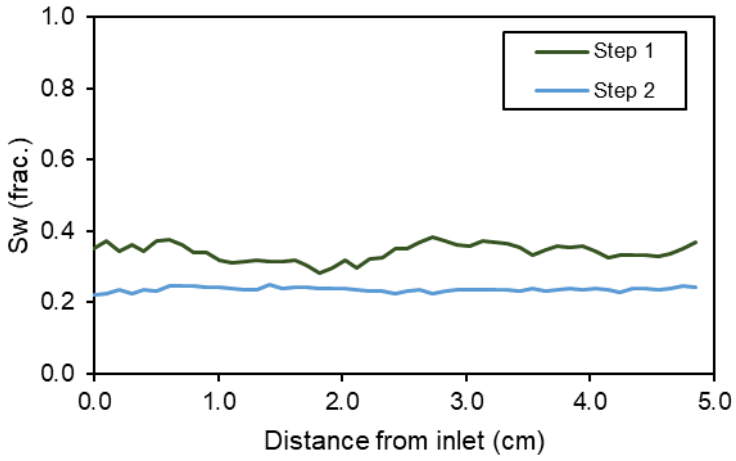

Figure 121 - Water saturation evolution after transition from Step 1 to Step 2 of HDT (EST-HDT-01).

- $\overline{S_{w_{Step\ 1}}} = 34.1\%$
- $\overline{S_{w_{Step\ 2}}} = 23.7\%$

We cut the data at around 2.5 cm from sample inlet because the measurement encountered an inversion problem at this point in the Spatial T_2 measurement at the

end of Step 1 (this may even be confirmed in Figure 116, where we observe a disturbed behavior at around 0.0 cm of the Field of View).

EST-HDT-02

To conduct a comparative study between the Hybrid Drainage Technique (HDT) and Viscous Oil Flood (VOF) at the same S_{wi} conditions, we have taken another Estaillades sample and established the same target of S_{wi} value as EST-VOF-01 with the same couple of fluids (B2 and Marcol^{TM}-52). The objective of this study is to verify that pore filling in the case of a dual-porosity sample is different using HDT and VOF, thus the results regarding wettability alteration and waterflooding may also differ. Moreover, we are able to investigate the issues of homogenizing the S_w profile during VOF by reversal flow.

We established S_{wi} by performing two flowrate steps during Step 1 of VOF followed by the application of $Pc = 1\ bar$ during Step 2. Flowrate steps are presented in Table *24*:

Flowrate Step	Flowrate	Capillary Number
Q1	30 cc/h	2.4 10^{-6}
Q2	60 cc/h	4.8 10^{-6}

Table 24-Flowrate steps and capillary number for EST-HDT-02 primary drainage (Marcol^{TM}-52)

The S_w profile obtained from an SE-SPI profile measurement at the end of primary drainage is presented in Figure 122. It is possible to notice that the targeted S_{wi} value was attained (around 35 %) and a homogeneous S_w profile was generated without reversal flow.

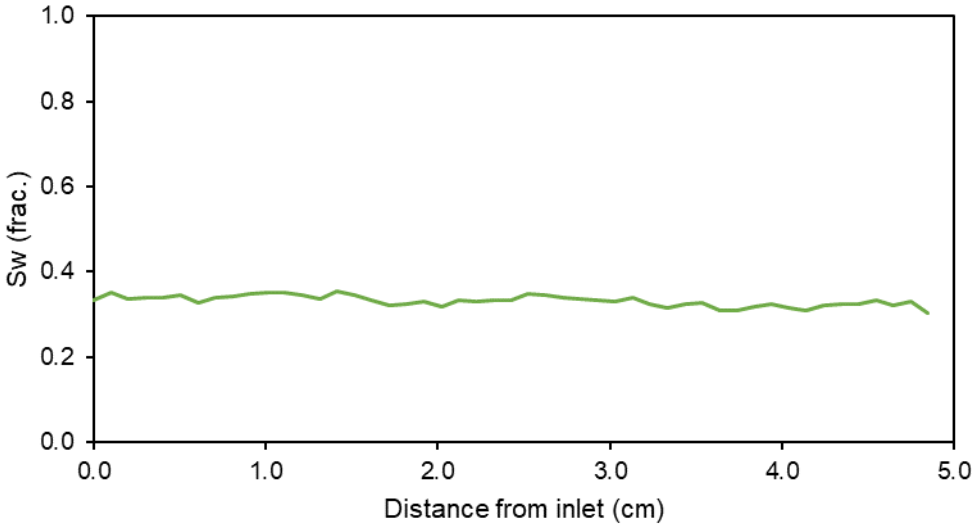

Figure 122 - S_w profile of EST-HDT-02 at the end of primary drainage ($Pc = 1\ bar$).

- $\sigma\ (S_w) = 1\ \%$
- $Max - min\ (S_w) = 5\ \%$

For this experiment we have used a double-spiral diffuser in the inlet face of the sample, as it can be seen in Figure 123. It has proven to be a good solution for the artifact in saturation observed close to the inlet during RCH-HDT-01 and RCH-HDT-02 experiments.

Figure 123 - Double-spiral diffuser used for HDT experiments of Estaillades limestone samples.

EST-HDT-03-MP

In order to observe the behavior of fluids at the pore-scale during HDT, we imaged the experimental cycle of an Estaillades mini-plug by Micro-tomography, with 9.77 mm in diameter and 30.25 mm in length. Thanks to the Multi-Imagery cell, we were also able to perform NMR monitoring of this same mini-plug during the successive displacement phases of the experimental cycle. This multi-imagery approach allows a mutual validation between both methods regarding the porosity and water saturation profiles results during the experimental cycle, as well as pore-scale visualization of the fluids.

As a matter of initial characterization by NMR and µ-CT, we fully-saturate the sample by the synthetic mineral oil used for the tests (Marcol™-52). T_2 and SE-SPI profile of the sample at the 100% oil saturation state are presented in Figure 124 and Figure 125:

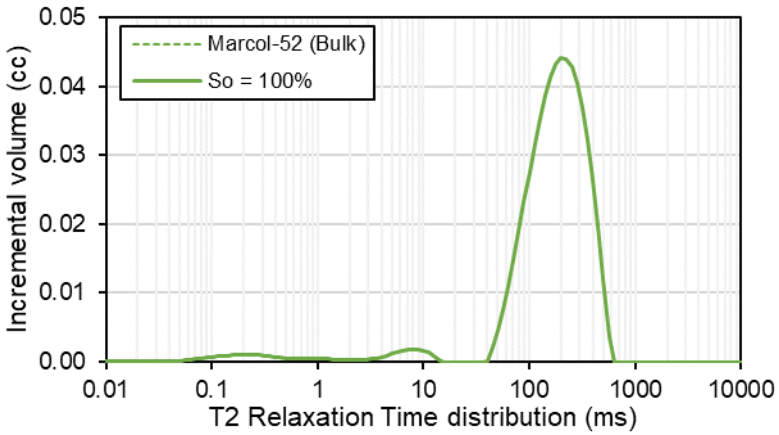

Figure 124 - T_2 Relaxation Time distribution for EST-HDT-03-MP at So =100% using Marcol™-52.

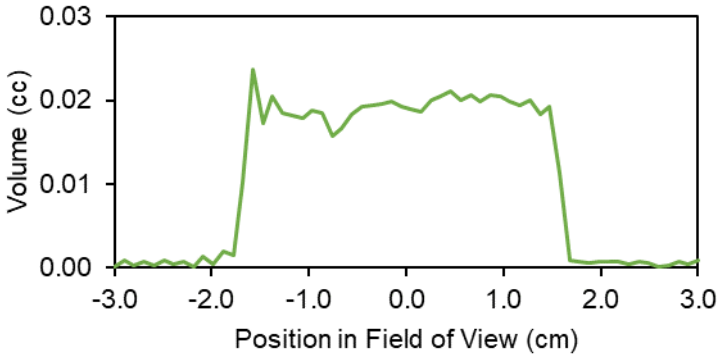

Figure 125 - SE-SPI profile for EST-HDT-03-MP at So = 100%

The Estaillades rock is considered water-wet at its initial state. For this reason, we are not able to observe the dual-porosity aspect in T_2 relaxation time distribution at the oil-saturated state presented in Figure 124. Despite putting the sample under vacuum prior to oil-saturation at high pressure, a water film persists and covers the rock surface, preventing oil to interact with it. As there is no interaction between the oil phase and the rock surface, oil saturating the sample relaxes as bulk fluid.

For a complete porosity characterization of EST-HDT-03-MP using the NMR, we cleaned the sample using the Soxhlet method, dried it in the oven, and saturated it with an H_2O-based brine (B3) for performing a brine-saturated NMR characterization. In order to confirm not only the dual-porosity aspect of the sample, but also to investigate the pore-size distribution along the sample longitudinal axis, we performed a spatially-resolved T_2 test.

The results the spatially-resolved T_2 test is presented in Figure 126, and the stack plot with the field of view restricted to the sample length is presented in Figure 127.

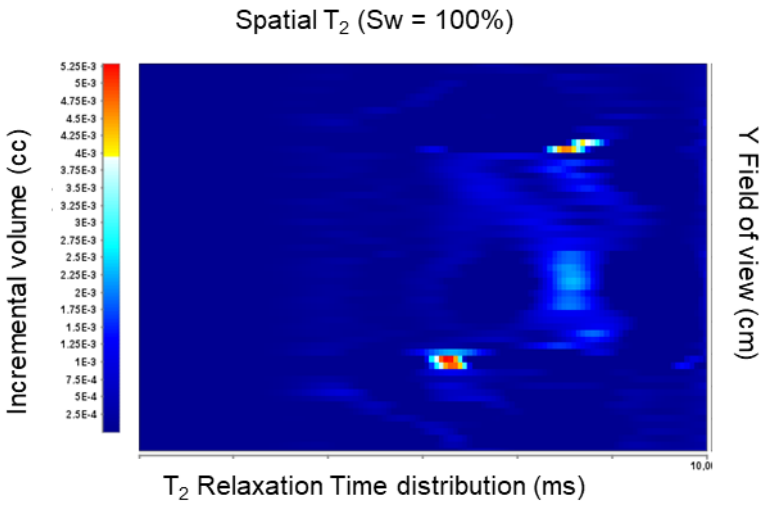

Figure 126 - Spatially-resolved T_2 EST-HDT-03-MP at $S_w = 100\%$.

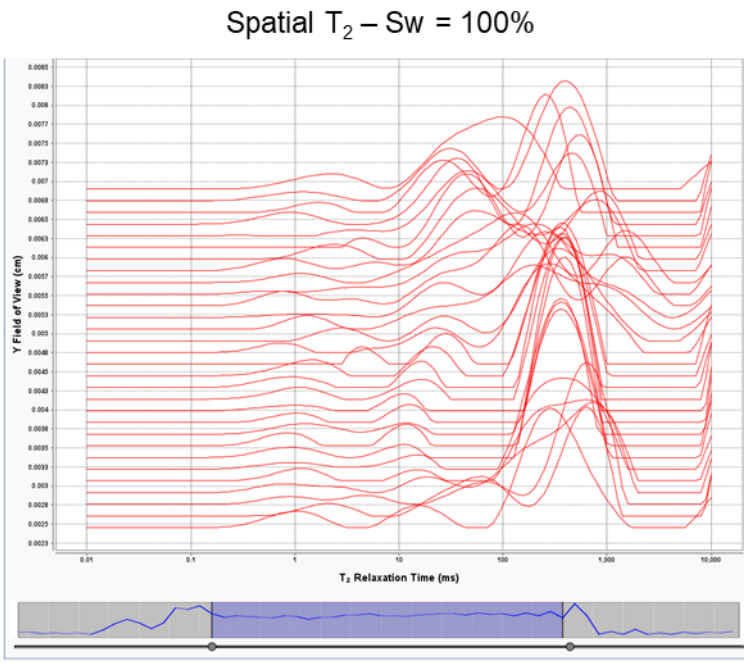

Figure 127 - Stack plot of EST-HDT-03-MP saturated with B3.

There are some interesting features to be investigated from the spatially-resolved test. We confirm the dual-porosity aspect of the sample, but also identify a longitudinal porosity heterogeneity, that could not be detected by the SE-SPI test performed at the oil-saturated state, as SE-SPI tests are not sensitive to relaxation time. This result is intriguing, because the Estaillades rock is considered a dual-porosity homogeneous sample. Therefore, we suspect that using the 10 mm in diameter mini-plug reduced the Representative Elementary Volume below r_{micro} as presented in Figure 4 (section 1.2.2).

Furthermore, we decided to investigate the contribution of both micro and macro pores to the total porosity of the sample. To perform this analysis, we defined a cut-off between micro and macro-porosities at $T_2 = 200\,ms$. This decision was based on a thorough study presented by Fleury *et al.* (2007), where they investigate the appropriate cut-off to separate macro and micro pores on several rocks, including the Estaillades limestone. To calculate the porosity profile by NMR, we use the following equation:

$$\varphi_i = \frac{V_{w,i}}{\left(\frac{\pi D^2}{4}\right) dz} \tag{100}$$

where φ_i is the porosity value at position "i", $V_{w,i}$ is the water volume in the position "i", D is the sample diameter and dz is the slice width, which corresponds to the resolution of the spatially-resolved experiment.

The three porosity profiles obtained with this processing are presented in Figure 128:

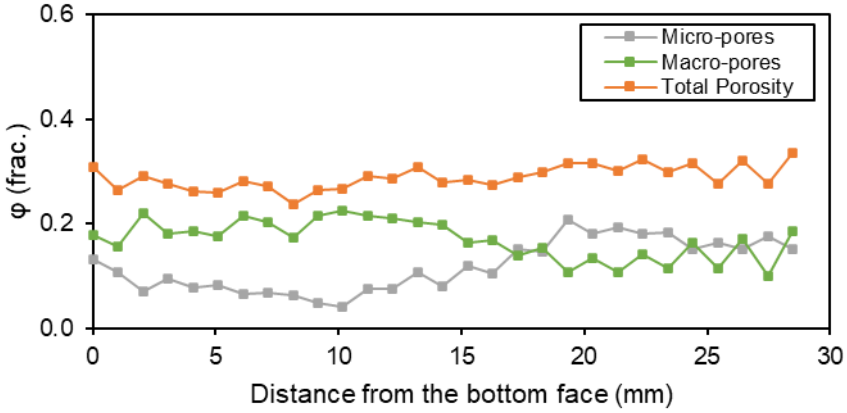

Figure 128 – Porosity profiles of EST-HDT-03-MP obtained by NMR.

The porosity heterogeneity is clearly visible. It is possible to observe two porosity gradients: the macro-pore population decreases from the bottom to the top face of the sample, and micro-pores follow an inverse tendency. The total profile is, nonetheless, homogeneous, corroborating the SE-SPI experiment performed at oil saturation (Figure 125).

In addition, we obtained the total, micro and unresolved porosity profiles by µ-CT imaging. To perform this processing, we used the µ-CT scan of the sample saturated in oil, a scan of the sample saturated with high-doped brine (D_2O + KI @ 300 g/l) and a scan of the mini-plug saturated with the brine used in the experiments (B2). We used D_2O-based brine for unambiguously detection of phases during NMR acquisitions in the subsequent steps of the experimental cycle.

In Figure 129 we present the same slice at each saturation state used for differential imaging of the porosity, as mentioned in the above paragraph. Given the high attenuation coefficient of the highly-doped brine, the position in the grayscale of the rock matrix and the pores is inverted (darker gray – rock; lighter gray - pores) compared to the B2 and mineral oil scans (darker gray – pores; lighter gray - rock).

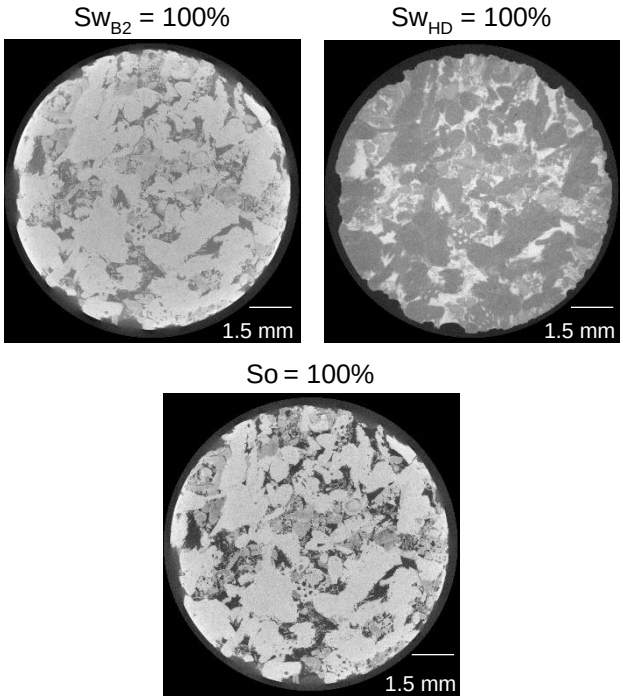

Figure 129 - Scans of the same slice with different saturating fluids: B2, High-Doped brine and Marcol^{TM}-52.

Therefore, by means of the differential imaging processing, we were able to discretize the porosity between the macro and the unresolved porosity as done with the NMR tests. This is an important result, because we compare the performance of two independent imaging techniques regarding longitudinal profile calculation and porosity heterogeneity description. The result of the differential imaging processing is presented in Figure 130:

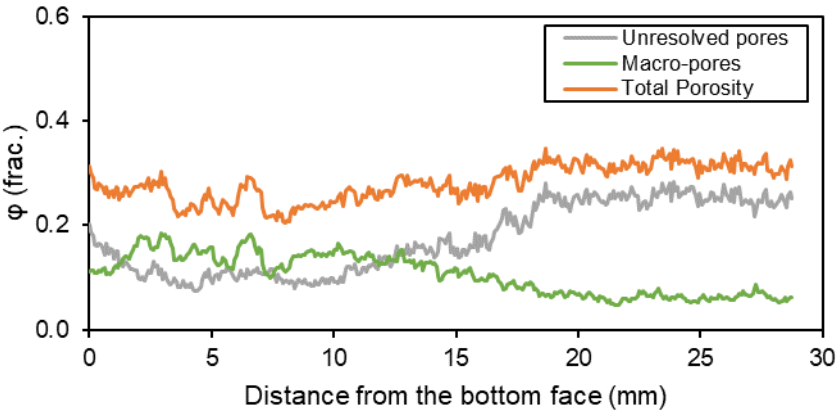

Figure 130 - Macro, unresolved and total porosity profile of sample EST-HDT-03-MP obtained by µ-CT differential imaging.

It is interesting to observe that both methods show the same tendency regarding the porosity profiles. Nonetheless, unlike NMR processing, the definition of the unresolved porosity by µ-CT is not based on a pore-size threshold. Therefore, as a part of the macro-porosity is unresolved, it is not counted as macro-porosity during differential imaging processing, thus being under-estimated. Highlighting this point is important, because the share of the porosities obtained by NMR and µ-CT do not

represent the same physical quantity: NMR identifies macro and micro-porosities by a defined threshold in the T_2 spectrum, and µ-CT identifies resolved (macro) and unresolved porosities. Notwithstanding, we present in Figure 131 the direct comparison between the macro-porosity curves obtained by NMR and µ-CT, where it is possible to verify the definition provided above.

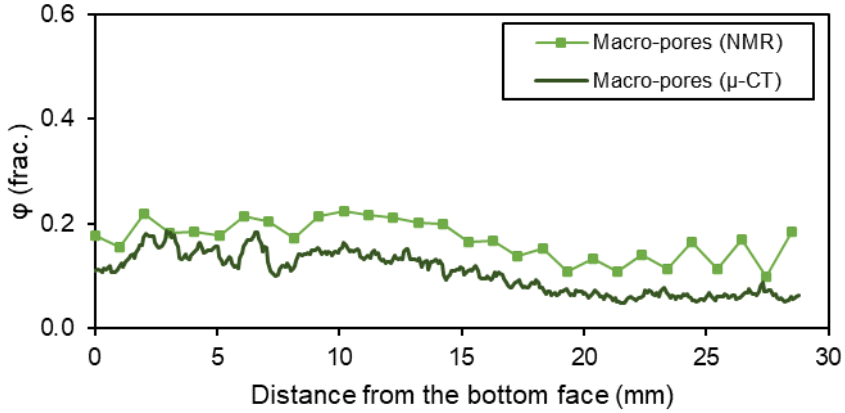

Figure 131 - Macro-pores longitudinal distribution obtained by NMR and µ-CT imaging (EST-HDT-03-MP).

On the other hand, the total porosity obtained with the two methods must present the same shape. An overwrite of the total longitudinal porosity profiles confirming this assumption is presented in Figure 132.

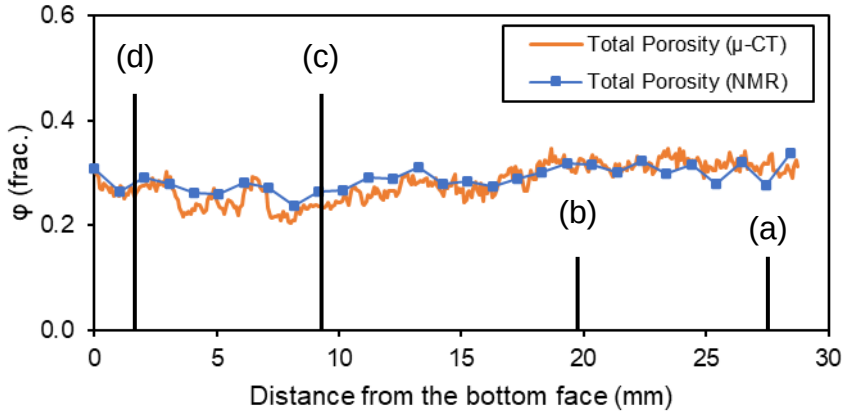

Figure 132 - Total porosity profile obtained by NMR and µ-CT imaging (EST-HDT-03-MP).

We observe a good match between NMR and µ-CT profiles, and the average porosity value obtained by both techniques are very close:

- $\bar{\Phi}_{NMR} = 28.9\%$
- $\bar{\Phi}_{\mu-CT} = 28.1\%$

In Figure 133 we present four slices at 100% brine saturation and their respective position in the sample. The slice order will be respected throughout this study.

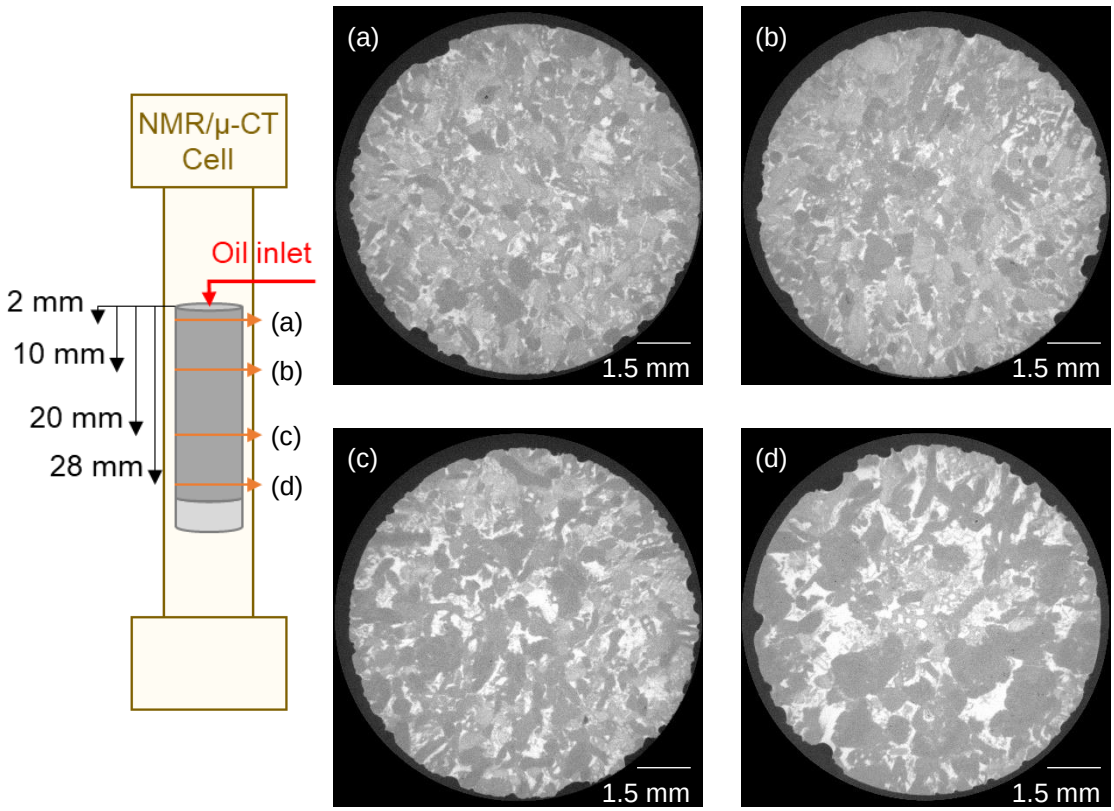

Figure 133 – Brine-saturated EST-HDT-03-MP. We present four slices at different positions in the sample: (a) at 2 mm from the top, (b) 10 mm, (c) 10 mm from the bottom and (d) 2 mm from the bottom.

After initial characterization, we perform a miscible replacement of the resident high-doped brine by B2 and Kw measurement prior to the beginning of the primary drainage step by HDT. We followed the same protocol as in EST-HDT-02, adapting the flowrates for the mini-plug from the capillary number used during Step 1 of HDT. Flowrates used in this experiment are presented in Table *25*:

Flowrate Step	Flowrate	Capillary Number
Q1	0.6 cc/h	$7.0\ 10^{-7}$
Q2	3.0 cc/h	$3.6\ 10^{-6}$

Table 25-Flowrate steps and capillary number for EST-HDT-03-MP primary drainage (Marcol™-52)

At the end of Step 1 of HDT, we performed both NMR SE-SPI profile and μ-CT imaging. At this state, we aimed to visualize fluid distribution in the pore space from μ-CT scans, and the capillary end-effects in the mini plug scale (NMR and μ-CT). Moreover, from differential imaging, we are able to obtain separate S_w profiles between the macro and the unresolved porosity. This is an interesting feature to analyze in the case of a bi-modal sample as Estaillades. First, we present, in Figure 134, the image of the four slices previously presented in Figure 133 after Step 1 of HDT.

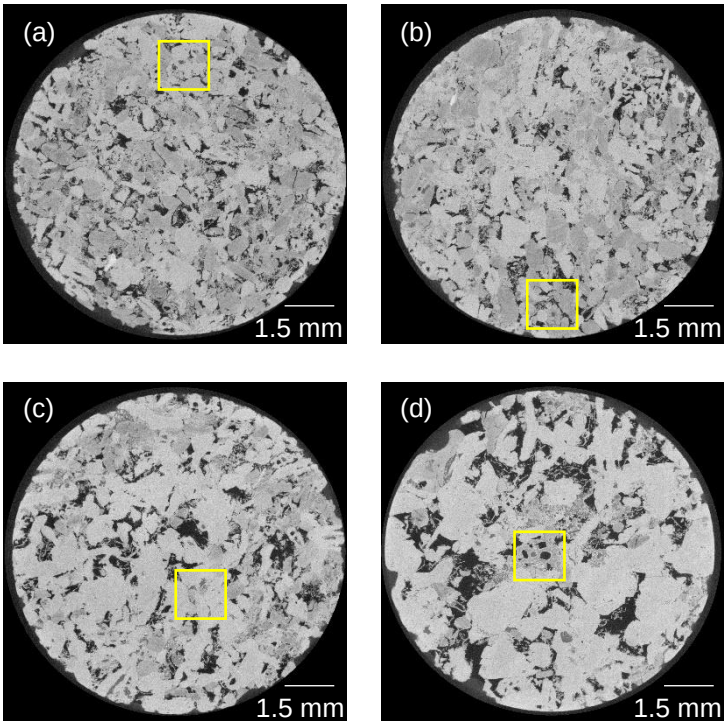

Figure 134 - EST-HDT-03-MP after Step 1 of HDT.

From a general observation, it is not possible to infer the fluids distribution in the pore scale. However, when we zoom in the four images in the yellow highlighted zones presented above, we are able to detect the presence of brine in the small porosity of the sample which was not flushed during Step 1 (bright attenuation in intermediate gray). We present in Figure 135 the four zooms in the studied slices for a clear visualization:

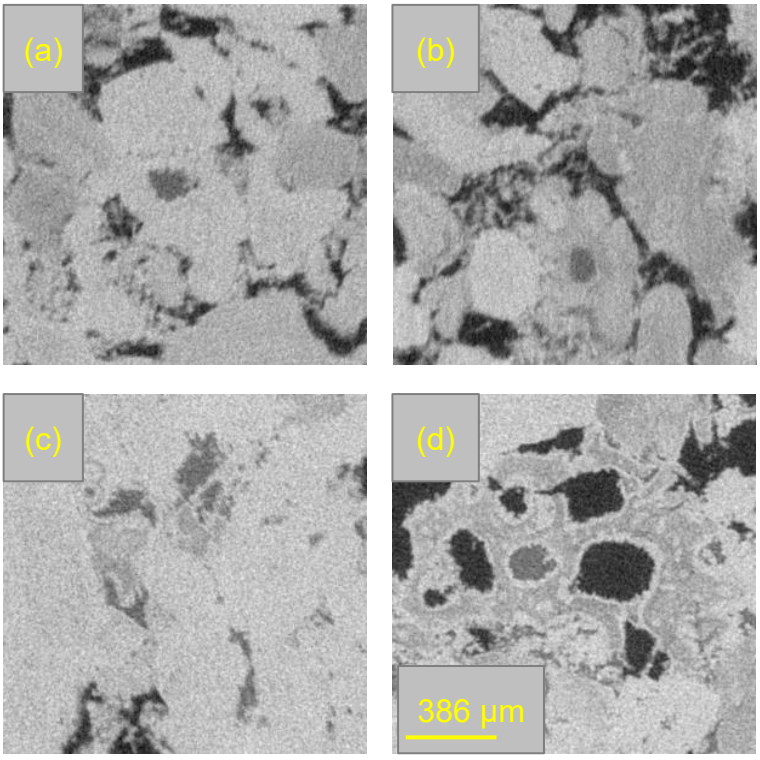

Figure 135 - Zoom in on images after Step 1 of HDT.

By performing the µ-CT image treatment and comparing to the NMR results, we are able to observe some interesting factors. If we take into consideration only the average S_w values, NMR and µ-CT present similar results, showing a good agreement between both methods, as seen in Figure 136. However, the sample behavior is far from the expected at the end of the Step 1 of HDT. Being a viscous-controlled step, we would expect well-defined capillary end effects.

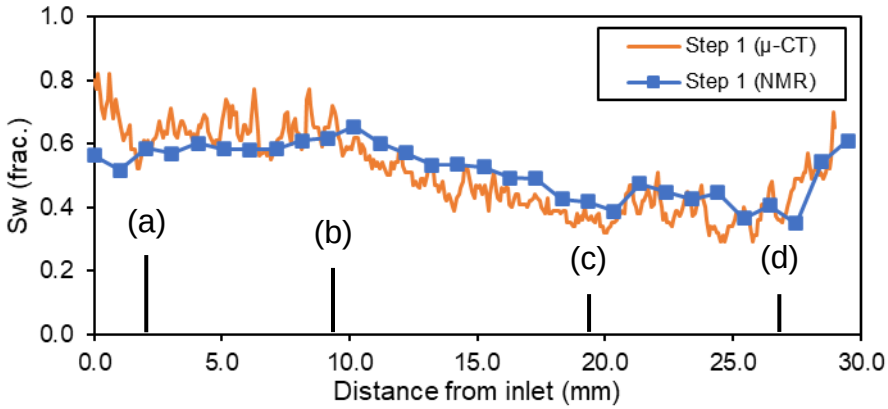

Figure 136 - S_w profiles at the end of Step 1 of HDT by NMR and µ-CT (EST-HDT-03-MP).

This unexpected behavior (absence of CEE) may be explained by the heterogeneity of the sample and by its bi-modal porosity. Performing the differential imaging treatment to separate the contribution of micro and macro porosities to the total water saturation profile, we can observe that macro-porosity has been largely desaturated and present CEE. On the other hand, micro-porosity stands for almost the totality of the remaining water saturation after Step 1 of HDT and seems unsensitive to CEE. Moreover, micro-porosity presents higher water saturation values where it dominates the average sample porosity (between 0 and (b) in Figure 137).

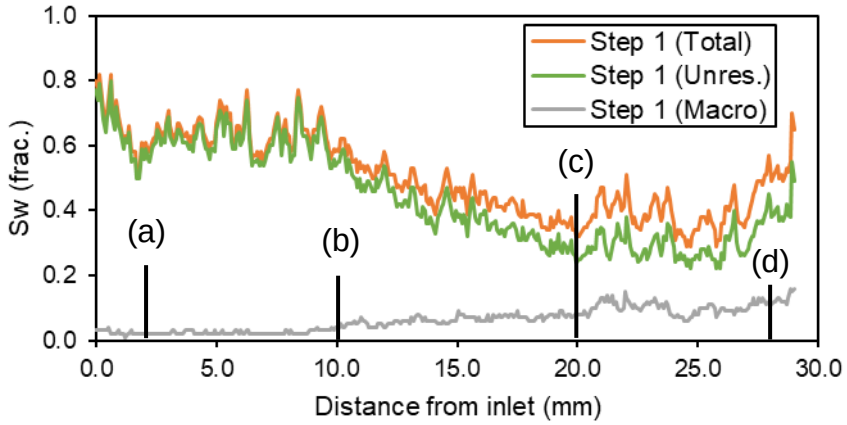

Figure 137 - Share of total S_w between micro and macro porosities after Step 1 of HDT (EST-HDT-03-MP).

As we are performing a twin experiment with EST-HDT-02, inlet pressure applied during Step 2 is also $P_c = 1\ bar$.

Analyzing the µ-CT scans taken after Step 2, it is possible to notice that brine previously present in the smaller porosity (intermediate gray) was flushed by oil (dark attenuation, close to black) during the Porous Plate part of HDT. This result is consistent with what we expected and represent an indication, at the pore scale, that the method is efficient to drain small pores in dual-porosity samples. This effect is

more pronounced close to the outlet of the sample (bottom face, slices c and d), because a bigger capillary pressure delta occurs between the viscous displacement at Step 1 and the porous plate at Step 2. Nonetheless, we observed the effect for the whole sample; and we made a zoom in the same regions as in Figure 135 for easier visualization of the phenomenon. In Figure 138 and Figure 139 we present the evolution from Step 1 to Step 2 by comparing the same slices at the end of each Step.

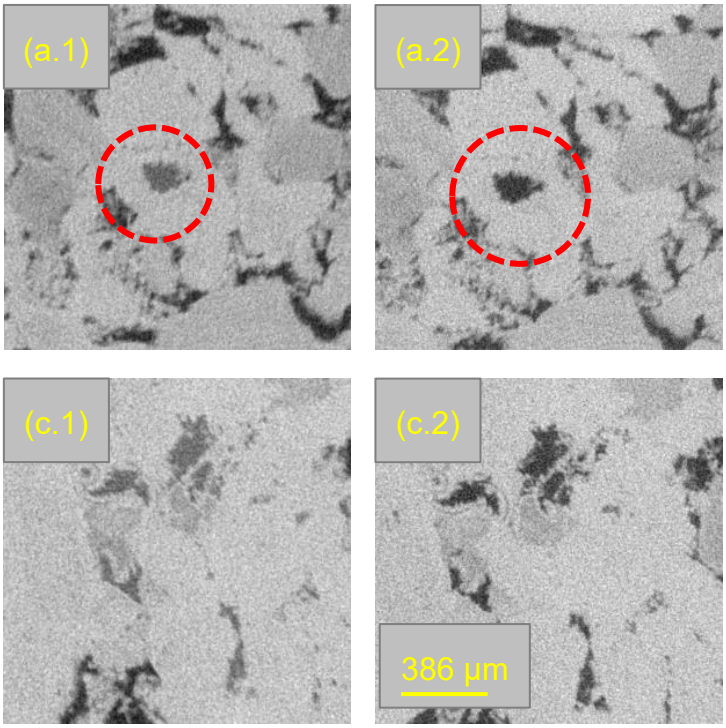

Figure 138 - Comparison between (a) and (c) slices at the end of Step 1 (subscript .1) and at the end of Step 2 (subscript .2).

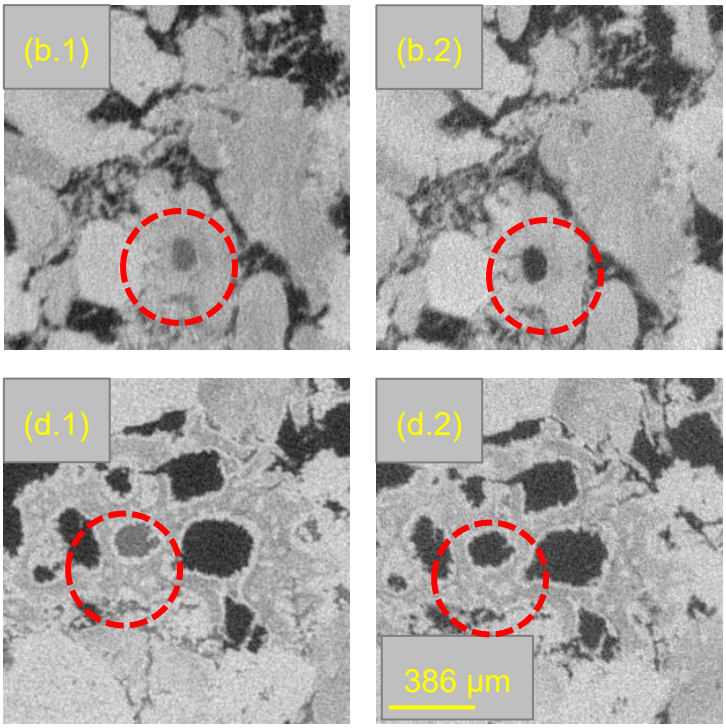

Figure 139 - Comparison between (b) and (d) slices at the end of Step 1 (subscript .1) and at the end of Step 2 (subscript .2).

Similarly to the Step 1, we obtained S_w profiles by NMR and µ-CT imaging for the Step 2. The resulting profiles are presented in Figure 140:

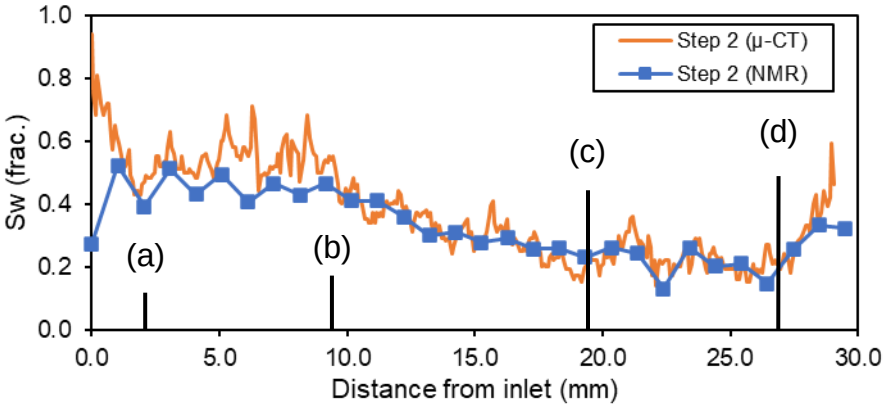

Figure 140 - NMR and µ-CT profiles at the end of Step 2 of HDT (EST-HDT-03-MP).

Because of the porosity heterogeneity observed for this sample, we do not observe an average homogeneous S_w profile at the end of Step 2 of HDT. Considering the porosity profile presented in Figure 130, we are able to understand the behavior of the profiles presented in Figure 141.

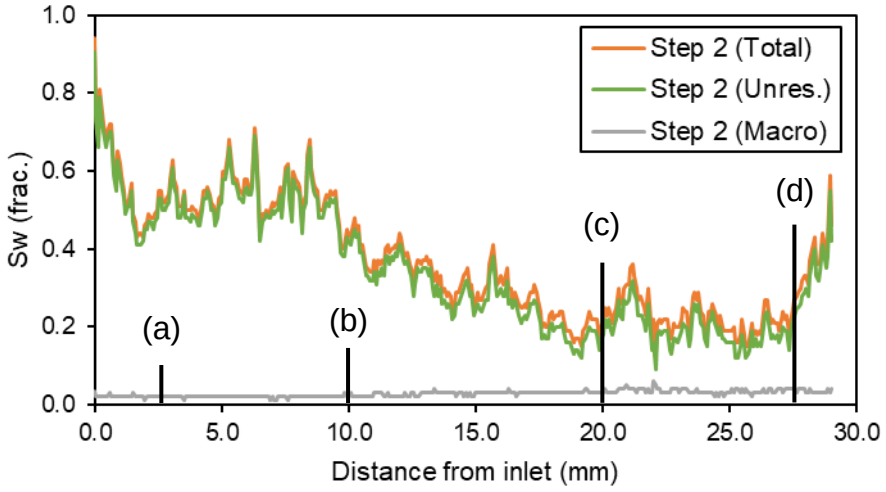

Figure 141 - Share of total S_w between micro and macro porosities after Step 2 of HDT (EST-HDT-03-MP).

Imposing homogeneous capillary pressure through a heterogeneous sample will not result on a homogeneous S_w profile. This is a condition related to the sample and does not represent a limitation of the Hybrid Drainage Technique, but a physical condition.

Despite the heterogeneity in both macro and micro porosities, an elimination of CEE present in the macro-pores was observed at the end of Step 2 of HDT.

It is difficult to conclude on the effects of HDT over the unresolved porosity, due to along axis heterogeneity. In the curves presented above, water saturation of macro and unresolved porosity was obtained by a ratio of the brine volume present in this part of the porosity by the total pore volume. For a better understanding of the phenomenology in the unresolved porosity during HDT and to remove the effect of

heterogeneities in the analysis, we normalized water saturation in Steps 1 and 2 using equation (101).

$$\left\|S_{w_{un}}(x)\right\| = \frac{V_{w_{un}}(x)}{\varphi_{un}(x)} \tag{101}$$

where $\left\|S_{w_{un}}(z)\right\|$ is the normalized water saturation in the unresolved porosity at a position x in the sample, $V_{w_{un}}(x)$ is the water volume in the unresolved position at the position x, and $\varphi_{un}(x)$ is the unresolved porosity in position (x).

This approach allows the elimination of porosity heterogeneity effects on the profiles. The results of the announced protocol are presented in Figure 142:

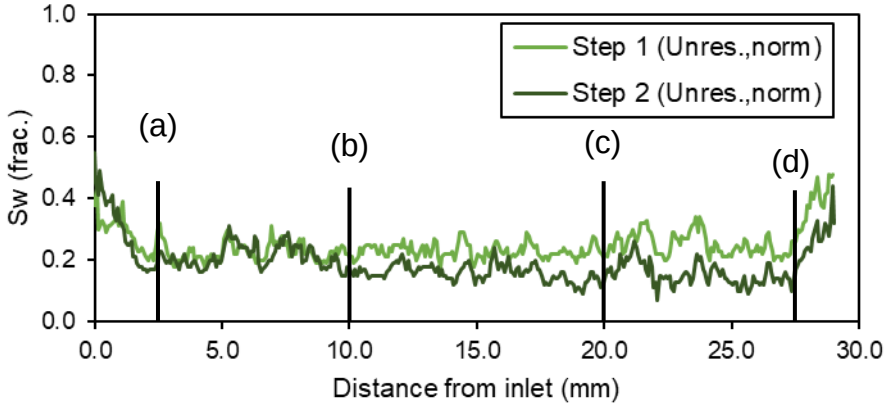

Figure 142 - Water saturation variation in the micro-porosity between Steps 1 and 2 of HDT (EST-HDT-03-MP). By normalizing the water saturation to the micro-porosity itself, we eliminate effects of porosity heterogeneity.

The curves evolution presented here above are an important indication that HDT is effective on accessing smaller porosity by imposing a homogeneous capillary pressure field in the core sample.

d. Reservoir samples R1 and R2

This reservoir sample presents almost the same dual-porosity characteristics as the Estaillades limestone. Therefore, it was used for the proof of concept of HDT for bimodal reservoir samples.

The S_{wi} target value for this case is around 10%, which is extremely hard to reach using viscous-controlled techniques. This was confirmed by full-size core experiments that are out of the scope of this study[2].

The strategy that was adopted for these cases is similar to the one used for EST-HDT-01 and EST-HDT-02: In the case of R1 we have used a H_2O-based brine to distinguish the phases during NMR acquisitions. For R2, we have used the same brine composition, but we have replaced water with deuterium oxide, to distinctly observe the behavior of the oil phase during primary drainage.

R1

For R1 primary drainage experiment, we have used B5, Isopar-L™ and Marcol™-52. We started Step 1 injecting Isopar-L™ and monitoring the T_2 Relaxation Time

[2] The full-size core experiment is part of TotalEnergies field development. No further information is provided for confidentiality purpose.

distribution during five different flowrate steps. Due to its low viscosity, this oil allows the separation of brine and oil signal in the T_2 spectrum. However, as we wanted to reach lower values of S_w during Step 1, we performed a miscible displacement of Isopar-L™ by Marcol™-52. The use of the latter allows desaturating the sample at higher capillary numbers without the application of extremely high flowrates. We used Marcol™-52 during 3 flowrate steps.

The total 8 flowrate steps used during Step 1 are presented in Table *26*:

Flowrate Step	Mineral Oil	Flowrate	Capillary Number
Q1	Isopar-L™	6 cc/h	$5.4\ 10^{-8}$
Q2	Isopar-L™	12 cc/h	$1.1\ 10^{-7}$
Q3	Isopar-L™	24 cc/h	$2.1\ 10^{-7}$
Q4	Isopar-L™	48 cc/h	$4.3\ 10^{-7}$
Q5	Isopar-L™	96 cc/h	$8.6\ 10^{-7}$
Q6	Marcol™-52	24 cc/h	$1.9\ 10^{-6}$
Q7	Marcol™-52	48 cc/h	$3.8\ 10^{-6}$
Q8	Marcol™-52	96 cc/h	$7.6\ 10^{-6}$

Table 26-Flowrate steps and capillary number for R1 primary drainage

dP and S_w *versus* time are presented in Figure 143:

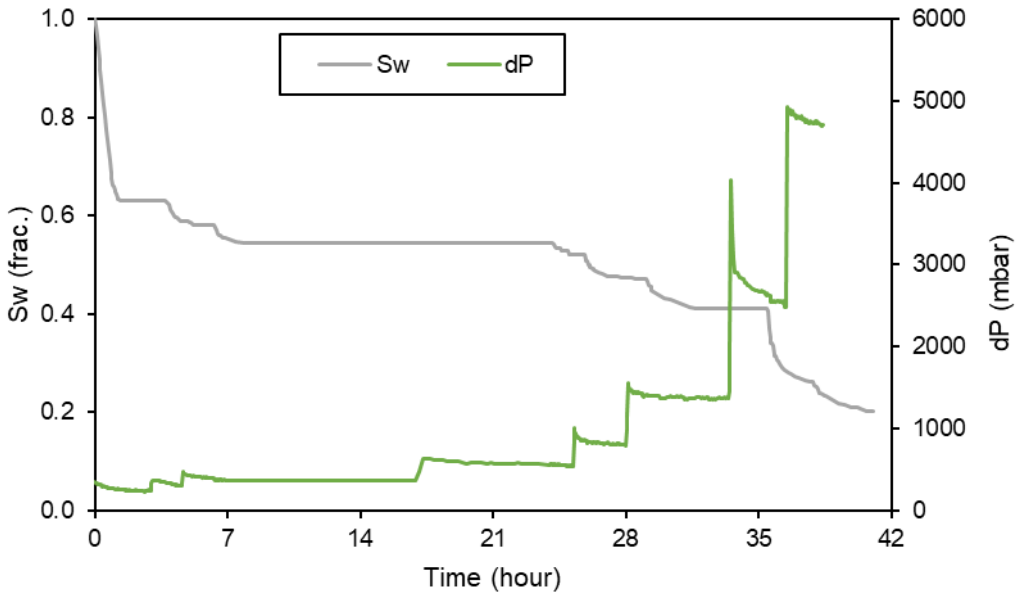

Figure 143 - R1 dP and S_w response to Step 1 of HDT with R1.

Moreover, during Step 1 (when Isopar-L™ was used) we performed a series of T_2 Relaxation Time distribution measurements. These tests showed an interesting aspect regarding the dynamics of the experiment, as we see a progressive shift in the longer T_2 signal from the surface relaxation at $S_w = 100\ \%$ towards Isopar-L™ bulk

relaxation time as the sample was desaturated. This behavior may be observed in Figure 144:

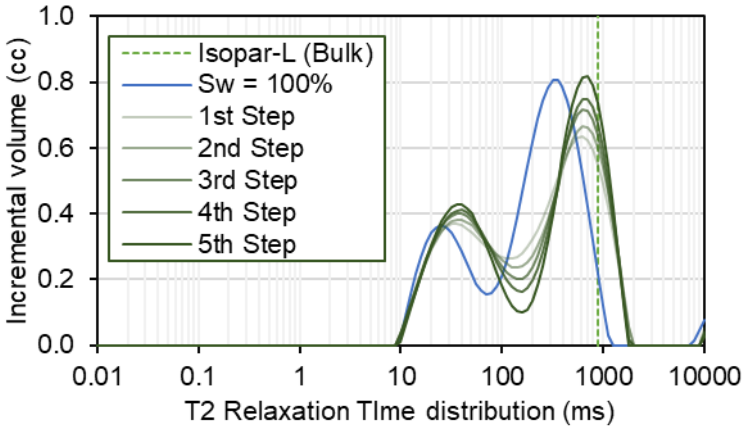

Figure 144 - T_2 Relaxation Distribution time tests during Step 1 of HDT primary drainage with R1 in Isopar-L™ and B5.

After miscibly replacing Isopar-L™ by Marcol™-52, T_2 signals of brine and oil overlapped subsequent Marcol™-52 injection (Q6, Q7 & Q8), therefore they are not presented here.

By performing a longer Step 1 desaturating the sample to an average value of S_w around 20 %, we reduced the experimental duration of Step 2, which is usually longer. Thus, we performed the transition to the second part of the experiment and applied a capillary pressure of $Pc = 5\,bar$. Moreover, in order to observe the experimental progress through T_2 relaxation time experiments, this time we replaced Marcol™-52 by Isopar-L™, given the lower viscosity of the latter, which enables unambiguously detection of both brine and oil phases. For monitoring the experimental advancement and to calculate the S_w profiles during primary drainage, we performed T_2 Relaxation Time distribution and Spatially-resolved T_2, respectively. As we are able to detect both phases separately in the T_2 spectrum, a spatially-resolved T_2 test allows the obtention of the fluids saturation profile along the sample longitudinal axis.

In Figure 145, the color gradient represent the temporal order of the acquisitions (from lighter to darker green). It is possible to notice that the signal of brine in the smaller porosity shifts slightly towards smaller T_2 relaxation times. This behavior is explained by the oil invasion of the smaller porosity as a non-wetting phase, thus occupying the center of the pores. This configuration restricts water presence to the corners, reducing its surface-to-volume ratio. At the same time, the amplitude of the oil signal increases and the signal peak shifts towards Isopar-L™ bulk relaxation time (around 1000 ms). At the final configuration (darkest green curve), no more transition between the brine and the oil signal is noticed (in the range between 70 ms and 300 ms).

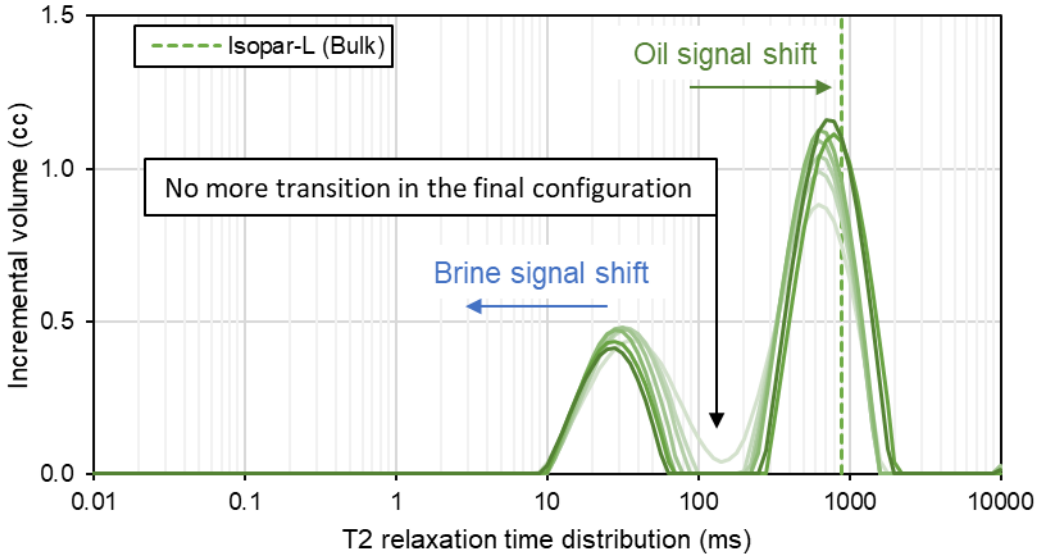

Figure 145 – T_2 Relaxation Time distribution during Step 2 of HDT with R1 in Isopar-L™ and B5.

For separating the brine signal from the porous plate and providing information regarding the saturation profiles, we use the Spatially-resolved T_2 experiments, such as for EST-HDT-01. Performing a sequence of acquisitions during Step 2 allows plotting the evolution of the saturation profiles until final equilibrium at the target S_{wi}. This result is presented in Figure 146:

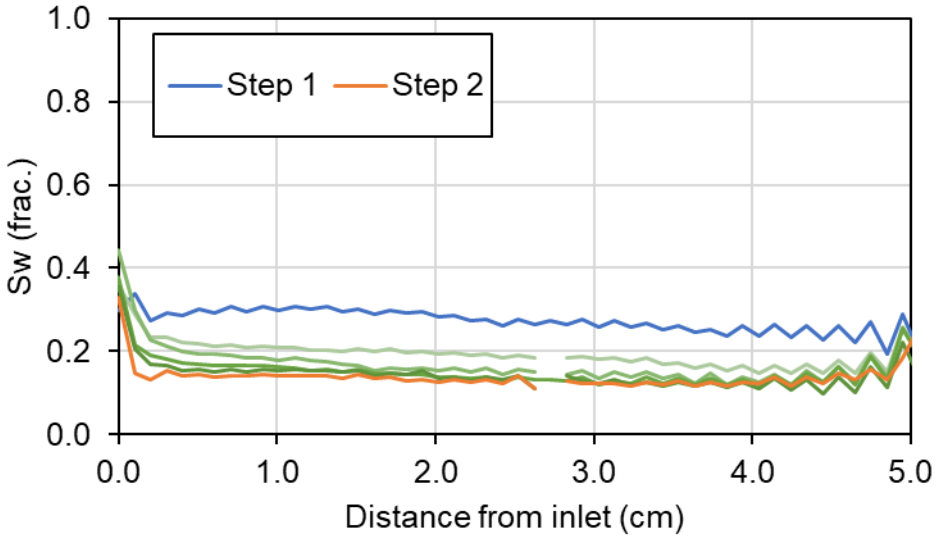

Figure 146 - Saturation profiles evolution during Step 2 of HDT (R1). We present the profile at the end of Steps 1 and 2 in different colors in order to highlight them from the intermediate profiles obtained during Step 2 of HDT.

The data treatment of the Spatially-resolved T_2 to obtain the S_w profiles generates artefacts at both ends of the sample. Therefore, for the quantification of the profile homogenization, we will cut around 2 mm from both ends. The metrics for the profile at the end of Step 1 and at the end of Step 2 are presented below:

- $\overline{S_{w_{Step1}}} = 27.3\ \% \rightarrow \overline{S_{w_{Step2}}} = 13.2\ \%$
- $\sigma\ (S_w)_{Step\ 1} = 2.6\ \% \rightarrow \sigma\ (S_w)_{Step\ 2} = 1.0\ \%$
- $Max - min\ \ (S_w)_{Step\ 1} = 11.4\ \% \rightarrow Max - min\ \ (S_w)_{Step\ 2} = 4.6\ \%$

R2

The experimental protocol for R2 primary drainage is the same as R1, however we will use a D_2O-based brine (B4) for unambiguous detection of the oil phase (Marcol^{TM}-52) in order to facilitate fluids saturation monitoring during the experimental cycle. Moreover, saturation profiles monitoring during the experiment is also possible.

R2 is a twin sample extracted 4 m apart in the reservoir from sample R1. It also presents the same porosity & bi-modality.

During R2 experiment, we pushed the limit of HDT further as we tried to reach an even lower value of S_{wi} than for R1. In this case, after performing Step 1 at two flowrate values (30 cc/h and 60 cc/h), we moved to Step 2 where we progressively increased capillary pressure. At first, we applied $Pc = 8\,bar$ until saturation profiles reached equilibrium. Then, as we were far from the S_{wi} target, we increased the pressure to the final capillary pressure of $Pc = 10\,bar$. Saturation profiles at each step of this experiment are presented in Figure 147: It is interesting to observe that CEE produced during Step 1 are substantially softer in this case. We used the same metrics mentioned during the proof of concept of HDT to compare the profile homogeneity at the end of Step 1 (2nd Flowrate) and at the end of Step 2 ($P_c = 10\,bar$).

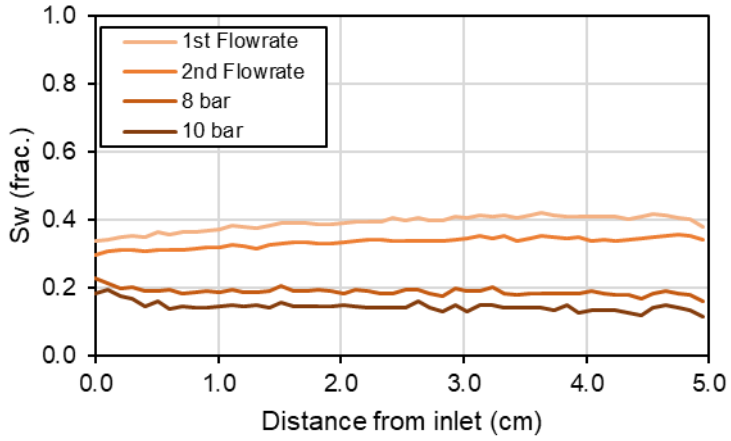

Figure 147 - S_w profiles during R2 primary drainage by HDT.

- $\overline{S_{w_{Step1}}} = 33.3\,\% \rightarrow \overline{S_{w_{Step2}}} = 14.4\,\%$
- $\sigma\,(S_w)_{Step\,1} = 1.5\,\% \rightarrow \sigma\,(S_w)_{Step\,2} = 1.4\,\%$
- $Max - min\ (S_w)_{Step\,1} = 5.8\,\% \rightarrow Max - min\ (S_w)_{Step\,2} = 8\,\%$

Considering the small effect observed close to the inlet face of the sample, the $Max - min\ (S_w)$ term has even increased after the transition to Step 2. This situation illustrates how light were CEE during the viscous-controlled step of this experiment.

4.2. Wettability challenges

After establishing initial water saturation, the next step in a classic experimental protocol is ageing the sample with crude oil. During this step, wettability alteration can occur. In this section, we will explore different ageing protocols used in the Petrophysics domain. The goal is to understand the efficiency of wettability alteration and whether experimental artifacts are produced following the ageing protocols. By an

efficient wettability alteration, we mean a homogeneous wettability profile, where the wettability alteration process may be considered completed.

4.2.1. Wettability alteration

The first aspect we discuss is whether an efficient wettability alteration may be achieved when performing either static or mono-directional flush of crude oil during ageing. For that, we have taken two Bentheimer sandstone samples (BEN-VOF-AM-02 and BEN-VOF-AM-03), set the same approximate S_{wi} by VOF (reversing flow for profile homogenization) using B1 and Marcol^{TM}-52, miscibly replaced the mineral oil by crude oil (O1) with an intermediate toluene flush to prevent asphaltene precipitation and followed two different protocols during ageing. Then, we performed a complete Amott-IFP cycle for both samples. Forced displacements were not performed in the centrifuge, as in classic Amott-Harvey tests, but by fluid injection using syringe pumps.

Flowrates used during primary drainage by VOF are presented in Table *27*:

Flowrate Step	Flowrate	Capillary Number
Q1	5 cc/h	4.0 10^{-7}
Q2	25 cc/h	2.0 10^{-6}
Q3	50 cc/h	4.0 10^{-6}
Q4	250 cc/h	2.0 10^{-5}
Q5	500 cc/h	4.0 10^{-5}

Table 27-Flowrate and Ca for BEN-VOF-AM-02 and BEN-VOF-AM-03 primary drainage (Marcol^{TM}-52)

a. Static ageing vs mono-directional crude oil flush during ageing

At the end of the primary drainage step, we performed an SE-SPI profile with the NMR to obtain the S_{wi} profile for both samples. This result is presented in Figure 148:

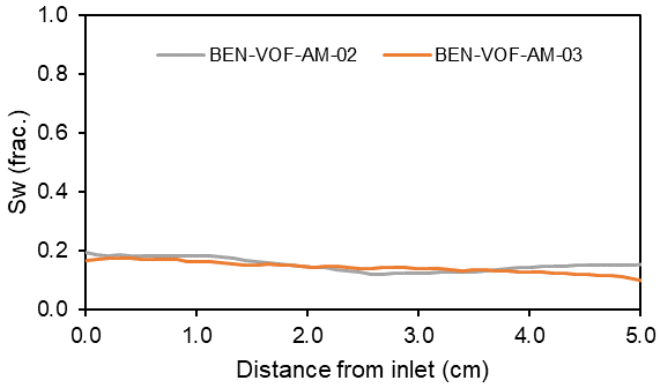

Figure 148 - S_{wi} profiles of BEN-VOF-AM-02 and BEN-VOF-AM-03.

- $\overline{S_{w}}_{\mathrm{BEN-VOF-AM-02}} = 15.2\ \%$
- $\overline{S_{w}}_{\mathrm{BEN-VOF-AM-03}} = 14.4\ \%$

In Figure 149 we present both samples T_2 relaxation time distributions before ageing. It is possible to notice that they have approximately the same response, as oil relaxes purely as bulk fluid, with no influence of interactions with the rock surface.

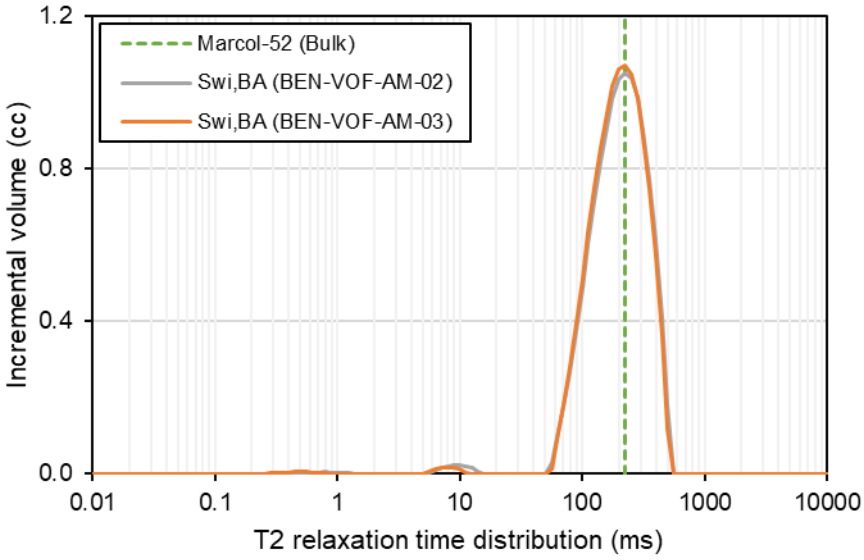

Figure 149 - T2 relaxation times distribution for BEN-VOF-AM-02 and BEN-VOF-AM-03 at S_{wi}, before ageing with crude oil.

After toluene flush and crude oil replacement, BEN-VOF-AM-02 undergoes static ageing and BEN-VOF-AM-03 is submitted to mono-directional crude oil flush. Ageing lasted for 14 days, and 15 Pore Volumes (PV) of crude oil were flushed through BEN-VOF-AM-03.

Unfortunately, wettability alteration through T_2 relaxation time shortening was not visible by T_2 Relaxation Time experiments, as Bentheimer sandstone surface relaxation distribution peak is centered at longer T_2 times (708 ms) than mineral oil (Marcol^{TM}-52) bulk relaxation times (251 ms). Therefore, it will not be possible to observe shifts in the T_2 spectrum representing wettability alteration.

Besides T_2 relaxation times shortening, there is another way to observe wettability alteration through T_2 relaxation times tests. Let's consider a water-wet rock sample composed of big pores, which results on a surface T_2 relaxation distribution peak centered at long T_2 times (*e.g.,* 700 ms). This sample is initially fully-saturated with a D_2O-based brine and follows primary drainage with mineral oil. Performing a T_2 relaxation time distribution test at this stage will result in pure T_2 bulk relaxation behavior, as oil is located in the center of the pores with no interaction with the rock surface. Considering that the T_2 bulk relaxation time response of the mineral oil is centered at the same T_2 time as the rock surface relaxation, *i.e.,* 700 ms, no shift towards short values of T_2 relaxation times will be observed after wettability alteration, even though oil wets the rock surface after wettability alteration. The reason for this behavior is that it is not possible to obtain T_2 relaxation times than are shorter than the surface relaxation time of the rock. Nonetheless, rock samples usually present broader T_2 relaxation times distribution than that of bulk mineral oil. Therefore, a broader T_2 relaxation times distribution may represent oil wetting the rock surface, although no left-shift was observed in the T_2 spectrum.

The behavior explained herewith was observed for both samples, as presented in Figure 150.

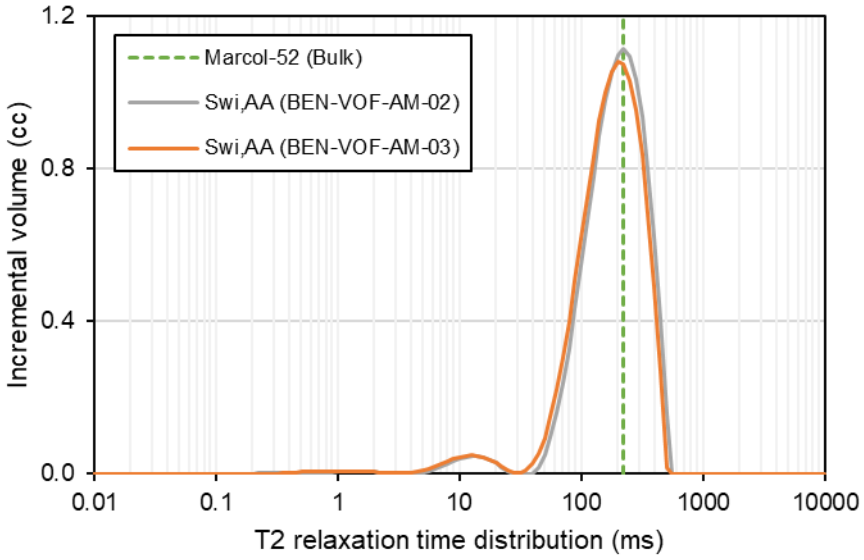

Figure 150 – T_2 relaxation time distribution test of samples BEN-VOF-02 and BEN-VOF-AM-03 after ageing.

After the ageing step, samples are loaded in the spontaneous imbibition apparatus. Oil production (and brine imbibition) during this step already indicates different brine affinities between the samples, as seen in Figure 151:

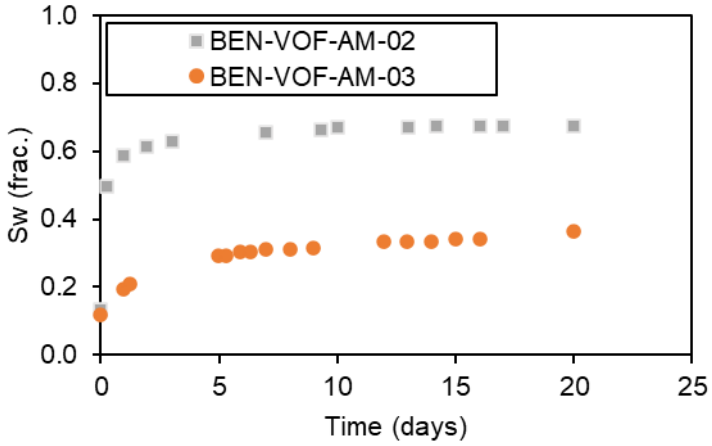

Figure 151 - Brine production during spontaneous imbibition (BEN-VOF-AM-02 and BEN-VOF-AM-03).

- $V_{w_{2\,\mathrm{BEN-VOF-AM-02}}} = 7.68$ cc
- $V_{w_{2\,\mathrm{BEN-VOF-AM-03}}} = 3.64$ cc

Furthermore, water saturation profiles after spontaneous imbibition indicate completely different behavior between the samples. The sample submitted to static ageing has a homogeneous profile for around 80 % of its length, whereas the sample submitted to mono-directional crude oil flush presents an important saturation gradient along its longitudinal axis. The saturation gradient increases in the direction of crude oil injection during replacement and ageing, which may indicate a wettability gradient in the sample. These results are presented in Figure 152:

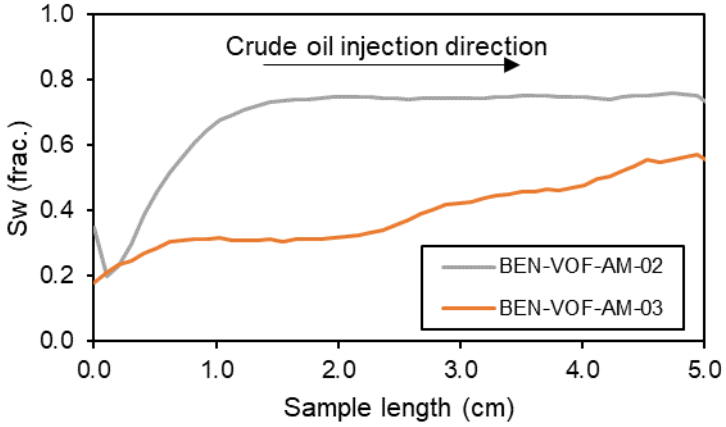

Figure 152 - S_w profiles after spontaneous imbibition (BEN-VOF-AM-02 and BEN-VOF-AM-03).

Forced imbibition was performed by brine injection at constant flowrate. Brine injected during forced imbibition had the same composition of resident brine (B1). The three flowrate steps used during forced imbibition are presented in Table *28*:

Flowrate Step	Flowrate	Capillary Number
Q1	5 cc/h	$3.9\ 10^{-8}$
Q2	50 cc/h	$3.9\ 10^{-7}$
Q3	200 cc/h	$1.6\ 10^{-6}$

Table 28-Flowrate and Ca for BEN-VOF-AM-02 and BEN-VOF-AM-03 forced imbibition

S_w profiles after forced imbibition are presented in Figure 153. It is possible to notice a limited presence of CEE, but both profiles are almost superimposed. Moreover, we are able to calculate the Amott Index to water using equation (18):

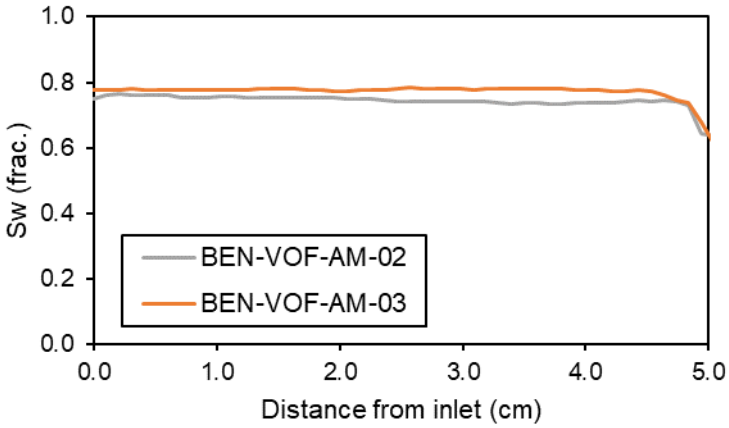

Figure 153 - S_w profiles after forced imbibition (BEN-VOF-AM-02 and BEN-VOF-AM-03).

- $V_{w_{3\,\mathrm{BEN-VOF-AM-02}}} = 0.92$ cc $\rightarrow$ $\mathbf{I_{w_{BEN-VOF-AM-02}} = 0.89}$
- $V_{w_{3\,\mathrm{BEN-VOF-AM-03}}} = 5.74$ cc $\rightarrow$ $\mathbf{I_{w_{BEN-VOF-AM-03}} = 0.39}$

As expected, the Amott Index to water "I_w" of the sample submitted to a larger PV number of crude oil during ageing presented a lower value, meaning that the

sample BEN-VOF-AM-03 has less affinity to brine than BEN-VOF-AM-02. As mentioned in section 1.8.4, dedicated to wettability alteration according to the ageing technique adopted, the classical justification for this behavior is that wettability alteration is dependent on the amount of crude oil flushed during the ageing step.

Progressing to the secondary drainage part of the Amott-IFP cycle, samples were loaded into spontaneous drainage cells with Marcol^{TM}-52. However, brine production, thus oil retained, by both samples was little, even though a slightly bigger retainment was noticed for the sample submitted to dynamic ageing (BEN-VOF-AM-03), besides presenting some desaturation at the inlet face used for oil flush during ageing. S_w profiles after spontaneous drainage are presented in Figure 154, followed by oil retainment (V_{O_2}):

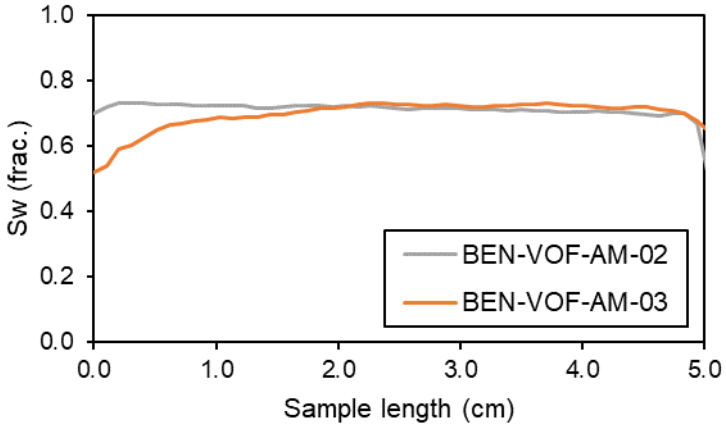

Figure 154 - S_w profiles after spontaneous drainage with Marcol^{TM}-52 (BEN-VOF-AM-02 and BEN-VOF-AM-03).

- $V_{O_2}{}_{\mathrm{BEN-VOF-AM-02}} = 0.49$ cc
- $V_{O_2}{}_{\mathrm{BEN-VOF-AM-03}} = 1.25$ cc

Finally, the last step of the Amott-IFP cycle was performed with the forced drainage with Marcol^{TM}-52. The results are as follows:

- $V_{O_3}{}_{\mathrm{BEN-VOF-AM-02}} = 7.77$ cc $\rightarrow$ $\mathbf{I_{o_{BEN-VOF-AM-02}} = 0.06}$
- $V_{O_3}{}_{\mathrm{BEN-VOF-AM-03}} = 8.11$ cc $\rightarrow$ $\mathbf{I_{o_{BEN-VOF-AM-03}} = 0.13}$
- $\mathbf{I_{AIFP_{BEN-VOF-AM-02}} = 0.83}$
- $\mathbf{I_{AIFP_{BEN-VOF-AM-03}} = 0.25}$

This result clearly shows the difference in performing static or dynamic ageing regarding the total wettability alteration, which confirms data from the literature and previous works from other authors. Furthermore, performing mono-sense crude oil flood during ageing allowed the confirmation, by SE-SPI NMR profiles, of the results observed by Graue *et al.* (2002).

EST-PP-AM-01

The main objective of this experiment is observing a clear shift in the T_2 signal due to wettability alteration besides showing the risk of generating a heterogeneous wettability profile even for a sample initialized by the Porous Plate method (reference technique for setting S_{wi}) when performing mono-directional crude oil flush. Estaillades

samples are a good candidate for this analysis, as its natural T_2 surface relaxation times is shorter than Marcol^{TM}-52 bulk relaxation times, besides having the dual-porosity aspect.

Sample EST-PP-AM-01 was initialized by the Porous Plate method using B2 and Marcol^{TM}-52 as couple of fluids. The last capillary pressure step of primary drainage was performed at $Pc = 5\ bar$. A homogeneous saturation profile was generated after primary drainage, as seen in the SE-SPI test presented in Figure 155 and in the Spatially-resolved T_2.presented in Figure 156.

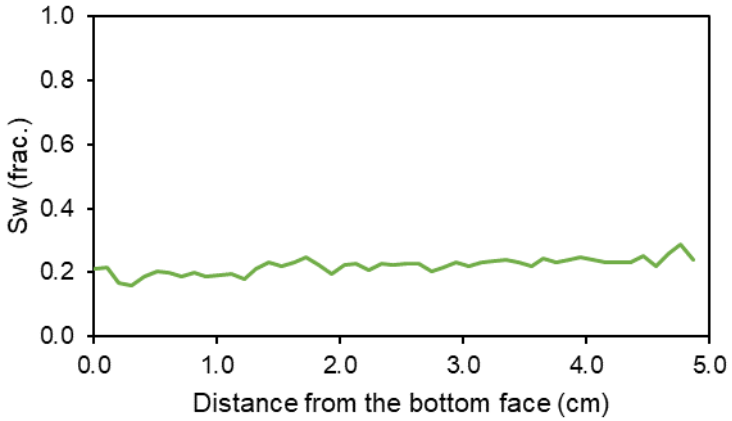

Figure 155 – S_w profile after primary drainage by Porous Plate (EST-PP-AM-01).

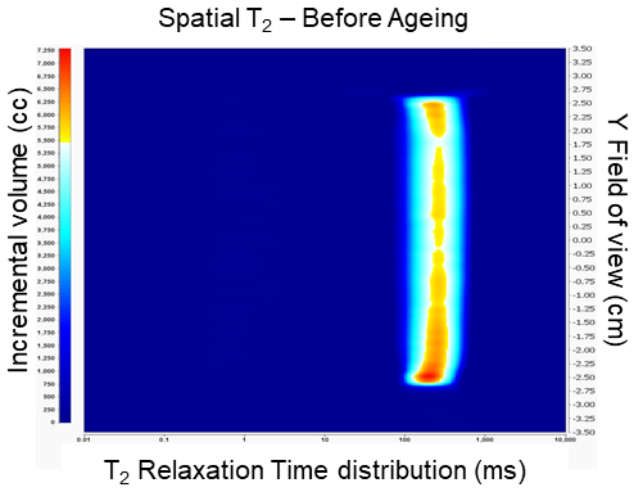

Figure 156 - Spatially-resolved T_2 measurement before ageing with EST-PP-AM-01 in Marcol^{TM}-52 and B4.

It is also interesting to observe that the dual-porosity aspect of the sample is not visible in Spatial T_2 at this point, as oil relaxes purely as bulk fluid.

Ageing was performed following the same protocol as BEN-VOF-03, with 15 VP of crude oil flushed in one direction exclusively. It is important to notice that water saturation profile after ageing is still homogeneous, as presented in Figure 157.

Figure 157 – S_w volume profiles before and after ageing (EST-PP-AM-01).

Nonetheless we observe several interesting parameters when comparing T_2 relaxation times distribution prior and after ageing, presented in Figure 158

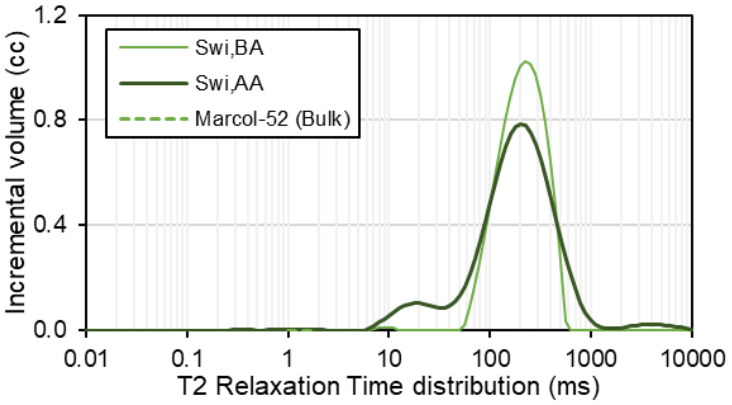

Figure 158 – Superimposition of T2 relaxation time distribution tests performed prior and after ageing with EST-PP-AM-01 in Marcol™-52 and B4.

The results obtained by Spatially-resolved T_2 (regular and stack-plot visualization) after ageing are presented in Figure 159. An important note regarding the spatially-resolved tests: the plug orientation is inversed to the orientation used in the SE-SPI experiments (1D S_w profiles).

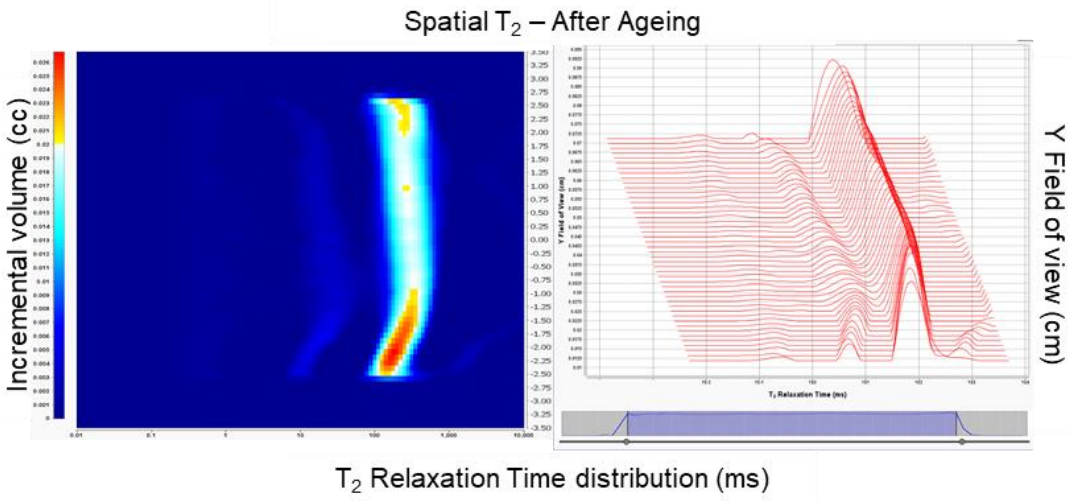

Figure 159 - Spatially-resolved T_2 measurement after ageing with EST-PP-AM-01 in Marcol™-52 and B4.

We observe the emergence of a signal representing the small pores in both tests that was not present in the measurement performed before ageing, indicating that oil did enter the smaller porosity of the sample during primary drainage, and, after ageing, oil wets this region at some extent, changing from a bulk T_2 relaxation before ageing to a surface T_2 relaxation after ageing. In addition, a left-shift in the T_2 relaxation time position of bigger pores in the sample extremities indicates that oil increased its surface relaxation signal, thus wetting the surface. It is possible to notice a big left-shift of the T_2 relaxation time in the inlet used for crude oil flood during ageing, in the bottom part of Figure 159.

During spontaneous imbibition, no production was observed in the cell. However, little production was noticed by mass balance and T2 NMR. Considering the mass balance values, we have for the brine volume imbibed:

- $V_{w_{2\,\mathrm{EST-PP-AM-01}}} = 1.4$ cc

The water saturation profile after spontaneous imbibition shows a gradient in water saturation, the same way as seen for BEN-VOF-AM-03, which presents bigger oil presence close to the inlet face where crude oil was injected during ageing; In Figure 160 we present the S_w profiles after ageing and after spontaneous imbibition:

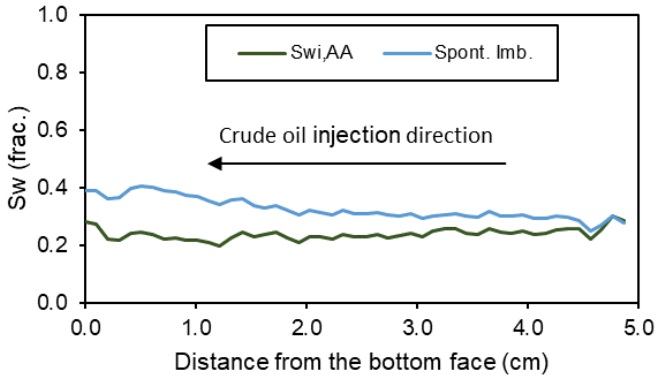

Figure 160 – S_w profile after ageing and spontaneous imbibition, and the direction of crude oil injection during ageing (EST-PP-AM-01).

We then loaded the sample in the centrifuge for performing the forced imbibition step. We used the same resident brine for forced imbibition (B2). Rotational speeds used in the experiment, the associated capillary pressure, and the Bond Number are presented in Table *29*:

Rotational speed	Inlet P_c (o/w)	Bond Number
500 rpm	0.08 bar	$1.1\ 10^{-6}$
700 rpm	0.16 bar	$2.1\ 10^{-6}$
1000 rpm	0.33 bar	$4.2\ 10^{-6}$
1500 rpm	0.73 bar	$9.4\ 10^{-6}$
3500 rpm	3.98 bar	$5.1\ 10^{-5}$

Table 29-Rotational speed steps, inlet P_c and Bond Number for EST-CEN-01 forced imbibition by centrifugation.

After forced imbibition, we have performed another SE-SPI profile measurement in the NMR for observation of the generation of CEE during imbibition, as presented in Figure 161.

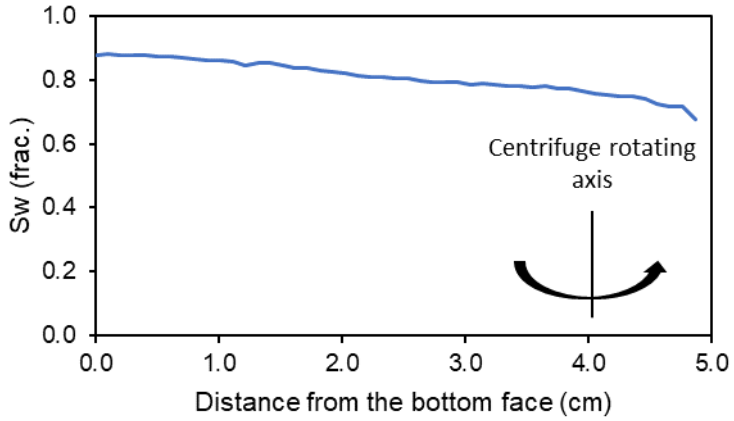

Figure 161 - S_w profile after forced imbibition (EST-PP-AM-01).

Moreover, we weighted the sample to obtain the produced oil volume during this step, for further calculation of the Amott Index to water, presented here below:

- $V_{w_{3\,\mathrm{EST-PP-AM-01}}} = 7.6\ \mathrm{cc} \rightarrow \mathbf{I_{w_{EST-PP-AM-01}}} = \frac{\mathbf{Vw_2}}{\mathbf{Vw_2+Vw_3}} = \frac{\mathbf{1.4}}{\mathbf{1.4+7.6}} = \mathbf{0.16}$

From the brine production monitoring data, we are able to define the imbibition capillary pressure curve *versus* water saturation. This curve must be corrected from the CEE generated during centrifugation. We use the analytical solution of Forbes to perform this correction (Forbes, 1994). The experimental points obtained during centrifugation and the corrected forced imbibition P_c *versus* S_w curve is presented in Figure 162:

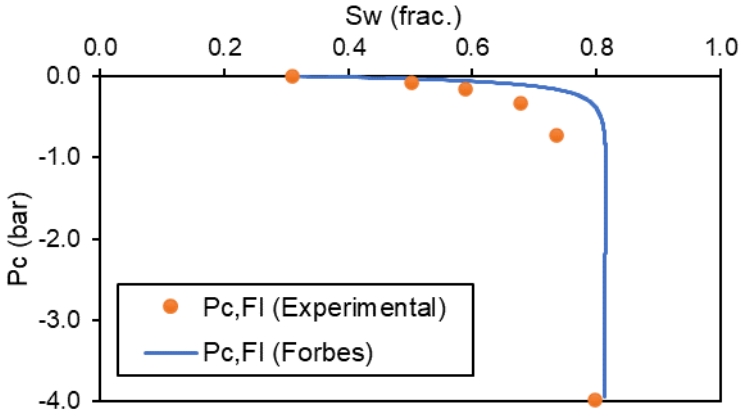

Figure 162 - Forced imbibition P_c versus S_w curve for EST-PP-AM-01.

These results confirm the expected behavior of this sample after wettability alteration through ageing with crude oil, as we observe a minor affinity to brine, represented by the small amount of water spontaneously imbibed, and the shape of the imbibition capillary pressure curve. The next steps are the verification of the sample affinity to oil during spontaneous drainage and the establishment of irreducible water saturation during a secondary drainage (forced drainage).

After loading the sample in the spontaneous drainage cell with Marcol™-52, we did not notice any brine production in the burette of the cell. This result was confirmed by mass balance measurements, meaning that the sample does not present affinity to oil either.

- $V_{O_{2_{EST-PP-AM-01}}} = 0.03\ cc$

Nonetheless, NMR SE-SPI profile measurement shows a small oil imbibition in the face submitted to higher capillary pressure during forced imbibition and a general homogenization of the S_w profile. This result is presented in Figure 163:

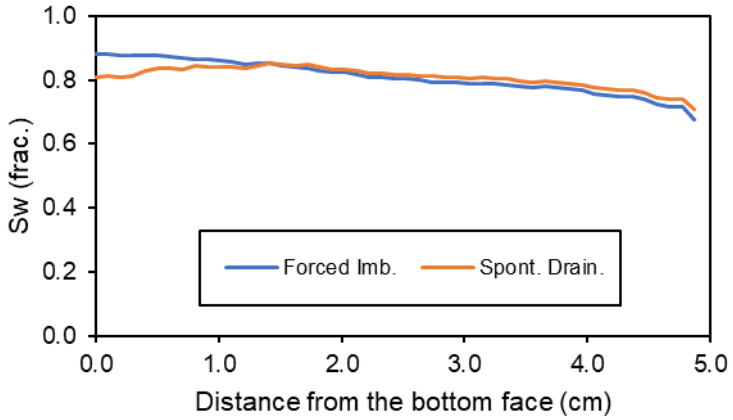

Figure 163 - S_w profiles after forced imbibition and spontaneous drainage (EST-PP-AM-01).

To finish the Amott-Harvey cycle, we loaded the sample in the centrifuge to perform the secondary drainage (forced drainage). We used Marcol™-52 to ensure the coherence between the entire experimental cycle. The rotational speed steps, the associated capillary pressure, and the Bond Number are presented in Table *30*:

Rotational speed	Inlet P_c (o/w)	Bond Number
500 rpm	0.08 bar	$1.1\ 10^{-6}$
1000 rpm	0.32 bar	$4.2\ 10^{-6}$
1500 rpm	0.73 bar	$9.4\ 10^{-6}$
2000 rpm	1.30 bar	$1.7\ 10^{-5}$
2500 rpm	2.03 bar	$2.6\ 10^{-5}$
3000 rpm	2.92 bar	$3.8\ 10^{-5}$

Table 30-Rotational speed steps, inlet P_c and Bond Number for EST-CEN-01 forced drainage by centrifugation.

In possession of the production data and the associated capillary pressure points, we were able to perform once more Forbes analytical correction (Forbes, 1994). In Figure 164, we present the secondary drainage P_c *versus* S_w curve.

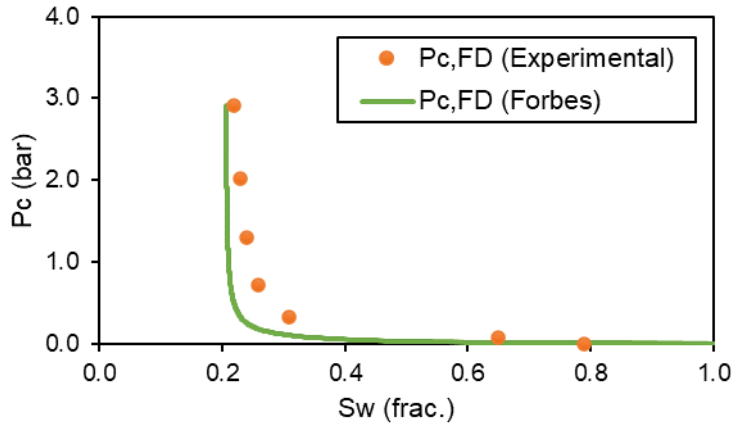

Figure 164 - P_c versus S_w curve for EST-PP-AM-01 secondary drainage. We present the experimental points and the analytical Forbes correction.

Furthermore, we have imaged the sample with the NMR to obtain the final profile after secondary drainage. This result is presented in Figure 165.

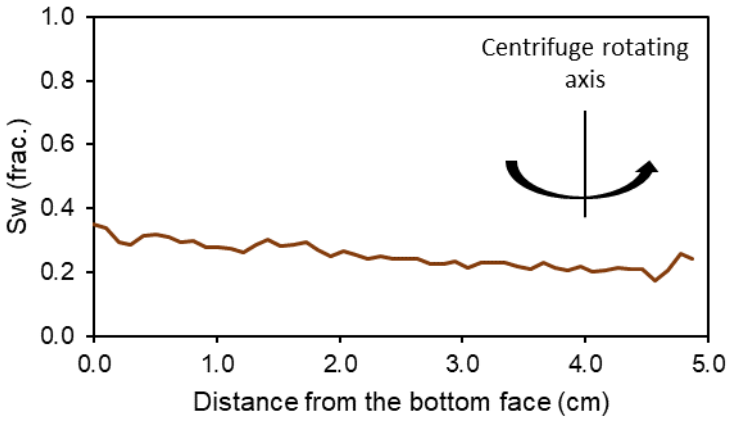

Figure 165 - S_w profile after forced drainage (EST-PP-AM-01)

At this stage, we have all the elements to calculate the Amott-Harvey wettability Index.

- $V_{O_{3\,\mathrm{EST-PP-AM-01}}} = 8.76$ cc $\rightarrow$ $\mathbf{I_{o_{EST-PP-AM-01}} = 0.00}$
- $\mathbf{I_{AH_{EST-PP-AM-01}} = 0.16}$

In addition, as we performed the forced steps of this experiment in the centrifuge, we are also able to calculate the USBM Wettability Index, as follows:

- $A_{1_{EST-PP-AM-01}} = 0.053; A_{2_{EST-PP-AM-01}} = 0.039$
- $\boldsymbol{I_{USBM_{EST-PP-AM-01}} = log\left(\frac{A_1}{A_2}\right) = 0.13}$

It is interesting to notice that both $\mathbf{I_{AH}}$ and $\mathbf{I_{USBM}}$ indicate a sample with intermediate wettability. This result is mainly controlled by the extremely low amount of oil imbibed during the spontaneous drainage step.

b. Crude oil flush during ageing with flow reversal

We used flow reversal during crude oil flush for samples EST-HDT-01, EST-VOF-01, EST-HDT-02 and EST-HDT-03-M, as these samples are supposed to follow

the same experimental protocol, except for the primary drainage technique used for setting S_{wi} and the different S_{wi} target for EST-HDT-01.

Prior replacing mineral oil (Marcol™-52 in all of these cases) by crude oil, we performed a toluene flush to prevent crude oil and mineral oil contact, which could destabilize asphaltenes and cause premature precipitation. During the ageing phase, we injected 15 Vps of crude oil (under dP monitoring) for 14 days, alternating injection direction. dP monitoring allows the observation of K_{eff} evolution during ageing, indicating that wettability is being altered through the process. In addition, we performed a comparison of T_2 Relaxation Time distribution prior and after ageing, to monitor wettability alteration.

EST-HDT-01

We have performed oil flush reversal during ageing by injecting at low flowrate $\left(Q = 0.1\frac{cc}{min}\right)$ in order to prevent further brine production during this process. dP monitoring was done for each injection interval during ageing. In order to present this phenomenon in only one figure, we concentrated every dP *versus* time curves of each injection in one graph and used a color gradient to represent the different days and injection direction. The positive dP values (green color) represent downwards injection and negative dP values (orange color) represent upwards injection. Furthermore, color gradient identify ageing days: curves get darker according to the corresponding ageing day. It is possible to notice an absolute increase in the dP signal over ageing time, tendency currently associated with wettability alteration. This process may be observed in Figure 166:

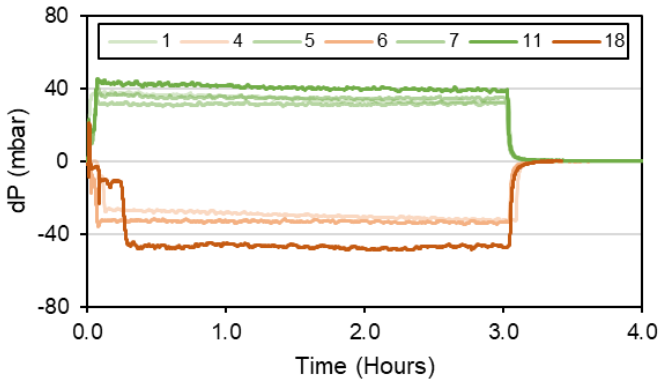

Figure 166 - dP monitoring during crude oil injection with flow reversal (EST-HDT-01). Color darkening represent time evolution, and negative values of dP represent inlet swapping as we reversed flow direction during ageing.

We observed for this sample a slight reduction in effective permeability to oil after ageing, as presented below. We discussed every effective permeability reduction after ageing for the ensemble of Estaillades samples at the section dedicated to EST-HDT-03-MP.

- $K_{o,eff_{BA}} = 147\ mD \rightarrow K_{o,eff_{AA}} = 125\ mD \therefore K_{row_{AA}}(S_{wi}) = 0.85$

T_2 experiments on this sample present quite interesting results. We have used a H_2O-based brine, thus allowing the visualization of both brine and oil phases throughout the experimental cycle. Prior ageing, we have intentionally replaced mineral oil by toluene to enhance contrast between oil and water phases in the T_2 spectrum, given low viscosity of the toluene. Although we have confirmed that oil (toluene, in this case) had invaded the smaller porosity during Step 2 of HDT from the

response of the brine signal amplitude, its own T_2 signal did not reflect smaller porosity invasion, as it relaxes as bulk fluid. However, as oil breaks water films during ageing and coats the rock surface, oil T_2 relaxation time distribution changes its shape, better describing the pore structure, which is an indication of surface coating. In addition, it is possible to notice a left-shift in oil T_2 signal peak, related to this same phenomenon. These results may be observed in T_2 relaxation time distribution tests performed after ageing, that are presented in Figure 167 together with the test performed before ageing for comparison.

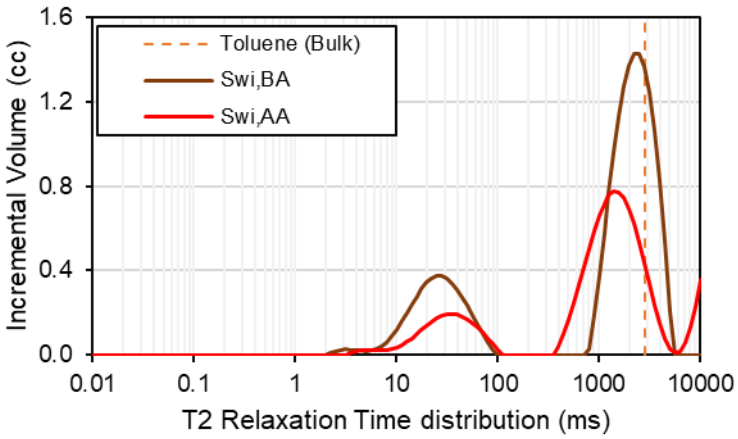

Figure 167 - T_2 curves before and after ageing (H_2O-based brine – B3 and toluene) - EST-HDT-01.

To analyze the water phase behavior in this case, we must take the result of the spatially-resolved T_2 test, once brine saturating the porous plate fades the signal of S_{wi} brine present in the sample. Observing this result, presented in Figure 168 and in Figure 169 as a stack plot, it is possible to see that the brine signal presents a huge left shift, probably due to brine concentration in the corners of the smaller pores, as oil broke the water films coating the rock surface during ageing.

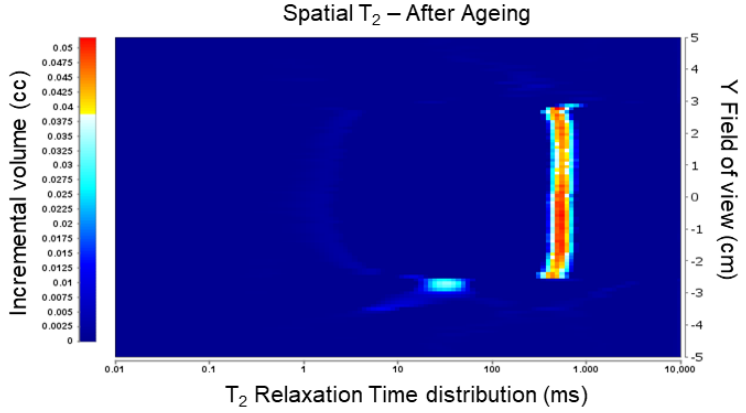

Figure 168 - Spatially-resolved T_2 test with EST-HDT-01 performed after ageing (Toluene as the oil phase and B4).

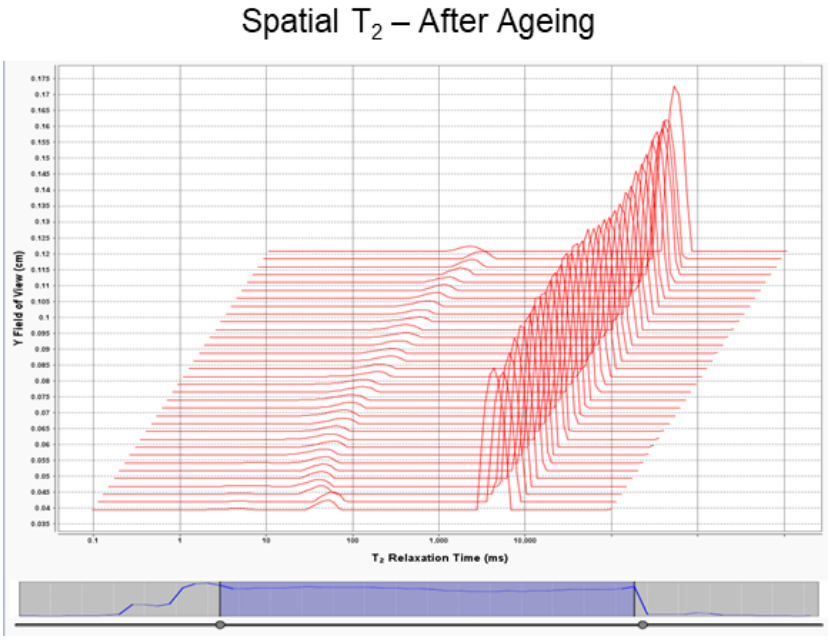

Figure 169 - Stack plot of the T_2 relaxation time distribution curves of EST-HDT-01 performed after ageing.

The sequence of the experimental protocol involves a toluene replacement by Marcol™-52. Given the substantial viscosity difference between Marcol™-52 and B2 ($^{\mu_o}/_{\mu_w} \approx 11.3$), it is possible to separate phases signals by means of their diffusion coefficient. Therefore, we performed a $T_2, Diff$ test, which allowed the distinct visualization of oil present in the smaller porosity ($T_2 \approx 25\, ms$ and $D_{coeff} \approx 1\,10^{-8}\ ^{cm^2}/_{ms}$). In addition to this signal, we are also able to observe the contribution from oil in bigger porosity ($T_2 \approx 251\, ms$) and the brine phase ($D_{coeff} \approx 7\,10^{-8}\ ^{cm^2}/_{ms}$). These results are presented in Figure 170, where the boarders limiting brine and oil diffusion coefficients are represented by the horizontal lines.

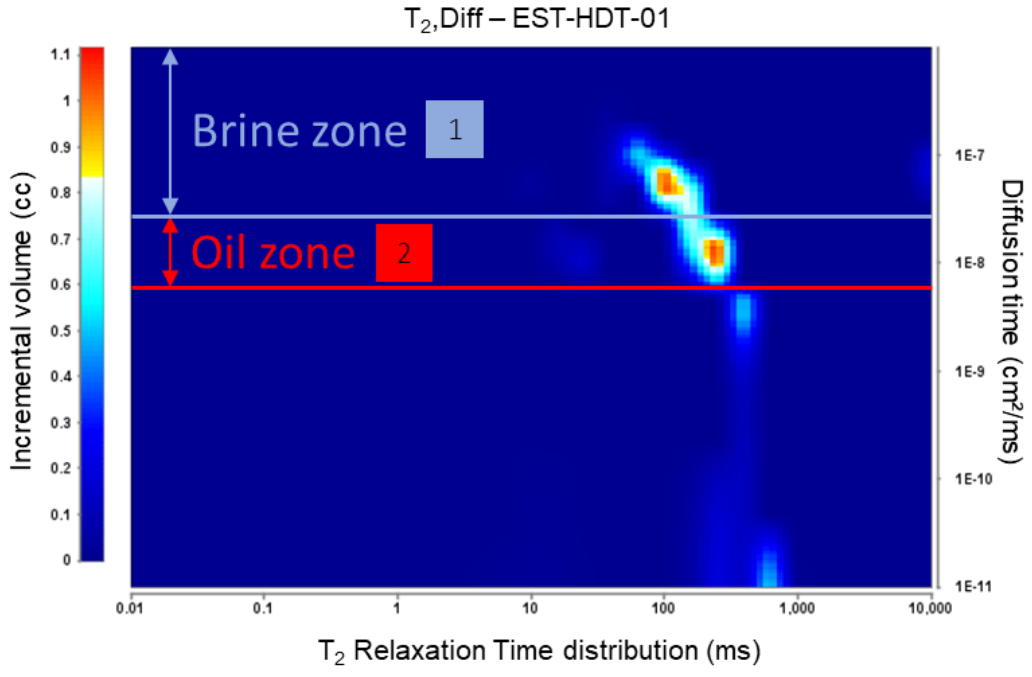

Figure 170 - T_2,Diff experiment for EST-HDT-01 after ageing (Marcol™-52 and B3).

EST-VOF-01

In the same way as done for EST-HDT-01, we have monitored dP during multidirectional crude oil injection. This result is presented in Figure 171, and the same color code was used in this case: time advancing is represented by the transition from brighter to darker colors.

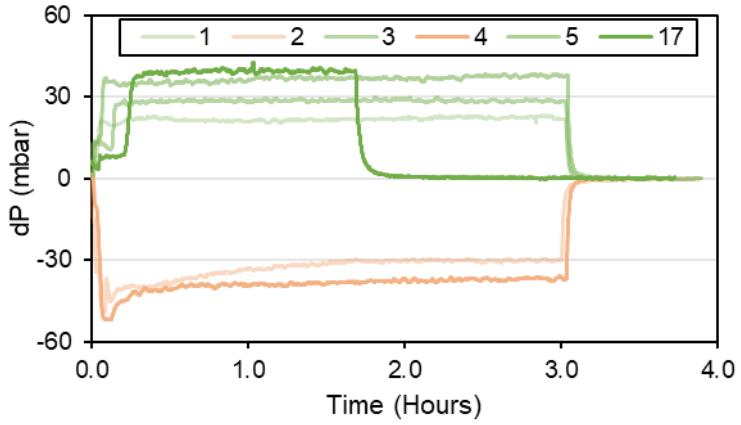

Figure 171 - dP monitoring during crude oil injection with flow reversal (EST-VOF-01).

Unfortunately, some curves could not be included in the previous figure, due to a problem with the acquisition system.

Effective permeability alteration is mentioned below:

- $K_{o,eff_{BA}} = 201\ mD \rightarrow K_{o,eff_{AA}} = 160\ mD \therefore K_{row_{AA}}(S_{wi}) = 0.79$

The main reason for the struggle in reaching low values of S_{wi} ($S_{wi} < 35\%$) by the Viscous Oil Flood method on Estaillades is the dual-porosity and poor pore connectivity of these samples. Given that oil primary drainage relative permeability is controlled by the bigger porosity, a viscous-controlled method such as VOF is not capable of acceding the smaller pores.

This assumption is visible when we compare T_2 Relaxation Time distribution tests prior and after ageing. In the case of EST-VOF-01, initialized by Viscous Oil Flood, we see a minor T_2 Surface Relaxation signal after ageing, which is related to oil wetting the rock surface in the smaller porosity. Therefore, this finding confirms the expected physical behavior of oil during primary drainage, by-passing almost completely this fraction of the rock porosity. The comparison of T_2 tests before and after ageing is presented in Figure 172:

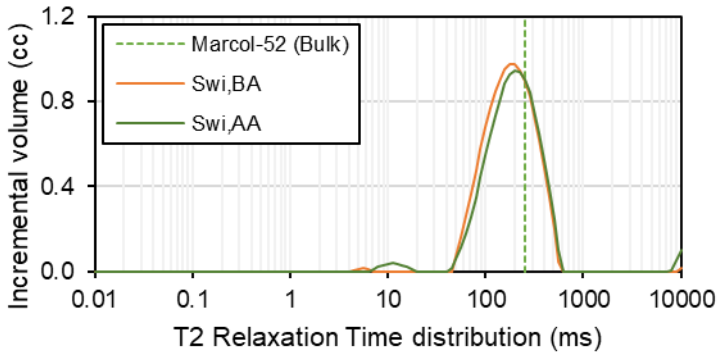

Figure 172 - Comparison of the T_2 response before and after ageing for sample EST-VOF-01 at S_{wi} with Marcol™-52 and B4.

In the case of a capillary-controlled primary drainage method, *e.g.*, HDT, we will observe that, even though the same S_{wi} was set such as in EST-VOF-01, the oil invasion process is different, resulting in oil invading both bigger and smaller porosities. This result will be furtherly discussed in the presentation of EST-HDT-02 and EST-HDT-03-MP.

EST-HDT-02

The same ageing protocol was used for this sample, however due to technical issues, dP curves during ageing were not recorded. Notwithstanding, we measured the effective permeability to oil alteration between before and after ageing. In this case we notice a more substantial change than that observed for EST-VOF-01, despite at the same level of S_{wi}. This result is presented here below:

- $K_{o,eff}{}_{BA} = 258\ mD \rightarrow K_{o,eff}{}_{AA} = 106\ mD \therefore K_{row}{}_{AA}(S_{wi}) = 0.41$

In the case of this sample, we have performed NMR imaging at S_{wi} on crude oil, *i.e.,* prior to crude oil replacement by mineral synthetic oil with an intermediate toluene flush. The imaging at this precise state presents interesting results in terms of T_2 relaxation time left-shift of the oil phase, indicating wettability alteration. As in this case we have used a D_2O-based brine (B2) such as for EST-VOF-01, there is no brine and oil signal overlapping, as only the oil phase is visible by NMR.

T_2 relaxation times distribution presents a main signal (originally from oil present in the larger porosity) that is shifted from O1 T_2 Bulk relaxation time. Moreover, it is also possible to observe the signal associated to oil present in the smaller porosity. This result is presented in Figure 173:

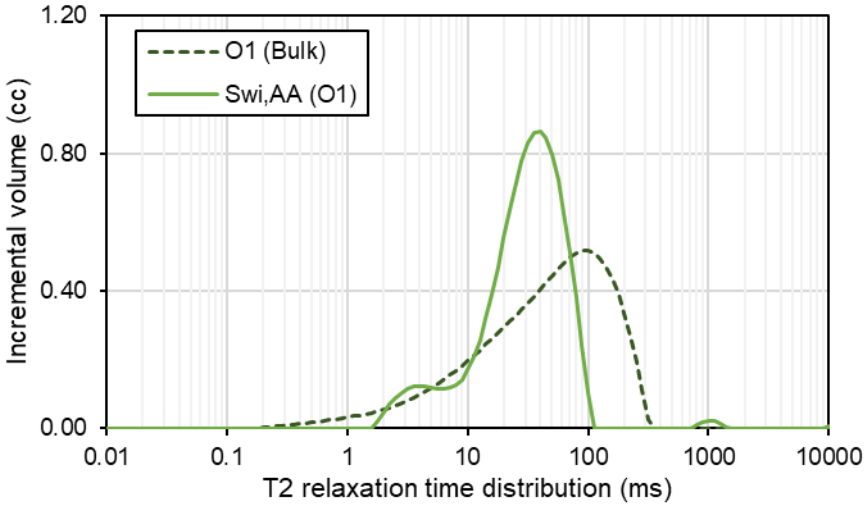

Figure 173 - T_2 Relaxation time distribution for EST-HDT-02 at S_{wi} in crude oil (O1), after ageing (B4 as the brine phase).

Moreover, a spatially-resolved T_2 (Figure 174) experiment showed that the overall left-shift of the T_2 signal is homogeneously distributed through the sample, which indicates a homogeneous wettability alteration after ageing.

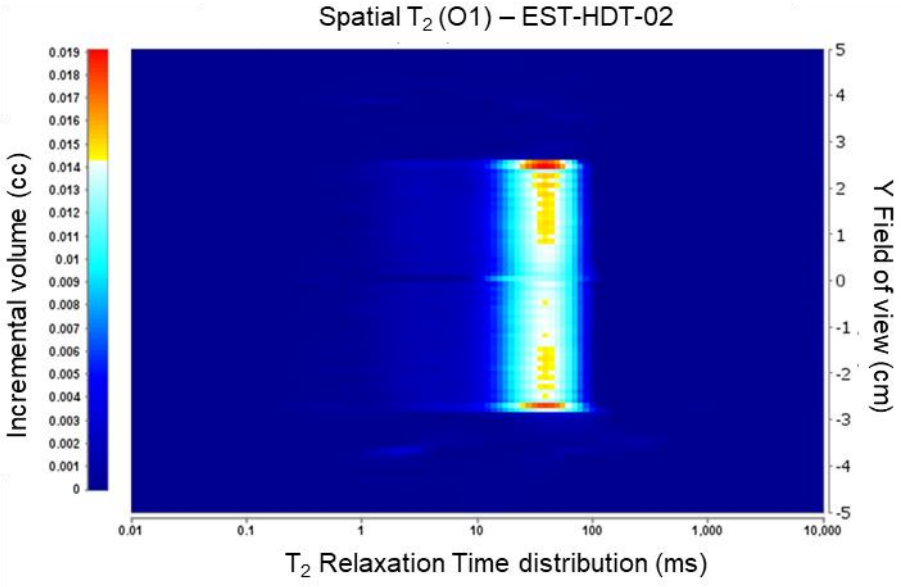

Figure 174 - Spatially-resolved T_2 of EST-HDT-02 at S_{wi} in crude oil (O1) after ageing (B4 as the brine phase).

In addition, since acquisition of the sample in crude oil after ageing seems to be more sensitive to a left-shift related to wettability alteration, we performed a $^{T_1}/_{T_2}$ chart acquisition, because this is considered as the reference technique for wettability alteration investigation by NMR analysis (Valori *et al.*, 2017; Valori & Nicot, 2019).

The result from the T_2 relaxation time experiment indicates that an important shift of the oil phase in terms of $^{T_1}/_{T_2}$ is expected. As we have seen previously, an up-leftwards shift from the main diagonal represents an alteration in the relaxation mechanism of the liquid, meaning that T_2 bulk relaxation is impacted by T_2 surface

relaxation, hence representing wettability alteration. $^{T_1}/_{T_2}$ chart of EST-HDT-02 at S_{wi} in crude oil after ageing is presented in Figure 175.

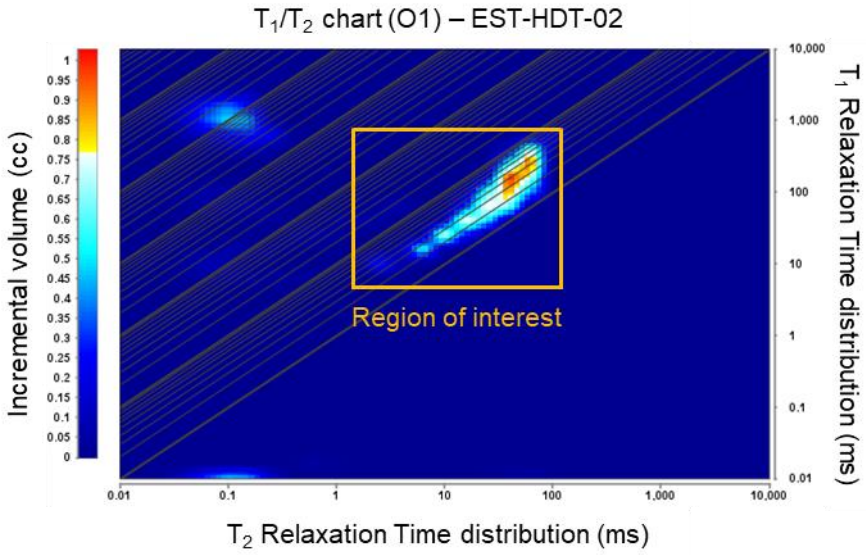

Figure 175 - T_1/T_2 chart for EST-HDT-02 at S_{wi} in crude oil (O1) after ageing and B4 as the invisible brine phase.

It is possible to notice that the up-leftwards shift is homogeneous to all the signal spectrum, which represents a homogeneous response of the sample to the wettability alteration. Taking the average $^{T_1}/_{T_2}$ ratio, we obtain $^{T_1}/_{T_2} = 4$, far from the expected ratio of a water-wet sample ($^{T_1}/_{T_2} = 1$). This is another indication of the wettability alteration of this sample.

After performing the crude oil replacement by Marcol™-52, we repeated the same series of NMR tests. The results in terms of the left-shift in the T_2 signal associated to wettability alteration were less clear in this case. Even so, we observed the emergence of a signal at the relaxation time associated to smaller porosity, indicating wettability alteration in these pores, and an overall spread of the signal related to Marcol™-52 T_2 response after ageing. These two indications confirm that a wettability alteration occurred, despite the light left-shift of the oil T_2 peak.

The results obtained by T_2 and Spatially-resolved T_2 are presented in Figure 176 and Figure 177:

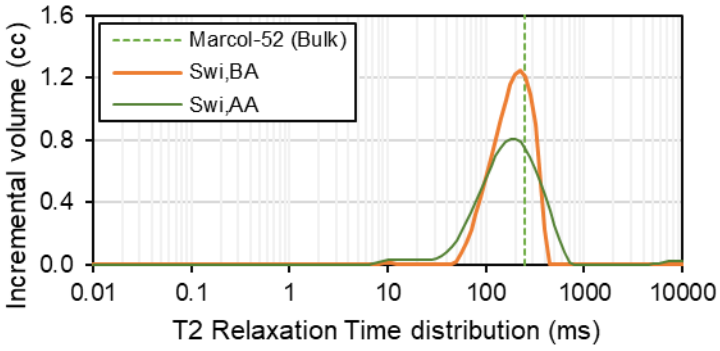

Figure 176 – Superimposition of T_2 results before and after ageing for EST-HDT-02 at S_{wi} with Marcol™-52 and B4 as oil and brine phases, respectively.

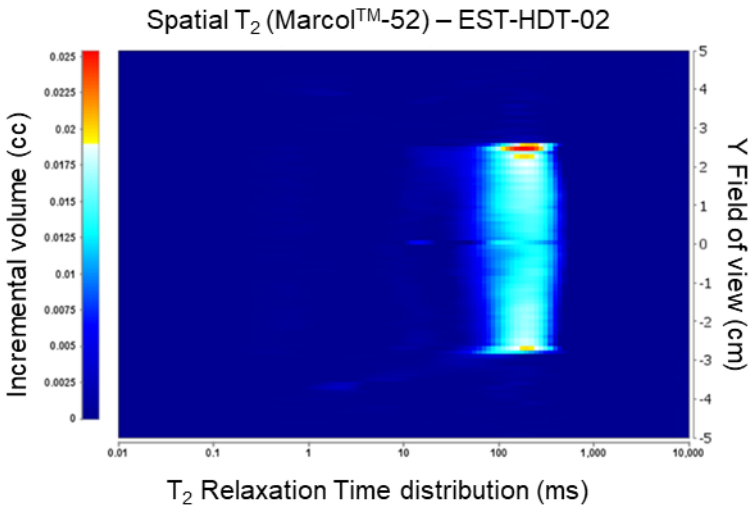

Figure 177 - Spatially-resolved T_2 test of EST-HDT-02 at S_{wi} with Marcol™-52 after ageing (B4 as the invisible brine phase).

Nonetheless, the T_1/T_2 ratio shift was not noticed at the same intensity after the crude oil replacement by mineral oil (Marcol™-52). The reason for this behavior is still uncertain. Considering that Marcol™-52 has a lower viscosity than O1, thus a longer Bulk T_2, we would expect an even bigger shift from Bulk T_2 towards T_2 Surface Relaxation.

EST-HDT-03-MP

When comparing µ-CT images before and after ageing at the same location in the sample, it is possible to notice some brine droplets appearing at the center of the pores (they are represented at intermediate gray attenuation at µ-CT scans). The theory of film rupture under high capillary pressure and temperature states that the water from the broke film will accumulate in the pore corners . Nonetheless, the result obtained by CT scan helps to illustrate the notion that, after ageing, effective permeability can be reduced, as the oil phase must flow in contact with the pore walls and has obstacles (brine droplets) located in the center of the pores. We are able to observe this phenomenon in two out of the four slices presented at the end of Steps 1 and 2. The two slices are shown in Figure 178.

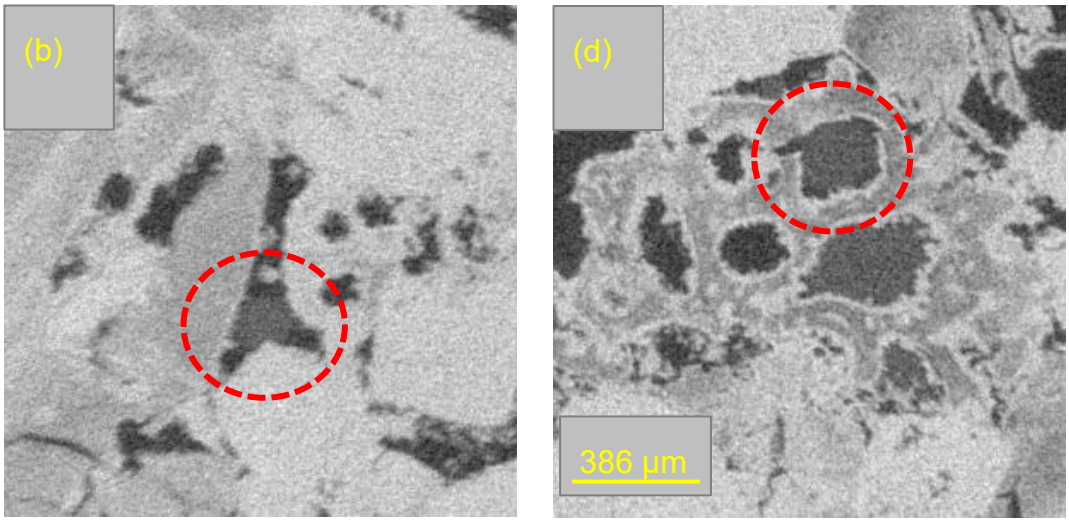

Figure 178 - 4 sections of EST-HDT-03-MP after ageing.

Effective permeability alteration from before to after ageing states is mentioned below:

- $K_{o,eff}{}_{before\ ageing} = 216\ mD \rightarrow K_{o,eff}{}_{after\ ageing} = 91\ mD$

We observe for this sample a reduction of $K_{o,eff}$ after ageing of the same magnitude as for EST-HDT-02. Despite the same level of S_{wi}, the reduction for EST-VOF-01 is less pronounced. The main assumption for this behavior is pore occupancy by the oil phase at the end of primary drainage. Considering that EST-VOF-01, EST-HDT-01 and EST-HDT-03-MP have the same S_{wi}, they do not have the same fluid distribution, as they were submitted to a different displacement process during primary drainage. In the case of the sample initiated by a exclusively viscous-controlled regime (EST-VOF-01), oil only invaded the smaller porosity where the applied capillary pressure exceeded the entry-pressure threshold, as previously presented in . Therefore, in order for the total average S_w be the same as for the HDT experiments ($Sw \approx 36\%$), brine in the bigger pores has very low saturation and is present in the form of thin films. When these films are broken during the ageing process due to wettability alteration of the rock, there is very limited volume of brine that will occupy the center of the pores, which seems to be the main reason for $K_{o,eff}$ reduction after ageing.

In the case of samples initiated by the Hybrid Drainage Technique, EST-HDT-02 and EST-HDT-03-MP, brine saturation in the big pores is higher than in the case of EST-VOF-01 for the same level of total S_{wi}. For these samples oil occupies both the big and small pores homogeneously along the sample longitudinal axis, as the Step 2 is a capillary-pressure controlled method, thus applying a homogeneous capillary pressure during primary drainage. Therefore, wettability alteration is supposed to be different than in the case of EST-VOF-01, as oil is more homogeneously distributed in the pore space. These assumptions are based in the pore-scale observation of some pores of EST-HDT-03-MP after ageing, where it is possible to notice a large presence of brine in the center of some big pores that, prior ageing, where fully-saturated in oil. The images comparing the same pores before and after ageing are presented in Figure 179:

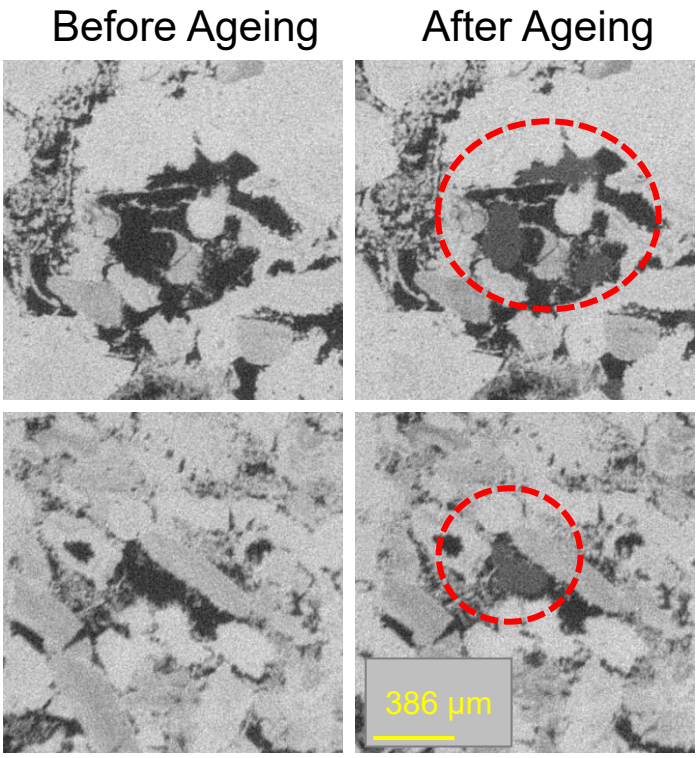

Figure 179 – Two couples of slices in different positions in the sample where it is possible to observe brine emergence after the ageing step.

The water droplets emergence in the center of big pores was captured during S_w profile calculation by µ-CT after ageing. Considering that the brine appearing in the center of the pores after ageing is originated from water films breaking (water films are not quantified by µ-CT imaging), it is expected that the water saturation viewed by µ-CT would increase. Another interesting factor that corroborates this hypothesis, is that the increase in water saturation is more pronounced where macro porosity prevails. The comparison of the water saturation profiles before and after ageing are presented in Figure 180, together with the macro-porosity profile.

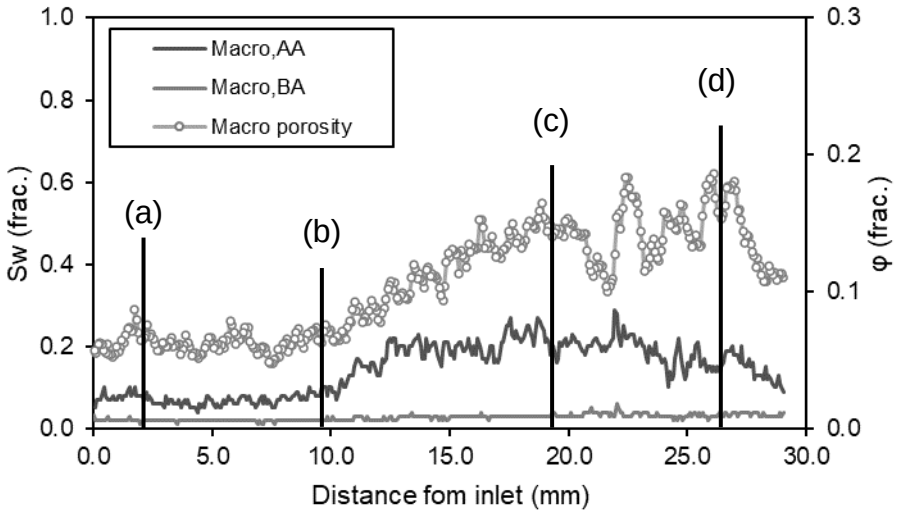

Figure 180 - Water saturation profiles of the macro porosity before and after ageing, and the macro porosity profile (EST-HDT-03-MP).

If we do the normalization of the S_w profile to remove the effect of porosity heterogeneity, as did for the unresolved porosity in the primary drainage analysis, it is possible to observe that the shift in the water saturation profile is nearly homogeneous along the longitudinal axis. This processing may be seen in Figure 181.

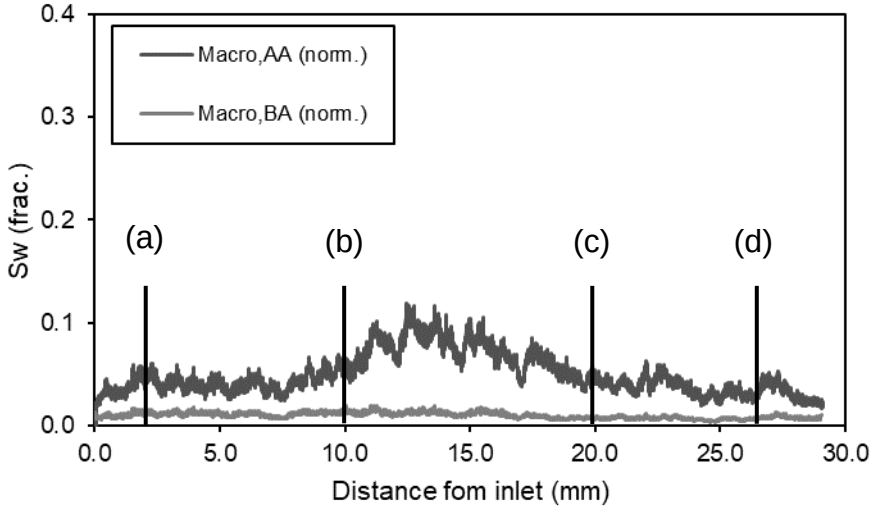

Figure 181 - Normalized macro pores S_w profiles before and after ageing (EST-HDT-03-MP).

On the other hand, water saturation in the unresolved porosity had minor alteration in the comparison of before and after ageing scans, as seen in Figure 182.

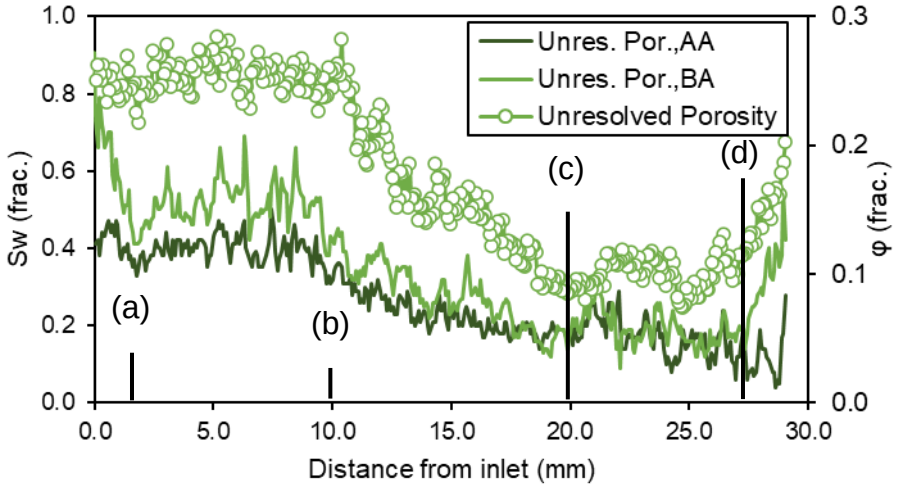

Figure 182 - S_w profile of the unresolved porosity before and after ageing (EST-HDT-03-MP).

When analyzing the total water saturation profiles by NMR and µ-CT, we observe once again the same tendency between imaging tools (Figure 183). We observe, nonetheless, a small change in the profile, that was homogenized.

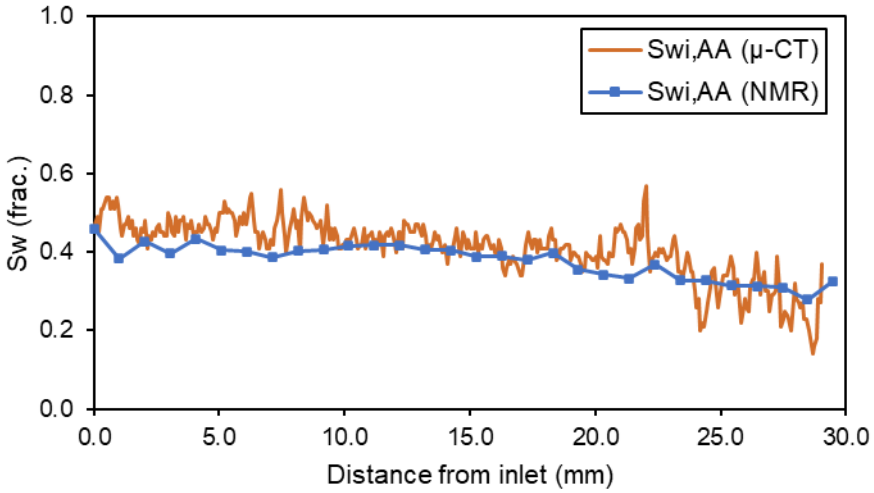

Figure 183 - S_w profiles after ageing obtained by NMR and µ-CT imaging (EST-HDT-03-MP).

Moreover, the comparison of NMR T_2 results before and after ageing agree with the wettability alteration observed in µ-CT images, as we may observe the manifestation of the signal related to the smaller porosity after wettability alteration ($10\ ms < T_2 < 40\ ms$). This result confirms the observed for EST-HDT-01 and EST-HDT-02, as oil did enter the smaller porosity during primary drainage by the Hybrid Drainage Technique, but not yet as a wetting phase. Only after the ageing step it is possible to notice oil manifestation in the smaller porosity, as it increases its T_2 Surface Relaxation. Oil entry in this fraction of the pore space could not have occurred during ageing, since the imposed capillary pressure during this step was considerably lower than that used during primary drainage. This result is presented in Figure 184:

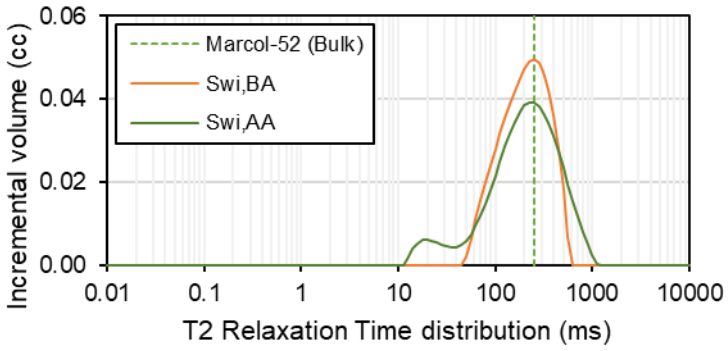

Figure 184 - Comparison between T_2 Relaxation Times for EST-HDT-03-MP at S_{wi} before and after ageing (Marcol™-52 and B4 as oil and brine phases, respectively).

4.3. Waterflooding results (Viscous Oil Flood *versus* Hybrid Drainage Technique)

Considering the different NMR results observed for the samples initialized by VOF and HDT, we expect that history match of the waterflooding of these samples will confirm the observations.

In order to perform a clear comparison between the results, we used roughly the same protocol during imbibition for samples EST-VOF-01 and EST-HDT-02, apart from the initial injection flowrate. We added a flowrate step for the imbibition of sample EST-HDT-02, as it may be seen in Table *31*:

Flowrate Step	Flowrate	Capillary Number
Q1*	3 cc/h	$2.6\ 10^{-8}$
Q2	6 cc/h	$5.2\ 10^{-8}$
Q3	12 cc/h	$1.0\ 10^{-7}$
Q4	24 cc/h	$2.1\ 10^{-7}$
Q5	48 cc/h	$4.2\ 10^{-7}$
Q6	96 cc/h	$8.4\ 10^{-7}$
Q7	192 cc/h	$1.7\ 10^{-6}$

Table 31-Flowrate and Ca for EST-VOF-01 and EST-HDT-01 waterflooding.

Q1 was used only for EST-HDT-01, as EST-VOF-01 started at Q2.

The history match of the pressure drop (dP), oil production (V_O) and S_w profiles for EST-VOF-01 is performed following the process evoked in section (1.7.2) and the specific K_r and P_c models described in 1.7.3 and 1.8.3, respectively. The history-matched experimental data of waterflooding are presented in Figure 185, Figure 186, and Figure 187:

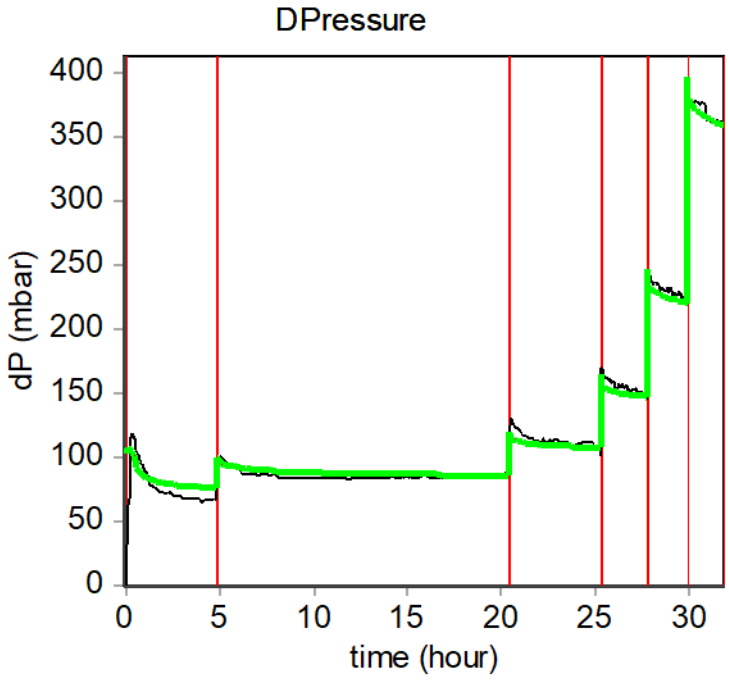

Figure 185 - History-match of the dP experimental data of EST-VOF-01 waterflooding.

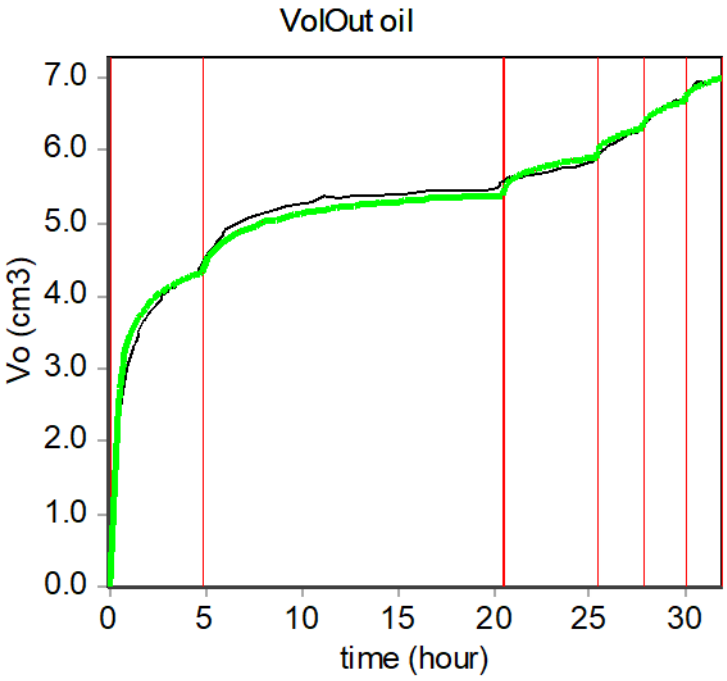

Figure 186 - History-match of the produced oil (V_O) during EST-VOF-01 waterflooding.

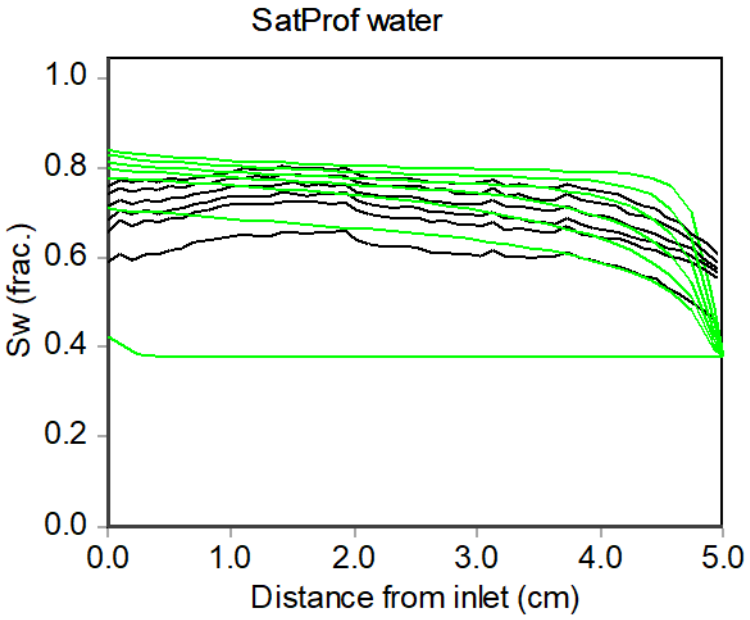

Figure 187 - History-match of the S_w profiles during EST-VOF-01 waterflooding.

Imbibition $\boldsymbol{K_r}$ and $\boldsymbol{P_c}$ curves obtained from EST-VOF-01 waterflooding history-match are presented in Figure 188:

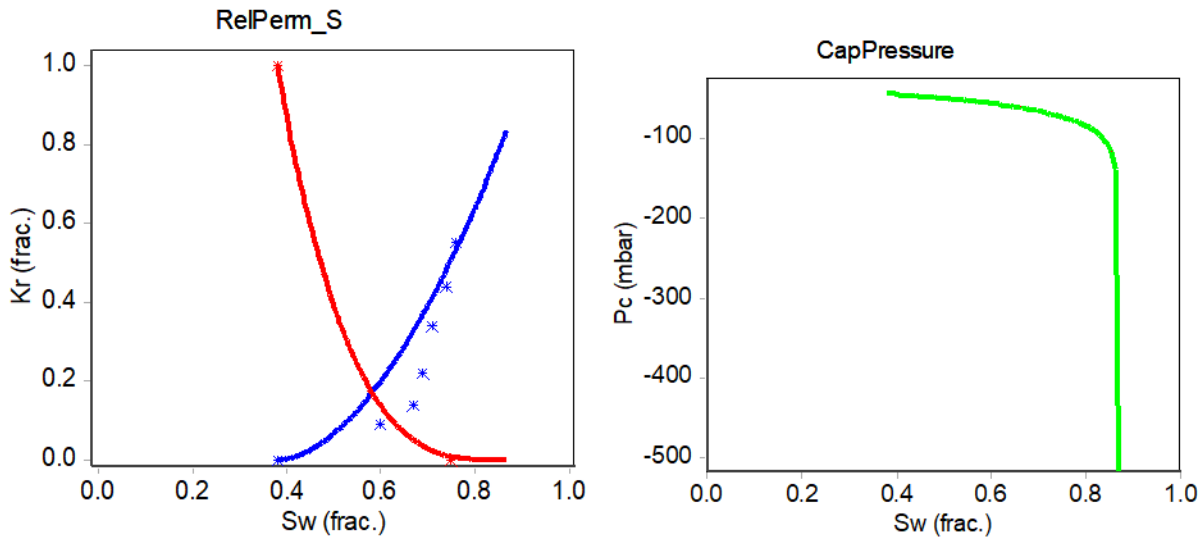

Figure 188 - K_r and P_c imbibition curves for EST-VOF-01.

The history-match of the imbibition experimental data followed Corey and Logbeta behavior. These parameters are presented in Table 32:

Parameter	Value
$K_{rw,max}$	0.84
$K_{ro,max}$	1.00
S_{wi}	0.38
S_{or}	0.87
N_w	1.8
N_o	3.3
P_o	20.56 mbar
P_t	-43.29 mbar

Table 32-Set of parameters used for EST-VOF-01 imbibition K_r and P_c history match.

Similarly, we present the history-matched dP, V_O and S_w profiles for EST-HDT-02 waterflooding in Figure 189, Figure 190, and Figure 191:

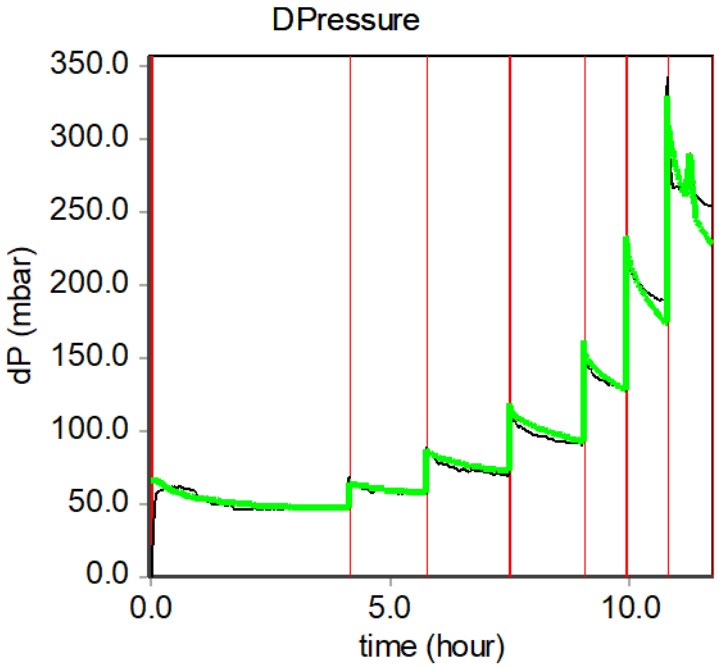

Figure 189 - History-match of the experimental dP values for EST-HDT-02 waterflooding.

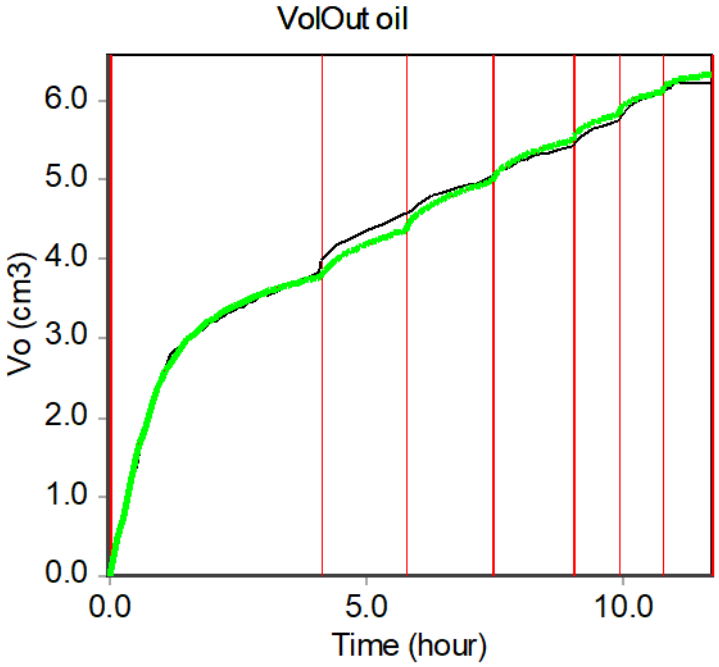

Figure 190 - History-match of the oil production (V_o) during EST-HDT-02 waterflooding.

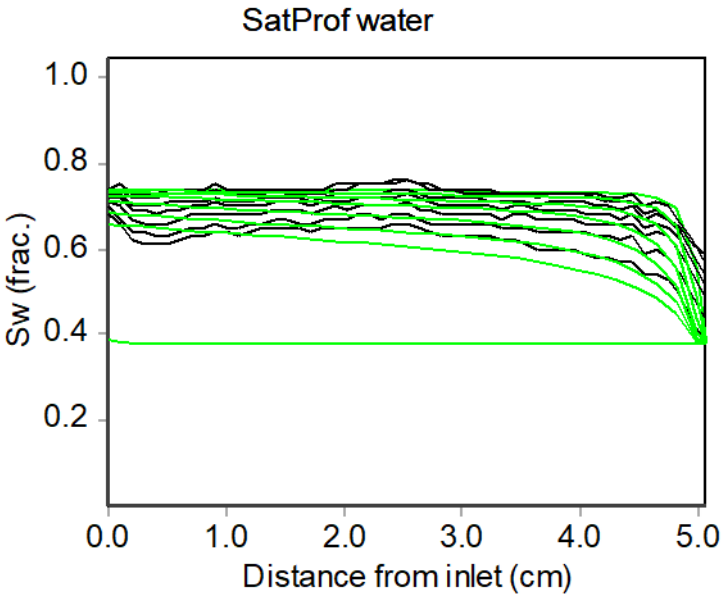

Figure 191 - History-match of the water saturation profiles during EST-HDT-02 waterflooding.

The resulting imbibition K_r and P_c from the waterflooding history-match are presented in Figure 192:

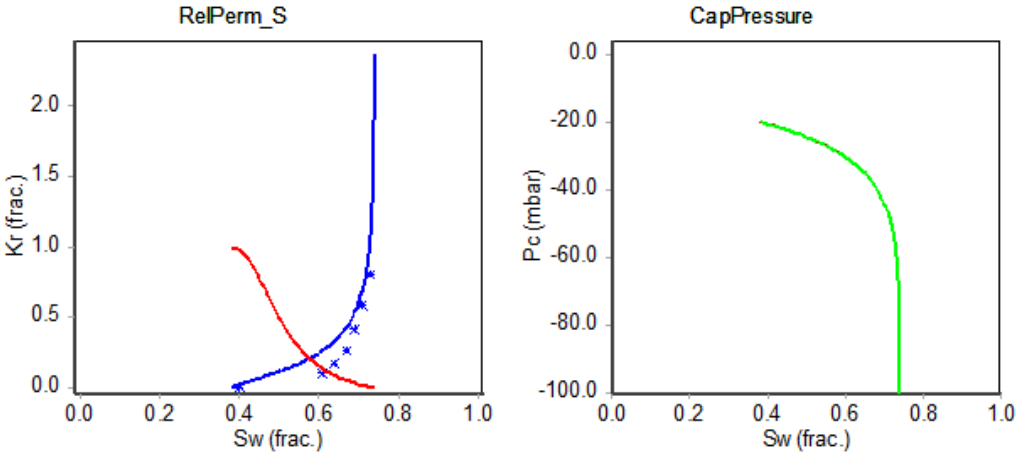

Figure 192 - K_r and P_c imbibition curves for EST-HDT-02.

The setup of parameters used for the history match of EST-HDT-02 waterflooding is presented in Table *33*:

Water parameter	Value	Oil parameter	Value
L	0.78	L	0.93
E	10.73	E	6.20
T	0.64	T	2.00
$K_{rw,max}$		2.37	
$K_{ro,max}$		1.00	

S_{wi}	0.38
S_{or}	0.74
P_o	11.0 mbar
P_t	-20.0 mbar

Table 33-Set of parameters used for EST-HDT-02 imbibition K_r and P_c history match.

When comparing both relative permeability curves obtained after history match, we face some interesting findings. For a clear comparison of the behavior of the samples during imbibition, we present both curves in the same picture in both linear and semi-log scale (Figure 193).

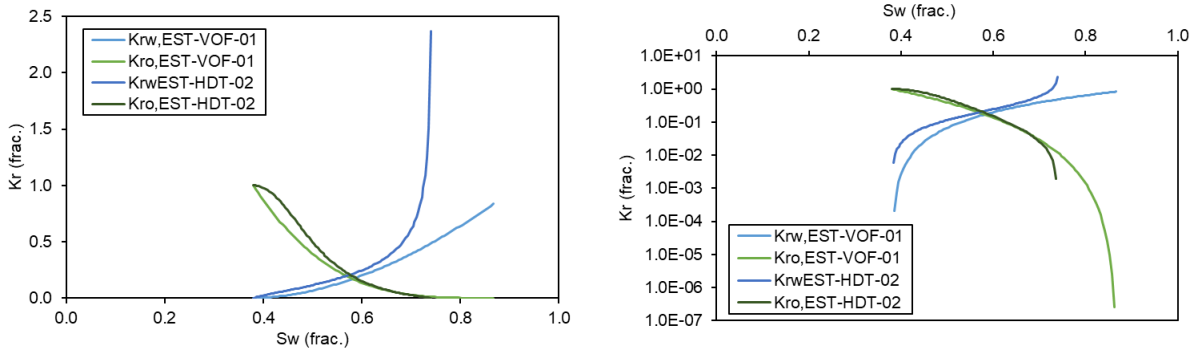

Figure 193 - K_r curves in linear and semi-log scale for EST-VOF-01 (lighter colors) and EST-HDT-02 (darker colors).

Kr expression used for the history match and lower Sw range behavior

Performing the history match using Corey expressions is only possible for EST-VOF-01. This result shows that smaller porosity has very reduced impact in flow during waterflooding. The monotonic behavior of the K_r curves during imbibition confirms the observations after ageing, that during primary drainage, virtually no oil was flushed inside the smaller porosity.

This is not the case for EST-HDT-02. For this sample, acceptable waterflooding history match for relative permeability curves definition is only possible using the LET expression, suited for matching samples with S-shaped behavior. In this case, oil entered the small pores during primary drainage due to the filling process of Step 2 (capillary-controlled). This assumption is supported by Spatially-resolved T_2 tests performed after ageing, and by µ-CT imaging of sample EST-HDT-03-MP. Furthermore, we presented the indication of wettability alteration of the smaller porosity. Considering this process, first oil production occurs by capillarity of the smaller pores, as brine slowly invades the sample during the first flowrate step. As oil relative permeability is controlled by the bigger porosity and smaller porosity has minor impact in the general oil conductivity, we notice a slow decrease in oil relative permeability for the lower range of water saturation ($S_{wi} \approx 0.38 \leq S_w \leq 0.5$). From this point on, oil production will continue by displacement of oil present in the bigger porosity, where a faster decrease in oil relative permeability may be observed.

This behavior is even more pronounced in the case of EST-HDT-01 history-match. As this sample was initiated at a lower value of S_{wi}, ($S_{wi} \approx 0.2$), there is a more substantial presence of oil in the smaller porosity, which results in a longer capillarity-

production of smaller pores for lower values of water saturation ($S_{wi} \approx 0.2 \leq S_w \leq 0.5$). EST-HDT-01 history matched imbibition K_r and P_c are presented in Figure 194 for illustration of the mentioned behavior.

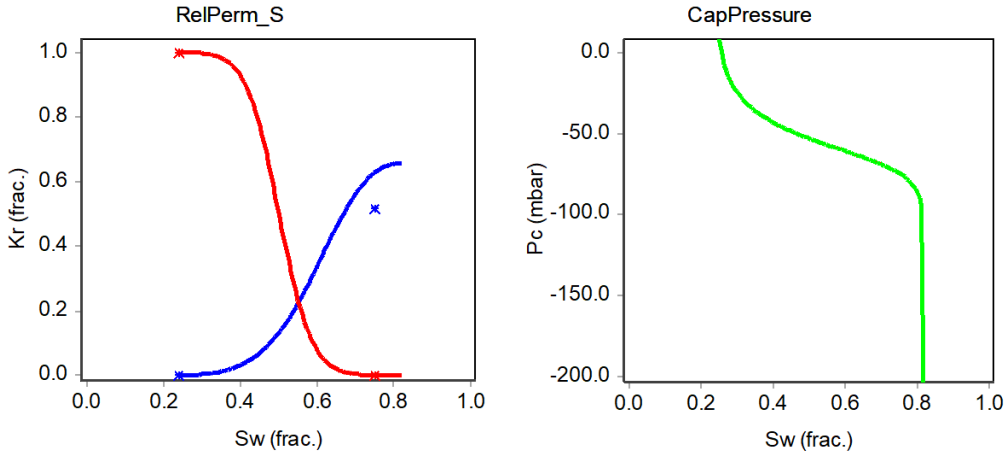

Figure 194 - Imbibition K_r and P_c curves for EST-HDT-01.

Regarding the behavior of water relative permeability curves in the lower range of water saturation, a difference between the curves is only noticeable in the semi-log plot. It is possible to observe that $K_{rw}(VOF)$ increases sharply, whereas $K_{rw}(HDT)$ has a slower increase. This result is coherent with the interpretation presented in the previous paragraphs. For VOF, as water replaces oil present in the bigger porosity, it significantly increases its conductivity. In the case of HDT, a slow increase in K_{rw} is related to an initial production of oil present in the smaller porosity, which have a minor impact in water relative permeability.

S_{or} ranges

One important parameter when analyzing imbibition relative permeability curves regarding wettability is S_{or}. At a first look, we would be tempted to state that only EST-VOF-01 behaves as an oil-wet sample and the behavior of EST-HDT-02 would be rather related to a water-wet rock, given both samples S_{or}. However, in the case of Estaillades, S_{or} analysis may hide some aspects regarding the total volume of trapped oil after waterflooding. Considering that Estaillades are dual-porosity rocks, we should consider the presence of oil in both big and small pores.

The waterflooding is a viscous-controlled process such as the Viscous Oil Flood, meaning that the same constraints regarding small pores by-passing will be valid to this process. Then, if a sample presents oil in both big and small pores, it is logical to state that oil will be trapped in smaller pores by the doublet mechanism. Hence, even though high S_{or} is observed, the corresponding sample may still behave as mixed or oil-wet.

Given these considerations, we may interpretate the high S_{or} value obtained for EST-HDT-02 as oil trapping in smaller pores. As we have seen by NMR results of primary drainage and ageing steps, oil invaded small pores during Step 2 of HDT. Moreover, EST-HDT-03-MP provided a pore-scale visualization of the Hybrid Drainage process, which validated oil phase invasion in smaller porosity. On the other hand, as Viscous Oil Flood primary drainage does not allow oil to invade smaller pores homogeneously, the sample behavior during waterflooding is governed mostly by the bigger pores, hence as a monomodal porosity sample. It makes sense to observe a

lower S_{or} value in this case, as there is much less oil trapping in smaller pores due to the doublet mechanism. We present in Figure 195 two slices of EST-HDT-03-MP at the end of waterflooding where it is possible to notice oil presence in the smaller pores of the sample, corroborating the analysis described here above.

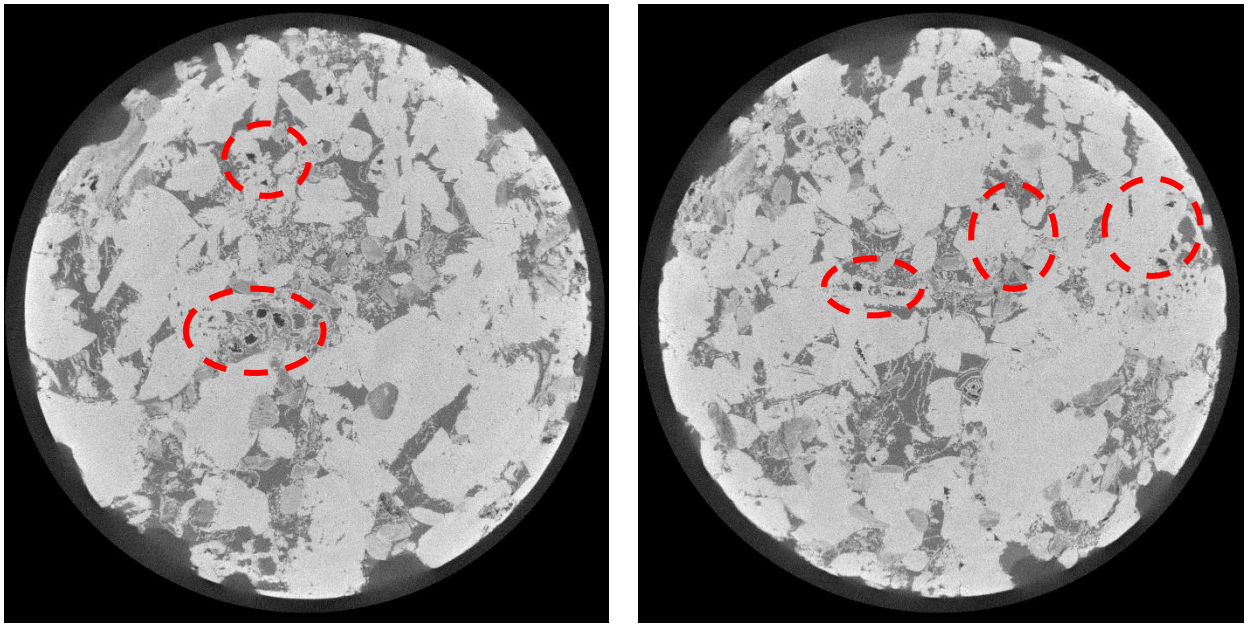

Figure 195 - EST-HDT-03-MP after waterflooding. The red circles highlight the smaller pores where it is possible to notice oil presence.

Considering the K_r ratio curves for EST-HDT-02 and EST-VOF-01 presented in Figure 196, we notice that the behavior during waterflooding is quite similar for a wide range of S_w ($0.5 \leq S_w \leq 0.7$). The K_r ratio between the history matched relative permeabilities are different in the range close to S_{wi}, because of the reasons evoked in the sub preceding sub-section, and differ once again for values close to Sor, which corroborates the analysis of oil trapping in the smaller porosity at the end of waterflooding.

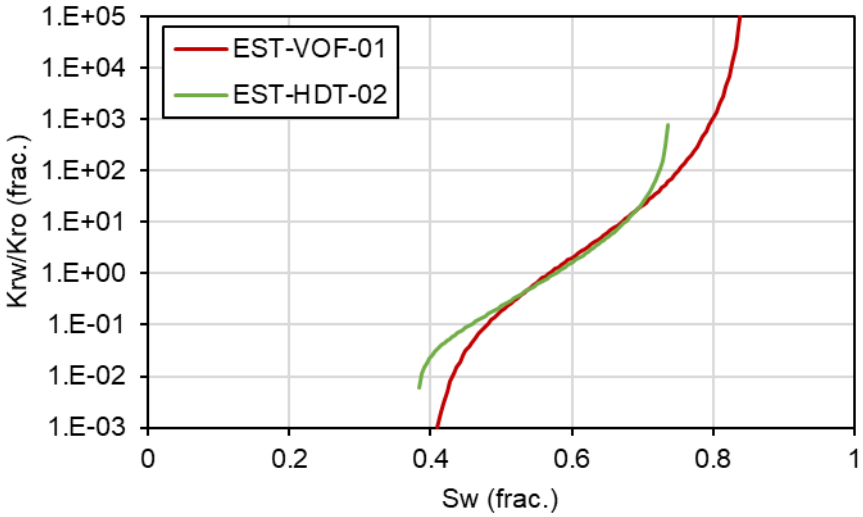

Figure 196 - K_{rw}/K_{ro} ratio for the waterflooding of EST-VOF-01 and EST-HDT-02.

Moreover, by performing differential imaging treatment, we are able to identify the brine presence in both macro and unresolved porosities (after ageing and at ROS).

A normalization of macro and unresolved porosities saturations was done, as previously performed and presented in Figure 142.

There are some interesting points to highlight in the analysis of Figure 197:

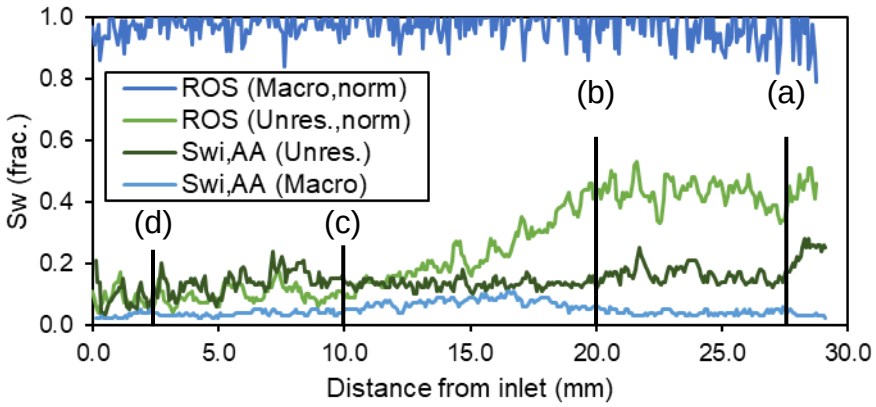

Figure 197 - Average S_w profile and the normalized profiles for micro and macro porosities at S_{wi} after ageing and at ROS (EST-HDT-03-MP).

Regarding the macro-porosity, it is possible to notice that a recovery value close to unity was obtained from a very low initial water saturation. This is possibly due to a film recovery mechanism, which would represent an oil-wet behavior of this fraction of the sample. The residual oil present in this region is held back in the form of thin films, that are difficult to detect by µ-CT imaging.

The normalized unresolved porosity water saturation supports the hypothesis of early production by capillarity and oil trapping at the end of waterflooding. Considering that this network was poorly flushed by crude oil during ageing due to the pore network configuration of the Estaillades samples, it is logical to presume that wettability alteration was less pronounced than in the bigger porosity network. Therefore, early production by capillarity through water-wet thin networks would explain the evolution of the S_w profile from S_{wi} to ROS. This evolution indicates that oil production is not due to the application of viscous forces since brine accumulates in the opposite face of brine injection during waterflooding. Furthermore, it is clearly visible that residual oil saturation is trapped in the smaller-pore network, which supports the hypothesis announced in this section.

K_{rw} behavior close to S_{or}

Another indication of oil trapping in the smaller porosity for EST-HDT-02 and EST-HDT-03-MP is K_{rw} behavior close to S_{or}. It is clearly noticeable that water relative permeability increases sharply until a $K_w@S_{orw}$ value close to the initial k_w value, despite a high S_{or} value. This behavior of the K_r curve indicates that brine flows at the center of the bigger pores at almost the same conductance as in a monophasic flow, despite the presence of residual oil. This effect may be related to what is usually found for water-wet samples at the end of primary drainage ($k_{ro}(Swi) > k_w$).

5. Conclusions and future work

The main objectives of this research was to analyze and estimate the efficiency of the different protocols used in petrophysical laboratories to set the initial state in plug samples. We concentrated the analysis on primary drainage to set a S_{wi} target value and ageing to restore the initial wettability, and the implications of using one particular method for setting fluids in the porous media over the waterflooding or Amott-Harvey/IFP test results.

5.1. Primary drainage

Regarding the primary drainage step, we analyzed the three major techniques of setting initial water saturation (Viscous Oil Flood, Centrifugation and Porous Plate) in terms of reaching the target S_{wi} value and producing a homogeneous S_{wi} profile for a variety of samples in terms of mineralogy, composition, porosity, pore size distribution, and permeability. Furthermore, we proposed and validated the proof of concept of a new primary drainage method, called the Hybrid Drainage Technique, with the objective of combining the advantages of VOF (experimental duration) and Porous Plate (reaching a target S_{wi} value with a homogeneous S_w profile) and dealing with the disadvantages of both methods (CEE and generating unwanted imbibition while homogenizing the profiles for VOF, experimental duration and necessity of unloading the sample for the Porous Plate).

Let us divide the conclusion by primary drainage technique:

5.1.1. Viscous Oil Flood

Most currently used technique for setting S_{wi} value in full-size cores during SCAL routines, the VOF presents the main disadvantage of generating CEE during primary drainage in water-wet samples. We tested the solution of reversing injection direction for the reduction of Capillary-End Effects, which has proven to be efficient. However, we showed, by NMR imaging and for two different rocks, that this approach mobilizes brine present in the sample outlet, which is re-injected following an imbibition process. Members of our team have recently started dealing with this situation with experiments imaged by µ-CT and proved that it may, indeed, impact states initialization (Nono et al., 2022).

Moreover, dealing with CEE in our case was simple as during our VOF drainage experiments we were always close to the irreducible water saturation asymptote. However, if the target S_{wi} is higher, i.e., far from S_{wirr} asymptote, the control of capillary end-effects elimination may be more difficult.

In addition, being a viscous-controlled method, VOF is not suited for the desaturation of dual-porosity samples for low targets of S_{wi} value. During this project we tested the method on an Estaillades sample and reaching values of S_{wi} below 35% has proven to be impossible.

5.1.2. Centrifugation

Centrifugation is a powerful tool to apply a given capillary pressure in the sample, which is useful for the determination of the primary drainage P_c versus S_w curve, forced displacements during Amott-Harvey wettability tests, etc. However, this technique imposes limitations regarding sample sizes; also manipulation is required between experimental tests and classic ISSM methods are non-applicable. Notwithstanding,

we tested this method regarding the possibility of setting a target S_{wi} value and of generating a homogeneous S_w profile.

During our experiments, we confirmed the presence of CEE, by NMR imaging, between centrifugation steps. Thanks to the NMR imaging device, we could monitor S_w profiles homogenization, which revealed to be difficult to control. In the first attempt using a Bentheimer sandstone sample, we swapped the sample orientation in the centrifuge bucket and launched the centrifuge at the last step of rotational speed for 18 hours until production ceased. When imaged again in the NMR, we noticed that we simply displaced the CEE to the other face of the sample. In a second attempt, we used an Estaillades sample, and, after the last step of centrifugation, we swapped the sample in the centrifuge bucket and centrifugated at lower rotational speed (1000 rpm) for about 1 hour. We succeeded in eliminating CEE using this approach, however we observed the same re-imbibition phenomenon as in VOF experiments.

5.1.3. Porous Plate

Considered to be the reference technique for setting S_{wi} as it respects the behavior of the reservoir during hydrocarbon primary migration, the Porous Plate method was also tested for different rocks and different S_{wi} target values.

During all tests, PP generated S_w profiles at the correct target S_{wi} value for basically all range of permeability and pore distribution, by controlling imposed capillary pressure. These results were controlled by both T_2 Relaxation Times distribution and SE-SPI profiles in the NMR. The main disadvantage of this method is the experimental duration, that is prohibitive if we consider experiments on full-size cores. Moreover, the necessity to unload the sample from the experimental cell for performing further steps of a SCAL program is another disadvantage of this method.

5.1.4. Hybrid Drainage Technique

This method was designed during this research and aims uniting the advantages and getting rid of the inconvenient of VOF and PP.

The technique was tested on all the rocks used in this work, proving to be useful for a large spectrum of permeabilities and pore size distributions. Moreover, its use in dual-porosity samples is recommended, once target S_{wi} is possible to reach at reduced experimental time compared to PP.

We verified the homogeneity of the produced saturation profiles by NMR and µ-CT imaging, as well as pore occupancy change (µ-CT) between Steps 1 and 2, which showed the desaturation of zones not invaded by oil during the viscous-based displacement during Step 1.

5.2. Ageing

We tested three different methods for ageing rock samples in crude oil: static, mono-directional and crude oil flush with flow reversal.

Performing Amott-Harvey and Amott-IFP tests to compare static and mono-directional ageing was useful to understand to what extent flushing several PV of crude oil during ageing is efficient for wettability alteration. Moreover, SE-SPI profiles and spatially-resolved T2 analysis indicated that mono-directional ageing generates a wettability gradient, with the sample affinity oil (and inversely aversion to brine) increasing as we move from the inlet (used for oil flushing during ageing) to the outlet.

Crude oil flush with flow reversal was also tested during the experiments used for comparing the waterflooding results. Even though we did not perform an Amott-Harvey test to compare this method to the other two, homogeneous shifts in the spatially-resolved T_2 show a good indication of homogeneous wettability alteration.

In addition, NMR tests such as $Diff, T_2$ and Spatially-resolved T_2 were useful to provide indicators of wettability alteration and presence of oil in the smaller porosity, in the case of dual-porosity samples. Unfortunately, we were not able to define a relationship between wettability change and the shift in the Spatially-resolved T_2 measurement, which could be useful as a tool for wettability alteration evaluation.

5.3. Waterflooding comparison

We compared the waterflooding history match of Estaillades samples initiated by two different primary drainage techniques (Viscous Oil Flood and Hybrid Drainage Technique). The difference between the resulting imbibition K_r and P_c curves are related, mostly, to the ability of the techniques to invade both bigger and smaller porosities of the sample during the primary drainage step.

As HDT experiments are able to invade smaller pores during primary drainage, they present higher S_{or} as there is oil trapping in smaller pores by the doublet mechanism. Moreover, we observed major $K_{o,eff}(S_{wi})$ reduction after ageing, which is also related to smaller porosity invasion and bigger water saturation in bigger pores at the same level of S_{wi} than the sample initiated by VOF. In addition, difference in k_{rw} behavior close to S_{wi} and S_{or} may also be explained by the difference in pore occupancy after primary drainage. These assumptions and hypotheses are based on the history match results and also a pore-scale visualization by µ-CT.

The resulting history matched K_r and P_c curves are used to feed numerical simulations to provide production profile in reservoir engineering. As these are among the most relevant parameters in waterflooding experiments on core samples analysis, the importance of using a primary drainage method representative of the reservoir behavior is quite clear, proving all the value of the proposed Hybrid Drainage Technique.

5.4. Future work

Among all the tests and analysis performed in this work, there are some interesting points to be explored in the future. They are:

- Primary drainage using crude oil:

Performing primary drainage using crude oil would be the best representation of the reservoir behavior during fluid migration. One of the biggest challenges of conducting this experiment is WAT (Wax Appearing Temperature), which may impose the necessity of performing this experiment at high temperature.

- Test HDT on Mixed-wet/oil-wet samples:

Once initial cleaning may be ineffective in restoring the rock natural wettability (water-wet) (Hamon, 2000; Hamon, 2004), this experiment would give insights about the impact of the initial wettability. According to previous studies (Kralik *et al.*, 2000), S_{wi} in these cases would be higher, which would significantly impact relative permeability determination.

- Test the new dual-spiral diffuser on Richemont samples for eliminating the effect observed during RCH-HDT-01 and RCH-HDT-02 tests:

As using a “bulls-eye” diffuser during the proof of concept of HDT produced an undesired effect close to the sample inlet, it would be interesting to test the dual-spiral diffuser in these cases. This diffuser has proven to be useful during EST-HDT-02 drainage, therefore it seems to be a good solution for eliminating this effect.

- Perform Amott-Harvey wettability tests on a Bentheimer sandstone submitted to crude oil flush reversal during ageing:

This experiment would complete the set of experiments performed for the evaluation of the ageing techniques described in this work.

- Define a relationship between shifts in Spatially-resolved T_2 and associated wettability alteration:

As discussed in the bibliographic review, different authors have worked on relating shifts in the T_2 signal to wettability alteration, even providing equations to relate the shifts to the Amott index (Valori *et al.*, 2017). However, as we saw in this document, T_2 Relaxation Time distribution is purely dependent on the pore-size distribution, the rock wettability and the fluid being tested. Therefore, shifts in the T_2 signal will be affected by these limitations.

Nonetheless, a more-thorough study may be conducted for exploring these features, as it may provide interesting information about the wettability profile by performing the ratio between Spatially-resolved T_1 and T_2.

An important aspect to be thoroughly explored is the difference observed between samples imaged by NMR in crude or mineral oil after ageing. T_2, Spatially-resolved T_2 and T_1/T_2 presented quite different results in terms of shifts indicating wettability alteration. Samples imaged in crude oil after ageing presented substantial shift from T_2 Bulk relaxation time and $T_1/T_2 \gg 1$. After crude oil replacement by mineral oil with an intermediate toluene flush step, NMR indications of wettability alteration are considerably softer, yet still visible. The reason for these observations remain uncertain, and *a priori*, intermediate toluene flush prior to mineral oil injection does not clean the sample to a water-wet state, as it was possible to see on the µ-CT scans of EST-HDT-03-MP in Marcol™-52 after ageing that still presented an oil-wet behavior.

- Use super-resolution image treatment for µ-CT on 38mm samples

Performing optimal imaging by NMR and µ-CT requires different sample sizes, as they depend on different parameters to perform high resolution imaging. NMR analysis, that provides quick core-scale imaging, rely on the amount of signal generated by the magnetization of fluids present in the sample. On the other hand, µ-CT imaging is based in the attenuation of fluids inside the sample and the rock matrix. Therefore, the smaller the sample, better the resolution obtained by tomography. A possible solution to obtain a good balance between NMR Signal to Noise Ratio and µ-CT resolution may be by using artificial intelligence for performing ultra-resolution µ-CT imaging (Regaieg *et al.*, 2022). This way, we may obtain optimal NMR SNR and quick core-scale observation and enough µ-CT resolution to investigate the same sample at the pore-scale.

6. References

Al-Mahrooqi, S. H., Grattoni, C. A., Muggeridge, A. H., & Jing, X. D. (2005). Wettability alteration during aging: The application of NMR to monitor fluid redistribution. *SCA*, (pp. 21-25).

AlQuaimi, B. I., & Rossen, W. R. (2018). Capillary desaturation curve for residual nonwetting phase in natural fractures. *SPE Journal*, 788-802.

Amott, E. (1959). Observations Relating to the Wettability of Porous Rock. *Transactions of the AIME, 216*(01), 156-162.

Anderson, W. (1986). Wettability literature survey-part 2: Wettability measurement. *Journal of petroleum technology, 38*(11), 1246-1262. doi:10.2118/13933-PA

Anderson, W. A. (1956). Nuclear magnetic resonance spectra of some hydrocarbons. *Physical review, 102*(1), 151.

Andriamananjaona, P. (2020). *Wettability in porous media–From macroscopic measurements to pore-scale characterization La mouillabilité dans les milieux poreux–D'une mesure macroscopique à sa caractérisation à l'échelle des pores.* Université de Pau et des Pays de l'Adour.

Apourvari, S. N., & Arns, C. H. (2016). Image-based relative permeability upscaling from the pore scale. *Advances in Water Resources, 95*, 161-175.

Appel, M. (2004). Nuclear magnetic resonance and formation porosity. *Petrophysics, 45*(3), 296-307.

Arganda-Carreras, I., Kaynig, V., Rueden, C., Eliceiri, K. W., Schindelin, J., Cardona, A., & Sebastian Seung, H. (2017). Trainable Weka Segmentation: a machine learning tool for microscopy pixel classification. *Bioinformatics, 33*(15), 2424-2426.

Arnold, J. (1956). Magnetic resonances of protons in ethyl alcohol. *Physical review, 102*(1), 136.

Arnold, J. T., Dharmatti, S. S., & Packard, M. E. (1951). Chemical effects on nuclear induction signals from organic compounds. *The journal of chemical physics, 19*(4), 507.

Aspenes, E., Graue, A., & Ramsdal, J. (2003). In situ wettability distribution and wetting stability in outcrop chalk aged in crude oil. *Journal of Petroleum Science and Engineering, 39*(3-4), 337-350.

Austad, T., Strand, S., Puntervold, T., & Ravari, R. R. (2008). New method to clean carbonate reservoir cores by seawater. *SCA.*

Batchelor, G. K., & Green, J. T. (1972). The hydrodynamic interaction of two small freely-moving spheres in a linear flow field. *Journal of Fluid Mechanics, 56*(2), 375-400.

Beyea, S. D., Balcom, B. J., Mastikhin, I. V., Bremner, T. W., Armstrong, R. L., & Grattan-Bellew, P. E. (2000). Imaging of heterogeneous materials with a turbo spin echo single-point imaging technique. *Journal of magnetic Resonance, 144*(2), 255-265.

Bijeljic, B., Mostaghimi, P., & Blunt, M. J. (2013). Insights into non-Fickian solute transport in carbonates. *Water resources research, 49*(5), 2714-2728.

Bloch, F. (1946). Nuclear induction. *Physical review, 70*(7-8), 460-474.

Blunt, M. J. (2017). *Multiphase flow in permeable media: A pore-scale perspective.* Cambridge University press.

Bond, W., & Newton, D. (1928). Bubbles, drops, and Stokes' law. . *Philosophy Magazine*, 794-800.

Bousseau, C., Liu, Y., & Buckley, J. (1995). Wetting alteration of silicate surfaces by brine and crude oil. *SCA*, (pp. 12-14).

Brown, C. E., & Neustadter, E. L. (1980). The wettability of oil/water/silica systems with reference to oil recovery. *Journal of Canadian Petroleum Technology*.

Brownstein, K. R., & Tarr, C. E. (1979). Importance of classical diffusion in NMR studies of water in biological cells. *Physical review A, 19*(6), 2446.

Bruce, W. A., & Welge, H. J. (1947). The restored-state method for determination of oil in place and connate water. *Drilling and production practice*.

Buades, A., Coll, B., & Morel, J. M. (2011). Non-local means denoising. *mage Processing On Line, 1*, 208-212.

Buckley, J. S. (1995). Asphaltene precipitation and crude oil wetting. *SPE Advanced TEchnology Series, 3*(01), 53-59.

Buckley, J. S., & Liu, Y. (1998). Some mechanisms of crude oil/brine/solid interactions. *Journal of Petroleum Science and Engineering*, 155-160.

Buckley, J. S., & Morrow, N. R. (1990). Characterization of crude oil wetting behavior by adhesion tests. *SPE/DOE Enhanced Oil Recovery Symposium*.

Buckley, J. S., & Wang, J. (2002). Crude oil and asphaltene characterization for prediction of wetting alteration. *Journal of Petroleum Science and Engineering, 33*(1-3), 195-202.

Buckley, J. S., Liu, Y., & Monsterleet, S. (1998). Mechanisms of wetting alteration by crude oils. *SPE journal, 3*(01), 54-61.

Buckley, S. E., & Leverett, M. (1942). Mechanism of fluid displacement in sands. *Transactions of the AIME, 146*(01), 107-116.

Bush, I. (2019). *NMR Studies of Enhanced Oil Recovery Core Floods and Core Analysis Protocols.* Doctoral Thesis, University of Cambridge.

Bynum, R. S., & Koepf, E. H. (1957). Whole-core analysis methods and interpretation of data from carbonate reservoirs. *Journal of Petroleum Technology, 9*(11), 11-15.

Callaghan, P. T. (1991). *Principles of nuclear magnetic resonance microscopy.* New York: Oxford University Press.

Cantrell, D. L., & Hagerty, R. M. (1999). Dave L. Cantrell, Royal M. Hagerty. *GeoArabia, 4*(2), 129-154.

Carr, H. Y., & Purcell, E. M. (1954). Effects of diffusion on free precession in nuclear magnetic resonance experiments. *Physical review, 94*(3), 630.

Chang, C. S. (1988). Measuring density and porosity of grain kernels using a gas pycnometer. *Cereal Chem., 65*(1), 13-15.

Chatzis, I., & Morrow, N. R. (1984). Correlation of Capillary Number Relationships for Sandstone. *SPE Journal*, 555-562.

Chen, J., J., H. G., & Flaum, M. (2006). NMR wettability indices: Effect of OBM on wettability and NMR responses. *Journal of Petroleum Science and Engineering, 52*(1-4), 161-171.

Corey, A. T., Rathjens, C. H., Henderson, J. H., & Wyllie, M. R. (1956). Three-phase relative permeability. *Journal of Petroleum Technology, 8*(11), 63-65.

Cuiec, L. (1984). Rock/crude-oil interactions and wettability: An attempt to understand their interrelation. *SPE annual technical conference and exhibition.*

Cuiec, L. E. (1975). Restoration of the natural state of core samples. *Fall Meeting of the Society of Petroleum Engineers of AIME*.

Cuiec, L. E. (1975). Restoration of the Natural State of Core Samples. *Fall Meeting of the Society of Petroleum Engineers of AIME.* Dallas.

Cuiec, L. E. (1977). Study of Problems Related to the Restoration Of the Natural State of Core Samples. *Journal of Canadian Petroleum Technology, 16*(04).

CYDAREX. (2021). *CYDAR-SCAL User Manual.* Retrieved from http://cydarex.fr.

D'Agostino, C., Brett, G. L., Miedziak, P. J., Knight, D. W., Hutchings, G. J., Gladden, L. F., & Mantle, M. D. (2012). Understanding the Solvent Effect on the Catalytic Oxidation of 1, 4-Butanediol in Methanol over Au/TiO2 Catalyst: NMR Diffusion and Relaxation Studies. *Chemistry-A European Journal, 18*(45), 14426-14433.

D'Agostino, C., Mitchell, J., Mantle, M. D., & Gladden, L. F. (2014). Interpretation of NMR relaxation as a tool for characterising the adsorption strength of liquids inside porous materials. *Chemistry–A European Journal*, 13009-13015.

Danielczick, Q., Faurissoux, P., & Nicot, B. (2021). Wireless acquisition for Resistivity Index in Centrifuge – WiRI: A new method to estimate Archie's Law Parameters. *SCA.*

Darcy, H. (1856). *Les fontaines publiques de la ville de Dijon* (Vol. 2). V. Dalmont.

Davies, S., & Packer, K. J. (1990). Pore size distribution from NMR spin-lattice relaxation measurements of fluid saturated porous solids. I Theory and Simulation. *Journal of applied physics, 67*, 3163-3170.

Davies, S., Packer, K. J., Roberts, D. R., & Zelaya, F. O. (1991). Pore-size distributions from NMR spin-lattice relaxation data. *Magnetic resonance imaging, 9*(5), 681-685.

de Gennes, P. G. (1985). Wetting: statics and dynamics. *Reviews of modern physics, 57*, 827.

de Gennes, P. G., Brochard-Wyart, F., & Quéré, D. (2004). *Capillarity and wetting phenomena: drops, bubbles, pearls, waves.* New York: Springer.

Derjaguin, B. V., & Kussakov, M. (1939). Anomalous properties of thin polymolecular films. *Acta Physicochim, 10*(1), 25-44.

di Chiara Roupert, R. (2009). *Développement d'un code de calcul multiphasique multiconstituants.* PhD Thesis, Université de Strasbourg, Strasbourg.

Dickey, P. A. (1981). *Petroleum development geology.*

Donaldson, E. C., & Thomas, R. D. (1971). Microscopic observations of oil displacement in water-wet and oil-wet systems. *Fall Meeting of the Society of Petroleum Engineers of AIME.*

Donaldson, E. C., Thomas, R. D., & Lorenz, P. B. (1969). Wettability determination and its effect on recovery efficiency. *Society of Petroleum Engineers Journal, 9*(01), 13-20.

Esfahani, M. R., Kazem, Z. E., Hashemi, S. M., & Karimaei, H. (2003). Determination of wettability of Iranian carbonate reservoir rocks in restored-state. *SCA.*

Faurissoux, P., Colombain, A., Pujol, G., Fraute, O., & Nicot, B. (2018). Ultra-fast capillary pressure and Resistivity measurements. *SCA.*

Fernandes, V., Brugidou, R., Nono, F., & Caubit, C. (2022). *France Patent No. PAT22-056.*

Fernandes, V., Caubit, C., Nicot, B., Pairoys, F., Bertin, H., & Lachaud, J. (2022). Hybrid Technique for setting initial water saturation on core samples. *SCA.* Austin.

Fernandes, V., Nicot, B., Caubit, C., & Pairoys, F. (2022). *France Patent No. PAT22-055.*

Flaum, M., Chen, J., & Hirasaki, G. J. (2005). NMR Diffusion Editing for D-T2 Maps: Application to Recognition of Wettability Change. *Petrophysics-The SPWLA Journal of Formation Evaluation and Reservoir Description, 46*(1).

Fleury, M. (1998). *Caractérisation de structures poreuses par relaxométrie RMN.* Paris: Institut Français du Pétrole.

Fleury, M. (1998). FRIM: a fast resistivity index measurement method. *SCA*, (pp. 14-16).

Fleury, M. (2009). The Spinning Porous Plate (SPP) Method: A new technique for setting irreducible water saturation on core samples. *SCA*, (pp. 1-12).

Fleury, M., & Deflandre, F. (2003). Quantitative evaluation of porous media wettability using NMR relaxometry. *Magnetic Resonance Imaging, 21*(3-4), 385-387.

Fleury, M., & Romero-Sarmiento, M. (2016). Characterization of shales using T1–T2 NMR maps. *Journal of Petroleum Science and Engineering, 137*, 55-62.

Fleury, M., Santerre, Y., & Vincent, B. (2007). Carbonate rock typing from NMR relaxation measurements. *SPWLA 48th Annual Logging Symposium*.

Forbes, P. (1994). Simple and accurate methods for converting centrifuge data into drainage and imbibition capillary pressure curves. *The Log Analyst, 35*(04).

Fordham, E. J., Hall, L. D., Ramakrishnan, T. S., Sharpe, M. R., & Hall, C. (1993). Saturation gradients in drainage of porous media: NMR imaging measurements. *AIChE journal*, 1431-1443.

Freedman, R., & Heaton, N. (2004). Fluid characterization using nuclear magnetic resonance logging. *Petrophysics-The SPWLA Journal of Formation Evaluation and Reservoir Description, 45*(3).

Gallegos, D. P., Munn, K. S., & Stermer, D. L. (1987). A NMR technique for the analysis of pore structure: application to materials with well-defined pore structure. *Journal of colloid and interface science, 119*(1), 127-140.

Gao, Y., Raeini, A. Q., Blunt, M. J., & Bijeljic, B. (2019). Pore occupancy, relative permeability and flow intermittency measurements using X-ray micro-tomography in a complex carbonate. *Advances in Water Resources, 129*, 56-59.

Godefroy, S., Korb, J. P., Fleury, M., & Bryant, R. G. (2001). Surface nuclear magnetic relaxation and dynamics of water and oil in macroporous media. *Physical Review E, 64*(2).

Graue, A., Aspenes, E., Bognø, T., Moe, R. W., & Ramsdal, J. (2002). Alteration of wettability and wettability heterogeneity. *Journal of Petroleum Science and Engineering, 33*, 3-17.

Green, D., Gardner, J. S., Balcom, B. J., McAloon, M., & Cano-Barrita, J. (2008). Comparison study of capillary pressure curves obtained using traditional centrifuge and magnetic resonance imaging techniques. *SPE Symposium on Improved Oil Recovery*.

Hamon, G. (2000). Field-wide variations of wettability. *SPE annual technical conference and exhibition.* OnePetro.

Hamon, G. (2004). Revisiting Ekofisk and Eldfisk wettability. *SPE annual technical conference and exhibition.* OnePetro.

Hamon, G., & Roy, C. (2000). Influence of heterogeneity, wettability and coreflood design on relative permeability curves.

Hassler, G. L., & Brunner, E. (1945). Measurement of capillary pressures in small core samples. *Transactions of the AIME, 160*(01), 114-123.

Hazlett, R. D. (1993). On surface roughness effects in wetting phenomena. *Contact Angle, Wettability and Adhesion*, 173-181.

Helmig, R. (1997). *Multiphase flow and transport processes in the subsurface: a contribution to the modeling of hydrosystems.* Heidelberg: Springer Berlin.

Hfirlimann, M. D., Venkataramanan, L., Flaum, C., Speier, P., Karmonik, C., Freedman, R., & Heaton, N. (2002). Diffusion-editing: New NMR measurement of saturation and pore geometry. *SPWLA 43rd Annual Logging Symposium.* OnePetro.

Hilfer, R., Armstrong, R. T., Berg, S., Georgiadis, A., & Ott, H. (2015). Capillary saturation and desaturation. *Physical Review E, 92*.

Hirasaki, G. J., Rohan, J. A., Dubey, S. T., & Niko, H. (1990). Wettability evaluation during restored-state core analysis. *SPE Annual Technical Conference and Exhibition.*

Hognesen, E. J., Strand, S., & Austad, T. (2005). Waterflooding of preferential oil-wet carbonates: Oil recovery related to reservoir temperature and brine composition. *SPE Europec/EAGE annual conference.*

Huang, D. D. (1998). Capillary end effects in coreflood calculations. *Journal of Petroleum Science and Engineering*, 103-117.

Hurd, B. G., & Fitch, J. L. (1959). The Effect of Gypsum on Core Analysis Results. *Transactions of the AIME, 216*(01), 221-224.

Hürlimann, M. D., & Venkataramanan, L. (2002). Quantitative measurement of two-dimensional distribution functions of diffusion and relaxation in grossly inhomogeneous fields. *Journal of Magnetic Resonance, 157*(1), 31-42.

Hürlimann, M. D., Flaum, M., Venkataramanan, L. F., Freedman, R., & Hirasaki, G. J. (2003). Diffusion-relaxation distribution functions of sedimentary rocks in different saturation states. *Magnetic resonance imaging, 21*(3-4), 305-310.

Hürlimann, M. D., Matteson, A., Massey, J. E., Allen, D. F., Fordham, E. J., Antonsen, F., & Rueslåtten, H. G. (2004). Application of NMR diffusion editing as chlorite indicator. *Petrophysics-The SPWLA Journal of Formation Evaluation and Reservoir Description, 45*(5).

Hussain, R. (2015). *NMR studies of carbon dioxide sequestration in porous media.* PhD Thesis, University of Cambridge.

Jadhunandan, P. P., & Morrow, N. R. (1991). Spontaneous imbibition of water by crude oil/brine/rock systems. *In Situ, 15*.

Jadhunandan, P. P., & Morrow, N. R. (1995). Effect of wettability on waterflood recovery for crude-oil/brine/rock systems. *SPE reservoir engineering*, 40-46.

Jerauld, G. (1997). General three-phase relative permeability model for Prudhoe Bay. *SPE reservoir Engineering, 12*(04), 255-263.

Jia, D., Buckley, J. S., & Morrow, N. R. (1991). Control of core wettability with crude oil. *SPE International Symposium on Oilfield Chemistry*.

Jia, D., Buckley, J. S., & Morrow, N. R. (1991). Control of core wettability with crude oil. *SPE International Symposium on Oilfield Chemistry.*

Jia, D., Buckley, J. S., & Morrow, N. R. (1994). Alteration of wettability by drilling mud filtrates. *SCA.*

Johannesen, E. B., Graue, A., Baldwin, B. A., & Tobola, D. P. (2007). Establishing mixed wet conditions in chalk-emphasis on wettability alteration and oil recovery. *SCA.*

Johannesen, E., Howard, J., & Graue, A. (2008). Evaluation of wettability distributions in experimentally aged core. *SCA.* Abu Dhabi.

Johannesen, E., Steinsbø, M., Howard, J. J., & Graue, A. (2006). Wettability characterization by NMR T2 measurements in chalk. *SCA.* Trondheim.

Jones, S. C., & Roszelle, W. O. (1978). Graphical techniques for determining relative permeability from displacement experiments. *Journal of Petroleum Technology, 30*(05), 807-817.

Jurin, J. (1718). *II. An account of some experiments shown before the Royal Society; with an enquiry into the cause of the ascent and suspension of water in capillary tubes.* Philosophical Transactions of the Royal Society of London.

Katika, K., Saidian, M., & Fabricius, I. L. (2016). Wettability of chalk and argillaceous sandstones assessed from T1/T2 ratio. *EAGE conference and exhibition* (pp. 1-5). European Association of Geoscientists & Engineers.

Klinkenberg, L. J. (1941). The permeability of porous media to liquids and gases. *Am. Petrol. Inst., Drilling and Production Practice, 2*, 200-213.

Korb, J. P., Nicot, B., & Jolivet, I. (2018). Dynamics and wettability of petroleum fluids in shale oil probed by 2D T1-T2 and fast field cycling NMR relaxation. *Microporous and Mesoporous Materials, 269*(7-11), 7-11.

Kovscek, A. R., Wong, H., & Radke, C. J. (1993). A pore-level scenario for the development of mixed wettability in oil reservoirs. *AIChe Journal*, 1072-1085.

Kralik, J. G., Manak, L. J., Jerauld, G. R., & Spence, A. P. (2000). Effect of trapped gas on relative permeability and residual oil saturation in an oil-wet sandstone. *SPE Annual Technical Conference and Exhibition.* OnePetro.

Lake, L. W. (1989). *Enhanced Oil Recovery.*

Larson, R. G. (1981). Displacement of residual nonwetting phase from porous media. *Chem. Eng. Sci., 36*, 57-73.

Lasseux, D., Quintard, M., & Whitaker, S. (1996). Determination of permeability tensors for two-phase flow in homogeneous porous media: Theory. *Transport in Porous Media, 24*(2), 107-137.

Lenormand, R., Eisenzimmer, A., & Zarcone, C. (1993). A novel method for the determination of water/oil capillary pressures of mixed wettability samples. *SCA.*

Lenormand, R., Lorentzen, K., Maas, J. G., & Ruth, D. (2017). Comparison of four numerical simulators for SCAL experiments. *Petrophysics, 58*(01), 48-56.

Leverett, M. (1941). Capillary behavior in porous solids. *Transactions of the AIME*, 152-169.

Leverett, M. C. (1939). Flow of oil-water mixtures through unconsolidated sands. *Transactions of the AIME, 132*(01), 149-171.

Leverett, M. C., & Lewis, W. B. (1941). Steady flow of gas-oil-water mixtures through unconsolidated sands. *ransactions of the AIME*, 107-116.

Levorsen, A. I., & Berry, F. A. (1967). *Geology of petroleum.* San Francisco: WH Freeman.

Lin, Q., Al-Khulaifi, Y., Blunt, M. J., & & Bijeljic, B. (2016). Quantification of sub-resolution porosity in carbonate rocks by applying high-salinity contrast brine using X-ray microtomography differential imaging. *Advances in water resources, 96*, 306-322.

Lin, Q., Bijeljic, B., Foroughi, S., B. S., & Blunt, M. J. (2021). Pore-scale imaging of displacement patterns in an altered-wettability carbonate. *Chemical Engineering Science, 235*.

Lo, S. W., Hirasaki, G. J., House, W. V., & Kobayashi, R. (2002). Mixing rules and correlations of NMR relaxation time with viscosity, diffusivity, and gas/oil ratio of methane/hydrocarbon mixtures. *SPE Journal, 7*(1), 24-34.

Lomeland, F., Ebeltoft, E., & Thomas, W. H. (2005). A new versatile relative permeability correlation. *SCA*, *112.* Toronto.

Mangane, P. O., Gouze, P., & Luquot, L. (2013). Permeability impairment of a limestone reservoir triggered by heterogeneous dissolution and particles migration during CO2-rich injection. *Geophysical Research Letters, 40*(17), 4614-.

Mansfield, P., & Grannell, P. K. (1973). NMR 'Diffraction' in solids? *Journal of Physics C: Solid State Physics, 6*(22).

Mascle, M., Youssef, S., Deschamps, H., & Vizika, O. (2019). In-situ investigation of aging protocol effect on relative permeability measurements using high-throughput experimentation methods. *Petrophysics-The SPWLA Journal of Formation Evaluation and Reservoir Description, 60*, 514-524.

McCaffery, F., Buckley, J. S., Silveira, R., Lekkala, R., Goggin, D., & McCarty, A. (2002). Wettability and water-oil displacement investigations for some high permeability turbidite reservoirs. *SCA*, (pp. 22-26).

McCullough, J. J., Albaugh, F. W., & Jones, P. H. (1944). Determination of the interstitial-water content of oil and gas sand by laboratory tests of core samples. *Drilling and Production Practice*.

McDonald, P. J., Korb, J. P., Mitchell, J., & Monteilhet, L. (2005). Surface relaxation and chemical exchange in hydrating cement pastes: a two-dimensional NMR relaxation study. *Physical review E, 72*(1).

McPhee, C., Reed, J., & Zubizarreta, I. (2015). *Core analysis: a best practice guide.* Elsevier.

Meiboom, S., & Gill, D. (1958). Modified spin-echo method for measuring nuclear relaxation times. *Review of scientific instruments, 29*(8), 688-691.

Mitchell, J., & Fordham, E. J. (2014). Contributed review: Nuclear magnetic resonance core analysis at 0.3 T. *Review of Scientific Instruments, 85*(11).

Mitchell, J., Hürlimann, M. D., & Fordham, E. J. (2009). A rapid measurement of T1/T2: the DECPMG sequence. *Journal of Magnetic Resonance, 200*(2), 198-206.

Morrow, N. R., & Xie, X. (2001). Oil recovery by spontaneous imbibition from weakly water-wet rocks. *Petrophysics-The SPWLA Journal of Formation Evaluation and Reservoir Description*.

Morrow, N. R., Chatzis, I., & Taber, J. J. (1988). Entrapment and Mobilization of Residual Oil in Bead Packs. *SPE Res Eng 3*, 927-934.

Morrow, N. R., Cram, P. J., & McCaffery, F. G. (1973). Displacement studies in dolomite with wettability control by octanoic acid. *Society of Petroleum Engineers Journal, 13*(04), 221-232.

Morrow, N. R., Lin, H. T., & Ward, J. S. (1986). Effect of crude-oil-induced wettability changes on oil recovery. *SPE Formation Evaluation, 1*, 89-103.

Munn, K., & Smith, D. M. (1987). A NMR technique for the analysis of pore structure: Numerical inversion of relaxation measurements. *Journal of Colloid and Interface Science, 119*(1), 117-126.

Muskat, M. (1937). The flow of fluids through porous media. *Journal of Applied Physics, 8*(4), 274-282.

Muskat, M., & Meres, M. W. (1936). The flow of heterogeneous fluids through porous media. *Physics, 7*(9), 346-363.

Navier, C. L. (1823). Mémoire sur les lois du mouvement des fluides. *Mémoires de l'Académie Royale des Sciences de l'Institut de France*, 389-440.

Nono, F. L. (2014). *Caractérisation polyphasique de la zone de transition dans un réservoir pétrolier carbonaté.* PhD Thesis, Ecole Nationale Supérieure d'Arts et Métiers, Bordeaux.

Nono, F., Caubit, C., & Rivenq, R. (2022). Initial states of coreflooding techniques evaluation: a global pore-scale investigation. *SCA.* Austin, TX.

Nono, F., Moonen, P., & Berthet, H. (2019). Multiphase flow imaging through X-ar microtomography: Reconsideration of capillary end-effects and boundary condition. *SCA.* Pau.

Oh, S. G., & Slattery, J. C. (1979). Interfacial tension required for significant displacement of residual oil. *Society of Petroleum Engineers Journal, 19*(02), 83-96.

O'Meara Jr, D. J., Hirasaki, G. J., & Rohan, J. A. (1992). Part 1-Outflow boundary condition. In *Centrifuge measurements of capillary pressure* (01 ed., Vol. 7, pp. 133-142). SPE reservoir engineering.

Ott, H., Pentland, C. H., & Oedai, S. (2015). CO2–brine displacement in heterogeneous carbonates. *International Journal of Greenhouse Gas Control, 33*, 135-144.

Owens, W. W., & Archer, D. L. (1970). Effect of rock wettability on oil-water relative permeability relationships. *Pan American Petr. Corp.*

Pentland, C. H., El-Maghraby, R. M., Iglauer, S., & Blunt, M. J. (2014). The toroidal porous plate: a new method to facilitate waterflooding. *SCA*, (pp. 8-11).

Purcell, E. M., Torrey, H. C., & Pound, R. V. (1946). Resonance absorption by nuclear magnetic moments in a solid. *Physical review, 69*(1-2), 37-38.

Ramakrishnan, T. S., & Cappiello, A. (1991). A new technique to measure static and dynamic properties of a partially saturated porous medium. *Chemical engineering science*, 1157-1163.

Reed, J., Pruno, S., & Zubizarreta, I. (2022). Causal protocols to assess the viability of native state or restored state preparation. *SCA.* Austin, TX.

Regaieg, M., Nono, F., Farhana Faisal, T., Varloteaux, C., & Rivenq, R. (2022). Pore network simulations coupled with innovative wettability anchoring experiment to predict relative permeability of a mixed-wet rock. *SCA.* Austin.

Reynolds, O. (1883). An experimental investigation of the circumstances which determine whether the motion of water shall be direct or sinuous, and of the law of resistance in parallel channels. *Philosophical Transactions of the Royal society of London*, 935-982.

Romanenko, K., & Balcom, B. J. (2013). An assessment of non-wetting phase relative permeability in water-wet sandstones based on quantitative MRI of capillary end effects. *Journal of Petroleum Science and Engineering*, 225-231.

Rose, W., & Bruce, W. A. (1949). Evaluation of capillary character in petroleum reservoir rock. *Journal of Petroleum Technology*, 127-142.

Salathiel, R. A. (1973). Oil recovery by surface film drainage in mixed-wettability rocks. *Journal of petroleum technology*, 1216-1224.

Schechter, D. S., Zhou, D., & Orr Jr, F. M. (1994). Low IFT drainage and imbibition. *Journal of Petroleum science and Engineering, 11*(4), 283-300.

Schön, J. (2011). *Physical properties of rocks: A workbook* (Vol. 8). Elsevier.

Sharma, M. M., & Filoco, P. R. (2000). Effect of brine salinity and crude-oil properties on oil recovery and residual saturations. *SPE Journal*, 293-300.

Sheppard, A. P., Sok, R. M., & Averdunk, H. (2004). Techniques for image enhancement and segmentation of tomographic images of porous materials. *Physica A: Statistical mechanics and its applications, 339*(1-2), 145-151.

Skauge, A., & Ottesen, B. (2002). A summary of experimentally derived relative permeability and residual saturation on North Sea reservoir cores. *Society of Core Analysts.* Monterey.

Skauge, A., Vik, B., & Ottesen, B. (2003). Variation of special core analysis properties for intermediate wet sandstone material. *Society of Core Analysts*, (pp. 22-25). Pau.

Soxhlet, F. (1879). Die gewichtsanalytische Bestimmung des Milchfettes. *Dingler's Polytechnisches Journal, 232*, 461-465.

Spinler, E. A., Baldwin, B. A., & Graue, A. (1999). Simultaneous measurement of multiple capillary pressure curves from wettability and rock property variations within single rock plugs. *SCA.*

Spinler, E. A., Baldwin, B. A., & Graue, A. (2002). Experimental artifacts caused by wettability variations in chalk. *Journal of Petroleum Science and Engineering, 33*, 49-59.

Standnes, D. C., & Austad, T. (2000). Wettability alteration in chalk: 1. Preparation of core material and oil properties. *Journal of Petroleum Science and Engineering, 28*(3), 111-121.

Stokes, G. G. (1845). On the theories of the internal friction of fluids in motion, and of the equilibrium and motion of elastic solids. *Transaction of the Cambridge Philosphical Society, 8*, 287-305.

Sun, B., & Dunn, K. J. (2002). Probing the internal field gradients of porous media. *Physical Review E, 65*(5).

Taber, J. J. (1980). Research on enhanced oil recovery: past, present and future. *Pure and Applied Chemistry, 52*(5), 1323-1647.

Tang, G. Q., & Morrow, N. R. (1997). Salinity, temperature, oil composition, and oil recovery by waterflooding. *SPE Reservoir Engineering, 12*, 269-276.

Tang, G. Q., & Morrow, N. R. (1999). Oil recovery by waterflooding and imbibition-invading brine cation valency and salinity. *SCA.*

Tanino, Y., & Blunt, M. J. (2012). Capillary trapping in sandstones and carbonates: Dependence on pore structure. *Water Resources Research, 48*.

Tiab, D., & Donaldson, E. C. (2015). *Petrophysics: theory and practice of measuring reservoir rock and fluid transport properties.* Gulf professional publishing.

Tie, H. T., & Morrow, N. R. (2003). The effect of different crude oil/brine/rock combinations on wettability through spontaneous imbibition. *SCA.*

Tie, H., & Morrow, N. R. (2005). Oil recovery by spontaneous imbibition before and after wettability alteration of three carbonate rocks by a moderately asphaltic crude oil. *SCA.* Wyoming.

Tie, H., Tong, Z., & Morrow, N. R. (2003). The effect of different crude oil/brine/rock combinations on wettability through spontaneous imbibition. *SCA.*

Timur, A. (1969). Pulsed nuclear magnetic resonance studies of porosity, movable fluid, and permeability of sandstones. *Journal of Petroleum Technology*, 775-786.

Tong, Z., & Morrow, N. R. (2005). Wettability Control by Adsorption from Crude Oil–Aspects of Temperature and Increased Water Saturation. *SCA*, (pp. 21-25). Toronto.

Tong, Z., Xie, X., & Morrow, N. R. (2003). Crude oil composition and the stability of mixed wettability in sandstones. *Petrophysics-The SPWLA Journal of Formation Evaluation and Reservoir Description, 44*.

Valori, A., & Nicot, B. (2019). Review of 60 years of NMR wettability. *Petrophysics-The SPWLA Journal of Formation Evaluation and Reservoir Description, 60*(02), 255-263.

Valori, A., Hursan, G., & Ma, S. M. (2017). Laboratory and downhole wettability from NMR T1/T2 ratio. *Petrophysics-The SPWLA Journal of Formation Evaluation and Reservoir Description, 58*(04), 352-365.

Villard, J. M., Buckley, J. S., Morrow, N. R., & Gauchet, R. (1993). Wetting and waterflood oil recovery of a moderately viscous crude oil. *Advances in core technologies*.

Ward-Williams, J. (2020). *Applying NMR Relaxation Methods to the Study of Liquids in Porous Media.* Doctoral thesis, University of Cambridge.

Welge, H. J. (1952). A simplified method for computing oil recovery by gas or water drive. *Journal of Petroleum Technology, 4*(04), 91-98.

Wendel, D. J., Anderson, W. G., & Meyers, J. D. (1987). Restored-state core analysis for the Hutton Reservoir. *SPE Formation Evaluation*, 509-517.

Wendel, D. J., Anderson, W. G., & Meyers, J. D. (1987). Restored-state core analysis for the Hutton Reservoir. *SPE Formation Evaluation*, 509-517.

Whitaker, S. (1986). Flow in porous media I: A theoretical derivation of Darcy's law. *Transport in porous media*, 3-25.

Wolcott, J. M., Groves, F. R., Trujillo, D. E., & Lee, H. G. (1993). Investigation of crude-oil/mineral interactions: factors influencing wettability alteration. *SPE Advanced Technology Series*, 117-126.

Wyckoff, R. D., & Botset, H. G. (1936). The flow of gas-liquid mixtures through unconsolidated sands. *Physics, 7*(9), 325-345.

Young, T. (1805). III. An essay on the cohesion of fluids. *Philosophical transactions of the royal society of London*, 65-87.

Yra, A. (2006). *Dispersion active en milieux poreux hétérogènes contaminés par des produits hydrocarbonés.* PhD Thesis, Bordeaux.

Zarcone, C., & Lenormand, R. (1994). Détermination expérimentale du couplage visqueux dans les écoulements diphasiques en milieu poreux. *Comptes rendus de l'Académie des sciences. Série II, Mécanique, physique, chimie, astronomie, 318*(11), 1429-1435.

Zhang, P., & Austad, T. (2005). Waterflooding in Chalk: Relationship between Oil Recovery, New Wettability Index, Brine Composition and Cationic Wettability Modifier. *SPE Europec/EAGE Annual Conference.* Madrid.

Zhang, P., & Austad, T. (2006). Wettability and oil recovery from carbonates: Effects of temperature and potential determining ions. *Colloids and Surfaces A: Physicochemical and Engineering Aspects, 279*(1-3), 179-187.

Zhou, D., & Stenby, E. H. (1990). Immiscible displacement in a porous medium simulated by a statistical model. In A. Buller, E. Berg, O. Hjelmeland, J. Kleppe, O. Torsæter, & J. Aasen, *North Sea Oil and Gas Reservoirs* (pp. 271-280). Dordrecht: Springer.

Zhou, X. M., Torsæter, O., Xie, X., & Morrow, N. R. (1995). The effect of crude-oil aging time and temperature on the rate of water imbibition and long-term recovery by imbibition. *SPE Formation Evaluation*, 259-265.

Zinszner, B., & Pellerin, F. M. (2007). *A geoscientist's guide to petrophysics.* Editions Technip.